Title

Integration, Validation, and Calibration for the Simons Observatory and the Simons Array

Author

Tsan, Tran Que

Publication Date

2024

UNIVERSITY OF CALIFORNIA SAN DIEGO

Integration, Validation, and Calibration for the Simons Observatory and the Simons Array

A dissertation submitted in partial satisfaction of the
requirements for the degree Doctor of Philosophy

in

Physics

by

Tran Tsan

Committee in charge:

Professor Kam Arnold, Chair
Professor Ertugrul Cubukcu
Professor Raphael Flauger
Professor Brian Keating
Professor Tongyan Lin

2024

The Dissertation of Tran Tsan is approved, and it is acceptable in quality and form for publication on microfilm and electronically.

University of California San Diego

2024

DEDICATION

To my family, forever my strongest support.

EPIGRAPH

Mở tung một cánh cửa lòng.
Gởi người muôn dặm cái không có gì.

Thích Pháp Hoà

Sometimes, somewhere you take something to be the truth.
If you cling to it so much,
when the truth comes in person and knocks at your door, you will not open it.

The Buddha from Our True Nature by Thích Nhất Hạnh

You can't connect the dots looking forward; you can only connect them looking backward. So you have to trust that the dots will somehow connect in your future. You have to trust in something — your gut, destiny, life, karma, whatever. Because believing that the dots will connect down the road will give you the confidence to follow your heart even when it leads you off the well-worn path and that will make all the difference.

Steve Jobs

CONTENTS

Dissertation Approval Page iii

Dedication iv

Epigraph v

Contents vi

List of Figures ix

List of Tables xiv

Acknowledgements xv

Vita xx

Abstract of the Dissertation xxiii

Chapter 1 Introduction 1
- 1.1 The Standard Model of Cosmology 2
- 1.2 Inconsistencies in the Cosmological Model and Cosmic Inflation 7
  - 1.2.1 The Flatness Problem 8
  - 1.2.2 The Horizon Problem 9
- 1.3 The Cosmic Microwave Background (CMB) 10
  - 1.3.1 CMB Temperature Anisotropies 11
  - 1.3.2 CMB Polarization 14
  - 1.3.3 Gravitational Lensing 17
- 1.4 Astrophysical Foregrounds 20

Chapter 2 The Simons Observatory (SO) 23
- 2.1 Overview 23
- 2.2 The Small Aperture Telescope (SAT) 25
  - 2.2.1 The SATs and Their Platforms 26
  - 2.2.2 Cryogenic Design 28
  - 2.2.3 Optical Design 30
- 2.3 Detector and Readout 32
  - 2.3.1 Detectors: OMT coupled feedhorn array 32
  - 2.3.2 Readout: microwave SQUID multiplexing system 34

Chapter 3 Pulse Tube Cryocooler Testing 37
- 3.1 Pulse Tube Overview 38
- 3.2 PT420-1 Pulse Tube 41
  - 3.2.1 In-lab setup 41
  - 3.2.2 Testing methodology 45

3.2.3 Data Reduction 47
3.2.4 Cooling performance vs inclination angle fitting results 48
3.2.5 Temperature uniformity over tilt range 51
3.2.6 Rotational axis dependence results 55
3.2.7 Summary and future implications 56
3.3 Other PTCs 57
3.3.1 Performance Difference between various PT420 units 59
3.3.2 Stability of the PT420s 61
3.3.3 Other checks on cooling effect 62
3.3.4 Summary 63

Chapter 4 SAT Mechanical Design 65
4.1 Carbon-Fiber (CF) Truss Design Simulation 65
4.1.1 FPA CF Truss Simulation 66
4.1.2 CRA 2 CF Truss Simulation 70
4.1.3 Selection of the Validation Criteria 73
4.2 Hoist Design for Lifting the SAT Into SATP 74
4.2.1 Interface with the Site Trailer 78
4.2.2 Interfaces to the SAT 79
4.2.3 Interfaces at Site 82
4.2.4 Hoist System Simulations 82

Chapter 5 SAT-MF1 Integration & Testing 86
5.1 Cryogenic Performance 87
5.1.1 PTC Stage Validation and Loading Estimates 88
5.1.2 Quantifying Thermal Performance on the DR Stages 93
5.1.3 Still and MC stage Heat Strap Conductivity Investigation 97
5.1.4 Frontend Filters Loading 101
5.2 Mechanical Heating Characterization 103
5.3 RF and DC Validation 108
5.3.1 Transmission Model Development 109
5.3.2 RF Check Criteria 113

Chapter 6 SO SAT-MF1 Site Commisioning 118
6.1 SAT-MF1 Deployment 118
6.1.1 Thermal Test 120
6.1.2 Thermal vibration pickup during scans 122
6.2 Discussion and Future Outlook 124

Chapter 7 The Simons Array (SA) 125
7.1 Overview of SA 125
7.1.1 PB-2b Optical and Cryogenic Design 126
7.1.2 Lenslet Sinuous Antenna Detectors 127
7.1.3 DfMux Readout 128

7.2 Gain Calibration Overview 130
 7.2.1 From Optical Power to Temperature 132
 7.2.2 Using Planets to Extract Gain 134
 7.2.3 From Gain to NET 136
 7.2.4 Stimulator Gain 138
7.3 Beam Reconstruction and Planet Gain 140
7.4 Future Outlook 145

Bibliography 146

LIST OF FIGURES

Figure 1.1. CMB temperature anisotropies map and power spectrum from the Planck Collaboration 2018 results. 13

Figure 1.2. A diagram of the Thomson Scattering process where photons from hot and cold regions scattered off electrons in a certain region, leading to a fractional polarization in the scattered light that travels toward us [1]. 15

Figure 1.3. Polarization patterns for E- (top) and B-modes (bottom). 16

Figure 1.4. Intensity and polarization (Q and U) maps at different observing frequency bands from the Planck 2018 results [2]. 18

Figure 1.5. Measurements of CMB B-mode polarization from the past couple of decades including CMB experiments such as BICEP/Keck, Planck, SPTpol, ATCPol, and POLARBEAR. 19

Figure 1.6. Temperature signal in Rayleigh-Jean brightness temperature unit for the CMB, galactic synchrotron, and thermal dust emission as a function of frequency [3]. The grey-shaded regions are the six observing bands for the Simons Observatory Small Aperture Telescopes (SATs). 21

Figure 2.1. The Simons Observatory (SO) at the Atacama Desert, Chile. 24

Figure 2.2. The atmospheric transmission at different precipitable water vapors (PWV). 25

Figure 2.3. The Large Aperture Telescope (LAT) overview. 26

Figure 2.4. The three SATs with their platforms and groundshields. 27

Figure 2.5. Cross-section view of SAT-MF1 showing the principal components. 28

Figure 2.6. SAT-MF1 frontend overview. 30

Figure 2.7. SAT-MF1 Optic Tube. Left displays the actual Optic Tube (OT) and its installation inside the SAT. Right is a cross-section view of the CAD rendering of the OT, showing its three silicon lenses. We successfully installed the OT during P6R1. 31

Figure 2.8. Structures inside a single pixel for an OMT coupled detector. 33

Figure 2.9. The Universal Focal Plane Module (UFM) overview. 34

Figure 2.10. The multiplexing circuit diagram for μMUX, which uses frequency division multiplexing. 35

Figure 3.1. Overview of the two-stage pulse tube. 39

Figure 3.2. Simulation of the gravitational effect on the PTC. 40

Figure 3.3. PT420-1 load curve data at 0°, 27.5°, and 48° with 0-51 W and 0-1.8 W on the first and second stage, respectively. 41

Figure 3.4. Experimental setup in lab showing the diodes, heaters, and the rotation of the PTC for various tilt tests. 42

Figure 3.5. Testing setup in lab for the ϕ tilt test. 46

Figure 3.6. Stage-1 performance and fit results (solid lines) using Equation 3.1 with parameter b_1 constrained to be the same for all power set points. 49

Figure 3.7. a_1 vs Stage-1 power. 50

Figure 3.8. Stage-2 performance and fit results (solid lines) using Equation 3.1 with parameter b_2 constrained to be the same for all power set points. 52

Figure 3.9. Characterization of a_2. 53

Figure 3.10. Temperature uniformity on both stages. 54

Figure 3.11. Rotational Axis Dependence on both stages. 55

Figure 3.12. Comparison between PT420-1 and SAT-1 PTC at 0° (left) and 27.5° (right). 59

Figure 3.13. Performance comparison using the same compressor but different pulse tubes (data sets 4-7). Both of the PT420-4 and PT420-1 temperature data have the same He line lengths (20 m), but PT420-4 have a slightly lower pressure. 60

Figure 3.14. Performance overtime of the PT420. 61

Figure 3.15. Impact from the different lengths of the Helium flex lines in cooling capacity using data sets 6-9. These data sets are at similar pressure setting. 62

Figure 3.16. Compressor pressure impact on cooling capacity using data sets 8-11. There is minimal impact on Stage-2, and about $\leq$3% effect on Stage-1. . . . 63

Figure 4.1. FPA carbon fiber truss. **A** portrays a 3D CAD model of the FPA truss from 1-0.1 K stage. **B** and **D** show the top and bottom view, respectively of the actual focal plane with the rings called out. **C** details one of the struts. . . . 66

Figure 4.2. FPA carbon fiber truss for tension simulation. 67

Figure 4.3. FPA carbon fiber truss for Compression Sim with the gravity vector and the force vectors. 68

Figure 4.4. FPA carbon fiber truss for Shear Sim. **A** shows the simulation setup. 69

Figure 4.5. CRA 2 (1-0.1 K) carbon fiber truss. 70

Figure 4.6. CRA 2 CF truss Simulation for Tension. **A** illustrates the simulation setup with 5g pointing up. This is the direction of gravity when the CRA is inside the SAT during transportation. **B** shows the resultant force on the Al caps. 71

Figure 4.7. CRA 2 Truss Simulation for Compression. **A** shows the simulation setup, which emulates the loads the CRA would experience during operation and installation with the SAT window facing skyward. **B** portrays the results and the direction of the net force. 71

Figure 4.8. CRA 2 CF truss Simulation Setup and Results for Shear Test. 72

Figure 4.9. An Overview of the Hoist System Assembly Integrated with SAT-MF1. . . 75

Figure 4.10. Assembly overview for the U-arch. 76

Figure 4.11. Assembly overview of the mini Support (mSupport). 77

Figure 4.12. U-channels design. The channels are tilted 40° from the vertical to clear the pointing rod in the el hub. The right figure shows the dimension of the design, which corresponds to a standard size that can be found in MetalsDepot. 78

Figure 4.13. SAT transportation from the highbay to the platform from the trailer. The picture portrays a mockup foundation and the SATP foundation, surrounded by a ground shied. The hoist system is bolted down to the foundation. 79

Figure 4.14. Clearance between the trailer and the U-arch. 80

Figure 4.15. The SAT Counterbalance System. 81

Figure 4.16. Simulation using Solidworks Finite Element Analysis (FEA) for the I-beam hoist system **case 1**. 83

Figure 4.17. Simulation using Solidworks Finite Element Analysis (FEA) for the I-beam hoist system **case 2**. 84

Figure 5.1. Cooldown timeline for SAT-MF1 to reach the base temperature of the PTCs. 87

Figure 5.2. URH COMSOL thermal loading analysis. 90

Figure 5.3. DR Validation. 93

Figure 5.4. DR revalidation vs the original validation. Black is the original validation back in 2019 using the 13 m long helium hoses and blue is the re-validation 4 years later using the 20 m long helium hoses. 94

Figure 5.5. DR load curve inside SAT-MF1. The DR was installed inside the telescope during P3R1, where the same detail load curves was applied. This load curve serves as a baseline to extract loading estimates for later cooldowns. 95

Figure 5.6. DR tilt test and the DR temperature response as a function of the cold heads' tilt angle. 96

Figure 5.7. Heatstraps placement on the Still stage. 97

Figure 5.8. Heatstraps placement on the MC stage. Two heatstraps (braided and rod) connect the DR MC to the focal plane and deliver cooling power to the detectors. The heater and thermometers are used for thermal conductivity tests. 98

Figure 5.9. Heatstrap conductivity for the Still HS during P6R1. 100

Figure 5.10. Heatstrap conductivity for the MC HS for laboratory tests (P6 and P10) and site run (SCR2). Similarly, the thermal conductivity is plotted as a function of the temperature at the hot end of the strap. 101

Figure 5.11. Frequency simulation of the 1-0.1 cold readout assembly (CRA) in Solidworks. 103

Figure 5.12. Setup for the vibration detector test for SAT-MF1 and SAT platform. Left: SAT-MF1 at UCSD. 104

Figure 5.13. Temperature fluctuation as a function of frequency. 105

Figure 5.14. Power spectral density (PSD) for SAT-MF1 and SATP. 106

Figure 5.15. Total power of the vibration measured at the accelerometer vs the temperature fluctuation on the FPA. 107

Figure 5.16. Schematic of the RF chain inside SAT-MF1. 108

Figure 5.17. The Universal Readout Harness (URH) used for SAT-MF1. 109

Figure 5.18. The two cold readout assemblies (CRAs). Left: Solidworks image of the two CRAs installed inside SAT-MF1. Right: CRA1 and CRA2 on the benchtop, together with the focal plane and the dummy wafers. 110

Figure 5.19. URH warm transmission measurement against the model. 114

Figure 5.20. URH cold transmission measurement against the model. 115

Figure 5.21. Full readout system (URH+CRAs) cold transmission measurements against the model. 115

Figure 6.1. SAT-MF1 fully assembled inside the site highbay. Top left: outside view of the whole telescope with all the vacuum hoses and electronics. Bottom left: Pictures of the UFMs on the benchtop. Right: view of the backend with the fully 7 detector wafers installed onto the FPA. 119

Figure 6.2. SAT-MF1 mounted on its platform. 120

Figure 6.3. Temperature of the focal plane during a CMB scan. Top: the focal plane temperature was regulated at 90 mK using PID. Bottom: The position of the telescope as it varied in azimuth from 100° to 137° at a fixed elevation of 50°. 123

Figure 7.1. SA observation site and 3D CAD models of the telescope and receiver . . . 126

Figure 7.2. Sinuous antenna detectors for SA. 128

Figure 7.3. Digital frequency-domain multiplexing (DfMux) circuit diagram. 129

Figure 7.4. A 3D CAD of the stimulator for PB-2b. 139

Figure 7.5. A source center map of Jupiter for a single detector with a pixel size of 0.04° or 2.4 arcmin. 141

Figure 7.6. Fits to Jupiter Signal for a Detector. 142

Figure 7.7. Historgram of the Beam Size for a Jupiter Observation. 143

Figure 7.8. Time-ordered data in K_{CMB}. The same TOD as in Figure 7.6 but this time converted to Kelvin-CMB. Notice that the signal direction flips, which makes sense that the planet signal should be a positive number. Again, the data is in blue and the fit is in red. 144

LIST OF TABLES

Table 3.1. This table lists the test settings for the two additional pulse tubes, including the ones from PT420-1. These are the main data sets used for subsequent analysis. * indicates some ambiguity in the He line length; however, the most likely scenario is 20 m. 58

Table 4.1. Simulation results for the FPA CF truss. This table displays the maximum forces that the strut cap would experience under the three different loading conditions. The numbers in the brackets are the force multiplied by the factor of safety. 70

Table 4.2. Simulation results for the CRA CF truss. This table displays the maximum forces that the strut cap would experience under the three different loading conditions. The numbers in the brackets are the force multiplied by the factor of safety. 73

Table 4.3. Summary of the pass criteria for individual strut validation. The forces here have accounted for the factor of safety. 73

Table 4.4. Factor of Safety for the I-beam hoist system. 84

Table 5.1. Estimated Loading for the PTC stages using load curves. 89

Table 5.2. URH measured loading vs predictions for the two PTC stages. 91

Table 5.3. Predicted and measured loadings for each temperature stage of SAT-MF1. . 92

Table 5.4. Loading estimates for the frontend filters. 101

Table 6.1. Loading estimates for the 40 and 4 K at the observation site. SCR1 is the first cooldown inside the site highbay, with SAT-MF1 fully integrated. 120

Table 6.2. Loading estimates for the Still and MC at the observation site. 121

Table 6.3. Predicted and measured loadings for each temperature stage of SAT-MF1 Site Edition. 122

ACKNOWLEDGEMENTS

Writing this section has proven to be both the most challenging and the most rewarding part of my dissertation. I have spent considerable time reflecting on how best to convey my gratitude and appreciation to all those who have supported, guided, and encouraged me throughout my graduate school journey. I am immensely thankful to each of you, and I know that I could not have reached these milestones without your support.

First and foremost, I would like to thank my thesis advisor, Professor Kam Arnold, for his guidance, patience, and support throughout my graduate career. His unique insight and sense of humor have been invaluable. During a particularly challenging period of self-doubt and burnout in the midst of the pandemic, Kam was extremely patient and fully supported my decision to change scenery and explore other work outside of SO SAT work. Despite his incredibly busy schedule (sometimes looking at his calendar gave me PTSD), Kam always made time to answer my questions, review my dissertation, and help plan for the future. I am especially thankful for this past year when he ~~grilled~~ prepped me for my defense and dissertation. I have learned so much about CMB and the field in the past few months and it is true that the more we learn, the more we realize how much we (I) don't know.

I would also like to extend my thanks to Professor Nicholas Galitzki, who has been like a second advisor to me. As a postdoc in our CMB lab, Nick's mentorship during the early stages of my degree was crucial. I have learned so much about instrumentation work from him. He taught me not only his technical skills and passion for CMB work but also essential soft skills such as organization and leadership. Nick's support in building my early career, from introducing me to important conferences to helping me with fellowship applications to advocating for outreach activities, has been invaluable. His teachings and my experience on the SAT will always be an integral part of my scientific journey. I am incredibly fortunate to have had two mentors whose support has been pivotal in my success.

Third, I would like to thank all my fellow cosmology labmates, both at UCSD and from other institutions, who have made working on SO so much more enjoyable: Jake Spisak, Michael

Randall, Max Silva-Feaver, Joe Seibert, Bryce Bixler, JB Lloyd, Jack Lashner, Remington Gerras, Aashrita Mangu, Lance Corbett, Jenna Moore, Kevin Crowley, and many others. Jake and Michael, I am extremely grateful for their support in the SAT work and during all those late nights that we had to pull to get back on schedule. They were always there when I needed them, sometimes even taking on the most tedious work to get things done. Michael, thank you for having my back when we had to integrate the SAT ourselves after Nick left for his professorship. Max and Joe, I learned so much about detectors and readout from them. I feel like I asked Max hundreds of times about μMUX, and he was always patiently explaining it to me. Bryce, similarly, thank you for your support in the SAT work. In this process, I have learned a lot about the CHWP. Thank you to JB, who was always ready and efficient in fulfilling my requests and helping me with my SAT work, especially with the MLI and enclosures. Thank you to Aashrita for being my confidant in SAT work, particularly during the last few months when we were scrambling to finish our dissertation and graduate. SAT work can never be the same without her savage sense of humor and sarcasm and Lance's low-key roasting comments.

I would also like to thank Jen Ito for her help with the graduate women in Physics (GWIP) and PB-2b. Leading GWIP with her has been a great experience and I appreciate all our talks about diversity, women in physics, imposter syndrome, and so on. Then I would like to thank Lindsay Lowry, Megan Russell, Kyohei Yamada, Tylor Adkins, Nicole Neto Godry Farias, and Kana Sakaguri for all their support in my SA work. Lindsay helped me a lot in answering questions about SA and PB-2b. Megan and I joined the SA analysis working group at the same time and I really am glad to have her support throughout. Kyohei was always patiently answering all my questions about gain calibration. I would have not been able to pick up on the analysis as quickly without his help and feedback. Tylor and Nicole gave me a very warm welcome during my stay at Berkeley for my fellowship work on SA and facilitated my integration into the work. Kana similarly helped answer a lot of my questions about the stimulator and just analysis in general.

I would like to thank Dr. Katie Harrington for being my SO mentor and providing me with perspective on how to navigate the CMB community as a female scientist. I would like to thank Dr. Sara Simon for her advice and resources during my postdoc application process.

Thank you to Professor Brian Keating, Raphael Flauger, Tongyan Lin, and Ertugrul Cubukcu for serving on my thesis committee. Thank you to Professor Shelley Wright for introducing me to the astrophysics department at UCSD when I was an undergrad.

Next, I would like to thank my Sloan family and mentors, especially Sinai Cota and Shana Slebioda for their support over the year. Sinai would meet with me quarterly and she always helped me through grad school from being a great listener to connecting me with resources to facilitate my academic career. She always checked in on me and helped plan out my graduation process. Her asking for accountabilities from me helped push me forward during the past year when I have been feeling so burned out.

Thank you to the Simons Foundation for providing me the opportunity to join the Simons Observatory and Simons Array and discover the wonderful field of CMB.

I would also like to thank all my friends and mentors that I have encountered through life for your encouragement and teaching are greatly appreciated.

Last but not least, thank you to my family for being the greatest support and advocate in my life. Thank you to my parents who have always silently believed in me and supported my decision to go to graduate school, even though this was a very foreign concept to them. As with all Asian parents, my mom wanted me to become a doctor. Well Mom, now I am also a Doctor (of Philosophy). Regardless of her wishes or her difficulty in understanding my field, she has always placed my well-being as her top priority. Every time I explained my work to her, she would think that I either was working to study the moon and planets or was doing construction work. This was the difficulty of trying to explain physics or CMB work to a family member using another language. Nevertheless, after every conversation (or the beginning of our conversations), the questions that she always asked were am I eating enough or going to sleep on time. My dad, on the other hand, is a person of few words. However, it was when I was feeling the most burned out, physically and mentally tired, and started doubting myself, he told me that I don't have to work so hard, that I can quit if I want as he will always support me. He just suddenly dropped this sentence during dinner without me even explaining what I was going through. If I have to say, my family is a very typical Asian home so excellence is always expected. It was their acceptance and care that gave me the freedom and confidence to explore what I want to do in life since they will always be my greatest support. Then there are my older siblings and their partners, who have played an integral part in my life. My two older sisters are my role models and spiritual teachers in life, and they have taught me so much. I learned to breathe, be patient, be confident, and be beautiful from them. From childhood to now, my brother has always been there for me and he has never missed any of the important events in my life even when my parents could not make some of them. Thank you for always being there to help me navigate through a new school, a new country, a new language, and now grad school. My sister-in-law, my friend and fellow foodie, let us aim to taste all the vegetarian cuisines around the world. Finally, thank you to my two adorable nephews who have always brightened my day.

The dissertation author acknowledges Professor Raphael Flauger and David Tytler's teaching and guidance in my preparation for Chapter 1 and the subsequent thesis defense. Prof. Flauger's cosmology class provided a very systematic formulation of the CMB and its polarization, while Prof. Tytler's class provided a much-needed conceptual view of cosmology.

Chapter 3 is a reprint of the material as it appears in Tran Tsan, Nicholas Galitzki, Aamir M. Ali, Kam Arnold, Gabriele Coppi, Tamar Ervin, Logan Foote, Brian Keating, Jack Lashner, John Orlowski-Scherer, Michael J. Randall, Joseph Seibert, Jacob Spisak, Grant P. Teply, Zhilei Xu, and Ningfeng Zhu. The effects of inclination on a two stage pulse tube cryocooler for use with a ground based observatory. The dissertation author was the primary investigator and author of this paper. *Cryogenics*, 117:103323, July 2021. The last portion of this chapter (Section 3.3) includes additional results from other tests.

Chapter 4 (Section 4.1) and Chapter 5, in part, have been submitted for publication of the material to The Astrophysical Journal Supplement Series, 2024. Nicholas Galitzki, Tran Tsan, Jake Spisak, Michael Randall, Max Silva-Feaver, Joseph Seibert, Jacob Lashner, Shunsuke

Adachi, Sean M. Adkins, Thomas Alford, Kam Arnold, Peter C. Ashton, Jason E. Austermann, Carlo Baccigalupi, Andrew Bazarko, James A. Beall, Sanah Bhimani, Bryce Bixler, Gabriele Coppi, Lance Corbett, Kevin D. Crowley, Kevin T. Crowley, Samuel Day-Weiss, Simon Dicker, Peter N. Dow, Cody J. Duell, Shannon M. Duff, Remington G. Gerras, John C. Groh, Jon E. Gudmundsson, Kathleen Harrington, Masaya Hasegawa, Erin Healy, Shawn W. Henderson, Johannes Hubmayr, Jeffrey Iuliano, Bradley R. Johnson, Brian Keating, Ben Keller, Kenji Kiuchi, Anna M. Kofman, Brian J. Koopman, Akito Kusaka, Adrian T. Lee, Richard A. Lew, Lawrence T. Lin, Michael J Link, Tammy J. Lucas, Marius Lungu, Aashrita Mangu, Jeffrey J McMahon, Amber D. Miller, Jenna E. Moore, Magdy Morshed, Hironobu Nakata, Federico Nati, Laura B. Newburgh, David V. Nguyen, Michael D. Niemack, Lyman A. Page, Kana Sakaguri, Yuki Sakurai, Mayuri Sathyanarayana Rao, Lauren J. Saunders, Jordan E. Shroyer, Junna Sugiyama, Osamu Tajima, Atsuto Takeuchi, Refilwe Tanah Bua, Grant Teply, Tomoki Terasaki, Joel N. Ullom, Jeffrey L. Van Lanen, Eve M. Vavagiakis, Michael R Vissers, Liam Walters, Yuhan Wang, Zhilei Xu, Kyohei Yamada, and Kaiwen Zheng. The Simons Observatory: Design, integration, and testing of the small aperture telescopes, 2024.

VITA

2017	Bachelor of Science, University of California Los Angeles
2024	Doctor of Philosophy, University of California San Diego

PUBLICATIONS

Nicholas Galitzki, Tran Tsan, Jake Spisak, Michael Randall, Max Silva-Feaver, Joseph Seibert, Jacob Lashner, Shunsuke Adachi, Sean M. Adkins, Thomas Alford, Kam Arnold, Peter C. Ashton, Jason E. Austermann, Carlo Baccigalupi, Andrew Bazarko, James A. Beall, Sanah Bhimani, Bryce Bixler, Gabriele Coppi, Lance Corbett, Kevin D. Crowley, Kevin T. Crowley, Samuel Day-Weiss, Simon Dicker, Peter N. Dow, Cody J. Duell, Shannon M. Duff, Remington G. Gerras, John C. Groh, Jon E. Gudmundsson, Kathleen Harrington, Masaya Hasegawa, Erin Healy, Shawn W. Henderson, Johannes Hubmayr, Jeffrey Iuliano, Bradley R. Johnson, Brian Keating, Ben Keller, Kenji Kiuchi, Anna M. Kofman, Brian J. Koopman, Akito Kusaka, Adrian T. Lee, Richard A. Lew, Lawrence T. Lin, Michael J Link, Tammy J. Lucas, Marius Lungu, Aashrita Mangu, Jeffrey J McMahon, Amber D. Miller, Jenna E. Moore, Magdy Morshed, Hironobu Nakata, Federico Nati, Laura B. Newburgh, David V. Nguyen, Michael D. Niemack, Lyman A. Page, Kana Sakaguri, Yuki Sakurai, Mayuri Sathyanarayana Rao, Lauren J. Saunders, Jordan E. Shroyer, Junna Sugiyama, Osamu Tajima, Atsuto Takeuchi, Refilwe Tanah Bua, Grant Teply, Tomoki Terasaki, Joel N. Ullom, Jeffrey L. Van Lanen, Eve M. Vavagiakis, Michael R Vissers, Liam Walters, Yuhan Wang, Zhilei Xu, Kyohei Yamada, and Kaiwen Zheng. The simons observatory: Design, integration, and testing of the small aperture telescopes, 2024. *Submitted to The Astrophysical Journal Supplement Series.*

Megan Russell, Kana Sakaguri, Lindsay Ng Lowry, Tylor Adkins, Kam Arnold, Carlo Baccigalupi, Kevin T. Crowley, Tucker Elleflot, Nicole Farias, Masashi Hazumi, Jennifer Ito, Oliver Jeong, Adrian Lee, Michael Lew, Jacob Nelson, Praween Siritanasak, Tran Tsan, and Polarbear Collaboration. Deployment of POLARBEAR-2b. *Journal of Low Temperature Physics*, May 2024.

K. Yamada, B. Bixler, Y. Sakurai, P. C. Ashton, J. Sugiyama, K. Arnold, J. Begin, L. Corbett, S. Day-Weiss, N. Galitzki, C. A. Hill, B. R. Johnson, B. Jost, A. Kusaka, B. J. Koopman, J. Lashner, A. T. Lee, A. Mangu, H. Nishino, L. A. Page, M. J. Randall, D. Sasaki, X. Song, J. Spisak, T. Tsan, Y. Wang, and P. A. Williams. The simons observatory: Cryogenic half wave plate rotation mechanism for the small aperture telescopes. *Review of Scientific Instruments*, 95(2), February 2024.

Nadia Dachlythra, Adriaan J. Duivenvoorden, Jon E. Gudmundsson, Matthew Hasselfield, Gabriele Coppi, Alexandre E. Adler, David Alonso, Susanna Azzoni, Grace E. Chesmore, Giulio Fabbian, Ken Ganga, Remington G. Gerras, Andrew H. Jaffe, Bradley R. Johnson, Brian Keating, Reijo Keskitalo, Theodore S. Kisner, Nicoletta Krachmalnicoff, Marius Lungu, Frederick Matsuda, Sigurd Naess, Lyman Page, Roberto Puddu, Giuseppe Puglisi, Sara M. Simon, Grant Teply, Tran Tsan, Edward J. Wollack, Kevin Wolz, and Zhilei Xu. The simons observatory: Beam characterization for the small aperture telescopes. *The Astrophysical Journal*, 961(1):138, January 2024.

Kevin D. Crowley, Peter Dow, Jordan E. Shroyer, John C. Groh, Bradley Dober, Jacob Spisak, Nicholas Galitzki, Tanay Bhandarkar, Mark J. Devlin, Simon Dicker, Patricio A. Gallardo, Kathleen Harrington, Jeffrey Iuliano, Bradley R. Johnson, Delwin Johnson, Anna M. Kofman, Akito Kusaka, Adrian Lee, Michele Limon, Federico Nati, John Orlowski-Scherer, Lyman Page, Michael Randall, Grant Teply, Tran Tsan, Edward J. Wollack, Zhilei Xu, and Ningfeng Zhu. The Simons Observatory: A large-diameter truss for a refracting telescope cooled to 1 K. *Review of Scientific Instruments*, 93(5):055106, 05 2022.

Ningfeng Zhu, Tanay Bhandarkar, Gabriele Coppi, Anna M. Kofman, John L. Orlowski-Scherer, Zhilei Xu, Shunsuke Adachi, Peter Ade, Simone Aiola, Jason Austermann, Andrew O. Bazarko, James A. Beall, Sanah Bhimani, J. Richard Bond, Grace E. Chesmore, Steve K. Choi, Jake Connors, Nicholas F. Cothard, Mark Devlin, Simon Dicker, Bradley Dober, Cody J. Duell, Shannon M. Duff, Rolando Dünner, Giulio Fabbian, Nicholas Galitzki, Patricio A. Gallardo, Joseph E. Golec, Saianeesh K. Haridas, Kathleen Harrington, Erin Healy, Shuay-Pwu Patty Ho, Zachary B. Huber, Johannes Hubmayr, Jeffrey Iuliano, Bradley R. Johnson, Brian Keating, Kenji Kiuchi, Brian J. Koopman, Jack Lashner, Adrian T. Lee, Yaqiong Li, Michele Limon, Michael Link, Tammy J Lucas, Heather McCarrick, Jenna Moore, Federico Nati, Laura B. Newburgh, Michael D. Niemack, Elena Pierpaoli, Michael J. Randall, Karen Perez Sarmiento, Lauren J. Saunders, Joseph Seibert, Carlos Sierra, Rita Sonka, Jacob Spisak, Shreya Sutariya, Osamu Tajima, Grant P. Teply, Robert J. Thornton, Tran Tsan, Carole Tucker, Joel Ullom, Eve M. Vavagiakis, Michael R. Vissers, Samantha Walker, Benjamin Westbrook, Edward J. Wollack, and Mario Zannoni. The simons observatory large aperture telescope receiver. *The Astrophysical Journal Supplement Series*, 256(1):23, September 2021.

Tran Tsan, Nicholas Galitzki, Aamir M. Ali, Kam Arnold, Gabriele Coppi, Tamar Ervin, Logan Foote, Brian Keating, Jack Lashner, John Orlowski-Scherer, Michael J. Randall, Joseph Seibert, Jacob Spisak, Grant P. Teply, Zhilei Xu, and Ningfeng Zhu. The effects of inclination on a two stage pulse tube cryocooler for use with a ground based observatory. *Cryogenics*, 117:103323, July 2021.

Kenji Kiuchi, Shunsuke Adachi, Aamir M. Ali, Kam Arnold, Peter Ashton, Jason E. Austermann, Andrew Bazako, James A. Beall, Yuji Chinone, Gabriele Coppi, Kevin D. Crowley, Kevin T. Crowley, Simon Dicker, Bradley Dober, Shannon M. Duff, Giulio Fabbian, Nicholas Galitzki, Joseph E. Golec, Jon E. Gudmundsson, Kathleen Harrington, Masaya Hasegawa, Makoto Hattori, Charles A. Hill, Shuay-Pwu Patty Ho, Johannes Hubmayr, Bradley R. Johnson, Daisuke Kaneko, Nobuhiko Katayama, Brian Keating, Akito Kusaka, Jack Lashner, Adrian T. Lee, Frederick Matsuda, Heather McCarrick, Masaaki Murata, Federico Nati, Yume Nishinomiya, Lyman Page, Mayuri Sathyanarayana Rao, Christian L. Reichardt, Kana Sakaguri, Yuki Sakurai, Joseph Sibert, Jacob Spisak, Osamu Tajima, Grant P. Teply, Tomoki Terasaki, Tran Tsan, Samantha Walker, Edward J. Wollack, Zhilei Xu, Kyohei Yamada, Mario Zannoni, and Ningfeng Zhu. The simons observatory small aperture telescope overview. In Heather K. Marshall, Jason Spyromilio, and Tomonori Usuda, editors, *Ground-based and Airborne Telescopes VIII*. SPIE, Dec 2020.

Aamir M. Ali, Shunsuke Adachi, Kam Arnold, Peter Ashton, Andrew Bazarko, Yuji Chinone, Gabriele Coppi, Lance Corbett, Kevin D. Crowley, Kevin T. Crowley, Mark Devlin, Simon Dicker, Shannon Duff, Chris Ellis, Nicholas Galitzki, Neil Goeckner-Wald, Kathleen Harrington, Erin Healy, Charles A. Hill, Shuay-Pwu Patty Ho, Johannes Hubmayr, Brian Keating, Kenji Kiuchi, Akito Kusaka, Adrian T. Lee, Michael Ludlam, Aashrita Mangu, Frederick Matsuda, Heather McCarrick, Federico Nati, Michael D. Niemack, Haruki Nishino, John Orlowski-Scherer, Mayuri Sathyanarayana Rao, Christopher Raum, Yuki Sakurai, Maria Salatino, Trevor Sasse, Joseph Seibert, Carlos Sierra, Maximiliano Silva-Feaver, Jacob Spisak, Sara M. Simon, Suzanne Staggs, Osamu Tajima, Grant Teply, Tran Tsan, Edward Wollack, Bejamin Westbrook, Zhilei Xu, Mario Zannoni, and Ningfeng Zhu. Small Aperture Telescopes for the Simons Observatory. *Journal of Low Temperature Physics*, 200(5-6):461–471, April 2020.

ABSTRACT OF THE DISSERTATION

Integration, Validation, and Calibration for the Simons Observatory and the Simons Array

by

Tran Tsan

Doctor of Philosophy in Physics

University of California San Diego, 2024

Professor Kam Arnold, Chair

Ground-based Cosmic Microwave Background (CMB) experiments have significantly advanced our understanding of the universe. Theories of cosmic inflation predict a period of rapid expansion after the Big Bang, explaining the isotropy and flatness observed in our universe. This proposed inflationary period is expected to have generated gravitational waves, manifesting as primordial B-modes observable in the CMB polarization signal at large angular scales. Maps of CMB are the most straightforward method to search for primordial gravitation waves. Moreover, the CMB temperature and polarization maps offer insights into fundamental questions about neutrino mass, dark matter, and dark energy. This information holds the potential to significantly narrow down the theoretical framework governing the origin and evolution of our universe.

This dissertation outlines my work on two ground-based CMB experiments: the Simons Observatory (SO) and the Simons Array (SA). SO, an upcoming experiment in Chile, aims to measure the temperature and polarization of CMB in six frequency bands from 27 to 280 GHz. It will deploy three 0.5-meter Small Aperture Telescopes (SATs) and one 6-meter Large Aperture Telescope (LAT), housing over 60,000 cryogenic bolometers. The dissertation primarily focuses on the integration of the first 90/150 GHz SAT, encompassing cryogenic testing of subsystems, mechanical design & testing, RF and DC performance, and finally on-site deployment. Next, I present my work on the gain calibration analysis for SA, a neighboring current CMB experiment. Utilizing data from the second receiver, this analysis aims to characterize the instrument beams and calibrate the raw observation data to CMB temperature. Lastly, I provide a brief outlook on the future of the experiment.

Chapter 1

Introduction

After the Big Bang, the Universe started extremely compact and has been expanding ever since. Many astrophysical observations such as measurements from the Cosmic Microwave Background during the early times (section 1.3) and recession velocity measurements of galaxies during late times have supported this foundational concept of an expanding universe. As the universe expanded, various processes unfolded, such as the formations of protons, neutrons, and then deuterium. Notably, 380,000 years after the Big Bang, as the universe cooled to about 1 eV (T $\sim$ 3000 K), protons and electrons combined to form neutral hydrogen in a period known as recombination. Before this stage, the Universe was a hot plasma, with free electrons scattering off photons, rendering it highly opaque. The subsequent decrease in the number of free electrons allowed photons to free-stream, leading to the currently detectable radiation known as the Cosmic Microwave Background (CMB). Carrying imprints from the primordial universe, the CMB enables us to peer back to the epoch of recombination.

This dissertation begins with an overview of the standard model of cosmology and the cosmological challenges motivating CMB research in the first chapter, followed by an overview of the Simons Observatory in Chapter 2. Then chapter 3 dives into the characterization of the pulse tube cryocooler, an important cryogenic technology used in the telescope to cool the receiver. Chapter 4 describes my design and simulation analysis for SO Small Aperture Telescopes' (SAT) mechanical structures. Results from the testing and validation of the first

SO SAT are presented in chapter 5, rounding up with a summary of the site integration and commissioning work that I did for the SAT in chapter 6. Finally, chapter 7 outlines my calibration analysis for the Simons Array, a current CMB experiment located in Chile.

1.1 The Standard Model of Cosmology

The Standard Model of cosmology or the Λ-Cold-Dark-Matter (ΛCDM) model rests upon two foundational principles: the Standard Model (SM) of Particle Physics, which delves into the behavior of particles at the quantum mechanic level, and the general theory of relativity (GR), which governs the dynamics of massive celestial bodies. The SM elucidates the composition of matter through particles such as quarks (e.g. protons and neutrons), leptons (e.g. electrons and neutrinos), bosons, and Higgs bosons. Crucially, the SM extends its reach to the very early Universe, shedding light on the physics behind elemental abundances, the presence of the cosmic neutrino background, and the temperature at recombination, assuming the energy density follows the expectations prescribed by general relativity. The general relativity discussions are reproduced in some details below as the first step to understanding the expanding universe. Drawing from the teachings of Dr. Raphael Flauger's cosmology class, the derivation navigates through the line element for a flat, isotropic, and homogeneous universe — a metric tensor frequently employed in GR to delineate spacetime geometry. Combining this metric tensor with the Christoffer symbols, we can solve for the Ricci tensor to arrive at the Friedmann equation and the cosmological parameters that characterize the state of the universe. Solving the Friedmann equation elucidates the physics behind many of the astrophysical processes.

The spacetime geometry can be described by a metric tensor, $g_{\mu\nu}$ and a line element ds, in a general form of

$$ds^2 = g_{\mu\nu} x^\mu x^\nu \tag{1.1}$$

where μ and ν are indices that sum over the three spatial and one temporal dimensions. From the observations of the CMB, we can conclude that the universe is isotropic. Assuming that the universe is also homogeneous as we do not expect to be in a special point or there to be any preferred direction, we can then constrain the spacetime metric in Equation 1.1 to be in the following form:

$$ds^2 = -c^2dt^2 + a^2(t)\left(d\mathbf{x}^2 + K\frac{\mathbf{x}\cdot d\mathbf{x}}{1-K\mathbf{x}^2}\right) \tag{1.2}$$

where $K = 1$ for a closed universe, $K = -1$ for an open universe, and $K = 0$ for a flat universe [4]. The scale factor, a(t), describes how much the universe is expanding. For the rest of this chapter, any bold parameter, (e.g. **x**), represents a three-spatial-dimension vector. The line element in Equation 1.2 is often referred to as the Friedmann-LeMaitre-Robertson-Walker (FLRW) metric. Current experimental data suggest that our Universe is flat. So for an isotropic, homogeneous, and flat universe, the above metric simplifies down to

$$ds^2 = -c^2dt^2 + a^2(t)d\mathbf{x}^2. \tag{1.3}$$

In spherical polar coordinates, we can use $d\mathbf{x}^2 = dr^2 + r^2d\Omega$ where $d\Omega \equiv d\theta^2 + sin^2\theta d\phi^2$ to rewrite the line element as

$$ds^2 = -dt^2 + a^2(t)(dr^2 + r^2d\Omega), \tag{1.4}$$

in which we move into the unit system of the speed of light so $c = 1$.

Now with the spacetime metric above for a flat, homogeneous, and isotropic universe, let us introduce Einstein's field equations that relate this metric, $g_{\mu\nu}$, to matter and energy in the universe:

$$G_{\mu\nu} \equiv R_{\mu\nu} - \frac{1}{2}g_{\mu\nu}R = 8\pi GT_{\mu\nu} \tag{1.5}$$

$G_{\mu\nu}$ is also called the Einstein tensor. Later Einstein added a constant Λ to the field equation in an attempt to solve the problem of a static universe. The constant later became known as the cosmological constant and it describes dark matter and dark energy. So the field equation can be rewritten as

$$R_{\mu\nu} - \frac{1}{2}g_{\mu\nu}R + g_{\mu\nu}\Lambda = 8\pi G T_{\mu\nu} \tag{1.6}$$

The left of Einstein's field equation denotes the spacetime metric together with the Ricci scalar (R) and tensor ($R_{\mu\nu}$), describable by the Christoffer symbols ($\Gamma^{\mu}_{\alpha\beta}$). The Ricci scalar, R, takes the form of

$$R = g^{\mu\nu}R_{\mu\nu}, \tag{1.7}$$

where the tensor is

$$R_{\mu\nu} = \frac{\partial\Gamma^{\rho}_{\mu\nu}}{\partial x^{\rho}} - \frac{\partial\Gamma^{\rho}_{\rho\mu}}{\partial x^{\nu}} + \Gamma^{\rho}_{\mu\nu}\Gamma^{\sigma}_{\rho\sigma} - \Gamma^{\rho}_{\mu\sigma}\Gamma^{\sigma}_{\rho\nu}. \tag{1.8}$$

The Christoffel symbols by definition are

$$\Gamma^{\mu}_{\alpha\beta} = \frac{g^{\mu\nu}}{2}\left(\frac{\partial g_{\alpha\nu}}{\partial x^{\beta}} + \frac{\partial g_{\beta\nu}}{\partial x^{\alpha}} - \frac{\partial g_{\alpha\beta}}{\partial x^{\nu}}\right) \tag{1.9}$$

and $g^{\mu\nu}$ is the inverse of the matrix $g_{\mu\nu}$. For a flat universe, the only non-zero terms of the Christoffel symbols are

$$\Gamma^{0}_{ij} = \frac{1}{2}\frac{\partial g_{ij}}{\partial t} = a\dot{a}\delta_{ij} = Hg_{ij}, \tag{1.10}$$

$$\Gamma^{i}_{0j} = \delta_{ij}\frac{\dot{a}}{a} = H\delta_{ij} \tag{1.11}$$

where i, j run from 1 to 3 and are spatial coordinates. The overdots indicate the derivatives with respect to time. H is the Hubble rate or the rate of the expansion of the universe. See the full derivation in chapter 2 of Dodelson's Modern Cosmology [5].

Then to the right of the field equation is the energy-momentum tensor, $T_{\mu\nu}$. Isotropy and homogeneity in the universe imply that the only non-zero components of this tensor are

$$T^{00} = \rho(t), \tag{1.12}$$

and

$$T^{ij} = \frac{1}{a^2}\delta_{ij}p(t), \tag{1.13}$$

where $\rho(t)$ and p(t) are the energy density and pressure of the medium, respectively.

So far, we have discussed the spacetime metric and see how it relates to the expansion rate (from scale factor) and the energy densities in an FLRW universe. Next, let's examine the dynamic expansion and evolution of the universe. To do this, we need to derive the Friedmann equation from the field equation as they are crucial for understanding how the expansion rate has changed over time as the energy density and pressure in the universe changed. Using the Christoffel symbols from equations 1.10 and 1.11, we can solve for the Ricci tensor and rewrite the field equation (1.5) to get the following equations:

$$H^2 = \left(\frac{\dot{a}}{a}\right)^2 = \frac{8\pi G}{3}\rho \tag{1.14}$$

$$2\dot{H} + 3H^2 = -8\pi G p, \tag{1.15}$$

for the 00-component and ij-component, respectively. Equation 1.14 is called the Friedmann equation.

As the universe expanded, different energy densities became dominant and the universe experienced three different eras: radiation, matter, and cosmological constant dominated, sequentially. We are currently in the cosmological constant era. We can examine the state of the universe in each of these eras by first deriving the relationship between energy density and the scale factor from the stress tensor, $T_{\mu\nu}$, then rewriting the Friedmann equation accordingly. From the stress tensor in Equation 1.12 and 1.13 and the conversation of energy, we can extract the equation of state and the continuity equation to be

$$p = wp \tag{1.16}$$

$$\dot{\rho} + 3H(1+w)\rho = 0, \tag{1.17}$$

respectively. Here, w = 1/3, 0, and -1 for radiation, pressureless dust (matter), and vacuum energy (cosmological constant). Thus solving the continuity equation 1.17 gives us the energy density as a function of the scale factor during the three different eras:

$$\rho(t) = \rho_0 \left(\frac{a_0}{a(t)} \right)^4 \tag{1.18}$$

$$\rho(t) = \rho_0 \left(\frac{a_0}{a(t)} \right)^3 \tag{1.19}$$

$$\rho(t) = \rho_0. \tag{1.20}$$

We can see that for radiation or photons, the energy density scales inversely with a^4, where the three powers of the scale factor are from the comoving photons' number density and the fourth comes from radiation energy that scales like 1/a. As for matter, which is just like pressureless dust, the energy density scales inversely with the volume so a^{-3}. Finally, in the current cosmological constant era, we have a constant energy density. Thus the total energy density is simply

$$\rho(t) = \rho_{r0} \left(\frac{a_0}{a(t)} \right)^4 + \rho_{m0} \left(\frac{a_0}{a(t)} \right)^3 + \rho_{\Lambda 0}. \tag{1.21}$$

Now let's define the cosmological parameters that we often see in literature, starting with the present critical energy density as

$$\rho_{0,c} = \frac{3H_0^2}{8\pi G}, \tag{1.22}$$

where H_0 is the present Hubble rate and the cosmological parameters as

$$\Omega_m = \frac{\rho_{0m}}{\rho_{0,c}}, \tag{1.23}$$

$$\Omega_r = \frac{\rho_{0r}}{\rho_{0,c}}, \tag{1.24}$$

$$\Omega_\Lambda = \frac{\rho_{0\Lambda}}{\rho_{0,c}}, \tag{1.25}$$

which describes the present energy density ratio in matter, radiation, and vacuum energy (cosmological constant). Consequently, the Friedmann equation becomes

$$H^2 = H_0^2 \left[\Omega_\Lambda + \Omega_m \left(\frac{a_0}{a} \right)^3 + \Omega_r \left(\frac{a_0}{a} \right)^4 \right]. \tag{1.26}$$

Setting a = a_0, Equation 1.26 gives the following relationship for the total energy density ratio

$$\Omega_{tot} = \Omega_\Lambda + \Omega_m + \Omega_r = 1 \tag{1.27}$$

for a flat universe. The state of the universe is quantified by these cosmological parameters inside this equation, thus understanding them is critical in probing deeper into the physics that govern the universe.

1.2 Inconsistencies in the Cosmological Model and Cosmic Inflation

While the ΛCDM model offers a framework for understanding the universe, it remains incomplete, unable to account for cosmological phenomena such as the origin of the universe or Big Bang physics, matter-antimatter asymmetry, dark energy, dark matter, and inconsistencies like the horizon and flatness problem [6]. The theoretical concepts surrounding the Big Bang have been postulated, with a few observations supporting the notion of an expanding universe from an extremely dense and hot state. Yet, much of its cosmology and direct evidence remains a mystery. Similarly, much is still unknown about the nature of dark matter and dark energy even though they make up approximately 27% and 68% of the universe [6]. Adding to the complexity are two notable challenges in current cosmology— the flatness and the horizon problem— prompting the proposal of inflation as a potential solution to address these inconsistencies.

1.2.1 The Flatness Problem

For a flat universe, $\rho = \rho_c$ and $\Omega_{tot} = 1$. However, if we consider curvature, then we can generalize Equation 1.22 and 1.27 to be

$$\rho_c = \frac{3H^2}{8\pi G}, \tag{1.28}$$

$$\Omega = \frac{\rho}{\rho_c}, \tag{1.29}$$

and rewrite Equation 1.14 as

$$H^2 = \frac{8\pi G}{3}\rho - \frac{k}{a^2}. \tag{1.30}$$

Multiply Equation 1.30 by $\frac{3a^2}{8\pi G}$ and using the relations in Equation 1.28 and 1.29 with a bit of rearrangement, we get

$$\rho a^2(1-\Omega^{-1}) = \frac{3k^2}{8\pi G} = constant. \tag{1.31}$$

The above equation suggests that the left-hand side must remain constant throughout the evolution of the universe from the Big Bang to the present day. So we have[1]

$$\rho a^2(1-\Omega^{-1}) = \rho_0 a_0^2(1-\Omega_0^{-1}). \tag{1.32}$$

Using the relation of $a = a_0/(1+z)$, the above equation becomes

$$|1-\Omega^{-1}| = \frac{\rho_0}{\rho}(1+z)^2(1-\Omega_0^{-1}). \tag{1.33}$$

Early observation of the CMB has measured $\Omega_{tot} = 1.02^{+0.05}_{-0.06}$ [8], which is consistent with our expectations for a flat universe. Using this value for Ω_0 and looking back to $z_{eq} \sim 3000$ at the radiation dominated period where $\rho = \rho_0(1+z)^4$, then Equation 1.33 becomes

---

[1] this derivation follows the notes on [7].

$$\frac{|\Omega - 1|}{\Omega} = \frac{1 - 1.02^{-1}}{(1+z)^2} \tag{1.34}$$

$$\frac{|\Omega - 1|}{\Omega} \sim 2 \text{ x } 10^{-9} \tag{1.35}$$

As we go further back, z increases and Ω becomes increasingly fine-tuned, allowing almost no deviation from unity. This limit implies that if there was any tiny deviation from flatness during the early universe, then some mechanism must have adjusted and normalized it to the unity value that we see today. A group of theories suggests inflation as a solution, which claims that the early universe experienced a rapid expansion for a short period such that regardless of the initial energy density value, inflation would have flattened out the curvature.

1.2.2 The Horizon Problem

The remarkable uniformity and isotropy (one part in 10^5) observed in the CMB indicate that the early universe was in a state of thermal equilibrium and was causally connected [7]. Regions of the universe that were not causally connected at that time, meaning they were separated by distances greater than the distance light could have traveled given the age and expansion history, could not communicate with each other. At any point in the expansion history of the universe, there has always been a causal horizon, representing the limit beyond which regions cannot exchange information. During recombination, when CMB photons began to freely travel through space, the causal horizon corresponded to an angular scale of about 1°. However, the uniformity and isotropy of the CMB extend well above this scale [9]. This discrepancy between observations and expectations is called the horizon problem.

The theory of inflation, which claims that the universe experienced a period of rapid expansion by a factor of 10^{30} or more [7], addresses this paradox. In an inflationary scenario, regions initially considered beyond causal contact with each other under the standard Big Bang expansion are brought into closer proximity thus reaching thermal equilibrium. While inflation provides solutions to these cosmological challenges, direct evidence remains elusive. Questions persist about the specific mechanism and timeline of inflation. If inflation did occur, it would generate gravitational waves. The CMB, holding potential traces of these gravitational waves, becomes a crucial tool in unraveling the mysteries of inflationary physics. The next section delves into the CMB and its immense capacity to deepen our understanding of the early universe.

1.3 The Cosmic Microwave Background (CMB)

The Cosmic Microwave Background (CMB) is electromagnetic radiation from the early universe last scattering during the recombination epoch. CMB carries imprints from the primordial processes, offering invaluable insights into the universe's underlying physics. In 1964, Penzias and Wilson, along with Dicke's group in Princeton, made a landmark discovery: the detection of CMB radiation [10, 11]. Since then, numerous experiments have pursued increasingly precise measurements of the CMB. Notably, NASA's Cosmic Background Explorer (COBE) made a pivotal advancement by measuring the CMB black body spectrum using the Far Infrared Absolute Spectrophotometer. This measurement revealed a CMB temperature of $T_{CMB} = 2.726 \pm 0.010$ K [12]. Subsequently, advancements have further refined our understanding, with the current best measurement placing the CMB temperature at $T_{CMB} = 2.72548 \pm 0.00057$ K [13]. Although seemingly a single temperature value, these discoveries have significantly enriched our understanding, actively validating predictions from Big Bang nucleosynthesis (BBN). For instance, using Planck's black body radiation equation (as the measured CMB radiation follow closely the black body spectrum), one can estimate the number density of the CMB photons as

$$n_\gamma = \int_0^\infty d\nu \frac{8\pi\nu^2}{e^{h\nu/kT} - 1} \sim 410cm^{-3} \tag{1.36}$$

and the energy density as

$$\rho_\gamma = \int_0^\infty d\nu \frac{8\pi\nu^3}{e^{h\nu/kT} - 1} = \Omega_\gamma h^2 \rho_{0,c} h^{-2} = 2.47\text{x}10^{-5} \rho_{0,c} h^{-2}. \tag{1.37}$$

From Ω_γ, one can get Ω_r and derive the subsequent cosmological parameters, which can be used to estimate the universe's expansion rate. In addition to confirming the CMB's blackbody spectrum, COBE's Differential Microwave Radiometer (DMR) detected small temperature fluctuations or anisotropies, providing further insights into the early universe's conditions and lending support to the concept of cosmic inflation. In 2002, the discovery of CMB polarization by the Degree Angular Scale Interferometer (DASI) [14] heralded a new era of cosmic exploration, delving deeper into questions surrounding cosmic inflation, dark energy, dark matter, and the sum of neutrinos. The subsequent sections delve into the intricacies of CMB anisotropies, encompassing both temperature and polarization.

1.3.1 CMB Temperature Anisotropies

While the CMB showcases remarkable uniformity, it also reveals small intrinsic fluctuations on the order hundreds of μK, remnants from the early universe. These fluctuations are classified into primary and secondary anisotropies. Primary anisotropies were already present at the surface of the last scattering, whereas secondary anisotropies emerged as the CMB interacted with matter during its journey through the universe to reach us. The following sections focus on primary anisotropies aimed at uncovering evidence of inflation, which are the primary scientific interest for the Small Aperture Telescope, the focus of my dissertation project. CMB anisotropies encompass both temperature and polarization anisotropies. The next section offers a comprehensive exploration of the polarization mechanism and power spectra for the two modes of CMB polarization. Meanwhile, this section concentrates on temperature anisotropies, outlining the derivation of the power spectra, C_l^{TT}.

CMB fluctuations can be described as Gaussian and any scalar quantity on a sphere can be expanded using spherical harmonics:

$$\Delta T(\hat{n}) = \sum_{l,m} a_{lm}^T Y_{lm}(\hat{n}), \tag{1.38}$$

where a_{lm}^T are the multipole coefficients, Y_{lm} are the standard spherical harmonics functions, and $\hat{n}$ is a direction of radiation. The following derivation references Dr. Flauger's cosmology lecture notes and similar formulations in [4].

Often in cosmology, we can pick a phase convention such that $Y_{lm}^*(\hat{n}) = Y_{l,-m}(\hat{n})$. Since the temperature perturbations are real, with our chosen phase convention, we have

$$a_{lm}^{T*} = \int d^2\hat{n}\Delta T(\hat{n})Y_{lm}(\hat{n}) = \int d^2\hat{n}\Delta T(\hat{n})Y_{l,-m}^*(\hat{n}) = a_{l,-m}^T. \tag{1.39}$$

Assuming statistical isotropy (no preferred direction), the temperature power spectrum C_l^{TT} is a statistical ensemble average of

$$\langle a_{lm}^T a_{l'm'}^{T*}\rangle = C_l^{TT}\delta_{ll'}\delta_{mm'}, \tag{1.40}$$

and the 2-point correlation function is

$$\langle \Delta T(\hat{n})\Delta T(\hat{n}')\rangle = C^{TT}(\hat{n}\cdot\hat{n}') \tag{1.41}$$

Using the relations in Equation 1.38 and 1.40 and the property of the spherical harmonics functions

$$\sum_m Y_{ln}(\hat{n})Y_{l'm'}^*(\hat{n}') = \frac{2l+1}{4\pi}P_l(\hat{n}\cdot\hat{n}'), \tag{1.42}$$

where P_l are the Legendre polynomials, the temperature correlation function can be rewritten as

$$C^{TT}(\hat{n}\cdot\hat{n}') = \sum_l C_l^{TT}\left(\frac{2l+1}{4\pi}\right)P_l(\hat{n}\cdot\hat{n}'). \tag{1.43}$$

Conversely, the temperature power spectrum can also be written as a function of the 2-point correlation

$$C_l^{TT} = \frac{1}{4\pi}\int d^2\hat{n}d^2\hat{n}' P_l(\hat{n}\cdot\hat{n}')\langle\Delta T(\hat{n})\Delta T(\hat{n}')\rangle. \tag{1.44}$$

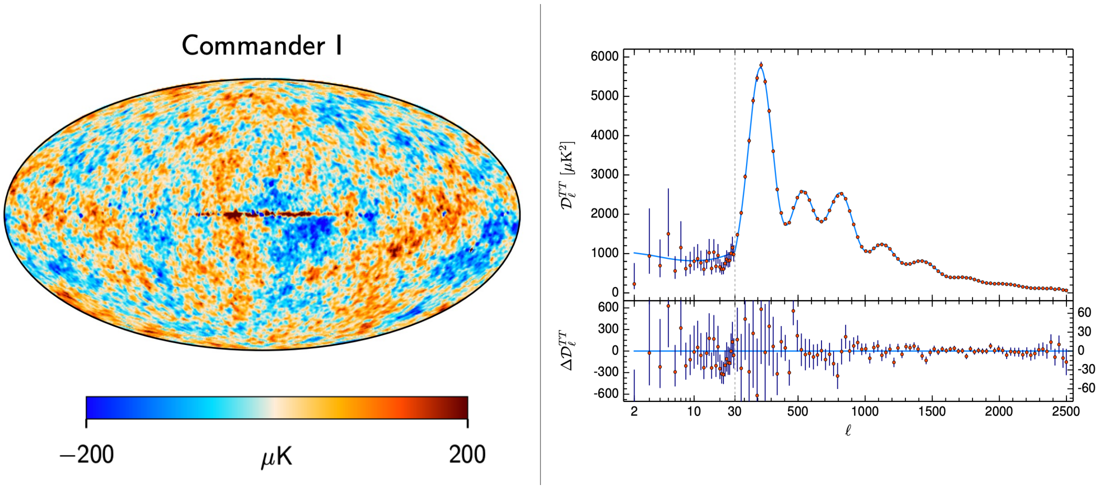

Figure 1.1. CMB temperature anisotropies map and power spectrum from the Planck Collaboration 2018 results. Left: Full sky temperature map using the Commander I component-separation method, which applies a Bayesian framework to extract CMB from the rest of the astrophysical foregrounds [2]. Right: The angular power spectra from Commander (TT) maps [15]. The data points are in red and the best-fit from ΛCDM model. $D_l = \frac{l(l+1)}{2\pi}C_l$.

The previous derivation assumes statistical isotropy with no bias in any direction $\hat{n}$, meaning ensemble averages for the power spectra are obtained through averaging measurements at different positions in the universe. However, in practice, the measured signal, $\hat{C}_l^{TT}$, is constrained to a single snapshot of the CMB in our position in the universe. The actual observed power spectrum is averaged over m but not position:

$$\hat{C}_l^{TT} = \frac{1}{2l+1}\sum_m |a_{lm}^T a_{lm}^{T*}|^2 = \frac{1}{4\pi}\int d^2\hat{n}d^2\hat{n}' P_l(\hat{n}\cdot\hat{n}')\Delta T(\hat{n})\Delta T(\hat{n}'). \tag{1.45}$$

Thus, in practice, we first compute the multipole coefficients from the measured signal and then compute the power spectrum for our sky using Equation 1.45. Ideally, this power spectrum exemplifies the true statistical average power spectra, and many experiments have tried to make precise measurements of the CMB. However, there is still a limitation on the measurements' precision such that there is a slight difference in the reconstructed power spectrum $\hat{C}_l^{TT}$ and the true spectrum C_l^{TT}. This difference, called cosmic variance ($\Delta\hat{C}_l^{TT}$), is the scatter around the true mean power spectrum, which we then add to our uncertainty budget.

$$\sqrt{\langle(\hat{C}_l^{TT} - C_l^{TT})^2\rangle} = \Delta\hat{C}_l^{TT} = \sqrt{\frac{2}{2l+1}} C_l^{TT}. \tag{1.46}$$

Figure 1.1 illustrates the all-sky temperature map (left) and power spectrum (right) using Planck's 2018 results. The temperature fluctuations or anisotropies are of order hundreds of μK. The temperature map applies the Commander I component-separation method to remove foregrounds, which follows a Bayesian framework that parameterizes the sky signal into CMB, Galactic synchrotron, thermal dust emission, CO, etc [2]. See section 1.4 for more details on foregrounds. The brightest regions around the Galactic plane are the remaining contamination that the component-separation method could not subtract out. These regions are masked in the later phase of the analysis. The right side of the figure depicts the temperature power spectrum in comparison to the best fit that uses the best estimations of the ΛCDM cosmological parameters.

1.3.2 CMB Polarization

CMB polarization came from the quadrupole anisotropies that existed during recombination. At decoupling, the temperature in the universe became inhomogeneous, creating hot and cold regions. Photons from different temperature regions would then scatter off the same free electrons in a process called Thomson Scattering, which leads to a partial linear polarization of the emitted light from a region (Figure 1.2).

Generally, the Stokes parameters, Q and U, characterize the two geometrical components of linear polarization. Instead of describing CMB polarization using the Stokes parameters that depend on the choice of coordinates, one can describe it by the polarization's orientation relative to itself: even parity E-modes and odd-parity B-modes. These two modes have no relation to the electromagnetic E- and B-field, but they are called that way due to their spin-2

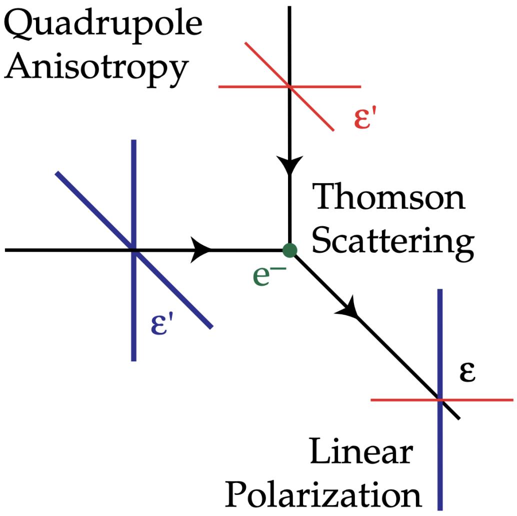

Figure 1.2. A diagram of the Thomson Scattering process where photons from hot and cold regions scattered off electrons in a certain region, leading to a fractional polarization in the scattered light that travels toward us [1].

analogs of divergence and curl patterns. E-modes result from scalar perturbations and tensor perturbations, while B-modes arise from tensor perturbations and weak gravitational lensing of E-modes. Perturbations in the density of cosmological fluids create overdense and underdense gravitational potentials, leading to hot and cold regions as photons traverse these potentials. In the case of tensor perturbations, primordial gravitational waves stretch and compress space, generating temperature variations. Both scalar and tensor perturbations contribute to E-modes, necessitating detailed analysis of their spectra to disentangle the contributions [5]. Moreover, this disentanglement makes it difficult to identify any evidence of tensors from gravitational waves. Primordial B-modes offer a unique signature as they exclusively originate from tensor contributions. Thus, the search for primordial B-modes is often characterized by the tensor-to-scalar ratio, r, serving as a potential indicator of primordial gravitational waves. The detection of B-modes holds the potential to revolutionize our understanding of inflationary theory. Figure 1.3 depicts examples of E- and B-mode polarization patterns.

Through a series of coordinate transformations, the Stokes Q and U can be broken down

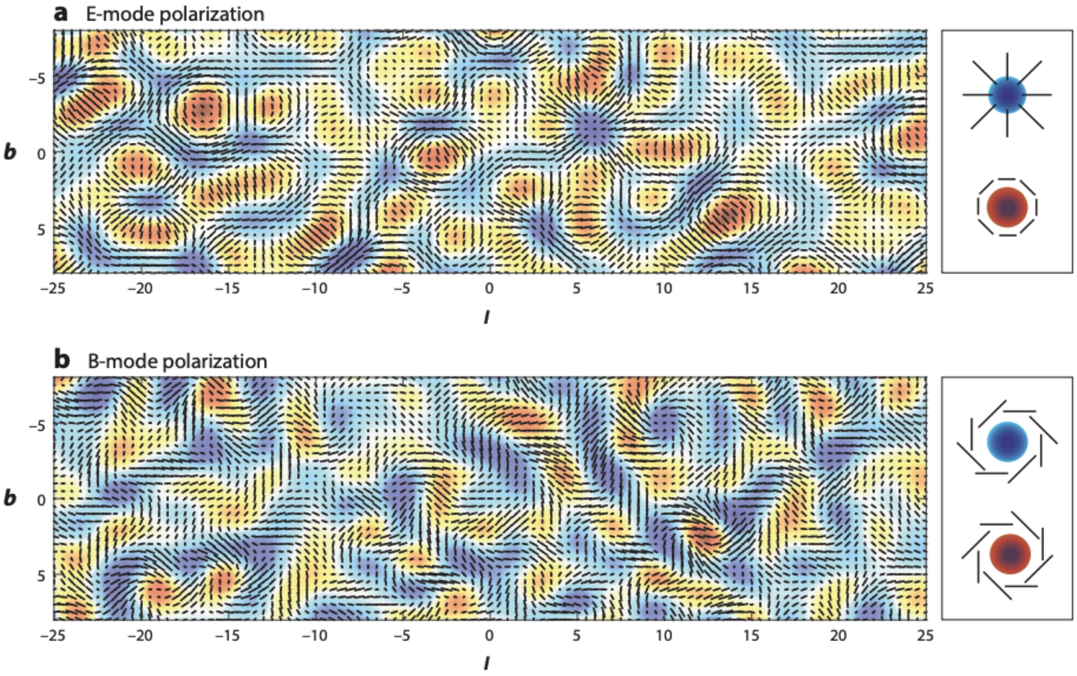

Figure 1.3. Polarization patterns for E- (top) and B-modes (bottom). The red and blue spots in the maps represent the hot and cold regions, respectively. The top pattern has a curl-free and divergence characteristics, hence the name E-mode. The bottom one shows a swirling/curling pattern, thus called B-modes. E-modes have been detected but primordial B-modes from gravitational waves at large angular scales, especially around $10 < l < 100$ where the signal peaks, have not been detected. The figure is taken from [16].

into E- and B-modes. Recall that the temperature anisotropies can be written as an expansion of the spherical harmonics. A similar process can be applied to polarization using spin-2 spherical harmonics as the Stokes parameters are components of a symmetric 2-tensor

$$Q(\hat{n}) + iU(\hat{n}) = \sum_{lm} a_{lm}^{P}\,{}_{2}Y_{lm}(\hat{n}), \tag{1.47}$$

where ${}_2Y_{lm}$ is the spin-2 spherical harmonics and a_{lm}^P are the multipole coefficients for polarization. Both are given in Chapter 7.4 of [4]. Then the multipole coefficients for E- and B-modes are just linear combinations of a_{lm}^{P}:

$$a_{lm}^{E} = -\frac{1}{2}(a_{lm}^{P} + a_{l,-m}^{P*}), \tag{1.48}$$

$$a_{lm}^{B} = -\frac{1}{2i}(a_{lm}^{P} - a_{l,-m}^{P*}). \tag{1.49}$$

From Equation 1.40, the angular power spectra for polarization and cross-power spectra can be extrapolated to be

$$\langle a_{lm}^{E} a_{l'm'}^{E*} \rangle = C_l^{EE} \delta_{ll'} \delta_{mm'}, \tag{1.50}$$

$$\langle a_{lm}^{B} a_{l'm'}^{B*} \rangle = C_l^{BB} \delta_{ll'} \delta_{mm'}, \tag{1.51}$$

$$\langle a_{lm}^{T} a_{l'm'}^{E*} \rangle = C_l^{TE} \delta_{ll'} \delta_{mm'}. \tag{1.52}$$

Under parity, all cross-correlations of the odd-parity B-modes vanish so $C^{EB} = C^{TB} = 0$. Generalizing Equation 1.45, we have

$$\hat{C}_l^{XY} = \frac{1}{2l+1} \sum_m |a_{lm}^{X} a_{lm}^{Y*}|^2 \tag{1.53}$$

where X and Y are T, E, or B. Figure 1.4 illustrates an example of CMB maps in intensity I, Q, and U at 4 different observing frequencies 70, 100, 143, and 217 GHz. These maps are from the Planck 2018 results.

1.3.3 Gravitational Lensing

The large-scale structure (LSS) in the universe from the surface of the last scattering to our current position in the sky can deflect the CMB and cause a slight distortion in the measured signal. For example, E-modes lensed by LSS can show up as a B-mode power spectrum that peaks at $l \sim 1000$. This process is called weak gravitational lensing. Using our understanding of the CMB and its polarization, we can investigate the statistical properties, structure, and

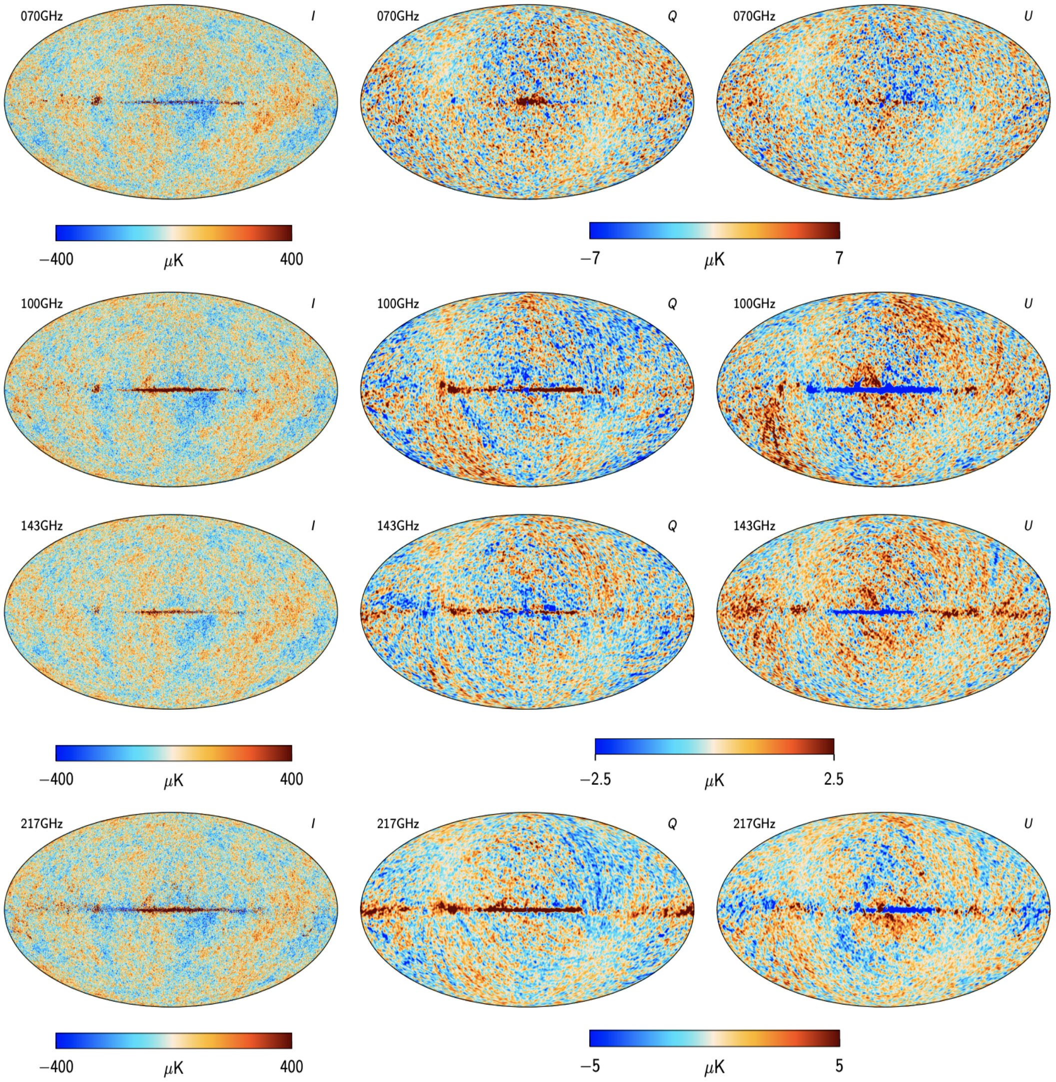

Figure 1.4. Intensity and polarization (Q and U) maps at different observing frequency bands from the Planck 2018 results [2].

distribution of the LSS through the lensing potential.

In the weak lensing limit, lensing dispaces the temperature ($\Theta(\hat{n}) = \Delta T(\hat{n})/T$) and polarization ($Q(\hat{n})$ and $U(\hat{n})$) by a deflection angle, $\mathbf{d}(\hat{n})$ [17]:

$$\Theta(\hat{n}) = \tilde{\Theta}(\hat{n} + \mathbf{d}(\hat{n})), \tag{1.54}$$

$$(Q \pm iU)(\hat{n}) = (\tilde{Q} \pm i\tilde{U})[\hat{n} + \mathbf{d}(\hat{n})] \tag{1.55}$$

where the tildes indicate the unlensed fields and $\mathbf{d}(\hat{n}) = \nabla\phi$ and

$$\phi(\hat{n}) = -2\int dD \frac{D_s - D}{DD_s}\Psi(D\hat{n}, D). \tag{1.56}$$

D and D_s are the comoving distance along the sight and the distance to the last scattering surface, respectively. $\Psi(D\hat{n}, D)$ is the gravitational potential. Using the deflection angle, one can extract the lensed maps in Q and U, and then through a coordinate transformation one can get them into E- and B-mode maps.

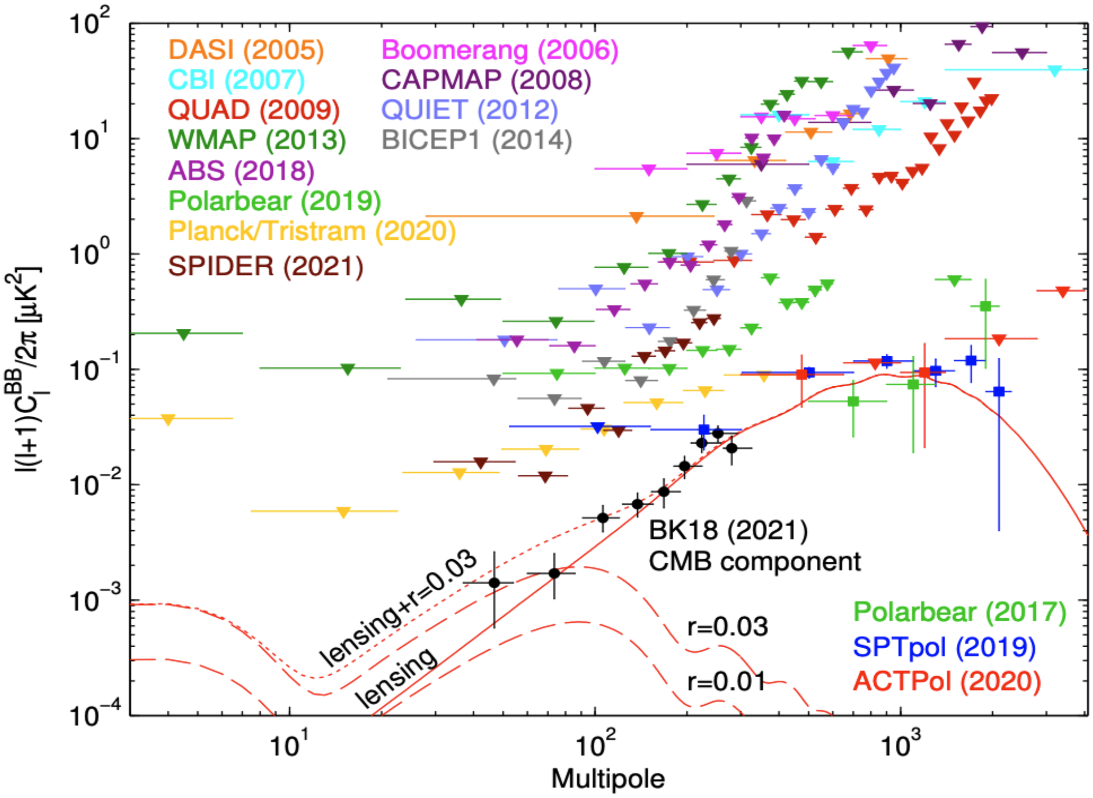

Figure 1.5. Measurements of CMB B-mode polarization from the past couple of decades including CMB experiments such as BICEP/Keck, Planck, SPTpol, ATCPol, and POLARBEAR. This figure is taken from [18]. The red lines are the theoretical curve for lensed B-modes (solid) and primordial B-modes (dashed).

Switching to harmonic space and considering small sections of the sky such that we can use flat-sky approximation. The lensing potential becomes

$$\phi(\hat{n}) = -i\int \frac{d^2 l}{(2\pi)^2}\phi(l)e^{-il\cdot\hat{n}}l \tag{1.57}$$

and the lensed B-map becomes

$$B(l) = \int \frac{d^2 l'}{(2\pi)^2}[l'\cdot(l-l')]E(l')\phi(l-l')sin(2\psi_{l'}) \tag{1.58}$$

where ψ_l is the angle l makes with the x-axis in an arbitrary chosen x-y coordinate [16]. The lensed B-mode power spectrum is then

$$C_l^{BB,lensed} = \int \frac{d^2 l'}{(2\pi)^2}[l'\cdot(l-l')]sin^2(2\psi_{l'})C^{\phi\phi}_{|l-l'|}C^{EE}_{l'}, \tag{1.59}$$

where $C^{\phi\phi}$ is the power spectrum for the projected potential. Figure 1.5 depicts lensed B-mode measurements from CMB experiments for the past decades. The red lines portray the theoretical power spectra for lensed B-modes (solid) and primordial B-modes (dashed line). The lensed B-mode power spectrum peaks at $l \sim 1000$.

1.4 Astrophysical Foregrounds

The faintness of the CMB signals in comparison to other astrophysical sources such as Galactic synchrotron and thermal dust emission imposes stringent constraints on quantifying the systematic errors and the foreground cleaning procedure. These astrophysical sources or foregrounds all emit radiation at microwave frequencies and dominate over the CMB signals, posing as significant sources of contamination. Figure 1.6 plots the root-mean-square brightness (RMS) in Rayleigh-Jean temperature unit for the polarized foreground and CMB as a function of frequency.

We expect synchrotron and thermal dust radiation to be partially polarized, influenced by

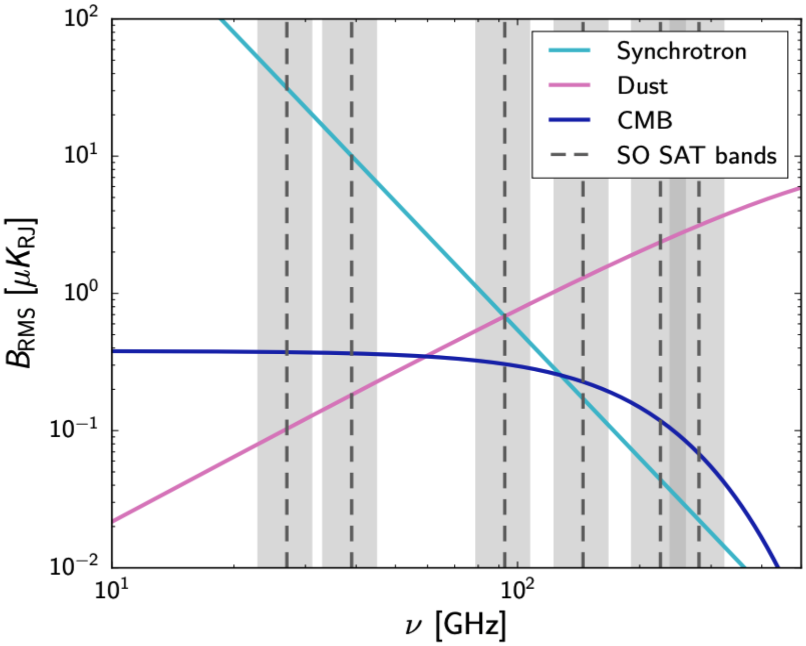

Figure 1.6. Temperature signal in Rayleigh-Jean brightness temperature unit for the CMB, galactic synchrotron, and thermal dust emission as a function of frequency [3]. The grey-shaded regions are the six observing bands for the Simons Observatory Small Aperture Telescopes (SATs).

the characteristics of the local magnetic field where the emitting particles reside. These emissions typically overshadow the polarized CMB signal. As depicted in the figure, synchrotron radiation dominates at low frequencies, often characterized as

$$I_{\nu,synch} \propto \nu^{\beta_s}, \tag{1.60}$$

where ν is the frequency and β_s is the synchrotron spectral index [19]. At the higher frequency end, thermal dust emission becomes significant. The dust emission can be parameterized as a modified black body spectrum

$$I_{\nu,dust} \propto \nu^{\beta_d} B_\nu(T_d), \tag{1.61}$$

where T_d is the black body dust temperature and β_d is the dust spectral index.

To extract a clean CMB signal, recent experiments have opted for multifrequency measurements, meaning a portion of the observations are spent observing multiple "low frequency" bands (e.g. 27/39 GHz) where synchrotron radiations dominate, and "high frequency" bands (e.g. 225/280 GHz) for thermal dust emission on top of the normal CMB frequency bands. The information from these low- and high-frequency bands would then be used to characterize foregrounds for the subsequent removal process.

Chapter 2

The Simons Observatory (SO)

2.1 Overview

The Simons Observatory (SO) is a next-generation CMB experiment, located in the Atacama Desert, Chile. SO shares the same observing site as other ground-based CMB experiments such as the Simons Array and the Cosmology Large Angular Scale Surveyor (CLASS) on Cerro Toco at 5200 meters ($\sim$ 17,000 feet) in elevation. Figure 2.1 presents a view of the site back in July 2023. The site overlooks the Atacama Large Millimeter Array (ALMA) on the Chajnantor Plateau. The site was chosen for its high elevation and low precipitable water vapor (PWV), which measures the height of water per unit area in a column of atmosphere. Cerro Tocco, one of the driest places on Earth, has a typical PWV of about 1-1.5 mm. Figure 2.2 plots the transmission through the atmosphere as a function of frequency, where the atmosphere becomes less transmissive the higher the PWV.

In addition to observing similar patches of the sky as those of other CMB experiments, SO's sky coverage will overlap with other optical and infrared surveys such as the Rubin Observatory Large Synoptic Survey Telescope (LSST), the Dark Energy Survey (DES), and the Dark Energy Spectroscopic Instrument (DESI). To ensure the planned coverage and address the science goals and forecasts listed in [3], SO is deploying a 6-meter Large Aperture Telescope (LAT) and an array of Small Aperture Telescopes (SATs). Altogether, SO will employ more than 60,000 cryogenic detectors, a sixfold increase compared to previous experiments that use

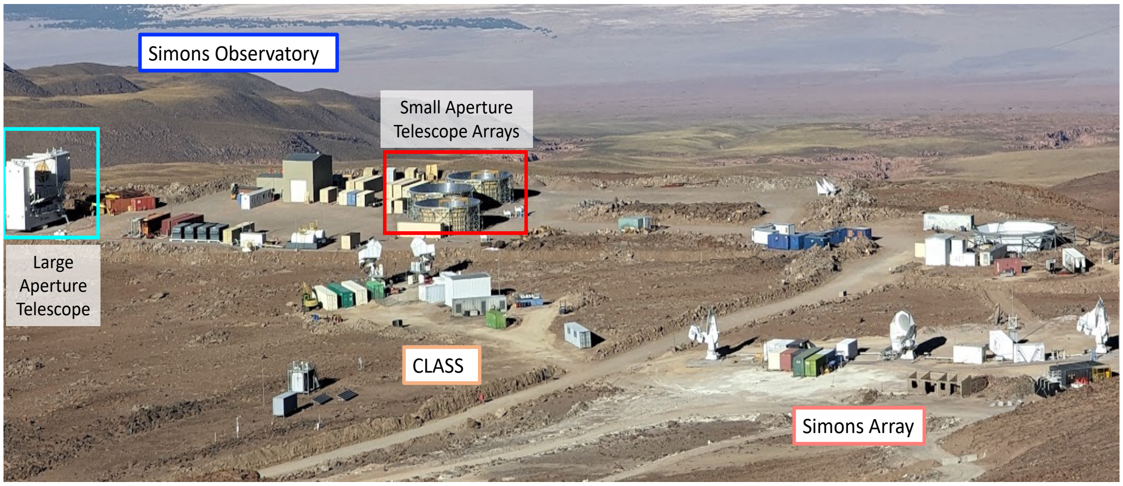

Figure 2.1. The Simons Observatory (SO) at the Atacama Desert, Chile. SO is a new generation of ground-based CMB experiment located at Cerro Toco, 5200 m in elevation. Next to SO are two current CMB experiments: the Simons Array and the Cosmology Large Angular Scale Surveyor (CLASS). SO is deploying a large aperture telescope (cyan) and an array of three small aperture telescopes (red). This image has been adapted and the original image is courtesy of Mark Devlin.

$\sim$10,000 detectors. SO will observe in six frequency bands, centered at 27, 39, 93, 145, 225, 280 GHz. The initial deployment involves two SATs: SAT-MF1 and SAT-MF2, observing at 90 and 150 GHz in the mid-frequency (MF) bands, and a third SAT, SAT-UHF, observing at 225 and 280 GHz in the ultra-high-frequency bands (UHF). A fourth SAT, SAT-LF, observing at 27 and 39 GHz, will be deployed in a later observing season. This multi-frequency band coverage ensures not only the detection of CMB in the MF bands but also allows investigation of foregrounds in the LF bands for synchrotrons and UHF bands for thermal dust as seen in Figure 1.6. The characterization of foregrounds would then create a model, which can then be used in the cleaning process to remove any contamination from foregrounds. The detailed band edges were chosen to avoid atmospheric emission lines, as shown in Figure 2.2.

As previously mentioned, the observatory plans to deploy a total of four telescopes for its first observing season. The next section, 2.2, gives an overview of the SAT, focusing on SAT-MF1 instrument design as this dissertation centers on the instrumentation work done on this telescope. Here, we give a brief introduction to the LAT design. For more details, see [21] and

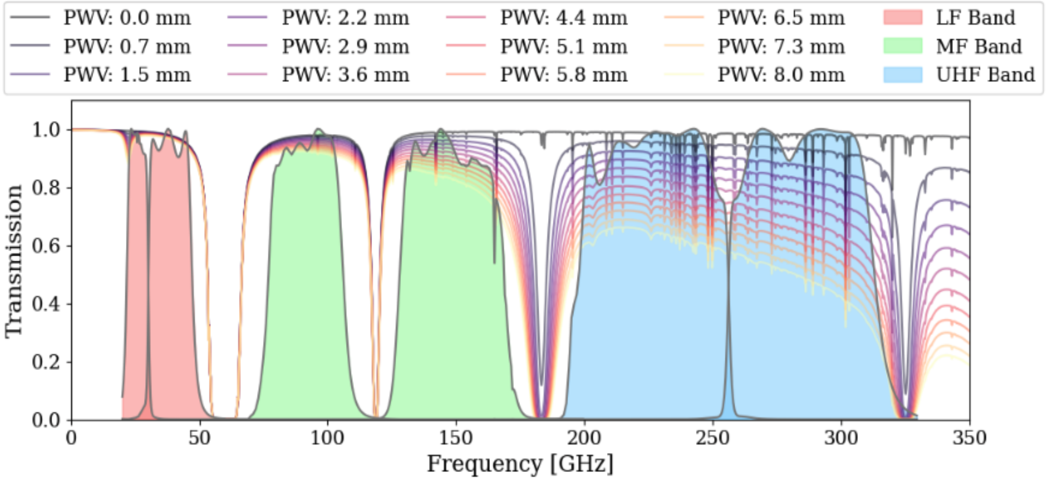

Figure 2.2. The atmospheric transmission at different precipitable water vapors (PWV). The three observing bands for SO are shaded in red for LF (27/39 GHz), green for MF (93/145 GHz), and blue for UHF (225/280 GHz). Cerro Tocco, as one of the driest places on Earth, has a median PWV of about 1-1.5 mm. This figure is taken from [20].

[22] on the LAT and its receiver. The LAT is a crossed-Dragone telescope with a 6-m primary and secondary mirror. The LAT will produce arcminute resolution maps in the mm-wave range, focusing on cosmological studies such as the sum of neutrino masses, galaxy evolution, dark energy, and dark matter. It is coupled to a receiver (LATR) that can contain 13 optics tubes and it will also observe in the aforementioned six frequency bands. The LATR has a diameter of 2.4 m and a length of 2.6 m, becoming the largest cryogenic mm-wave camera ever built. Over a 5-year survey, the LAT plans to cover $\sim$ 40% of the sky, overlapping with other astronomical surveys such as the Rubin Observatory, DESI, and DES. Figure 2.3 portrays a picture of the LAT currently at the observing site in Chile and a 3D model of the LATR inside the LAT.

2.2 The Small Aperture Telescope (SAT)

The Small Aperture Telescope (SAT) is a 42 cm aperture refractive telescope with a field of view (FOV) of 35°. Over a 5-year survey, the SAT will cover over $\sim$10% of the sky at the sub-degree angular resolution, overlapping with the projected BICEP Array [23] and SPIDER

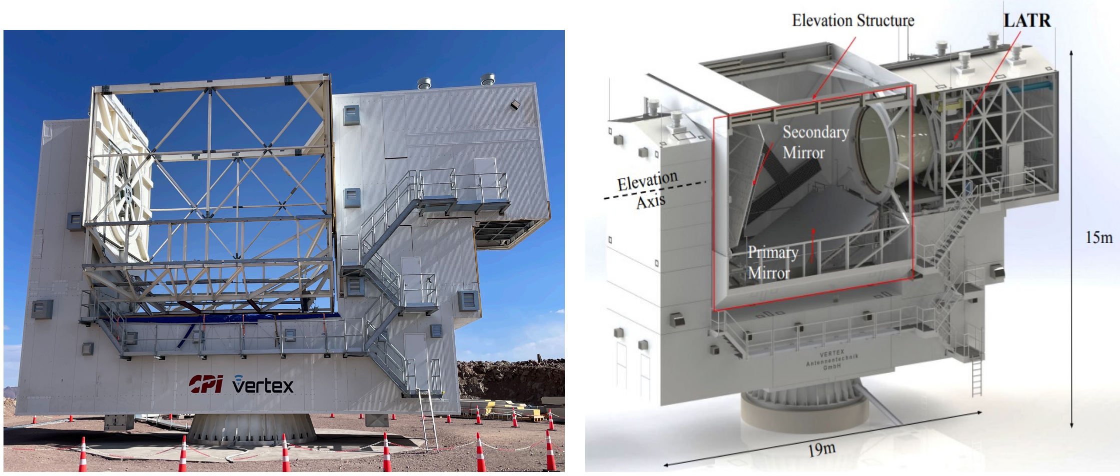

Figure 2.3. The Large Aperture Telescope (LAT) overview. The LAT is a crossed Dragone telescope with a 6-m diameter aperture to observe arcmin angular scale, targeting science goals such as the sum of neutrino masses, extragalactic sources, and transient studies on top of primordial CMB science. Left: picture of the LAT at the site. This picture is a courtesy of Anna Kofman. Right: a 3D rendering of the LAT and its receivers. This figure is adapted from [22].

coverage [3]. The SATs in the nominal configuration are expected to achieve a white noise level of 2 μK-arcmin in the combined 93 and 145 GHz bands. The SATs target large angular scale ($30 \leq l \leq 200$) CMB polarization science to constrain signals from primordial B-modes. The current constrains on r, the tensor-to-scalar ratio, come from BICEP/Keck Collaboration with $r < 0.036$ and σ(r)=0.009 for an $r = 0$ model [18]. SO aims to measure r at a target level of $\sigma(r)$ = 0.003[3]. Each SAT couples to seven 150 mm Universal Focal Plane Modules (UFMs), which contain a total of about 10,000 detectors per SAT. Section 2.3 describes the detectors and readout scheme used for the Simons Observatory. Here, we give an overview of the SAT and its design, focusing on SAT-MF1.

2.2.1 The SATs and Their Platforms

SO is deploying three SATs in its first observing seasons. Each SAT is mounted on a platform (SATP) that allows full rotation in azimuthal direction (0-540°) and in elevation (0-90°). The elevation stage is driven by a jackscrew mounted in the rear of the platform. There is a boresight rotation stage that allows SATP to rotate ±90° around the receiver's optical axis for additional polarization systematic uncertainty. The SATP has a diameter at its base of 6 m, allowing enough space to mount all the electronic racks and vacuum hoses around the SAT. Figure 2.4 illustrates the SAT mounted don't its platform together with the comoving shield and forebaffle. All three SATPs were fabricated and initially assembled at Vertex Antennentechnik in Germany[1].

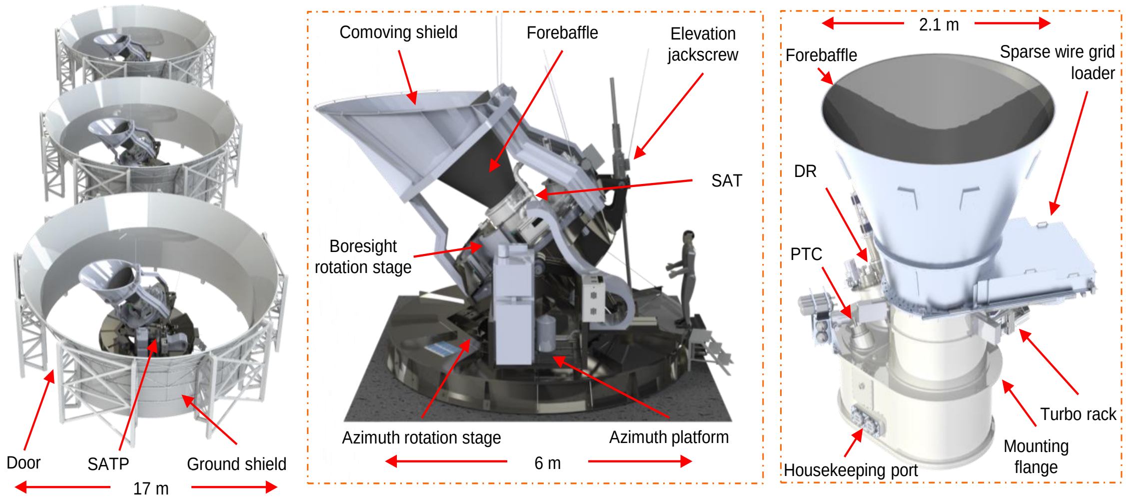

Figure 2.4. The three SATs with their platforms and groundshields. Left: An array of 3 SATs and their groundshields to block scattering from the surroundings. Center: a 3D model of the SAT mounted to its platform (SATP). Right: detailed view of the SAT with the forebaffle, grid loader, DR, and PTC. The figure is taken from [24].

To block stray lights from the surroundings, ground, and sun, the SAT installs a forebaffle and a co-moving shield on top of its window. These two structures ensure that stray light from ground illumination diffracts twice before entering the telescope at our observation angles. The forebaffle has a diameter of 2.1 m and a height of 1.7 m, stopping any rays with an incident angle larger than 40°. Each SAT is surrounded by a ground shield with an outer diameter of about 17 m and 5.66 m tall. The upper 2 m of the ground shield is angled at 30° from the vertical to reflect radiations, and the lip of the groundshield is curved with a radius of 5 cm.

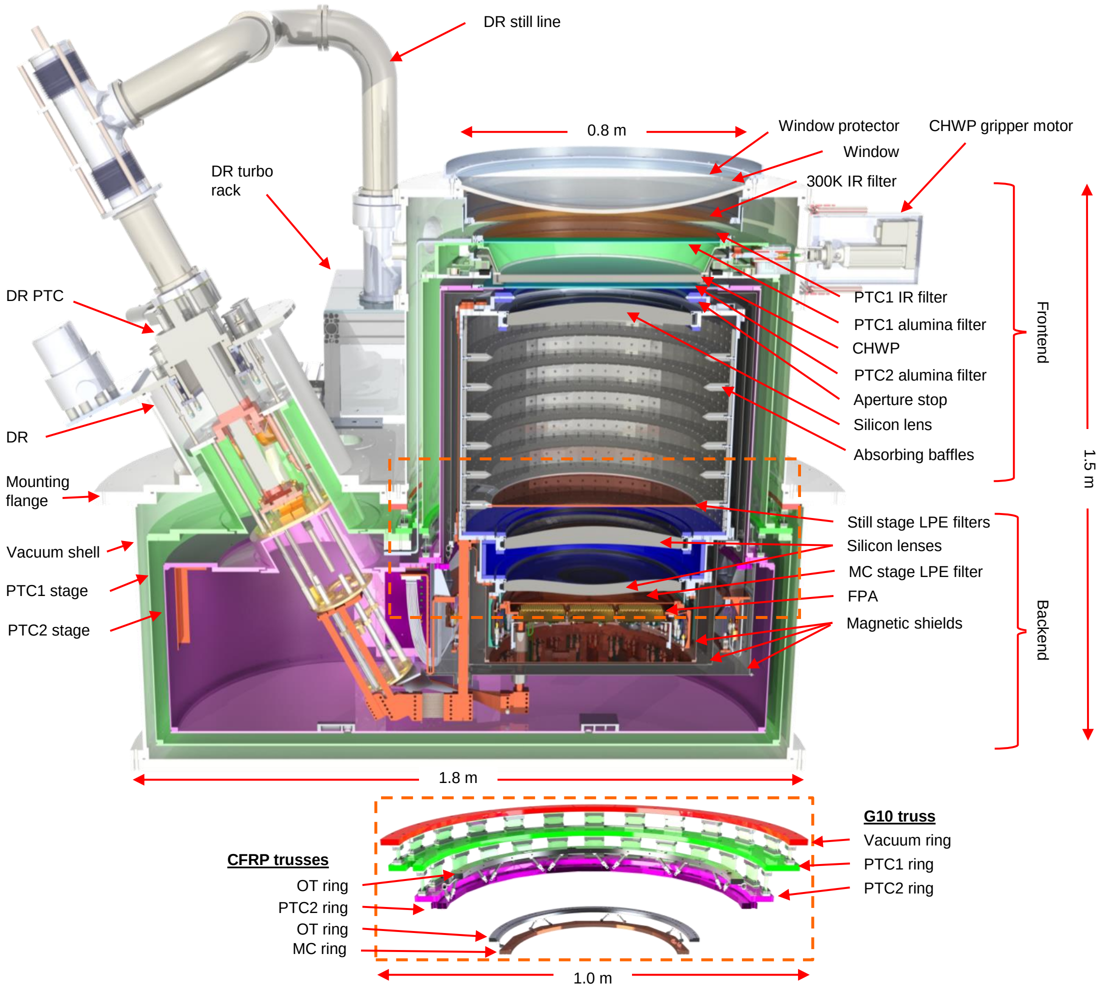

Figure 2.5. Cross-section view of SAT-MF1 showing the principal components. At the bottom is a zoom-in view of the mechanical trusses, which connect different temperature stages of the telescope. G10 trusses provide mechanical support from 300 K to 4 K (PTC2 stage), while the carbon fiber trusses connect the 4 K to 0.1 K (PTC2 to MC stage). This is a figure taken from [24].

2.2.2 Cryogenic Design

The SAT's scientific goals drive it to operate at sub-kelvin temperature to reduce optical loading and ensure that our detectors operate in a photon noise-dominated regime. Thus we employ various cryogenic technologies such as the pulse tube cryocoolers (PT420) from Cry-

---

[1] Vertex Antennentechnik GmbH, 47198 Duisburg, Germany

omech[2] and the dilution refrigerator (DR) from Bluefors[3]. The SAT is designed with nested thermal shells, starting with the vacuum shell at room temperature and then going inward to the PTC1 (40 K) and PTC2 (4 K) shells. Two PT420s, one standalone unit and one integrated with the DR unit, provide cooling power to cool the PTC1 and PTC2 shells to <40 K and 4 K, respectively. From there, the SD-400 DR unit cools our Optics Tubes and detector arrays on the focal plane to ≤ 1 K and 0.1 K, respectively, collectively forming four temperature stages inside the SAT. Both the PTC and DR are installed inside the SAT at 27.5° from the vertical. The angle was chosen to ensure maximum cooling capacity at all our scan strategies since the pulse tubes are well-known for their orientation effect. For example, observing at 40° in elevation would put the pulse tubes at 22.5°, an angle that would still ensure nominal cooling power as the results from chapter 3 suggested. A series of heatstraps with high thermal conductivity connects these cold heads to different parts of the SAT. On the PTC1 and PTC2 stages, copper braided strap and high purity aluminum foils (5N8 so 99.999% purity) connect the two PTC cold heads directly to the thermal shells, respectively. On the Still and MC, gold-plated copper heatstraps connect the DR cold head to the Optics Tube (OT) and the focal plane array (FPA), respectively. These straps are manufactured by Technology Applications, Inc. (TAI)[4]. A detailed analysis of these heatstraps is in section 5.1.3.

All the stages are mechanically connected via truss structures that minimize thermal coupling between the different temperature stages. Figure 2.5 provides a cross-section of SAT-MF1, highlighting the different principal components inside the telescope. The bottom is a cutout section view of the two different trusses that support the SAT. The G10 truss provides mechanical support from 300 K to 4 K (PTC2) stage, and the carbon fiber trusses support the 4 K to 0.1 K (PTC2 to MC) stage. Henceforth, the temperature stages' names are used interchangeably as PTC1, PTC2, Still, and MC for 40, 4, 1, and 0.1 K stages. The G10 truss is made up of three rings, which are bolted to the three big shells. G10 tabs wrapped in multi-layer insulation (MLI)

---

[2] Cryomech Inc., Syracuse, NY

[3] Bluefors Oy. Arinatie 10, 00370 Helsinki, Finland

[4] Technology Applications, Inc. 5303 Spine Rd. #101 Boulder, CO 80301.

connect the rings. Thin layers of aluminized mylar wrap around the outskirts of the tabs and between each ring, serving as radio frequency (RF) shields, minimizing RF noise injection into our readout system. The second type of truss uses carbon fiber reinforced polymer (CFRP) struts angled at 45° around two rings. There are four CFRP trusses. One truss connects the Optics Tube at 1 K to the 4 K shell, and the second one connects the readout components between 1 K and 4 K in the cold readout assembly 1 (CRA1). The third CFRP truss forms the cold readout assembly 2 (CRA2), which houses readout components from 1-0.1 K. The final truss connects the FPA on the 0.1 K (MC) stage to the Optics Tube at the 1 K (Still) stage. Similarly to the G10 truss, aluminized mylar is wrapped between the rings for RF shielding.

2.2.3 Optical Design

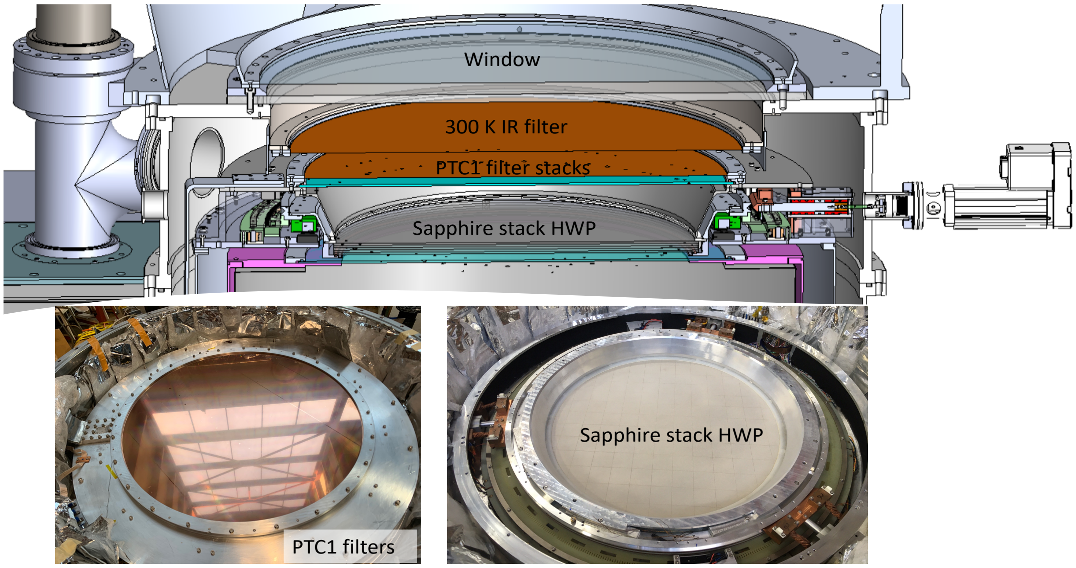

Figure 2.6. SAT-MF1 frontend overview. Top: 3D CAD cross-section of the frontend. The main optical components are the window and the infrared (IR) filter at 300K. Next, we have a series of filters in the PTC1 stage, on top of the CHWP. Below the CHWP is the PTC2 filter, which is not called out. Bottom: the filters and CHWP were installed inside the SAT during a lab cooldown at UCSD.

SAT-MF1's optics consist of a window and a series of filters in the frontend and an optics tube containing lenses and filters, shown in figures 2.6 and 2.7, respectively. When light passes through the window, the filters allow only microwave light to pass through. Then the cryogenic cold-half-wave plate (CHWP) modulates the incoming signal. Inward of the CHWP is the PTC2 alumina filter. The bottom pictures in Figure 2.6 show the PTC1 IR filter and the CHWP installed inside SAT-MF1 during a cooldown at UCSD. The window was a non-AR-coated 12 mm thick ultra-high molecular weight polyethylene (UHMWPE) plate at ambient temperature during the measurement runs. The final site deployable configuration uses an AR-coated 10 mm thick UHMWPE plate. The CHWP operates at 50 K to modulate the incident polarization signal, suppressing the atmospheric 1/f (low frequency) noise in the timestream. The CHWP, with heritage from the POLARBEAR-2b [25], consists of three layers of 0.5 m diameter sapphire suspended by a superconducting magnetic bearing. The multi-plate stack increases the bandwidth over which the sapphire is an effective HWP [25, 26]. The sapphire stack has mullite duroid anti-reflection coating (ARC). The CHWP's nominal spin speed is 2 Hz, which modules the CMB polarization at 8 Hz. See [27] for more details on CHWP testing for SO.

Next, the optics Tube (OT) holds all the optical components at the Still stage. As seen in Figure 2.7, there are three silicon lenses with metamaterial ARC inside the OT. The lyot stop is

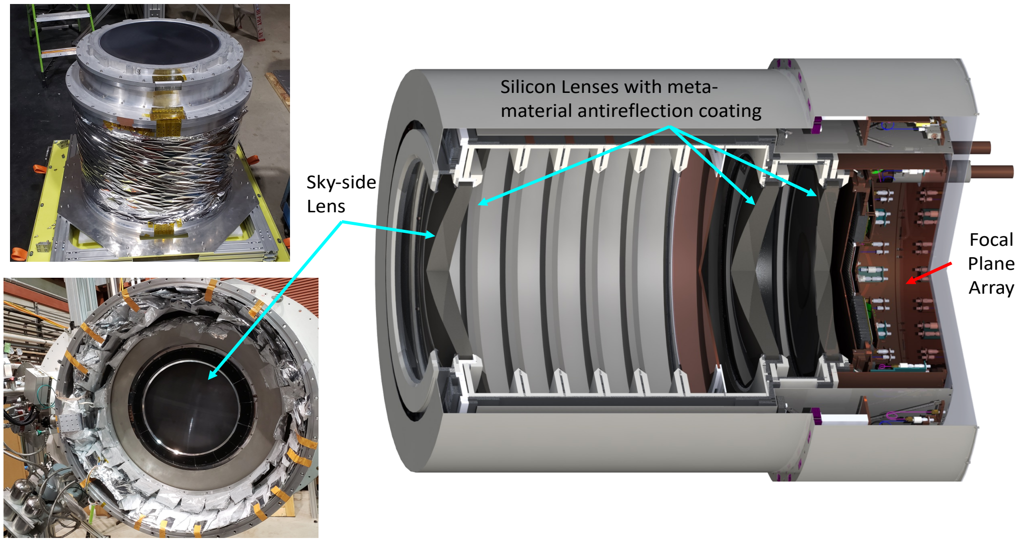

Figure 2.7. SAT-MF1 Optic Tube. Left displays the actual Optic Tube (OT) and its installation inside the SAT. Right is a cross-section view of the CAD rendering of the OT, showing its three silicon lenses. We successfully installed the OT during P6R1.

located at 1 K, on the sky side of the first lens (lens 1). There is a low pass edge filter on the sky side of lens 2. The two left pictures in this figure show the actual OT and its installation inside SAT-MF1, while the right is a cross-section view of a 3D CAD of the OT.

2.3 Detector and Readout

2.3.1 Detectors: OMT coupled feedhorn array

SO uses transition edge sensor (TES) bolometers or superconducting detectors that operate at extremely low temperatures since they are photon noise-limited. A TES bolometer is a thermistor with a resistance of R_{bolo} on an absorber that is weekly coupled to a thermal bath via a thermal link. The TES is designed to operate in its superconducting transition such that a small temperature change (dT) would cause a large change in resistance. This way, the TES can be extremely sensitive to the minute signals coming from the CMB anisotropies. Under a constant voltage bias, optical power (P_{opt}) from any incoming light would heat the thermistor, causing a change in the temperature which can be used to convert it to reading in current via the dR/dT relationship. In this superconducting transition phase, dR/dT creates a passive negative feedback mechanism because the Joule heating

$$P_{elec} = \frac{V^2}{R} \tag{2.1}$$

decreases when the resistance increases, leaving the total power,

$$P_{tot} = P_{opt} + P_{elec} \tag{2.2}$$

relatively unchanged. Thus an increase in P_{opt} would cause a large increase in R, which under a constant voltage bias equates to a negative change in current, $-\Delta I_{bolo}$. Hence, P_{elec} decreases. Through this relationship, one can equate ΔP_{opt} to ΔI_{bolo} and defined the responsivity of the bolometer as

$$S_I = \frac{dI_{bolo}}{dP_{opt}}. \tag{2.3}$$

SO TES bolometers operate at around 100 mK bath temperature, which is chosen to achieve low thermal noise.

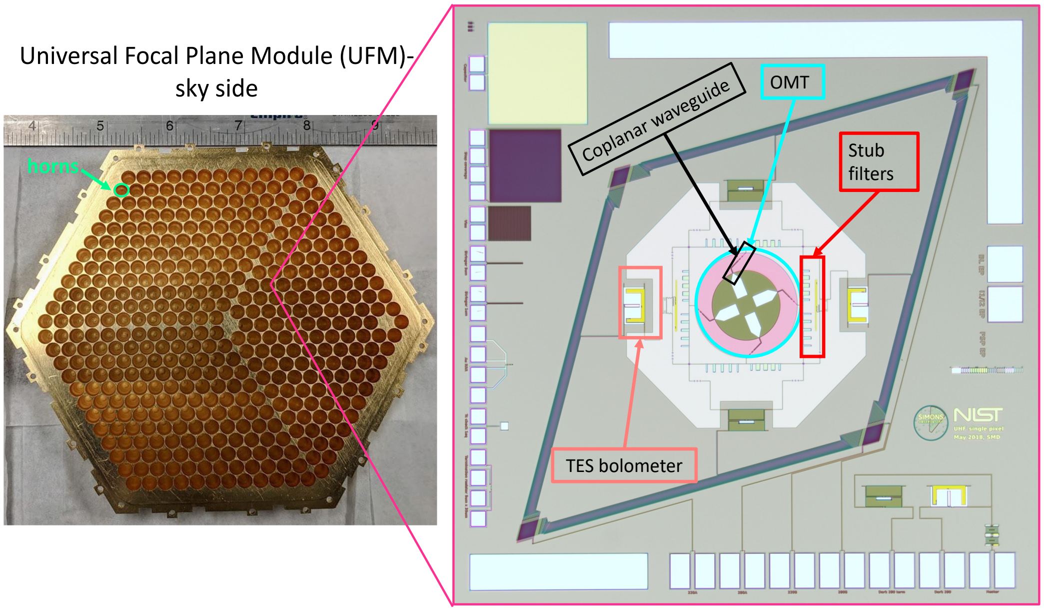

Figure 2.8. Structures inside a single pixel for an OMT coupled detector. Left is a sky-side view of a UFM, where one can see the feedhorn arrays. The right shows the different components inside a horn-coupled pixel. Each pixel is coupled to a planar orthomode transducer (OMT) to split the signal into two polarization directions. Each OMT connects to a coplanar waveguide that routes to diplexed stub filters that define the frequency bands. Finally, the signal is measured by a TES bolometer. There are 4 bolometers in a single pixel. One UFM contains 1728 optical detectors. Figure adapted from [28, 29].

SAT MF and UHF use the same horn-coupled detector technology manufactured by the National Institute of Standards and Technology (NIST) [30, 31, 32, 33], while SAT LF uses the lenslet-coupled sinuous antenna detectors fabricated by UC Berkeley [34, 35]. This section focuses on the detector technology for MF and UHF bands. The SATs use dichroic pixels that are sensitive to two linear polarization directions at two frequencies. Thus, one pixel contains four TES detectors. Each spatial pixel consists of a gold-plated aluminum horn that couples to a planar orthomode transducer (OMT) to split the signal into two polarization directions. Each of the OMT antennas connects to a superconducting coplanar waveguide that routes the signal from the OMT to a microstrip mm-wave feedline that is coupled to a diplexed stub filter. The filter defines the frequency band and allows each pixel to measure two frequencies of light in each linear polarization. After passing through the filter, the signal is measured by a TES bolometer. The detectors are then packaged into a hexagonal universal focal plane module (UFM). Figure 2.8 illustrates an example of an OMT-coupled pixel for one UFM.

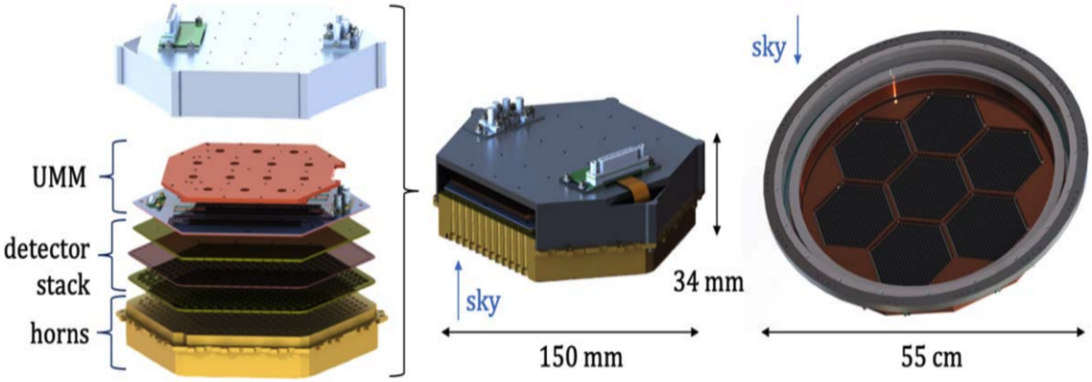

Figure 2.9. The Universal Focal Plane Module (UFM) overview. The UFM is the detector stack for the MF bands at 90/150 GHz and the UHF bands at 225/280 GHz. The UFM is composed of the universal μmux module that houses all the 0.1-1 K readout components such as the multiplexer chips, containing 1820 readout channels per wafer. The UMM is then coupled to the detector array/stack and finally to the feedhorns. This figure is taken from [30].

Each SAT contains 7 UFMs coupled to the focal plane array (FPA) base plate at the MC stage, and one UFM has 1728 optical detectors [30]. Hence, there are about 12,000 detectors in SAT-MF1. Besides the feedhorns and the detector stack as shown in the previous picture, the UFM also contains the universal μmux module that houses all the readout modules such as the multiplexer chips. There are 1820 readout channels per wafer, which are read out via two pairs of coaxial lines. Figure 2.9 shows an overview of the components inside a UFM.

2.3.2 Readout: microwave SQUID multiplexing system

SO uses a microwave SQUID multiplexing system (μMUX) that incorporates the Stanford Linear Accelerator Center (SLAC) microresonator radio frequency (SMuRF) electronics to read out thousands of detectors using a pair of coax chains. Due to the faintness of the CMB anisotropies ($< \mathcal{O}(3x10^{-2})\mu K$ for CMB-BB), modern CMB experiments have opted to increase the number of deployed detectors as the telescope's sensitivity is proportional to the square root of the number of detectors. With N_{det} reaching tens of thousands and even more for upcoming experiments, efficient cable management becomes imperative. This readout scheme ensures that only 14 coax chains are needed to read out over 10,000 detectors, significantly minimizing the resulting conductive heating power from cables.

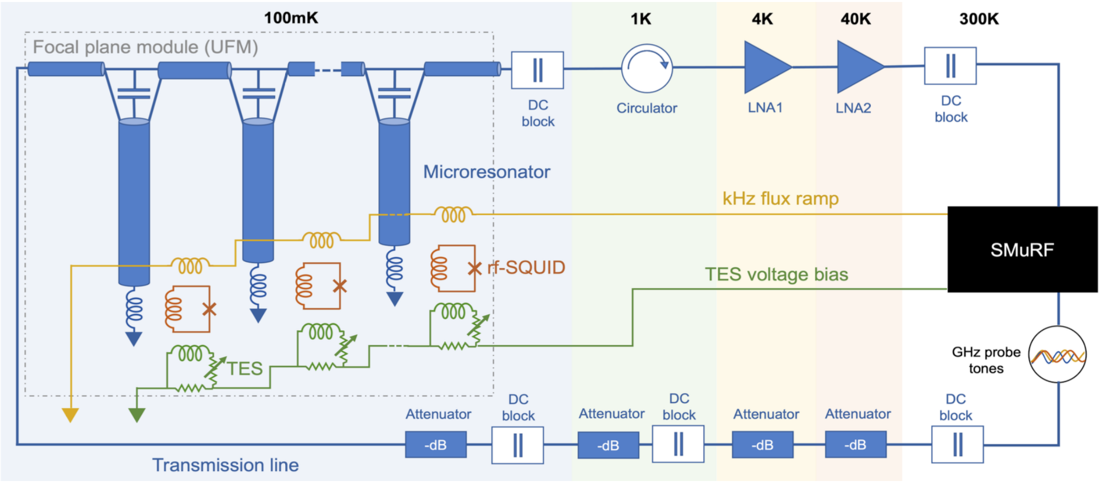

Figure 2.10. The multiplexing circuit diagram for μMUX, which uses frequency division multiplexing. Each TES is coupled to an RF-SQUID, which amplifies and reads out the bolometer's current as a variation in the magnetic flux. The SQUID is inductively coupled to a resonator, encoding each detector with a unique resonance frequency in the GHz. All the resonators couple to a common transmission line, where the low noise amplifiers (LNAs) amplify the output signal before SMuRF records it. This figure is taken from [36].

μMUX, a form of frequency division multiplexing, uses RF-SQUIDs to multiplex in the microwave frequencies from 4-8 GHz. RF-SQUID or microwave superconducting quantum interference devices are used to amplify and read out TES bolometers due to their sensitivity to magnetic flux. Figure 2.10 illustrates the μMUX readout scheme. In this schematic, a TES is coupled to an RF-SQUID so that any current change in the TES can be detected as a flux variation in the SQUID. Each SQUID is inductively coupled to a resonator with a unique resonance frequency in the GHz range, thus separating the detectors in the frequency domain.

All the resonators couple weakly to a common microwave transmission line. The TESs are voltage-biased on a single bias line via SMuRF. Incident optical power would cause a change in the TES current, which incidentally varies the SQUID flux and shifts the resonant frequency slightly. Thus, one can send a probe tone between 4-8 GHz down the transmission line to probe the resonator frequency and measure the bolometer current. The output signal with information on the shifts in resonant frequencies is then amplified using low-noise amplifiers (LNAs) at the 4 and 40 K stages. SMuRF then tracks and records information.

Chapter 3

Pulse Tube Cryocooler Testing

Cosmic Microwave Background experiments have been implementing cryogenic cooling techniques to increase the sensitivity of instruments and enable low-temperature detector technologies. Commercial pulse tube cryocoolers (PTCs) are frequently used to provide 40 K and 4 K stages as thermal shells in scientific instruments. The Simons Observatory uses the Bluefors PT420[1] model for its small aperture telescopes (SATs). However, PTC operation is known to be dependent on gravity, giving rise to changes in cooling capacity over the operational tilt range of pointed telescopes. This chapter presents the results of a study of three PTCs prior to their installation inside two different Small Aperture Telescopes. The last PTC serves as a spare. Section 3.1 provides a brief introduction to the pulse tube cryocooler and its operation mechanism. Section 3.2 focuses on the PTC for SAT-UHF, which henceforth will be called PT420-1. We did the most extensive testing on this pulse tube. This section goes over the testing methodology inside the lab at UC San Diego and the tilt test results published in [37]. Section 3.3 details the test results for SAT-1 PTC— the one that goes inside SAT-MF1— and PT420-4, the spare one.

---

[1] Bluefors Oy. Arinatie 10, 00370 Helsinki, Finland

3.1 Pulse Tube Overview

For the past few decades, the pulse tube cryocooler (PTC) has evolved significantly from its original design in 1963, as built by Gifford and Longsworth[38], to the current commercially available multi-stage PTCs. The basic components of a PTC include a compressor that serves as a piston, a regenerator to pre-cool the incoming gas, and a pulse tube with a heat exchanger at each end of the tube. The PTC operates in a closed and regenerative cycle through adiabatic compression and expansion processes. Unlike the Stirling cryocooler and the Gifford-McMahon (GM) cryocooler, which use a mechanical displacer to carry out the adiabatic process, the PTC uses the residential gas in the pulse tube as a displacer, reducing the number of moving components [39].

The gas goes through two main heat transfers inside the pulse tube: it deposits heat through the heat exchanger at the hot end during the compression, and it absorbs the heat from the cold end during the expansion. The general cooling process for a one-stage pulse tube starts with pressurization when the compressor pumps helium gas through the high-pressure helium flex line to the regenerator which then pre-cools the incoming gas. This new incoming gas continues to flow into the pulse tube, pushing back the original residential gas inside the tube. As a result, the gas undergoes adiabatic compression and heats up the pulse tube. This process generates a temperature gradient from one end to the other end. The hot end is kept at ambient temperature through its connection to a reservoir via a heat exchanger. During depressurization, the gas retreats and absorbs the heat from the pulse tube through the heat exchanger near the cold end, cooling any testing sample on this cold head. The inside of the pulse tube undergoes adiabatic expansion, creating another temperature decrease in the pulse tube. The gas flows back to the regenerator and eventually to the compressor through the low-pressure helium line. The temperature of the returning gas is lower than that of the incoming gas, making the gas start at a lower temperature in the next cycle. This whole process repeats until the base temperature is reached. More detailed explanations of pulse tube operation can be found in Radebaugh

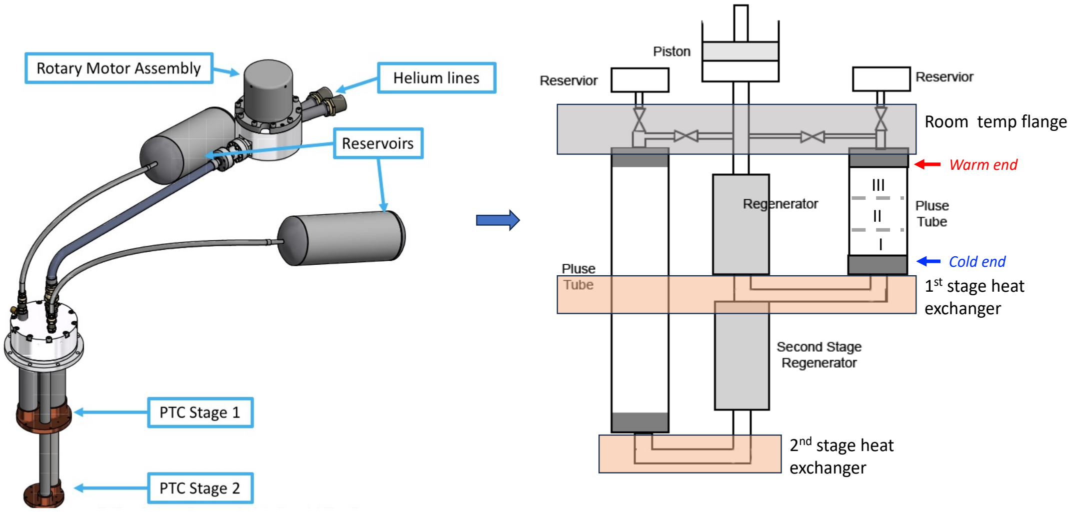

Figure 3.1. Overview of the two-stage pulse tube. Left: A 3D rendering of the PT420 from Cryomech with its remote motor assembly setup. The reservoirs for each of the stages and the 2 cold heads are called out here. Right: A schematic of the pulse adapted from the original figure in [41]. For the PT420, the two regenerators are in series with each other, while the pulse tubes are in parallel. In this figure, the warm and cold end of the pulse tube is called out for the first stage.

(1999) [39] and Raj et al. (2013) [40]. Figure 3.1 depicts what the PT420 looks like (left) and a schematic of a typical two-stage pulse tube configuration (right) in more detail. In this configuration, the two regenerators are in series, while the pulse tubes are in parallel. This allows the gas coming to the second stage pulse tube be cooled by two regenerators.

The gas in the pulse tube is subject to heat transfer by convection that occurs in fluids. In the normal operating mode at vertical orientation, the gas column reaches an equilibrium with a thermal gradient from the top to the bottom of the gas column and minimal convective mixing. The gas in the pulse tube is divided in such a way that the gases at the hot and cold ends do not mix. The gas is of one substance but there is a middle section of the gas that insulates the two ends to ensure a smooth thermohydrodynamics process. See Figure 3.1, where inside the pulse tube of the first stage, the three regions are being called out. The incoming gas occupies region (I), while the residential gas stays in region II and serves as a "separator" to prevent the gas from

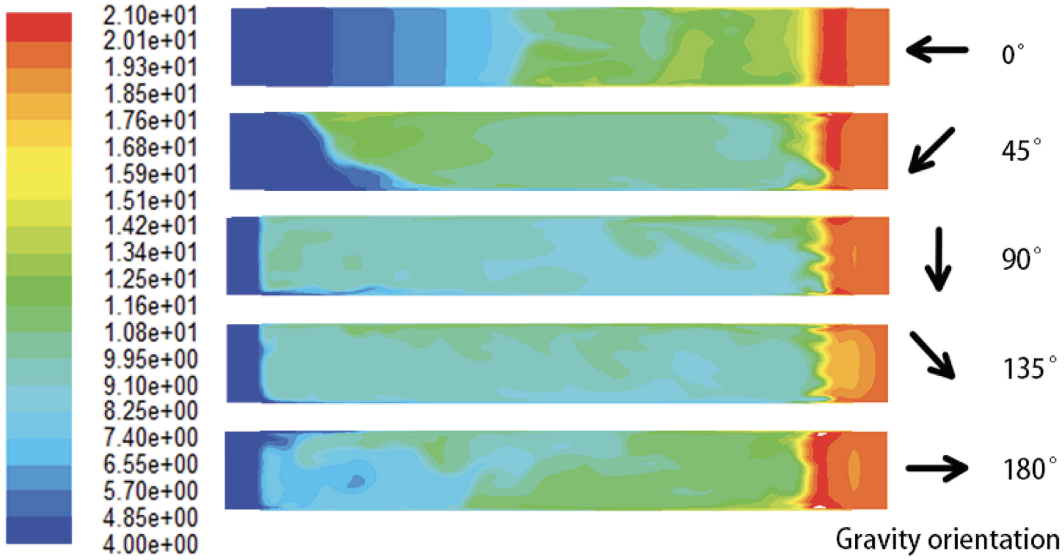

Figure 3.2. Simulation of the gravitational effect on the PTC. This figure is taken from [42], where the paper derives a relationship between the PTC inclined performance and its convection numbers for Stirling-type pulse tube (high-frequency) using 3D computational fluid dynamics (CFD) simulations. The temperature contours scales from 4 to 21 K. Notice that as the gravity orientation increases, the mixing between hot and cold gas increases, leading to a decrease in the amount of cold gas. Though this is a study for high frequency PTC, it serves as a nice illustration of the gas behavior in low-frequency PTC since the physics is pretty similar.

mixing. The gas in region III interacts with the reservoir. Once the PTC is tilted, convective processes can disrupt the thermal gradient, which can reduce the efficiency of the cooling cycle [39]. Therefore, the performance of a PTC is tied to the tilt angle of the system relative to the gravity vector, such that the cooling capacity of the PTC decreases as a function of the tilt angle. Figure 3.2 simulates the gas behavior due to convection, where the amount of cold gas decreases as the gravity orientation increases [42]. This is a simulation for high-frequency Stirling-type pulse tubes ($\sim$40 Hz); however, the concept is applicable to low-frequency pulse tubes. This convective effect in PTCs has been studied before by numerous literature (see, for example, [43, 44, 45]), with efforts to mitigate the effect focusing on high-frequency Stirling-type pulse tube for space-based applications [46]. However, the impact of tilt angle on low-frequency two-stage pulse tube systems ($\sim$1.4 Hz) has not been extensively explored.

3.2 PT420-1 Pulse Tube

3.2.1 In-lab setup

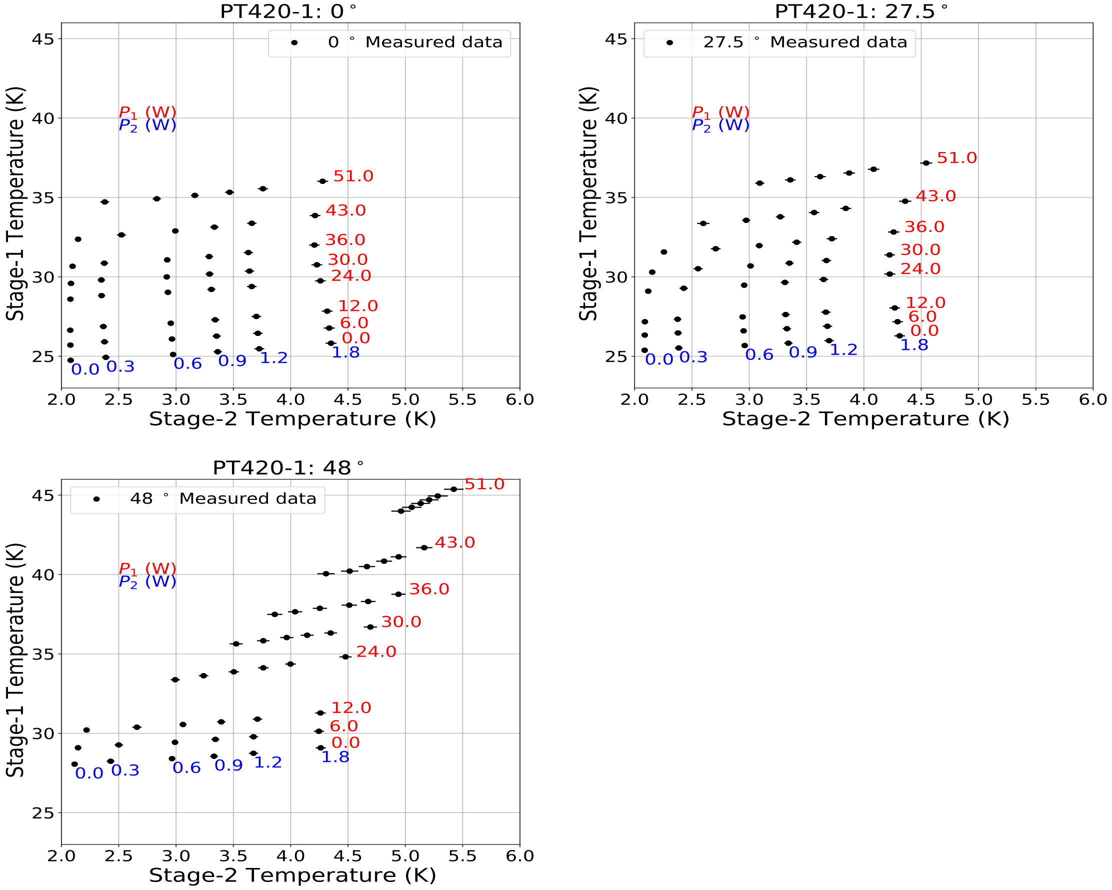

Figure 3.3. PT420-1 load curve data at 0°, 27.5°, and 48° with 0-51 W and 0-1.8 W on the first and second stage, respectively. The manufacturer validation at 0° for (P_1, P_2) = (0, 0) W and (0, 1.5) W yield (T_1, T_2) = (26.3, 2.16) K and (27.4, 4.20) K, respectively. Compared to the in-lab test load curve, PT420-1's performance exceeds the factory's by more than 9 W on Stage 1 and similar or slightly better performance on Stage 2. The 27.5° is a baseline for comparison for subsequent in-lab testing inside the cryostat as this is the angle when the PTC is installed inside the SAT. The 48° illustrates the contrast in performance from its initial non-tilt situation.

We developed a series of tests at UCSD to characterize the pulse tube behavior under different tilt conditions. We recorded the temperature of each of the PTC cold head stages over a range of angles from 0° to 55° with respect to gravity and over a range of thermal loading conditions, from 0 to 51 W and 0 to 1.8 W on the first and second stages, respectively.

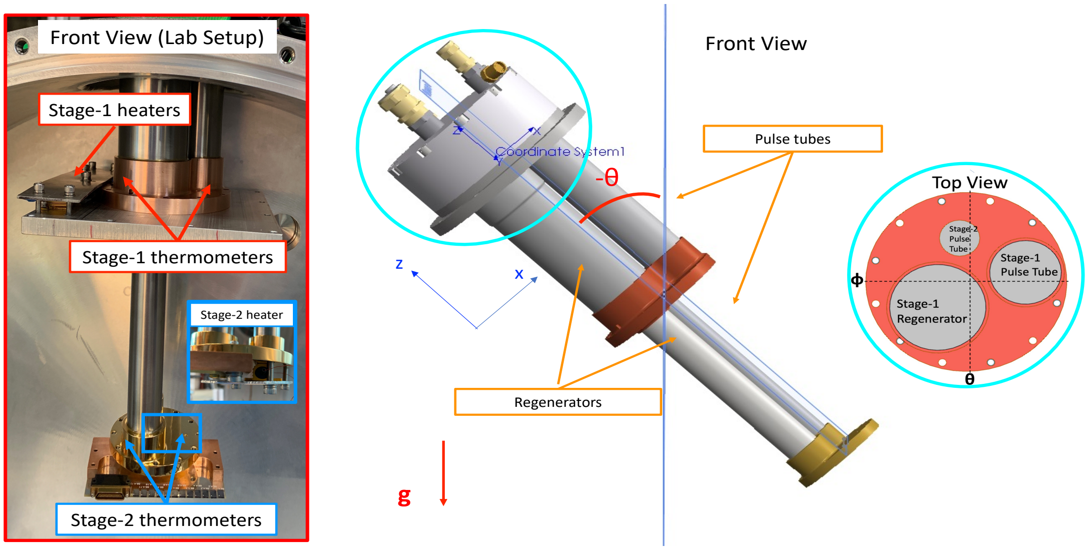

Figure 3.4. Experimental setup in lab showing the diodes, heaters, and the rotation of the PTC for various tilt tests. The right picture portrays the negative angle (-θ) tilt tests, with the positive angle (+θ) rotating the other way. We also rotate at an axis perpendicular to the θ axis, ϕ, as a parity check to the orientation effect on the PTC. See Figure 3.5 for the setup of ϕ test. The top right cutout illustrates the rotation axis for both θ and ϕ. The left picture is a zoom in picture of the thermometry and heater setup on both stages. The breakout were as follow: a 20 Ω heater bank and 2 diodes on the first stage and 500 Ω heater and 2 diodes on the second stage.

The test used a Bluefors PT-420 model, which was dictated by the available resources at the time. The specific PTC option we used for this experiment was a Bluefors PT-420 with the remote motor variation (PT420-RM) coupled to a CPA1114 Compressor, which has an advertised cooling power of 50 W at 45 K (stage 1) and 1.8 W at 4.2 K (stage 2). We focus on results obtained with a specific pulse tube, hereafter PT420-1, which has a manufacture-certified performance at 50 Hz and 260 psi static pressure of 68.0 W at 45 K and 1.87 W at 4.2 K.

The PT420-RM units procured for SO have two minor customizations relative to the stock version sold by Bluefors. Additional bolt holes were added in both stages to provide better mating to the cryostat thermal shells, where the SO version has eleven M5 holes versus six holes in the standard unit. The second customization is a gold-plated second-stage cold head to improve thermal contact with the mating heat strap in the telescope. We expect the impact of these changes on the test results detailed here to be negligible when compared to similar units.

The PT420-1 was connected to its compressor with 20-m helium lines provided by Bluefors, and it used the integrated motor driver in the Bluefors compressor. The remote motor option was chosen to reduce vibrational pickup in the cold heads. We mounted it on a separate plate using rubber offset feet that isolated the motor both electrically and vibrationally from the mounting surface. The compressor was delivered with a helium pressure level of 240 psi, which we did not adjust prior to testing. However, the recommended pressure for a 60 Hz system is 220 ± 5 psi. The manufacturer has indicated the increase in pressure may provide a small improvement in cryogenic performance, but it will primarily impact the power draw from the compressor. The magnitude of the effect can be seen by comparing our data to the manufacturer's data in Figure 3.3. We see slightly more than 9 W of additional cooling power on Stage 1 compared to the 0 W stage-1 data from Bluefors and a small improvement in capacity on Stage 2. Additionally, we performed a test to examine the impact on a different PT-420 system by changing the pressure from 233 to 240 psi while on the same power system of 60 Hz, which yielded $< 3\%$ improvement on the first stage heat lift and a smaller change in capacity on the second stage of $< 1\%$ for the higher pressure setting. The result from the pressure test is consistent with the manufacturer's statement above. The 9 W improvement in comparison to Bluefors's data may be due to various factors besides pressure settings such as operating on different testbeds at different power system (50 vs 60 Hz). See section 3.3 for more details on this pressure test and other tests done on other PTCs as we expect each PT-420 unit to have slight variations in performance. We chose to operate at the higher pressure as the system will ultimately operate on a 50 Hz electrical grid, which requires 260 ± 5 psi for best performance as specified in the Bluefors user manual.

The vacuum chamber utilized for the tests was originally the front section of the Microwave Bolometric Array Camera (MBAC) [47]. We re-purposed a small section of the original camera along with the front and back vacuum plates of the receiver to make a cylindrical vacuum chamber 28 cm long with a diameter of 95 cm. The PT420-1 was mated to the chamber through an existing port combined with an adapter collar. A second port was also modified to allow attachment of an ISO-100 Accu-Glass[2] hermetic feedthrough (50D2-L100) with two D-sub 50 (DD-50) ports. The modified vacuum chamber is referred to hereafter as mini-MBAC (mMBAC). Heater wires used to load the separate stages occupied one of the DD-50 feedthroughs while the second DD-50 feedthrough was used for thermometry. The remote motor was mounted to an adjustable shelf attached to a metal frame that was used to stabilize mMBAC during testing. The motor head and the two ballast tanks were connected to the cold head with flexible stainless steel lines.

A radiation shell was installed around the second stage of the PTC to decouple the stage from the radiative environment. A 6061-T6 1/2" thick aluminum plate was attached to the first stage of the installed PTC to form the top of the radiation shield. A 6061-T6 1/2" thick aluminum box was bolted to the plate to complete the shield. The box had a slit to allow wires to pass to the second stage and was wrapped in a multi-layer insulation (MLI) blanket composed of 10 individual layers. The estimated radiative loading on each stage is < 1 W and < 1 mW, respectively. The ambient loading from radiation is small in comparison to the loading applied from heaters for our set points. We ignore ambient loading from the PTC itself since it is intrinsic to the device.

Heaters and thermometers were attached to both stages of the PT420-1 to characterize the performance of the unit. Parameters for the heaters were chosen to cover the range of power advertised for the units from Bluefors, as well as to cover the expected loading in the SO cameras and similar cryogenic setups. The design parameters from these inputs motivated loading values in the range of 0 to 55 W for Stage 1 and 0 to 1.8 W for Stage 2. See Figure 3.4 for details of the test setup. The left of this figure shows the heaters and thermometer setup. The right side illustrates the tilt test which section 3.2.2 will be going over.

The first stage had a bank of five 100 Ω heaters connected in parallel (total resistance of 20 Ω) with fine gauge copper wires routing directly to a solder cup DD-50 connector. A power supply unit (PSU) with two 30 V outputs connected in series was used to drive these heaters,

---

[2] Accu-Glass Products, Inc., Valencia, CA 91355

providing a maximum loading of 180 W. For the second stage, we clamped a 500 Ω heater against the bottom of the cold head. The heater was connected to the same DD-50 hermetic feedthrough via fine gauge copper wires routed to the 30 V channel on a second PSU that could provide a maximum load of 1.8 W. The estimated loading from the wiring on each stage is < 0.3 W and <8 mW, respectively. The conductive heat loads are negligible compared to the loads from the heaters. We have accounted for them in the error bars as an additive contribution on top of the radiative loading and the power supplies' intrinsic accuracy specification.

We used Lakeshore[3] DT-670 silicon diodes mounted in custom copper bobbins developed for use across SO. The diodes have an advertised precision of about 22 mK on the first stage and 12 mK for the second stage. The uncertainty on our temperature measurements was dominated by oscillations in the cold head temperature itself and not by the thermometer performance. A cryogenic breakout board (CBOB) developed for SO was used to convert an input 50-pin micro-D miniature (MDM-50) cable into twelve four-wire thermometer measurement connections. The CBOB allowed us to use existing manganin weave cables. We mounted the CBOB to a copper plate that was attached to the second-stage cold head. Two diodes were bolted directly to the top copper surface of the PT420-1 first stage with wires routed to the CBOB on the second stage. An additional two diodes were bolted to the top of the second-stage cold head and also connected to the CBOB. A 50-pin cable with an MDM-50 connector on one end and a DD-50 connector on the other was used to route the signal from the four thermometers to the hermetic DD-50 connector.

3.2.2 Testing methodology

The cylindrical vacuum chamber made changing the angle relatively easy as we could roll the cryostat with the PTC installed to the desired angle. We attached a digital angle gauge to the top of the PT420-1, and we confirmed the setup gave us repeatable measurements to better than 1 degree. The remote motor and reservoir tanks were mounted on an adjustable shelf, which

---

[3] Lake Shore Cryotronics, Inc., Westerville OH 43082

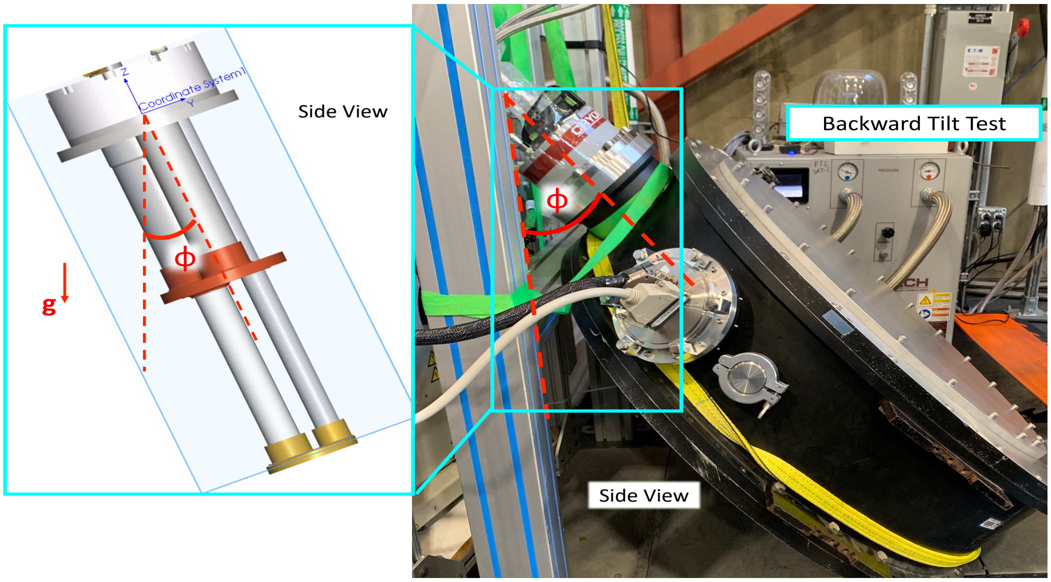

Figure 3.5. Testing setup in lab for the ϕ tilt test. This test explores the effect on the cooling power due to the asymmetry of the axis of rotation with respect to the regenerator and the pulse tube. The mMBAC was situated backward and strapped to a stand nearby. Due to the physical limitation of the setup, we could only tilt at 3 angles and up to 45°

allowed us to rotate the test chamber without disconnecting the remote motor and reservoir tanks.

We took data across an 8×6 grid over a range of power from 0 - 51 W on the first stage and 0 - 1.8 W on the second stage at 0°, 27.5°, 36°, 41°, and 48°. Figure 3.3 displays the load curve at a couple of angles (0° and 48°), where the change in performance from one angle to another is conspicuous. We also took more detailed angular data at five power set points: (P_1, P_2) = (0, 0) W, (0, 1.8) W, (24, 0.9) W, (51, 0) W, and (51, 1.8) W. We did not tilt beyond 60° due to physical limitations of our in-lab configuration.

We rotated the test chamber in both positive and negative directions ($\pm\theta$) as well as around an axis perpendicular to the cylinder axis (backward tilt tests, ϕ) to explore dependencies of the PT420-1 on the axis about which it was tilted as the rotation axes were not symmetric with respect to the regenerators and pulse tubes as shown in Figure 3.4 and 3.5.

The tilt-test load curves were obtained over a period of four weeks in November of 2019 in a highbay facility with fairly stable ambient temperatures that roughly follow the day night temperatures at UCSD. We did not observe any dependence on the diurnal cycle in our data.

3.2.3 Data Reduction

The diode thermometer four-wire measurements were performed using Lakeshore 240 Series Input Modules (LS-240s). LS-240s are programmable cryogenic readout instruments, each capable of simultaneously reading out up to eight independent voltage or resistance measurements down to 1 K. The diodes used for this analysis were calibrated by cooling them down on the same stage as a reference Lakeshore calibrated diode.

The LS-240s are connected via USB to a local computer, which records the temperature data to disk using the Observatory Control System (OCS) [48]. OCS is a distributed control system designed to coordinate data acquisition in astronomical observatories and is used throughout SO for control and data storage across dozens of electronic devices[4]. The thermometry data was recorded at a rate of 1.6 Hz. PSUs were also controlled through OCS via ethernet to supply power to both stages. We operated them in current command mode, and at each loading step the current levels were set using the nominal resistance values of the stage heaters to supply an appropriate amount of power to each stage. To cycle through all the power set points, we applied power to the first stage and iterated through the second stage loading points. We then changed the power level on the first stage and repeated the process. A wait time was set between each change in loading to allow temperatures to stabilize. Steps on the first stage loading had a two-hour wait time while changes on the second stage loading had a wait time of one hour. We iterated through all power set points before stepping the angle.

To obtain a single temperature value per step, per stage, we defined temperature stabilization criteria to select the range of data to be averaged. First, we found the extrema within the step in the direction the temperature was stabilizing. Then we selected all data after the temperature reached within 2% of the extrema, relative to the change between its minimum and maximum values during that step. In other words, we selected all data after the step was 98% "complete". We then applied a low pass filter to filter out the pulse tube intrinsic oscillation,

---

[4] OCS Github: https://github.com/simonsobs/ocs

where temperature fluctuated as a result of the adiabatic pressure oscillation in the pulse tube. Since our sampling frequency is not twice the intrinsic frequency of the pulse tube, there is some aliasing. So we applied a low pass filter to filter out these dominating aliased frequencies. Next, we selected the last 90% of the filtered section and calculated the median and standard deviation for the temperature data from this period. The average temperature of the two thermometers on each stage determined by this method was used in the analysis. As a sanity check, we checked the results after applying the low pass filter versus without the filter, and the temperature median values are mostly under 0.5%, with some rare cases close to 1% difference.

3.2.4 Cooling performance vs inclination angle fitting results

The extensive range of data we collected allows us to empirically constrain the performance of the PT-420-1 two stage PTC. We combined the high-density load curve data at sparse angles ($0-48^\circ$) with the sparse load curve data with more detailed angular sampling ($0-55^\circ$) as shown in Figure 3.6 and Figure 3.8. The parameter space of the data with angular information combined with the loading and temperature at two stages presents a number of potential combinations for analysis. For simplicity, we separate the data by stage and by power set points to compare temperature versus tilt angle. This section details the results from the PT420-1 data.

We empirically fit the data to an exponential function,

$$T_i(\theta, P_1, P_2) = a_i(P_i)e^{b_i\theta} + c_i(P_1, P_2) \tag{3.1}$$

where i is either 1 or 2 corresponding to the first and second stages, respectively. This formula provides a simple method to extract temperature from a given loading condition and tilt angle over the range we tested. The fit has an offset value c_i, which can be determined from the high-density load curves at 0° (see Figure 3.3), and it is equivalent to the temperature shift from extra loading at 0°. We utilize a parameter b_i in the model as a scaling of the angular dependence in the exponential that we leave fixed over our range of heat loads. The a_i term serves as a scaling parameter that can be fit as a function of the loading on the stage.

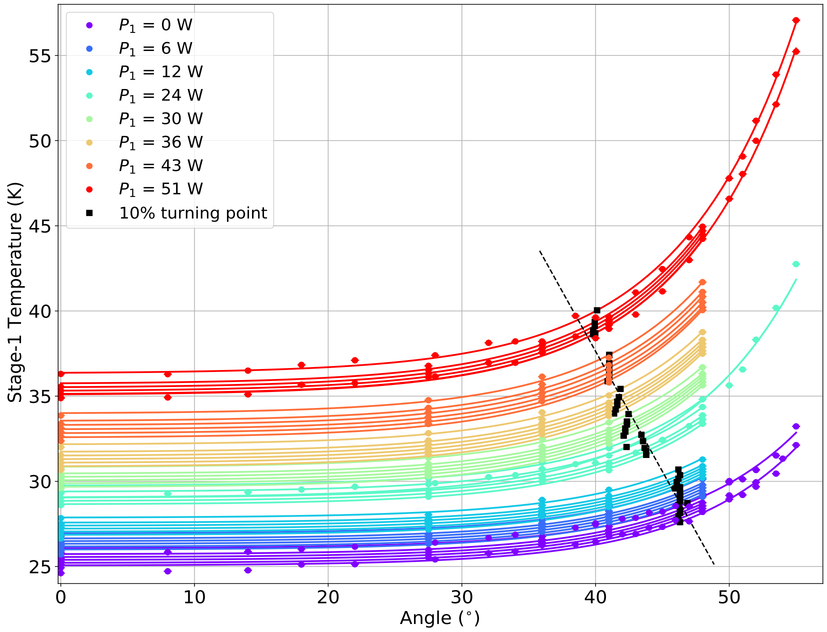

Figure 3.6. Stage-1 performance and fit results (solid lines) using Equation 3.1 with parameter b_1 constrained to be the same for all power set points. Here we include the tilt test data with fine angular sampling ($-\theta$) and the high-density load curves with sparse angular sampling (circles). The black squares are the temperatures from the fits that are 10% higher than the temperatures at 0°.

We constrain b_1 using a least-square minimization fitting method, which allows it to remain independent of loading set points. This method fits all data sets at once with the condition that b_1 stays the same throughout while a_1 and c_1 are fit to the data for each power set point, effectively fitting 97 unconstrained parameters. We found the best-fit value of $b_1 = 0.1152 \pm 0.0013$ (deg.$^{-1}$). Figure 3.6 shows that the first stage performance is well fit by an exponential function across the sampled parameter space. The sampled data are color-coded according to their Stage-1 power. The multiple lines of the same color are the fits of the data that have the same P_1 but different P_2s. Some data sets are more dense and extended beyond the 50° because they are from the fine angular sampling tilt tests. The black 10% turning points are also plotted and will be discussed in more detail in section 3.2.5.

As expected, a_1 exhibits a strong dependence on the first stage loading. A linear fit of a_1 versus first stage loading (Figure 3.7) allows the determination of the a_1 parameter from a given loading value. The c_1 parameter can be determined by interpolation of the dense load curves shown in Section 3.2.2. We also note that the second stage loading primarily creates an offset at the 0° temperature for stage-1 which is captured in c_1. We do not attempt to separate the stage 2 loading effect on the shape of the stage 1 exponential as our data set is insufficient to determine significant trends.

We use the same empirical model and fitting procedure to analyze the second-stage data. Stage 2 exhibits a strong dependence on both the first and second-stage loading values, which makes it more challenging to fit with a simple exponential. As such, the empirical model is less effective for the second stage, but it is still useful in describing the system (see Figure 3.8). In particular, the data from set points with $P_1 = 0$ exhibits unusual behavior that is not well fit by an exponential. For these points, the rise in temperature with angle is steeper and occurs at high

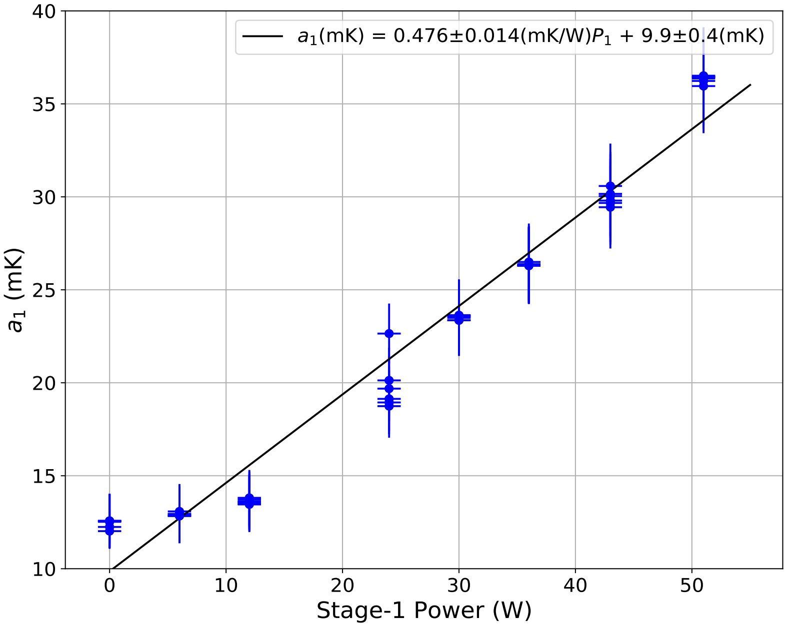

Figure 3.7. a_1 vs Stage-1 power. The black solid line is the best fit as a function of P_1. The error bars for P_1 account for the radiative loading from the 300 K, conductive loading from the wiring, and the power supplies' programming accuracy. Error bars for a_1 come from the square root of the covariance of the fitted parameters.

angles, which meant the sparse angle data at this set point could not be used as the response was flat across the $0-48^{\circ}$ range. Similarly, we did not include the sparse angle data for P_1 = 6 W and $P_1 = 12$ W for the same reason. Overall, there were 65 unconstrained parameters fitted to the second stage data, and we found the best-fit value of $b_2 = 0.096 \pm 0.006$ (deg.$^{-1}$).

The a_2 term displays a dependency on the loading from both stages. We develop a simple process to decouple the two power contributions to complete our empirical model. First, we fit a_2 as a function of P_2 with the slope, m_2, fixed for all P_1 set points, while letting the intercept float. The intercept is then plotted against P_1 to determine the dependence on the first stage power as shown in Figure 3.9. The end result is:

$$a_2(P_1, P_2) = m_2 P_2 + d_2 P_1 + f_2 \tag{3.2}$$

d_2 and f_2 are the slope and intercept, respectively, of the fit to the a_2 fit intercept values versus P_1 (Figure 3.9 right plot). From the fits, we have $m_2 = -4.8 \pm 0.5$ mK/W, $d_2 = 0.29 \pm 0.04$ mK/W, and $f_2 = 6.1 \pm 1.4$ mK. The linear fits effectively decouple the first and second-stage contributions, allowing us to complete our empirical model as a combination of exponential and linear fits to the data we obtained.

3.2.5 Temperature uniformity over tilt range

For many of the instruments that use PTCs over a wide angle range, such as telescope cameras on pointed platforms, a primary design goal is to reduce scan dependent temperature drifts. The data here clearly favor constant tilt angle scan patterns that are already employed by many instruments. However, it is worth examining the relatively stable temperature regime we observe across the loading steps and tilt angles.

The first stage temperature inflection follows the expected trend, with more rapid temperature change versus angle as the first stage power is increased, as shown in both Figure 3.6 and the left plot of Figure 3.10. Figure 3.6 depicts the angle turning point at which the temperature

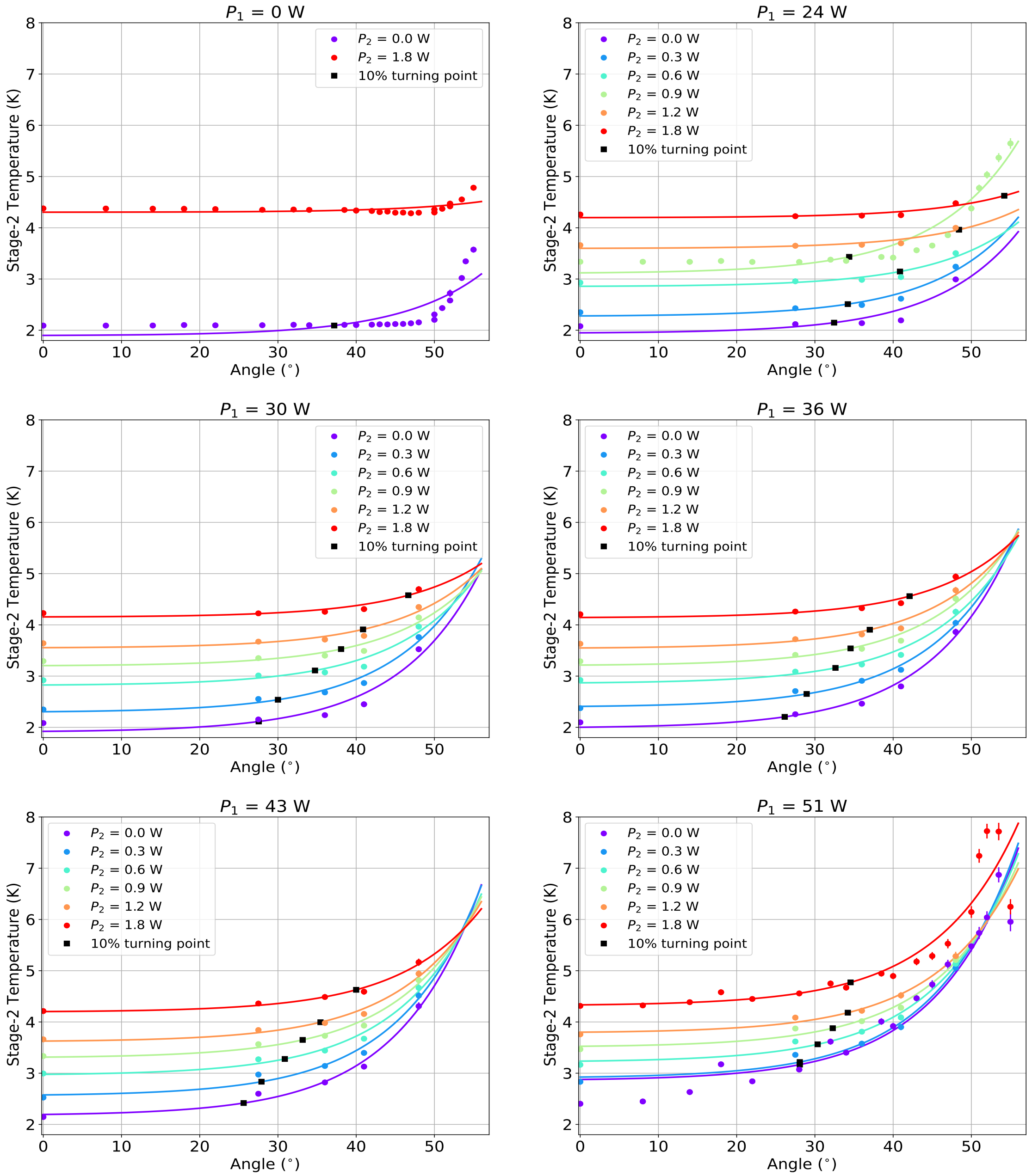

Figure 3.8. Stage-2 performance and fit results (solid lines) using Equation 3.1 with parameter b_2 constrained to be the same for all power set points. The data sets with sparse angle information for the $P_1 = 0$ set point are excluded as the response was flat over the angular range examined, resulting in an inability to fit an exponential function to that data. We also excluded the sparse angle data for $P_1 = 6$ W and $P_1 = 12$ W due to their similarly flat response. The black squares are the 10% turning points. For ($P_1 = 0$, $P_2 = 1.8W$, the turning point is outside the plot range.

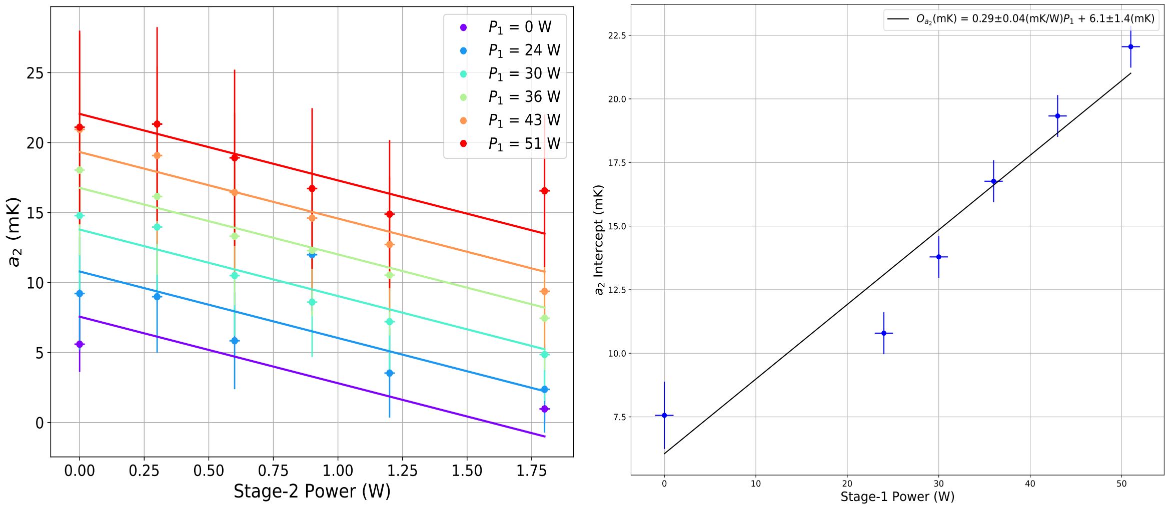

Figure 3.9. Characterization of a_2. Left: a_2 as a function of P_2 with colors corresponding to different P_1 values. The linear fits all have the same slope allowing us to use the fit intercepts to decouple the first-stage dependency. The error bars in the data points are calculated using the same method as mentioned in Figure 3.7. Right: The intercept values from the linear fits in the top figure are plotted against P_1 with a second linear fit used to complete the empirical model for a_2.

has increased by 10% from its initial non-tilt position. As expected, the angle turning points decrease almost linearly as P_1 increases, and there is little effect from Stage-2 power. Depending on the scanning strategy, one should be cautious when tilting beyond 40° as cooling capacity might be significantly impacted. The left plot in Figure 3.10 is a similar plot to Figure 3.6 but with the offset (c_i) removed, so the data all start from the same baseline. Here, the figure only includes the fits and not the data points. Similarly, the temperature remains uniform until $\theta \geq 40^\circ$, where T increases beyond 2 Kelvin. The effect of the second-stage loading on the first-stage temperature uniformity is also observed to be small and sub-dominant to the first-stage loading effects. For the range of data we sampled, we see a less than 2 K change in temperature up to tilt angles of 30°. For design requirements favoring temperature uniformity over wider tilt ranges, there is a clear preference for lower loading values in the first stage.

The behavior on the second stage is more complex given the second stage's cooling power is coupled to loading on both stages. As seen in the right plot of Figure 3.10, the rate of temperature change increases with the first stage loading as one might expect. However, for the two sets with fixed first-stage loading, we see the increase in second-stage loading actually produces a slower rate of temperature change with angle. The trend is also seen in the sparse angular data shown in Figure 3.8, though it would be useful to have more detailed data at higher angles to confirm our finding. In this figure, the 10% turning angles increase as P_2 increases for a set P_1. The behavior is also captured by the a_i slopes, where a_1 increases with P_1 as expected but a_2 has the opposite trend, decreasing with increased P_2.

The fact that the second-stage trends are more closely tied to the first-stage loading offers an important design input for projects, which favors a wider angular range of temperature uniformity on the second stage. The widest regime of minimal temperature change versus inclination angle is achieved with low power on the first stage but higher power on the second stage. The trend suggests that for best temperature uniformity over a tilt range, there is a preference to decrease the first stage loading over decreasing the second stage loading.

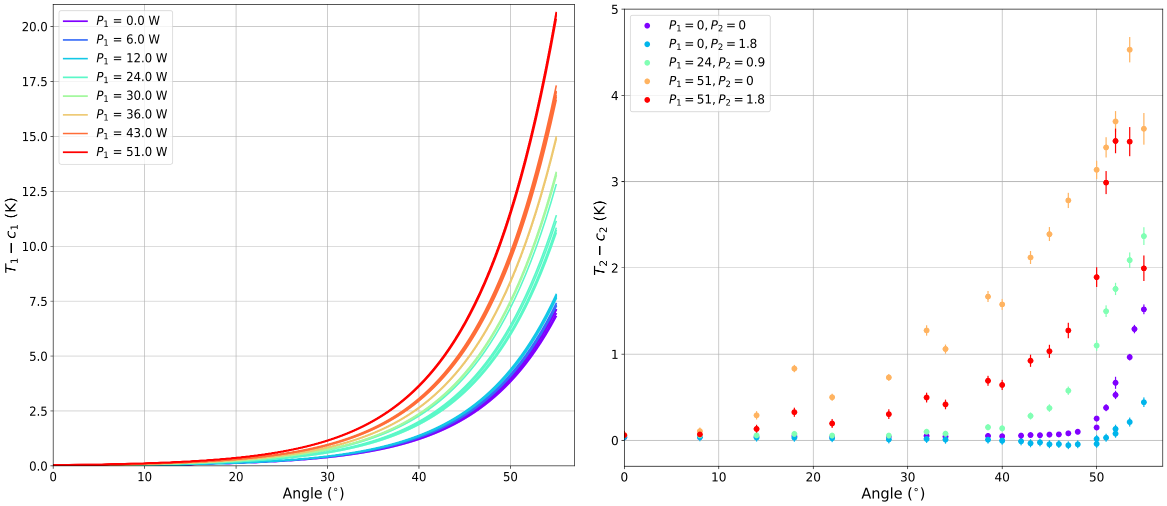

Figure 3.10. Temperature uniformity on both stages. The left and right plots show stage-1 fit functions and stage-2 detailed angular data, respectively, with the offset parameter c_i removed. The left plot has the fits for every power set point shown in Figure 3.6, with the different P_1 color-coded from purple ($P_1 = 0\ W$) to red ($P_1 = 51\ W$). The spread in the line of each color is from the changing P_2, which has a small effect on the overall trend. The right plot portrays the stage-2 detailed angular temperature data as the second stage fits are less effective at capturing the trends at higher angles.

3.2.6 Rotational axis dependence results

The geometry of a two-stage PTC is not symmetric about the primary central axis with regard to each stage's pulse tube and regenerator layout as shown in Figure 3.4. To explore whether this asymmetry produces a rotational axis-dependent effect of inclination angle versus cooling capacity, we tilted the PT420-1 unit in two additional rotational directions. First, we tilted the chamber in the opposite direction from 0°, in the $+\theta$ direction, primarily affecting the relative orientation of the first stage pulse tube and regenerator. Second, we tilted the unit backward along a rotational axis, ϕ, perpendicular to the θ axis which primarily affects the second-stage pulse tube and regenerator relative orientation (Figure 3.5). The results of these tests as compared to the primary rotation direction are shown in Figure 3.11.

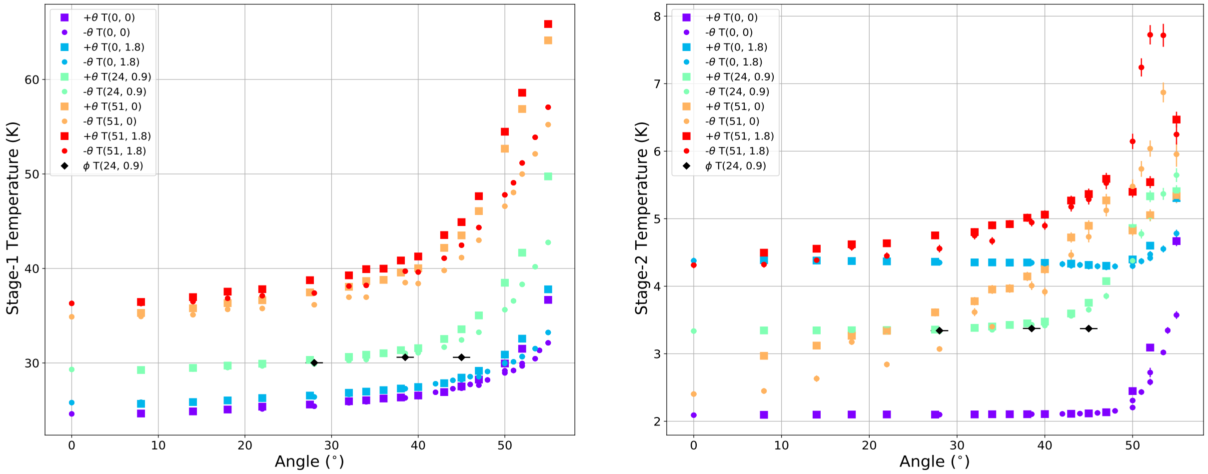

Figure 3.11. Rotational Axis Dependence on both stages. Temperature data ($T(P_1, P_2)$) for the +θ (squares), -θ (circles), and ϕ tests (diamonds) are plotted as a function of angle. According to Stage-1 data, the dependency on the tilt axis becomes prominent at high Stage-1 power and large tilt angle. This effect, however, is not as obvious on the second stage.

The data suggest a divergence between $\pm\theta$ on the first stage at higher angles and higher powers, favoring the $-\theta$ direction where the regenerator becomes lower than the pulse tube. However, additional data is needed to determine the magnitude of this trend. The backward tilt tests in ϕ are consistent with the other tilt directions which could be due to the fact that the second-stage pulse tube is longer and narrower compared to the first-stage pulse tube, which could reduce the impact of tilting in ϕ as the rotation primarily changes the orientation of the second stage components [49]. However, the challenges of tilting in that direction produced too sparse a set to fully explore the dependency.

3.2.7 Summary and future implications

Cryogenic cooling techniques have become prominent in telescope instrument applications as well as other branches of physics. Characterization of these cryogenic components is critical to guide instrument designs and ensure the achievement of science goals. We examined the performance of a Bluefors two-stage pulse tube cryocooler and produced an empirical model to quantify its cooling capacity. Given an expected loading on each stage, P_1 and P_2, the projected temperatures on each stage, T_1 and T_2, can be produced over a range of angles, θ, from 0 to 55 degrees using the following relationships:

$$T_1(\theta, P_1, P_2) = a_1(P_1)e^{b_1\theta} + c_1(P_1, P_2) \tag{3.3}$$

$$a_1(P_1) = 0.476(mK/W)P_1 + 9.9(mK) \tag{3.4}$$

$$T_2(\theta, P_1, P_2) = a_2(P_1, P_2)e^{b_2\theta} + c_2(P_1, P_2) \tag{3.5}$$

$$a_2(P_1, P_2) = -4.8(mK/W)P_2 + 0.29(mK/W)P_1 + 6.1(mK). \tag{3.6}$$

Here c_1 and c_2 can be produced by interpolating the load curve data at 0°. The exponential terms are $b_1 = 0.1152 \pm 0.0013(deg^{-1})$ and $b_2 = 0.096 \pm 0.006(deg^{-1})$ for the first and second stages, respectively. All the data sets, including the load curve for interpolation and fit results, can be accessed on github[5].

We found that the first-stage performance versus angle is dominated by loading on the first stage and shows little to no dependence on the second-stage loading over the ranges we explored. The first stage exhibits higher temperatures and a stronger angular dependence as

---

[5] Data GitHub: https://github.com/ttsan2521/Bluefors_PT420_Data.git

more loading is applied. The second stage's performance is more complex as its cooling capacity is dependent on the state of the first stage. The second stage tends to increase in temperature and exhibit a stronger angular dependence as more first-stage loading is applied. However, we see evidence of decreased angular dependence as more power is applied on the second stage, producing an inverse relationship. This effect suggests designs that optimize second-stage temperature uniformity rather than the absolute temperature would benefit most from higher second-stage loading and lower first-stage loading.

We also performed tilt angle tests to probe any axial dependence of the tilt direction. The tests suggest slightly lower first-stage temperatures when tilting in the $-\theta$ direction, while we did not see any significant dependence on the second stage. However, the data we obtained to explore this effect could be improved with more extensive measurements that explore a wider range of axial tilt directions and tilt angles than what we did in our tests.

The angular data sets we collected within our experimental time constraints were sufficient to construct a basic empirical model. However, the performance characterization of low-frequency two-stage PTCs would benefit from potential future investigations including measurements with a more detailed load curve at each angular step over a larger range of angles, which could be used to construct a more complete empirical picture or be used to inform an analytic model.

3.3 Other PTCs

This section describes work with other pulse tubes of the same PT420 unit under different settings (e.g. different helium hose lengths) and how they impact the cooling performance. We carried out tests on two additional pulse tube units: the PTC that is currently installed inside SAT-MF1 (in addition to the PTC that is integrated with the BlueFors dilution refrigerator) and a spare PTC. Henceforth, the two PTCs are called SAT-1 PTC and PT420-4. SO brought four standalone PTCs; one for each of the three SATs and one as a spare. Extensive tests have been done on three of them, and the results are included in this chapter. We have only done minimal tests on the last PTC, enough to validate its cryogenic performance against the manufacturer's specs. All PTCs are sourced from Bluefors under the same pulse tube and compressor types: PT420-RM and CPA1114 compressor. They have the same mechanical customization as mentioned in section 3.2.1. SAT-1 PTC tests were done with its own unit of pulse tube and compressor, which has a manufacture-certified performance at 50 Hz and 260 psi static pressure of 50 W at 45 K and 1.80 W at 4.2 K, the same certification as PT420-1. For the PT420-4's setup, its own pulse tube was connected to PT420-1's compressor. Bluefors tested the PT420-4 and certified it (in its own pulse tube and compressor unit) at 60 Hz and 220 psi instead. The specs at this setting are the same as the other two PTCs.

Table 3.1. This table lists the test settings for the two additional pulse tubes, including the ones from PT420-1. These are the main data sets used for subsequent analysis. * indicates some ambiguity in the He line length; however, the most likely scenario is 20 m.

Data Set	Unit	Angle	Compressor Pressure (psi)	He line lengths (m)
1	SAT-1 PTC	0° (2019)	236	20
2	SAT-1 PTC	0° (2022)	218	20*
3	SAT-1 PTC	27.5° (2022)	218	20*
4	PT420-1	0°	240	20
5	PT420-1	27.5°	240	20
6	PT420-4	0°	235	20
7	PT420-4	27.5°	235	20
8	PT420-4	0°	233	70
9	PT420-4	27.5°	233	70
10	PT420-4	0°	240	70
11	PT420-4	27.4°	240	70

The following tests were done inside the mMBAC using similar configurations, methodology, and data extraction as described in section 3.2.2 and 3.2.3. The subsequent results focus on the 0° and 27.5°, the angle at which the PTC is installed inside the cryostat. For SAT-1 PTC, the tests spanned from 2019-2022, with the initial validation in June 2019 and the re-validation in April 2022 to check the unit's performance stability over time. Between this time frame, this PTC had been installed inside SAT-1 and went through 11 cooldowns before its re-validation outside the SAT. As for PT420-4, we explored the impacts that different helium flex lines' lengths and compressor pressure settings would have on cooling capacity. These helium stainless steel lines connect to the compressor and deliver low- and high-pressure helium to the pulse tube. Table 3.1 summarizes the data sets used in the analysis.

3.3.1 Performance Difference between various PT420 units

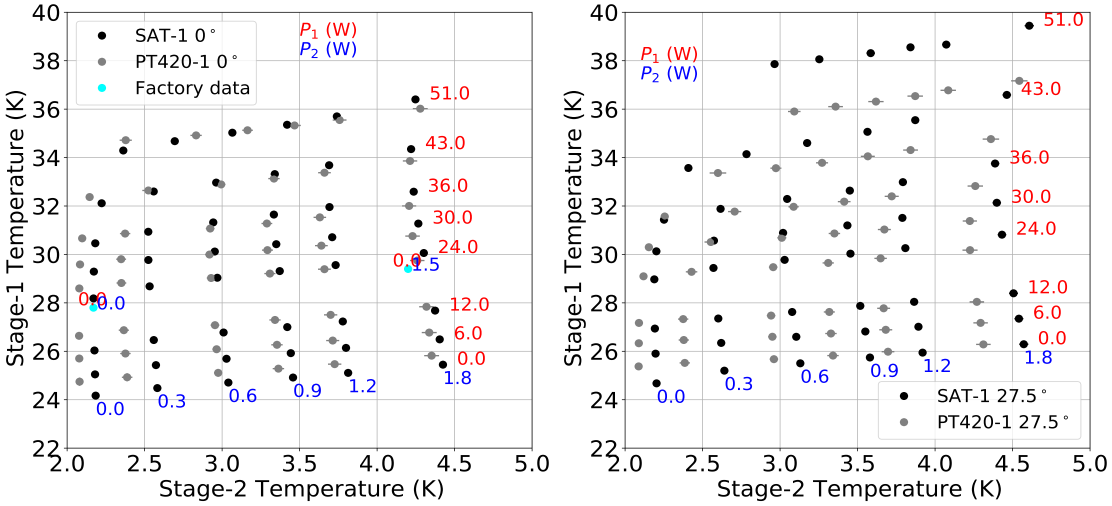

Figure 3.12. Comparison between PT420-1 and SAT-1 PTC at 0° (left) and 27.5° (right). The 0° load curves use data sets 1 and 4 together with SAT-1 PTC factory validation data. The differences between these two units are less than 3% on the first stage and less than 8% for the second stage. The 27.5° data (set 3 and 5) yield slightly larger effects: <6% and 10%, respectively.

The three PTCs come from the same PT420 family, but their performance varies even under identical testing conditions. These variations become more pronounced at higher P_1 and tilted angles for the first stage, while the second-stage results show larger discrepancies at colder temperatures. Figures 3.12 compare the load curves at 0° and 27.5° for SAT-1 PTC against PT420-1. At both angles, Stage-1 difference remains within 6%, with PT420-1 consistently exhibiting better cooling power as the angle increases. The largest difference occurs at $P_1 = 51$ W for $\theta = 27.5°$. The same trend is observed on Stage 2, with more prominent differences (up to 10%). Notably, the large differences occur when both power levels are low: $P_1 \leq 12$ W and

$P_2 \leq 0.3$ W.

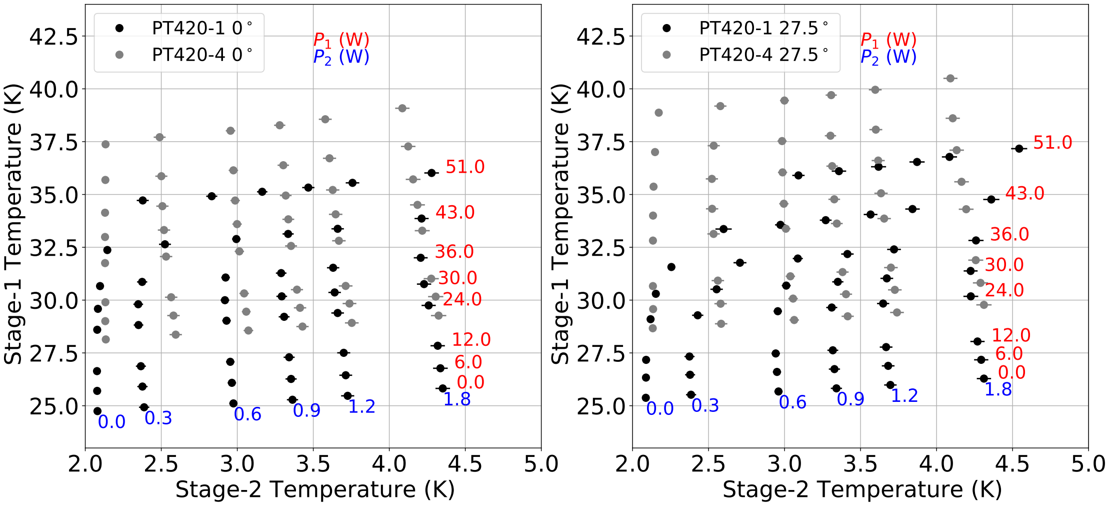

Figure 3.13. Performance comparison using the same compressor but different pulse tubes (data sets 4-7). Both of the PT420-4 and PT420-1 temperature data have the same He line lengths (20 m), but PT420-4 have a slightly lower pressure.

Since PT420-4 uses the PT420-1 compressor, a baseline check involves comparing its performance at 0° and 27.5° to that of PT420-1, as shown in Figure 3.13. We collected temperature data for PT420-4 at 235 psi with 20-m long He hoses. The PT420-1 data were collected under similar conditions but at a slightly higher pressure of 240 psi. As discussed later, this minor pressure difference is unlikely to account for the significant discrepancies observed in the first stage of the two plots. The results suggest that PT420-4 experienced an additional 24 W more than PT420-1. Note that PT420-4 was certified for a 60 Hz power system with a static pressure of 220 psi, whereas PT420-1 was certified for a 50 Hz power system with 260 psi. Given that the tests on both units deviated from their original operating parameters, changes in cooling performance were expected. However, pinpointing the exact contributing factors requires more dedicated testing in a controlled environment with setups identical to those used by the manufacturer.

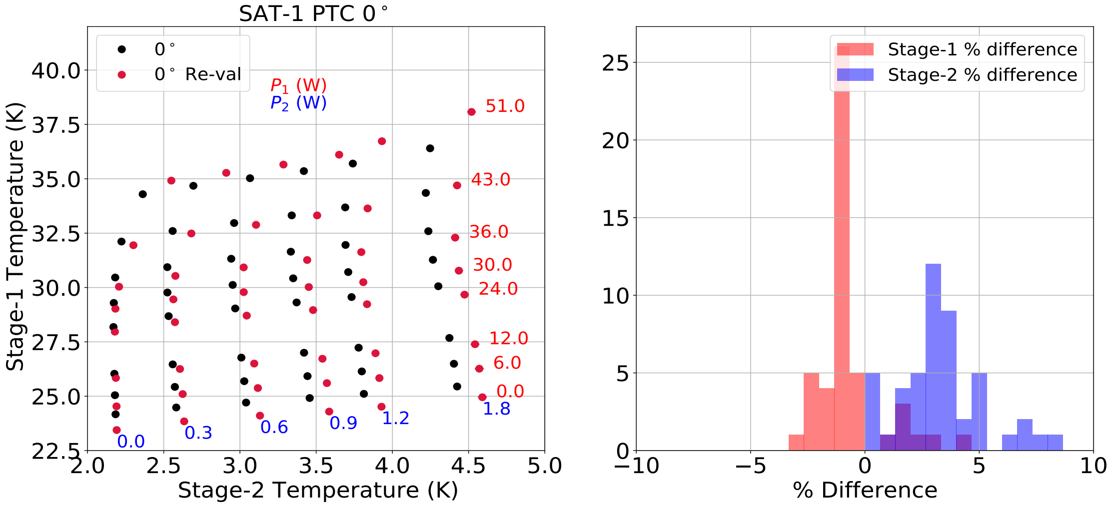

Figure 3.14. Performance overtime of the PT420. Left: The load curves of SAT-1 PTC. The original validation data (2019/data set 1) is in black and the re-validation (2022/data set 2) is in red. Right: a histogram distribution of the % difference between the two datasets. The baseline is the 2019 dataset, so negative indicates that the revalidation data perform better. The largest dT are 1.7 K and 0.2 K for Stages 1 and 2, respectively.

3.3.2 Stability of the PT420s

This section checks the stability of PT420s over time using the original validation data of the SAT-1 PTC in 2019 against the re-validation of it three years later. As seen from Table 3.1, the two data sets have slight differences in the compressor pressure: 236 vs. 218 psi. According to Figure 3.14, there are slight discrepancies in performance after three years. The first stage has slightly better cooling capacity at lower power, while stage-2 cooling power has decreased over time. However, most data points are within 5% difference. The temperature difference after three years of testing yield $dT_1 < 1.7$ K and $dT_2 <=0.2$ K for Stages 1 and 2, respectively, which may also possibly be due to the diurnal effect and the lab's room temperature. Diurnal swing from the changing room temperature had been observed to cause about 1 and 0.5 K change in Stage-1 and -2 temperature inside SAT-MF1, which is a much larger and more complicated testbed than the mMBAC. Thus we expect diurnal impact to be present but of smaller amplitude. Nevertheless, the overall cooling capacity does not degrade significantly and the PTC continues to perform much better than the factory validation.

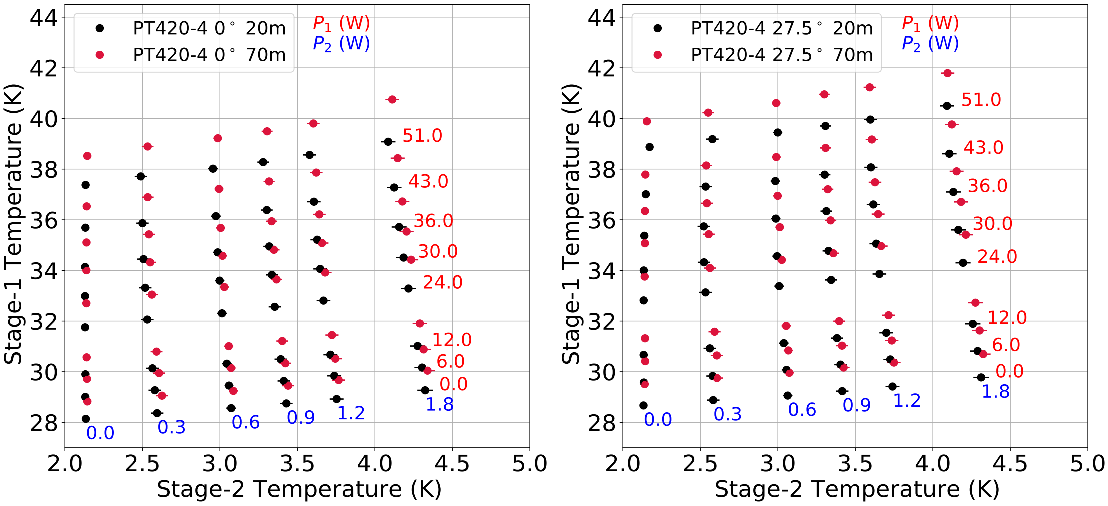

Figure 3.15. Impact from the different lengths of the Helium flex lines in cooling capacity using data sets 6-9. These data sets are at similar pressure setting.

3.3.3 Other checks on cooling effect

Besides the gravitational dependency effect, it would be interesting to see if hardware settings would also impact the cooling capacity of the pulse tube. Since the compressors are situated quite a distance from the actual telescope when the SAT is inside the observation platform, we need longer hoses to connect the compressors to the motorheads. SO sourced extra helium lines from a third party on top of the original ones from Bluefors. So we investigated the performance at both 20 m and 70 m long flex lines. Figure 3.15 depicts the results at both angles, 0° and 27.5°, for PT420-4. All four data sets are at similar pressure settings. This figure suggests that changing to a longer He hose decreases the cooling capacity, equivalent to adding 6 W or more on the first stage. There is minimal effect on the second stage.

We also carried out tests to check if there was any impact due to different pressure values. So keeping the same helium hose length (70 m), we ran the tests for two different pressures, 233 and 240 psi, at 0° and 27.5°. Figure 3.16 portrays the results from these runs. The increase in pressure has a negligible effect on the second stage, while it yields up to 3% drop in temperature (3% colder) on Stage-1 temperature. This effect becomes more significant at the high end of the load curve. Looking at the 0° plot, this corresponds to about 1.2 K colder on T_1.

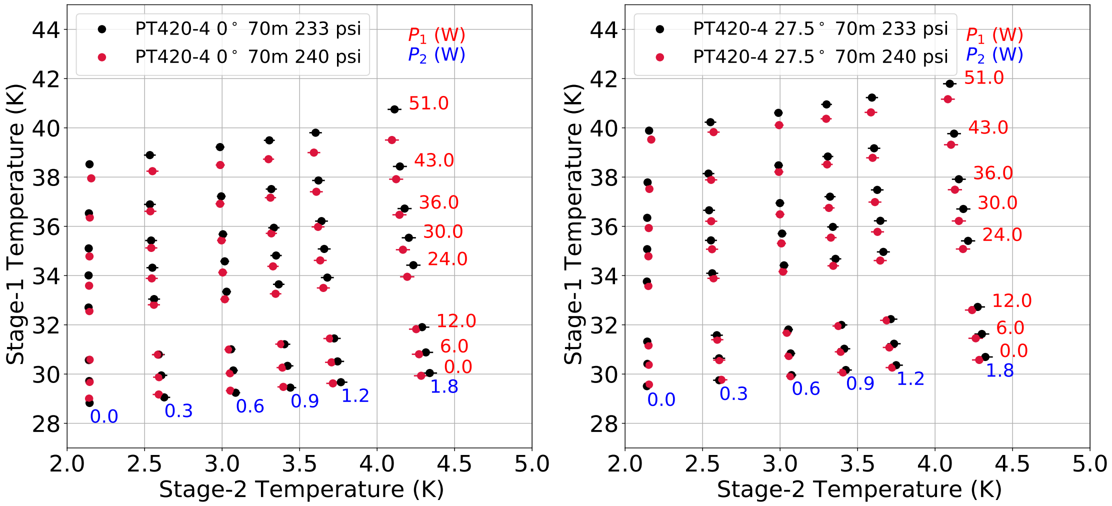

Figure 3.16. Compressor pressure impact on cooling capacity using data sets 8-11. There is minimal impact on Stage-2, and about $\leq 3\%$ effect on Stage-1.

3.3.4 Summary

We conducted tests on two additional pulse tubes, SAT-1 PTC and PT420-4, to evaluate (i) performance difference between PT420 units, (ii) pulse tube stability over time, and (iii) the impact of changing He line hoses and pressure. For (i), we found noticeable performance discrepancies between different units of PT420, with PT420-1 consistently demonstrating higher cooling capacity. This discrepancy becomes more apparent at increased tilt angles and higher Stage-1 loading, resulting in up to a 6% (2.3 K) difference in Stage-1 temperature between the units under the same loading conditions. For Stage 2, the largest difference of 10% occurred at 27.5°, indicating a slight angle dependence at lower P_1 levels. When comparing PT420-4 to PT420-1, using the same compressor during the test, PT420-1 again outperformed PT420-4, with an additional 24 W of cooling power on the first stage. More dedicated testing is needed to pinpoint the reasons for these performance differences, given that both units are certified under different conditions, which also differ from our test setup. For (ii), we observed a slight decrease in performance over a period of three years and 11 cooldowns. Nevertheless, SAT-1 PTC continues to exceed its factory validation performance. For (iii), we found that longer He hoses increased the loading on the first stage by approximately 6 W when using 70-m lines instead of 20-m lines. Increased pressure resulted in about a 3% rise in Stage 1 temperature. However, these changes had minimal impact on the second stage. Overall, the pulse tubes are validated for the full range of operations needed for the Simons Observatory and maintain consistent performance over time across multiple cooldowns. This comprehensive dataset on the characterization of low-frequency two-stage PTCs provides potential insights for future instrument designs involving moving cryogenic systems.

Chapter 3 is a reprint of the material as it appears in Tran Tsan, Nicholas Galitzki, Aamir M. Ali, Kam Arnold, Gabriele Coppi, Tamar Ervin, Logan Foote, Brian Keating, Jack Lashner, John Orlowski-Scherer, Michael J. Randall, Joseph Seibert, Jacob Spisak, Grant P. Teply, Zhilei Xu, and Ningfeng Zhu. The effects of inclination on a two stage pulse tube cryocooler for use with a ground based observatory. The dissertation author was the primary investigator and author of this paper. Cryogenics, 117:103323, July 2021. The last portion of this chapter (Section 3.3) includes additional results from other tests.

Chapter 4

SAT Mechanical Design

This chapter describes the designs and testing processes for two mechanical support structures for the SAT. Section 4.1 presents the redesign of the carbon-fiber trusses, focusing on simulations conducted under varied testing conditions. These simulation outcomes provided essential criteria for the validation of the two newly devised trusses, which support the SAT 1 K stage to 0.1 K stage. In section 4.2, the focus shifts to the design of a hoist system engineered for seamless transportation of the SAT onto the platform at the observation site.

4.1 Carbon-Fiber (CF) Truss Design Simulation

To minimize thermal conduction between the different stages while providing adequate mechanical support, the four different temperature stages inside the SAT are connected through several trusses as mentioned in Chapter 2. The bottom of Figure 2.5 depicts the carbon fiber and G10 trusses inside the SAT. After 5 thermal cycles (cooldowns), the Optics Tube (OT) carbon fiber truss (4-1 K) failed, which led to a reassessment of all the carbon fiber trusses. This section focuses only on the carbon fiber trusses that support the Cold Readout Assembly (CRA 2) and the focal plane from 1 K to 0.1 K stage. The OT truss fiber redesign, testing, and validation are detailed in [50, 24].

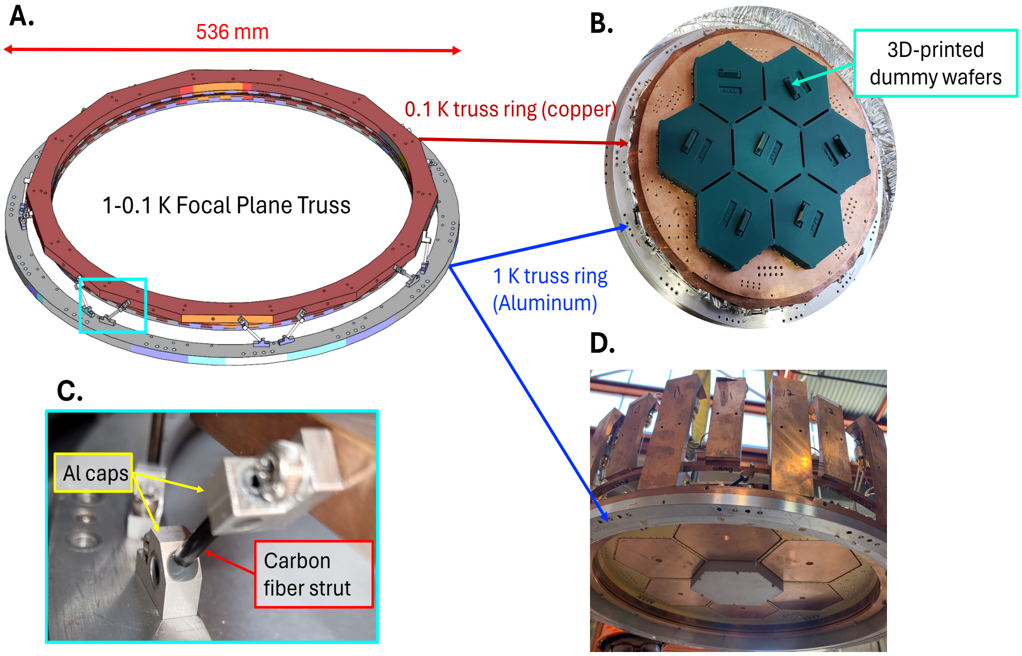

Figure 4.1. FPA carbon fiber truss. **A** portrays a 3D CAD model of the FPA truss from 1-0.1 K stage. **B** and **D** show the top and bottom view, respectively of the actual focal plane with the rings called out. **C** details one of the struts.

4.1.1 FPA CF Truss Simulation

The FPA's truss is composed of carbon-fiber-reinforced polymer (CFRP) struts running between two copper rings at $\sim 45°$. The CFRP tubes or struts are manufactured by vDijk Pultrusion Products[1]. Aluminum caps are epoxied to the end of each strut, which are then bolted to the two rings as shown in Figure 4.1A and C. 4.1A is a 3D CAD model of the truss. The top copper ring connects to the focal plane assembly on the 0.1 K or MC stage, and the bottom (wider) aluminum ring connects to the bottom ring of CRA 2 truss (Section 4.1.2) as seen in Figure 4.1D.

The redesigned CF trusses must offer robust support to the system, ensuring a sufficient margin of safety during regular observing operations, transportation, and installation procedures. To avoid the previous failure and ensure that the trusses meet the mechanical goals, simulations

---

[1] vDijk Pultrusion Products, Aphroditestraat 24, NL-5047 TW TILBURG, The Netherland

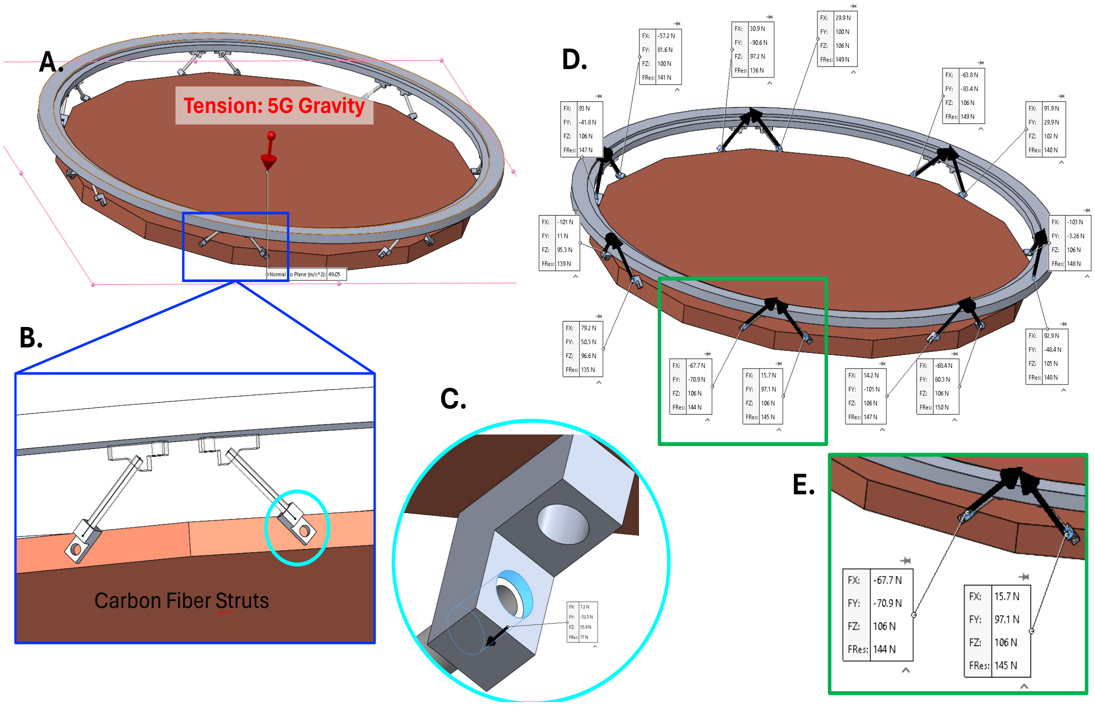

Figure 4.2. FPA carbon fiber truss for tension simulation. **A** shows the simulation setup with the gravity vector. During transportation, with the FPA inside SAT-MF1, this is the direction of gravity. The copper MC ring is changed to a flat copper plate of about 30 kg to replicate the mass of the FPA with all the detectors installed. **B** zooms into a pair of struts. The black lines are the central axes on the 2 struts used to compute the unit vectors. **C** outlines the force vector on the Al cap. **D** and **E** display the forces on the strut caps.

were done on the two trusses: FPA and CRA 2, further detailed in the subsequent section. These simulations established criteria, guiding the validation tests for individual struts. Each strut underwent rigorous testing, pushed to destruction in accordance with simulated load requirements. Subsequently, the validation results informed the parameters for the whole truss tests, conducted at moderately elevated loads rather than to destruction, prior to their integration into SAT-MF1. [24] outlines the validation process and results.

The simulations were done using Solidworks finite element analysis (FEA) on the truss as a whole for three cases:

1. Tension: 5 g (5x gravity) loading with the FPA facing the ground to simulate the worst-case impact during transportation from the site high bay to SATP. We require the factor of safety

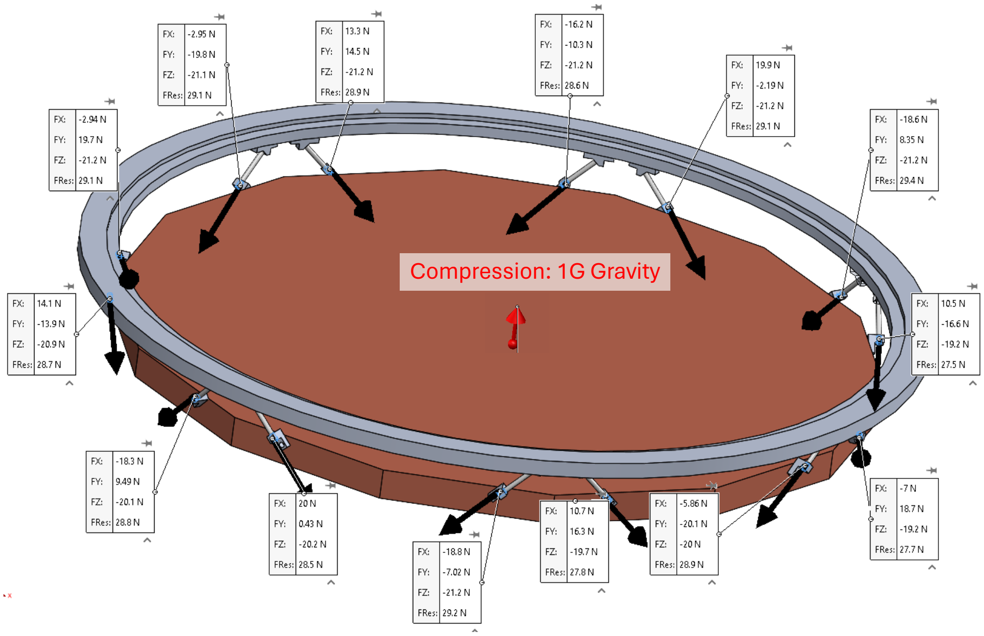

Figure 4.3. FPA carbon fiber truss for Compression Sim with the gravity vector and the force vectors.

(FoS) to be at least 2. Figure 4.2A illustrates the simulation setup for this test, where the red arrow indicates the direction of gravity.

2. Compression: 1 g loading in the opposite direction of the tension test. This case simulates the truss's condition during the in-lab integration and testing operations. The required FoS is 4. Figure 4.3 portrays the setup with the direction of gravity.
3. Shear: 1 g loading pointing horizontally. Required FoS = 4. Figure 4.4A shows the setup, with B displaying the resultant forces on individual strut cap.

In the simulations, several features such as bolt patterns are suppressed. Moreover, the MC ring is changed to a flat copper plate that weigh about 30 kg to replicate the mass that the FPA would hold with all the detectors installed. Component contact is set to bond everywhere and the Still (1 K) ring is fixed as that is where it bolts to the Optics Tube. So it serves as the best fixture point. Finally, gravity is applied to the whole assembly according to the three aforementioned scenarios.

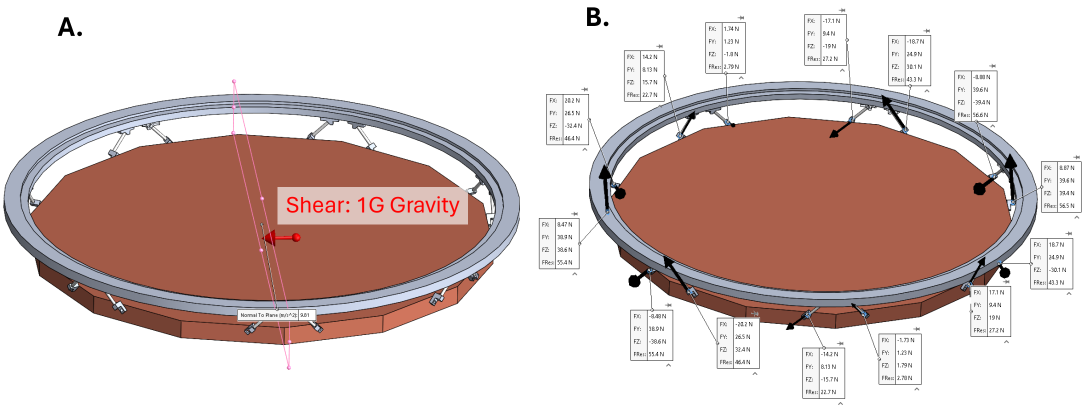

Figure 4.4. FPA carbon fiber truss for Shear Sim. **A** shows the simulation setup.

With the Still ring serving as a fixture, the greatest force that the struts experience happens at the MC ring end, more specifically at the Al cap and CF tube interface as seen in Figure 4.2. The forces acting on each CF strut cap can be broken down into two types: the tensile axial force that is normal to the cylindrical hole and the shear force. To compute the tensile axial force at the Al surface bonded to the strut, the dot product of the free-body force and the strut's unit vector are taken. The free-body force is computed at the surface of the hole in one of the strut caps as seen in Figure 4.2C, which is where the glue joint should be. The dot products of the forces and unit vectors yield the axial force, and the shear force is

$$F_{shear} = \sqrt{F_{net}^2 - F_{axial}^2} \tag{4.1}$$

Table 4.1 presents the maximum F_{axial} and F_{shear} for a strut cap under the three loading conditions. The forces here are then used to assess the criteria for the validation process of each strut. See section 4.1.3 for more details about the validation criteria used.

4.1.2 CRA 2 CF Truss Simulation

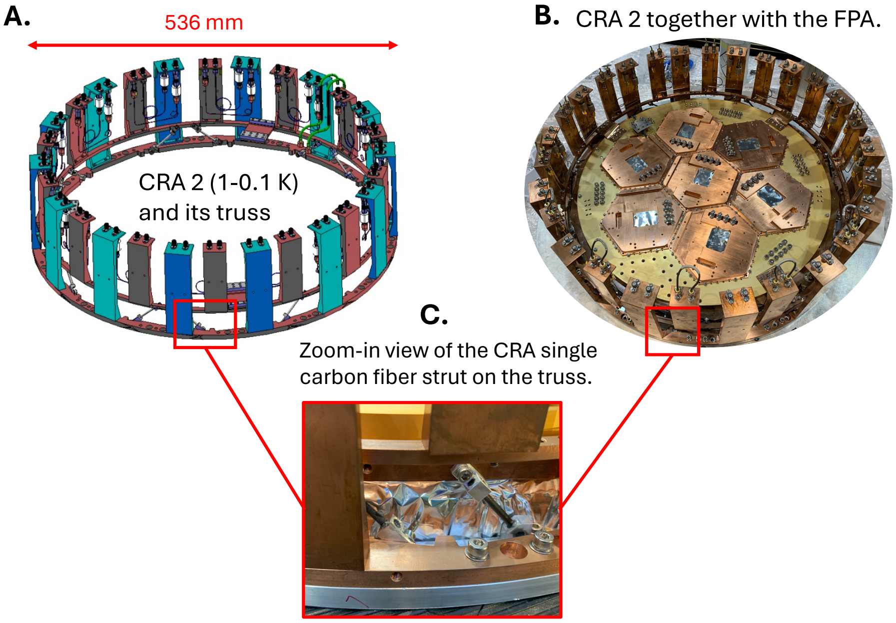

Figure 4.5. CRA 2 (1-0.1 K) carbon fiber truss. **A** portrays a 3D CAD model of the CRA 2 and its truss, and **B** shows what it looks like when installed to the focal plane. **C** centers on one CF strut. The top ring connects to the FPA at the MC stage (0.1K) through copper foil heatstraps and the bottom ring bolts to the FPA truss on the Still (1K) stage.

CRA 2's truss is similarly composed of CFRP struts running between two copper rings at $\sim 42^\circ$. Figure 4.5 portrays a CAD model of the truss assembly (**A**) and how it looks together with the FPA (**B**). The copper standoffs hold the readout components (e.g. cables, isolators) for the RF chains. The top ring connects to the FPA on the 0.1 K or MC stage through a series of copper foil heatstraps, while the bottom (wider) ring bolts to the bottom ring of the FPA truss on the 1 K or Still stage. Figure 4.5B depicts how the CRA 2 connects to the FPA. 4.5C is a zoom-in

Table 4.1. Simulation results for the FPA CF truss. This table displays the maximum forces that the strut cap would experience under the three different loading conditions. The numbers in the brackets are the force multiplied by the factor of safety.

Scenario	F_{axial} (FoS x F) [N]	F_{shear} (FoS x F) [N]
5 g tension (FoS = 2)	150 (300)	14 (28)
1 g compression (FoS = 4)	30 (120)	3 (12)
1 g shear (FoS = 4)	57 (228)	1 (4)

view of a single CF strut. The 7 wafers on the FPA are dummy wafers used for installation. The final UFMs are installed later in the integration process.

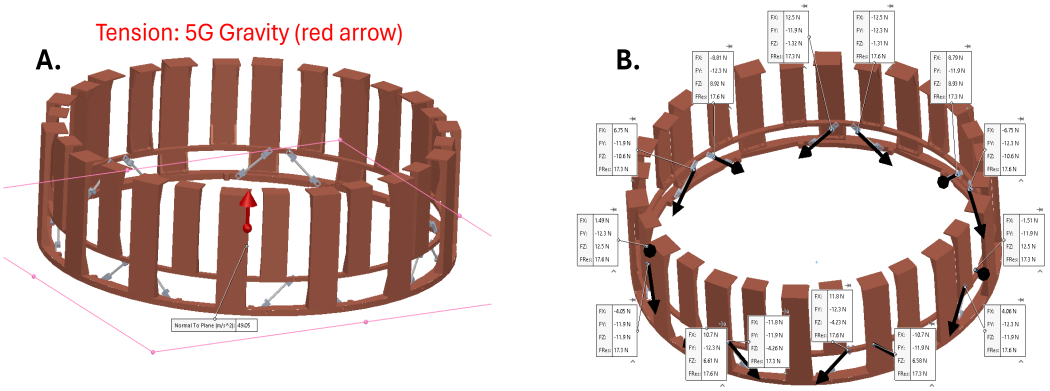

Figure 4.6. CRA 2 CF truss Simulation for Tension. **A** illustrates the simulation setup with 5g pointing up. This is the direction of gravity when the CRA is inside the SAT during transportation. **B** shows the resultant force on the Al caps.

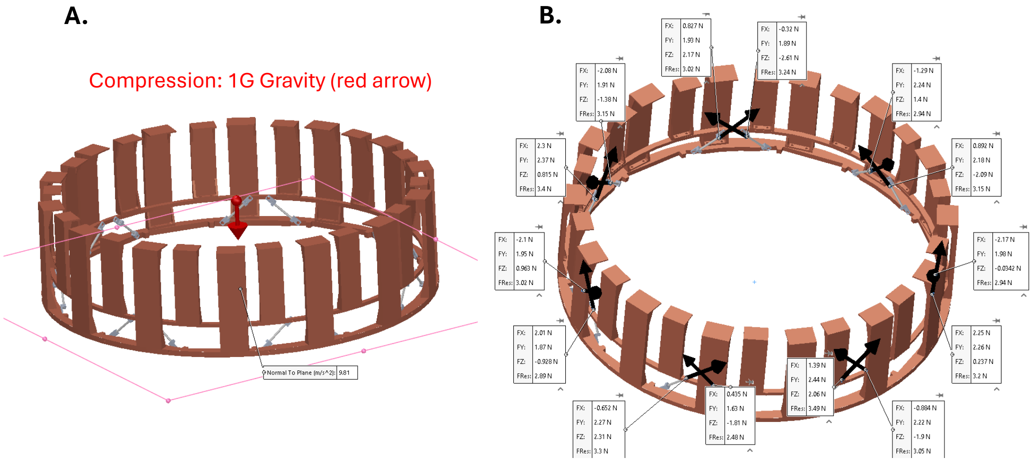

Figure 4.7. CRA 2 Truss Simulation for Compression. **A** shows the simulation setup, which emulates the loads the CRA would experience during operation and installation with the SAT window facing skyward. **B** portrays the results and the direction of the net force.

Similarly to the simulation setup mentioned in Section 4.1.1, several features such as bolt patterns, coaxes, and all the readout components are suppressed since they do not impact the simulation as the bolt sheer and tensile strengths are much higher than the forces being considered. The 0.1 K truss ring and the 14 copper standoffs weigh about 3.45 kg. Component contact is set to bond everywhere and the 1 K truss ring is fixed since that is where it contacts the FPA 1 K truss ring, serving as the best fixture point. The hole of each strut cap in the sim is made smaller for direct contact with the CF strut for a bonded contact. The actual holes are bigger for the glue to go in. However, modeling and simulating the glue would add a layer of complexity and uncertainty to the results as glue behavior is difficult to predict. Hence the sim assumes bonded contact where the glue should have been and this should be an adequate estimation of the loadings on the struts. Moreonver, the indicated factors of safety we are considering give conservative estimations.

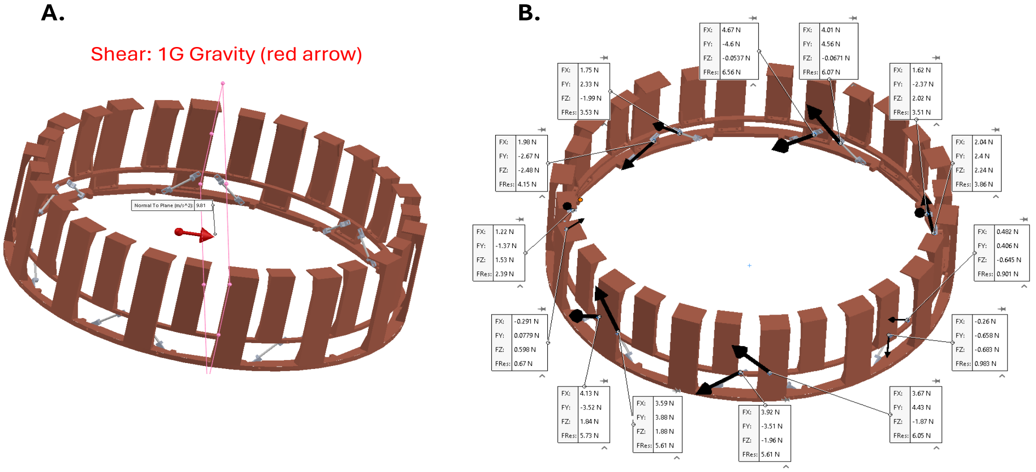

Figure 4.8. CRA 2 CF truss Simulation Setup and Results for Shear Test.

The resultant forces on each strut cap are computed in the same way as previously mentioned. Figure 4.6 - 4.8 display the simulation setup and the free-body forces on each strut cap. Table 4.2 shows the results for the three simulated cases. The 5g tension test yields the largest tensile axial force on the struts, while all three tests give similar shear force (3-4 N). We then use these results to compile comprehensive requirements for testing the struts, detailed in the next section.

Table 4.2. Simulation results for the CRA CF truss. This table displays the maximum forces that the strut cap would experience under the three different loading conditions. The numbers in the brackets are the force multiplied by the factor of safety.

Scenario	F_{axial} (FoS x F) [N]	F_{shear} (FoS x F) [N]
5 g tension (FoS = 2)	18 (36)	1.5 (3)
1 g compression (FoS = 4)	3.5 (14)	1 (4)
1 g shear (FoS = 4)	7 (28)	<1 (4)

4.1.3 Selection of the Validation Criteria

Table 4.3 outlines the pass criteria for a single strut validation, accounting for the FOS. Note that F Tension, Compression, and Shear in Table 4.3 do not refer to the three loading conditions. F tension is determined by looking at the maximum tensile axial force in the 5g tension tests. F compression is evaluated by looking at the max tensile axial force from the 1g shear and compression tests. As shown by the force vectors in Figure 4.3, 4.4, 4.7, and 4.8, theses tests both yield compressive force. Finally, F shear was taken by comparing all the shear forces of all three loading conditions. These become the passing criteria for testing individual struts until destruction. Then based on the validation results, the requirements for testing the full trusses are determined.

The validation tests, done by our collaborators from the University of Virginia, for the FPA strut tension test, reached $\sim 1.2kN$, while the CRA strut tension and shear test after thermal cycling with LN2 reached a minimum of 750 and 55 N, respectively.

Table 4.3. Summary of the pass criteria for individual strut validation. The forces here have accounted for the factor of safety.

Truss	F Tension [N]	F Compression [N]	F Shear [N]
FPA Truss	300 (5g tension test)	228 (1g shear)	28 (5g tension)
CRA 2 Truss	36 (5g tension test)	28 (1g shear)	4 (1g shear)

4.2 Hoist Design for Lifting the SAT Into SATP

On-site integration involved assembly inside the site highbay and a cooldown to validate performance. The complete telescope assembly was done inside the highbay, and then we transported it to the platform (SATP) using a trailer. This section describes the initial plan to transport the SAT from the trailer onto the platform and vice versa. We conducted a trade study between this plan and a plan that sourced a rolling gantry from a third party, and in the end, we chose the commercial gantry plan. I will describe the non-commercial-gantry plan here. The hoist system described in this chapter includes an I-beam mini support, a U-arch, and finally an I-beam as the main travel path for the hoist. Figure 4.9 illustrates the hoist assembly and how it is integrated into the platform. The full documentation and design drawings are listed in SO-SATP-DES-002 Hoist System Interface ICD.

The first major component of the hoist involves **the I-beam** as the travel path. According to Vertex's recommendation of an I300 profile I-beam, we chose the closest stock size, which follows the ASTM A992 standard specification. The beam is approximately 0.3 m tall and 0.13 m wide. There are two I beams in this system. One is the 6 m long I beam that sits on top of both the mini-Support (mSupport) and the U-arch. A second I beam (4.3 m long) forms the top of the U-arch. The two beams are clamped together via a perpendicular beam-to-beam clamp, which allows two degrees of freedom to adjust for any misalignment when trying to interface with the U-arch (bolted to the foundation) and the mSupport (bolted to the SATP). This clamp is a stock part from McMaster[2]. The SAT with its internal component and the lifting/counterbalance setup (see section 4.2.2 and 4.2.4) weighs about 2000 kg. Although the weight is very close to the clamp's maximum capacity, the actual distributed load on the two I-beams is much less as the main I-beam sits on top of the U-arch.

The next component of the assembly is **the U-arch** which supports one end of the hoist system and connects to the foundation. This arch is bolted down to the foundation through a

---

[2] McMaster-Carr. PN: 3008T25. https://www.mcmaster.com/3008T25/.

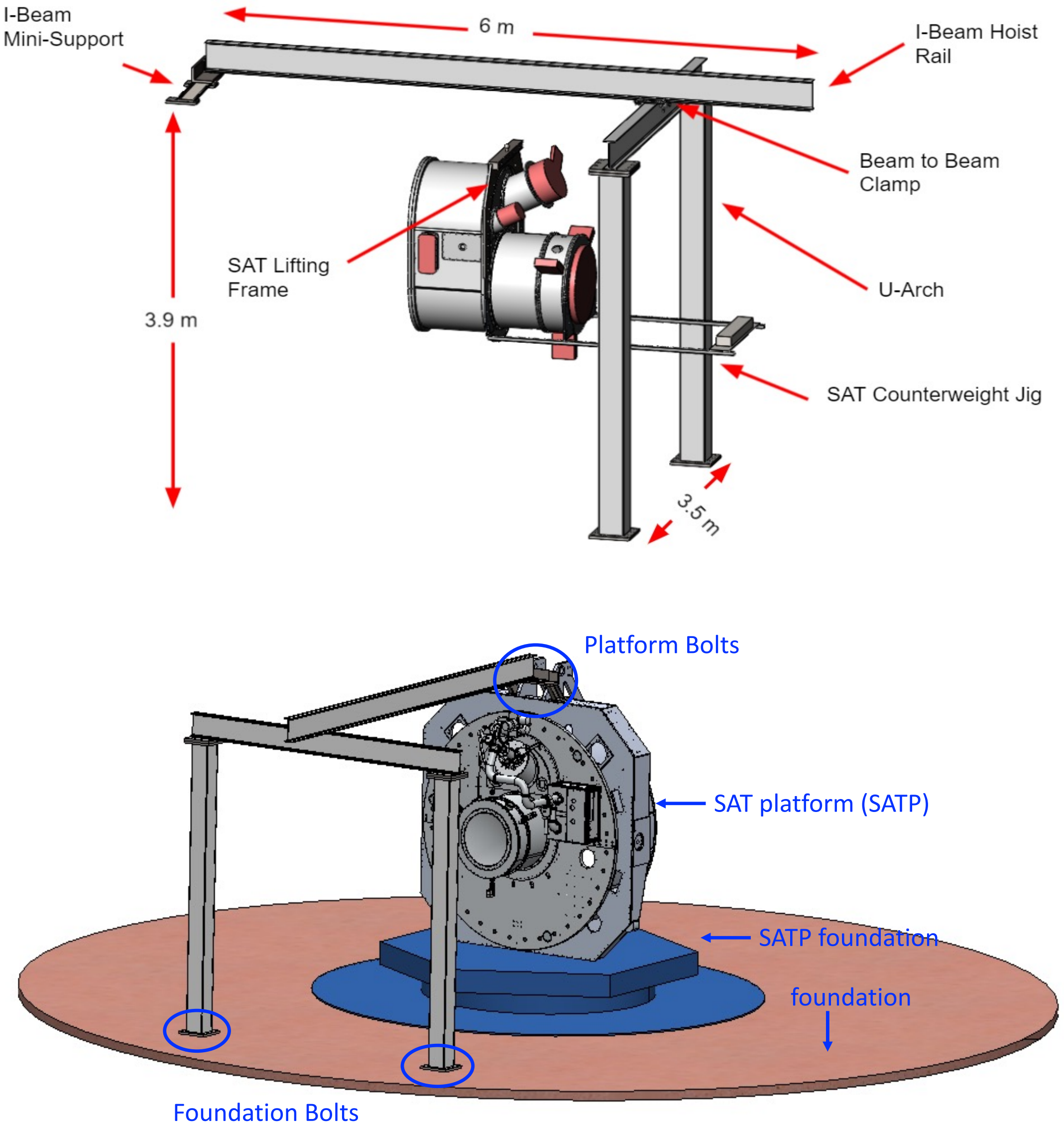

Figure 4.9. An Overview of the Hoist System Assembly Integrated with SAT-MF1. Top: A 3D CAD model in Solidworks for the hoist system assembly. The main components of the assembly are being called out here. The SAT moves along the I-beam rail via a chain-driven trolley with a chain hoist (not included in the picture). See Figure 4.15 for more details. Bottom: The hoist system is integrated into a mockup of the SATP and foundation. The system is bolted to the platform and the foundation at the site via two sets of bolt patterns.

M24 bolt pattern. In this arch, a second I-beam (same profile as the main I-beam) sits on top of two steel plates that are welded to the 2 square tubes. The square tubes have a cross-sectional dimension of 254x254x15.88 mm (10x10x5/8 in). They met the specifications of ASTM A500 Grade B steel. Figure 4.10 depicts an overview of this arch and a zoom-in view of the interface between the I-beam and the square tubes. At the top of the arch, the two square plates are welded to the ends of the I beam with hole patterns along two sides to match the M24 bolt pattern on the plate at the end of the square beam (right picture of Figure 4.10). Holes are slotted along the long direction of the I beam to take up any potential issues in the spacing of the foundation bolts. These plates are bolted to the plates that are welded to the ends of the square tubes. Note that the steel plates welded to the square tubes connect to the I-beam on one end and to the foundation on the other end. These are a set of M24 holes. Additionally, we allow for a set of shim plates of varying thicknesses with the same square profile between the two interface plates to ensure levelness at the top of the arch. Since any unevenness of the foundation can lead to a slight tilt of

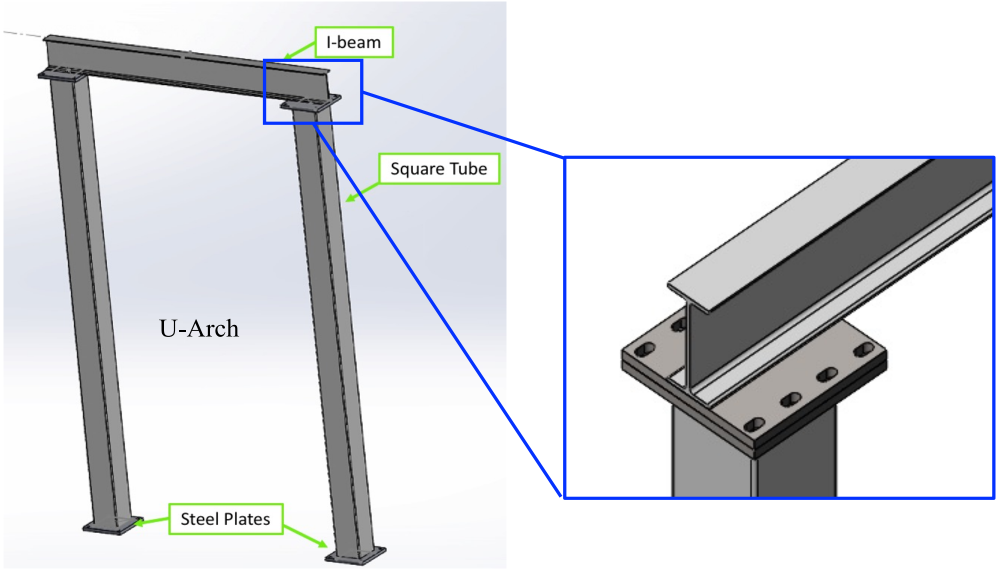

Figure 4.10. Assembly overview for the U-arch. Left: the arch with each of the components called out. Right: zoom in view at the top corner where the I-beam connects to the square holes via a set of plates. The I-beam is welded to 2 plates that are slotted to allow freedom to adjust. Similarly, the bottom plates with tapped holes are welded to the square beams. Between these plates is a set of shim plates to account for any angle between the arch and the SATP due to the unevenness of the foundation.

the square tubes, we can adjust the arch's overall height with these shim plates and control the angle between the arch and the SATP/platform.

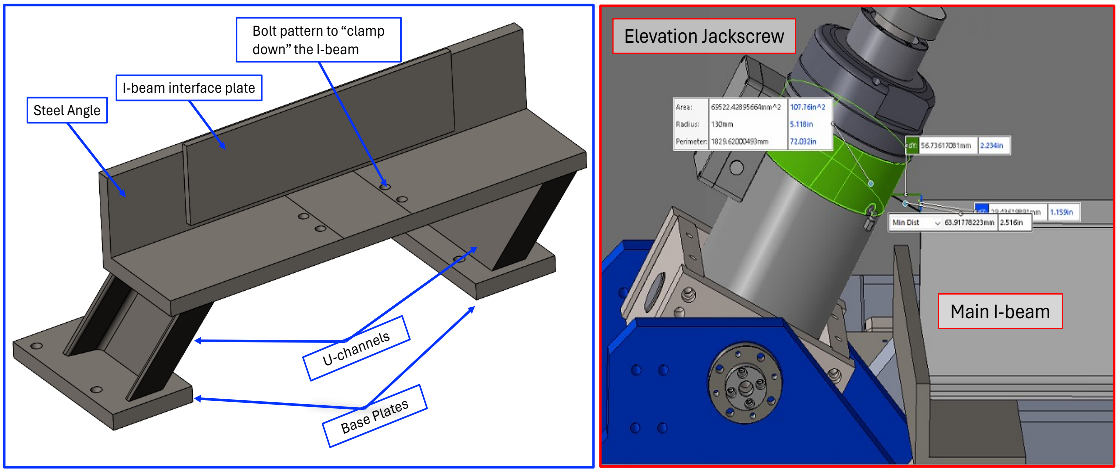

Figure 4.11. Assembly overview of the mini Support (mSupport). The mSupport (left) is composed of a steel angle welded to two U-channels. Each of the U-channels is welded to a base plate, which will then be bolted down to the SATP. The small interface plate on the steel angle is welded to the main I-beam. We plan to clamp down the I-beam to the steel angle via this plate on top of bolting it down to the base of the steel angle. The right figure shows a side view of this assembly with the I-beam and elevation jackscrew. There is about 64 mm of clearance between these two structures. Due to this clearance, the U-channels are designed to tilt 40° away from the verticle.

The final major subassembly is **the mini support or mSupport** system, which interfaces with both the I-beam and the SATP. This subassembly features two U-channels supporting a steel angle, creating a mini platform for the main I-beam to sit on top of. These U-channels are welded to two A36 steel base plates, which are bolted to the SATP using M16 holes. To accommodate the elevation jackscrew, the U-channels are tilted 40° from the vertical axis. Refer to Figure 2.4 for a complete view of the elevation jackscrew. Figure 4.11 presents a 3D Solidworks model of the mSupport and the clearance with the jackscrew. Figure 4.12 shows the U-channels' profile, a standard size corresponding to part number C2612 in MetalsDepot. As depicted in Figure 4.11, the I-beam is welded to the steel angle via the I-beam interface plate and secured with bolts. This dual approach ensures a robust connection between the I-beam, mSupport, and the platform. If necessary, the mSupport can be custom-machined instead of using welded commercial components.

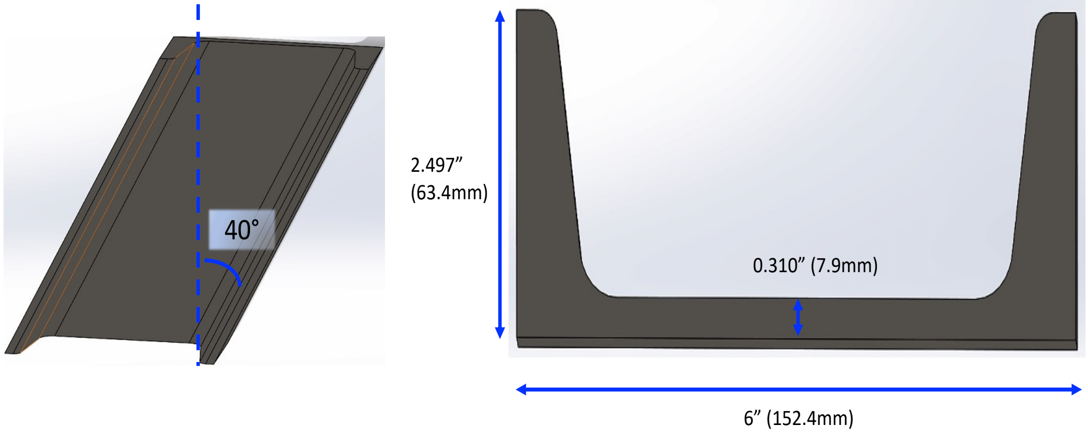

Figure 4.12. U-channels design. The channels are tilted 40° from the vertical to clear the pointing rod in the el hub. The right figure shows the dimension of the design, which corresponds to a standard size that can be found in MetalsDepot.

4.2.1 Interface with the Site Trailer

We transport the SAT, with all of its internal components integrated, from the site highbay to the platform via a trailer. The hoist system must be fully installed before the SAT is transported from the highbay to the SATP. The trailer will have the base of the SAT transportation crate attached securely to the bed of the trailer. Figure 4.13 depicts the SAT's transportation using the trailer. Once inside the ground shield, the SAT can be loaded and unloaded from the trailer using overhead hoists.

Due to the limited spacing between the ground shield and the SATP, the trailer has to move in reverse underneath the end of the hoist system. In this direction, we can position the SAT center of mass (CoM) directly underneath the hoist. Thus, the distance between the U-arch and the back end of the trailer needs to have enough clearance to carry out this process. Figure 4.14 displays the clearance between the U-arch and the trailer as it backs into the ground shield. From plate to plate, the arch allows up to 3.5 m of access. As long as we have a trailer that is within this width, the SAT can move inside such that its center of mass is underneath the hoist. Moreover, with a vertical distance of almost 2.2 m, the SAT sitting on top of the trailer should have enough room to go through and proceed with the lifting process. In the case that we want to install the SAT with a forebaffle, the U-arch is wide enough for such a procedure. The forebaffle's diameter is about 2.1 m, while the U-arch allows more than 3.5 m of access.

4.2.2 Interfaces to the SAT

Once the SAT is inside the platform and off the trailer (see previous section), it can be lifted using a chain-driven trolley with a chain hoist. This section details the design of the lifting frame and the counterbalance system on the SAT to avoid any tilt during the lift. Ethan Wadhwa, an undergraduate, spearheaded this portion of the design in conjunction with Dr. Nicholas Galitzki's and my guidance. For completeness, I am including this design here. Figure 4.15 depicts the counterbalance system for the SAT and the chain-driven trolley that we were considering for the hoist system.

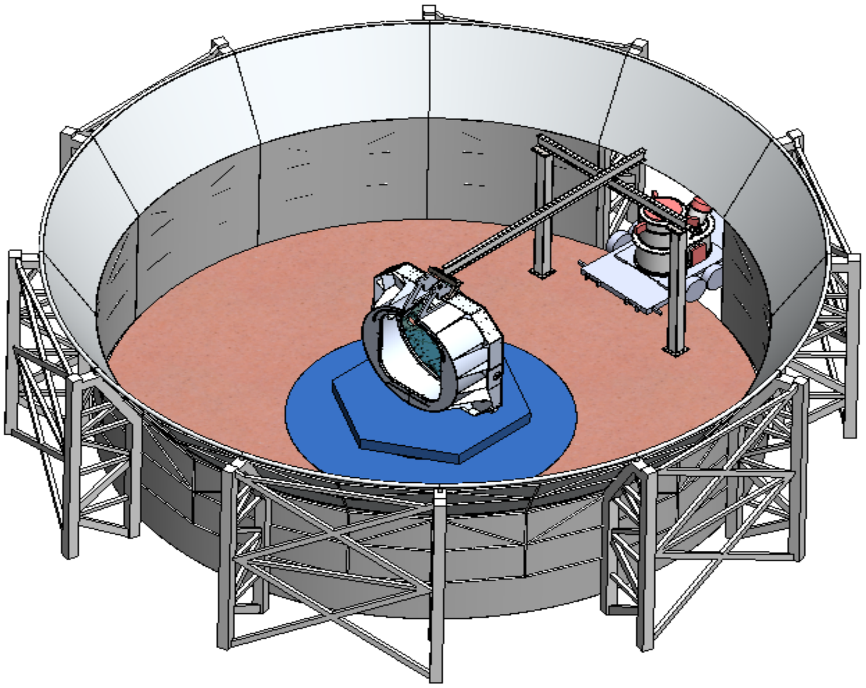

Figure 4.13. SAT transportation from the highbay to the platform from the trailer. The picture portrays a mockup foundation and the SATP foundation, surrounded by a ground shied. The hoist system is bolted down to the foundation.

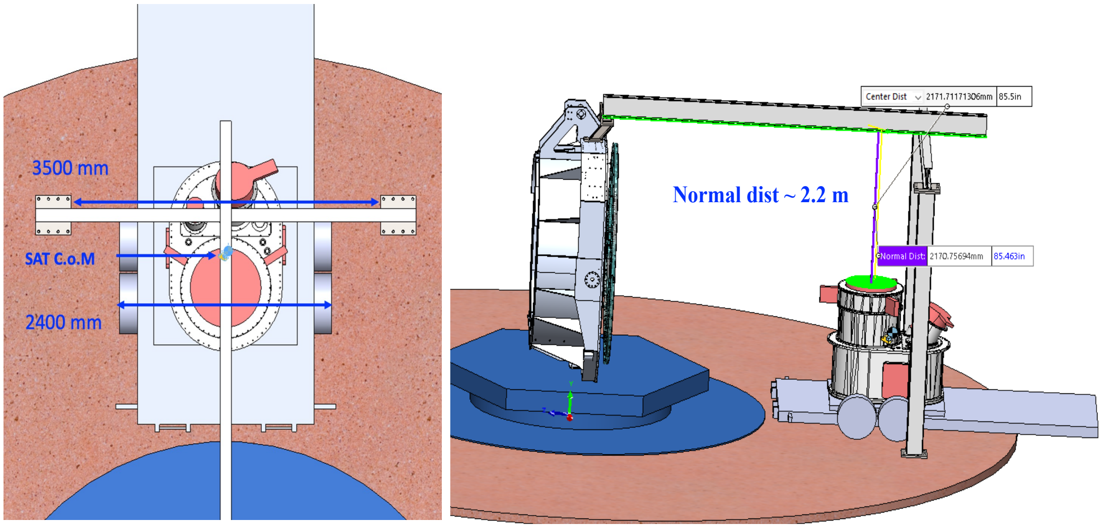

Figure 4.14. Clearance between the trailer and the U-arch. Left: a top view of the trailer reversing underneath the U-arch. According to the trailer we were looking at, from wheel to wheel, the distance is 2.4 m. The U-arch allows up to 3.5 m of travel access. Right: side view with the ground shield hidden. There is 2.2 m from the top of the SAT to the bottom of the main I-beam.

The chain hoist was chosen because it is both a chain hoist and chain-driven trolley, which allows control of the SAT position. The specific model was chosen as it complied with the vertical and horizontal clearances (Figure 4.14) needed to properly interface the SAT to the SATP. Nominally, the chain hoist should have at least a 3-ton (3000 kg) capacity as the SAT weighs about 1600 kg with all of its inside components installed. For a fully loaded SAT with turbo rack, bias crate, PTC motors, and ballast tanks, the mass is closer to 1700-1900 kg. The hoist ring is from McMaster with a rated 9,250 lbs (4200 kg).

For the ease of the lift and to increase contact with the lifting hardware, we designed a lifting frame that is attached to the telescope. The frame is composed of a central steel plate that attaches to the SAT via several bolts to hold the weight of the SAT. Then there is a long steel block attached to the top of this frame to create a stable platform for the hoist ring to bolt into.

The block is used to increase the horizontal clearance between the SAT and the SATP so it can be properly installed. This way, the hoist ring and the hook from the trolley won't hit against the SATP, ensuring the SAT can be bolted down to the SATP fully flushed. The central plate and the block will be mated using a combination of welds and bolts.

When lifting the SAT pointing at the horizon, the CoM with all internal components installed sits roughly 10 cm below the mounting plate, which will cause the SAT to tilt. To bring the flange vertical, a counterweight needs to be installed to bring the CoM underneath the lifting pointing just above the primary flange. We used a system that mounts to the tapped M8 holes on the principal SAT flange and on the window plate to mount the counterweight system plates. These plates then attach to the steel strut channel that allows us to attach a changeable mass at

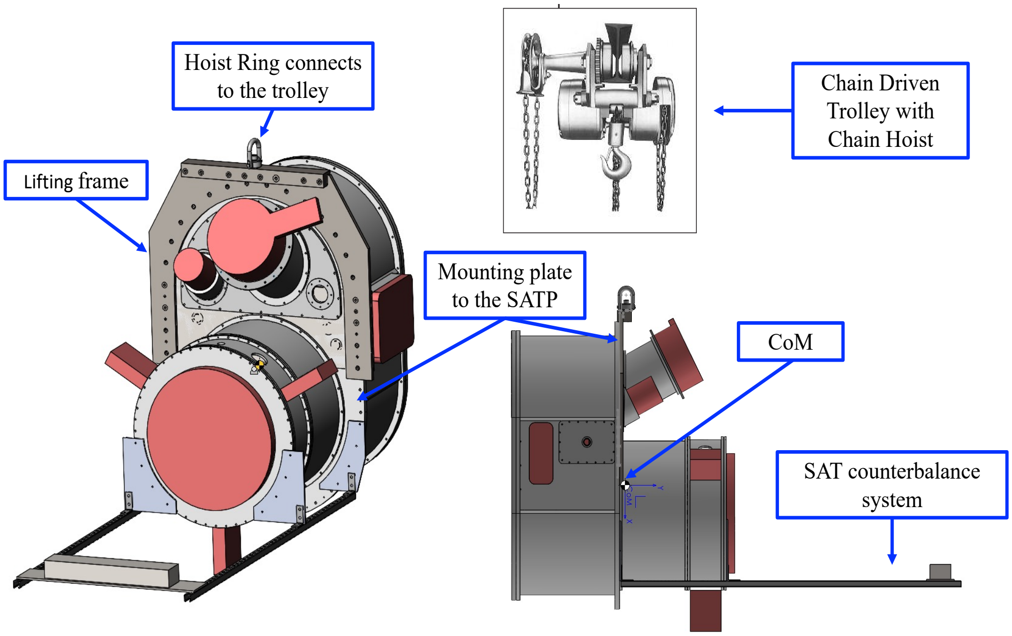

Figure 4.15. The SAT Counterbalance System. In this design, the SAT with its lifting frame connects to a chain-driven trolley via the hoist ring at the top of the figure. The trolley is installed to the main I-beam, allowing smooth control of the SAT position along the beam. Top right is an image of a commercial trolley that we were considering with a 3 ton capacity. When lifting the SAT via the hoist ring, the center of mass (CoM) sits roughly 10 cm below the mounting plate, causing a slight tilt. With this counterbalance system at the other end of the SAT, we can adjust the CoM to avoid such tilt during the lift. Bottom right shows the new CoM with the counterweights installed.

an adjustable distance from the front window. With a nominal distance and around 100 kg of weight, the SAT system can be balanced. The bottom right of Figure 4.15 illustrates the new CoM after adding the counterweights, which position the CoM very near the mounting plate.

4.2.3 Interfaces at Site

This section describes the I-beam hoist system's interface with the SATP assembly, focusing on the tight clearances encountered during installation. The system is bolted to the platform and foundation at the site via two sets of patterns: platform M16 bolts and foundation M24 bolts as shown at the bottom of Figure 4.9. When designing the system, I had to consider the potential interference with the elevation jackscrew, which facilitates the telescope's elevation movement. While ensuring the strength of the mSupport and minimizing yield stress on the U-channels during the telescope's installation (ensuring the U-channels are tilted no less than 45° from the vertical axis), the final design maintains a tolerance of about 64 mm between the I-beam and the jackscrew (Figure 4.11) and about 30 mm between the feet of the I-beam mSupport and the edge of the platform. This setup also provides a 30 mm clearance between the sides of the base plates to the jackscrew mount.

4.2.4 Hoist System Simulations

Simulations performed on the I-beam hoist system were used to evaluate the maximum stress it would experience during an actual lift. Utilizing Solidworks Finite Element Analysis (FEA), I examined two extreme cases. Setting the origin at the midpoint of the back of the mSupport L steel angle, case 1 places the SAT 3/4 (3355 mm) of the way from the origin, closer to the U-arch end. This case simulates the SAT's transfer process from the hoist system and the trailer. Conversely, case 2 places the SAT 1/4 (1118 mm) of the way from the origin, near the mSupport end, representing the scenario where the SAT is close to SATP and ready for installation. In both cases, gravity is applied to the system. The SAT and its lifting frame, along with counterbalance weights, were modeled as a 2000 kg remote load to emulate the system's

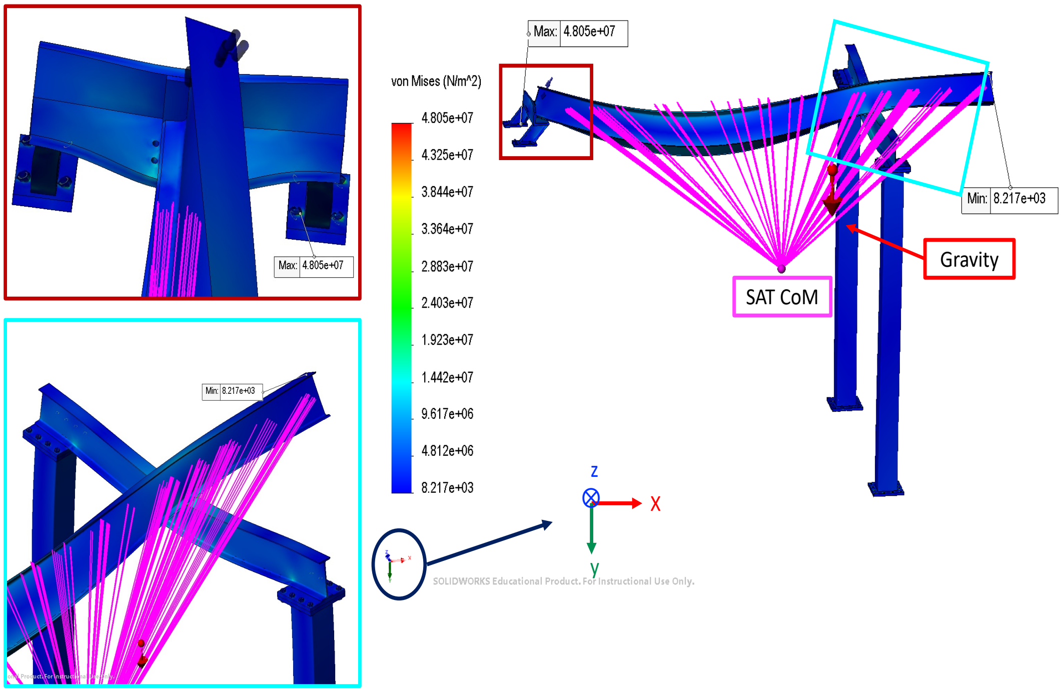

Figure 4.16. Simulation using Solidworks Finite Element Analysis (FEA) for the I-beam hoist system **case 1**. This simulation applied gravity (red arrow) and a remote load of 2000 kg at 3/4 of the way from the back of mSupport (3355 mm) to replicate the SAT. The sim parameters are as followed: foundation bolts at both the mSupport base plates and the foundation plates, counterbore with nuts at the rest of the bolt holes on the U-arch, x = 3355 mm, y = 2000 mm, z = 7 mm. The max stress occurs at the mSupport base plate. See Table 4.4 for the factor of safety.

center-of-mass (CoM). The load is approximately 2000 mm above the ground and slightly 7 mm in the z-direction. These studies focus not on the intricate details of the SAT, but rather on its impact on the hoist system. Thus, treating the SAT and counterbalance system as a remote mass significantly simplified the simulation, allowing for efficient and effective analysis. Figure 4.16 and 4.17 depict the simulation setup and results for cases 1 and 2, respectively.

The SAT with all internal components yields approximately 1600 kg, plus the additional mass from the lifting frame and the counterbalance system put it at about 2000 kg or 2 tons. The FEAs also apply two sets of foundation bolt fixtures to portray a more realistic loading on the mSupport base plate and the foundation plates on the U-arch side. The rest of the bolt holes on the U-arch are simulated as counterbores with nuts according to their sizes. Table 4.4 details the factor of safety (FoS = Yield/Working stress) for both cases. In these two scenarios, the

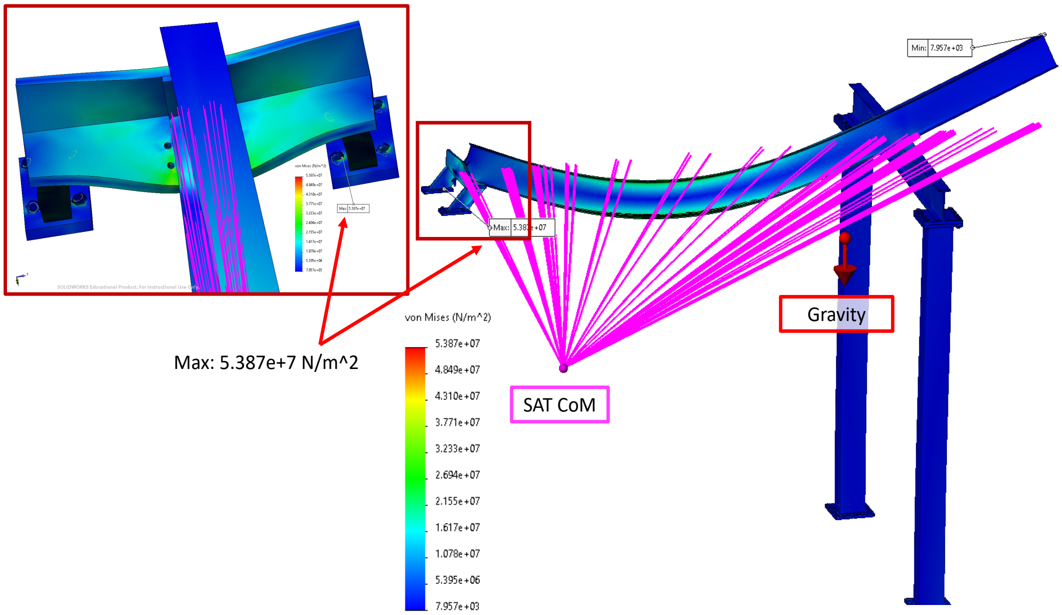

Figure 4.17. Simulation using Solidworks Finite Element Analysis (FEA) for the I-beam hoist system **case 2**. Similar setup as the ones in Figure 4.16, except that the remote load is closer to the mSupport now, about 1/4 of the way from the back of the mSupport. x = 1118 mm, y = 2000 mm, z = 7 mm. The max stress also occurs at the mSupport base plate. See Table 4.4 for the factor of safety.

mSupport base plates have the lowest FoS, 5 and 3.8, respectively. Though these FoS are lower comparatively, they are not at a concerning level yet.

Table 4.4. Factor of Safety for the I-beam hoist system. This table lists the main components of the system and their Solidworks FEA simulation results for two cases: Case 1 where the SAT is closer to the U-arch end, and Case 2 where the SAT is closer to the mSupport end. The Factor of Safety (FoS) is the yield stress/working stress. For both cases, I modeled the SAT as a remote load of CoM.

Component	Steel Grade	Case 1: U-arch end.	Case 2: mSupport end.
mSupport U-channel	A36	14.6	6.0
mSupport base plate	AISI 304	5.0	3.8
Main I-beam	A992	21.3	15.1
Foundation plate	AISI 304	8.4	8.4
U-arch I-beam	A992	11.9	22.7
U-arch square tube	A500	10.4	10.7

Chapter 4 (Section 4.1) and Chapter 5, in part, have been submitted for publication of the material to The Astrophysical Journal Supplement Series, 2024. Nicholas Galitzki, Tran

Tsan, Jake Spisak, Michael Randall, Max Silva-Feaver, Joseph Seibert, Jacob Lashner, Shunsuke Adachi, Sean M. Adkins, Thomas Alford, Kam Arnold, Peter C. Ashton, Jason E. Austermann, Carlo Baccigalupi, Andrew Bazarko, James A. Beall, Sanah Bhimani, Bryce Bixler, Gabriele Coppi, Lance Corbett, Kevin D. Crowley, Kevin T. Crowley, Samuel Day-Weiss, Simon Dicker, Peter N. Dow, Cody J. Duell, Shannon M. Duff, Remington G. Gerras, John C. Groh, Jon E. Gudmundsson, Kathleen Harrington, Masaya Hasegawa, Erin Healy, Shawn W. Henderson, Johannes Hubmayr, Jeffrey Iuliano, Bradley R. Johnson, Brian Keating, Ben Keller, Kenji Kiuchi, Anna M. Kofman, Brian J. Koopman, Akito Kusaka, Adrian T. Lee, Richard A. Lew, Lawrence T. Lin, Michael J Link, Tammy J. Lucas, Marius Lungu, Aashrita Mangu, Jeffrey J McMahon, Amber D. Miller, Jenna E. Moore, Magdy Morshed, Hironobu Nakata, Federico Nati, Laura B. Newburgh, David V. Nguyen, Michael D. Niemack, Lyman A. Page, Kana Sakaguri, Yuki Sakurai, Mayuri Sathyanarayana Rao, Lauren J. Saunders, Jordan E. Shroyer, Junna Sugiyama, Osamu Tajima, Atsuto Takeuchi, Refilwe Tanah Bua, Grant Teply, Tomoki Terasaki, Joel N. Ullom, Jeffrey L. Van Lanen, Eve M. Vavagiakis, Michael R Vissers, Liam Walters, Yuhan Wang, Zhilei Xu, Kyohei Yamada, and Kaiwen Zheng. The Simons Observatory: Design, integration, and testing of the small aperture telescopes, 2024.

Chapter 5

SAT-MF1 Integration & Testing

SAT-MF1 carried out its integration and validation at UCSD from June 2019 to March 2023, encompassing 13 cooldowns before shipping to the site for commissioning. Each cooldown henceforth is denoted as P*x*R*y* for Phase *x* Run *y*. Besides the first pump down, P1R1, where we validated the bare SAT at the vacuum level, each subsequent phase indicates the installation of major component(s).

SAT-MF1 was manufactured by Criotec Impianti[1] and delivered to UCSD with its three shells (vacuum/300K, PTC1/40K, and PTC2/4K shells) assembled. Our first run checked the vacuum system as we carried out an extensive leak check after installing compressible RF gaskets on the atmosphere side of the O-rings to ensure that the SAT would be RF-tight. Then at each of the following cooldowns, I validated and investigated the SAT's thermal and cryogenic environment (section 5.1), vibrational heating (section 5.2), and the readout transmission of the RF and DC components (section 5.3). Chapter 2 has already described an overview of the SAT instrument. Subsequently, this chapter highlights the integration of those aforementioned components and their impact on the SAT thermal, vibrational, and RF/DC transmission environment.

---

[1] Criotec Impianti S.p.A., 10034 Chivasso TO, Ital

5.1 Cryogenic Performance

The fully assembled SAT takes approximately 9 days to cool from room temperature to below 4 K on the PTC2 and lower temperature stages as seen in Figure 5.1. Once the DR circulation is turned on to start condensing, it takes about 4 hours to reach a base temperature on the MC (0.1 K) stage.

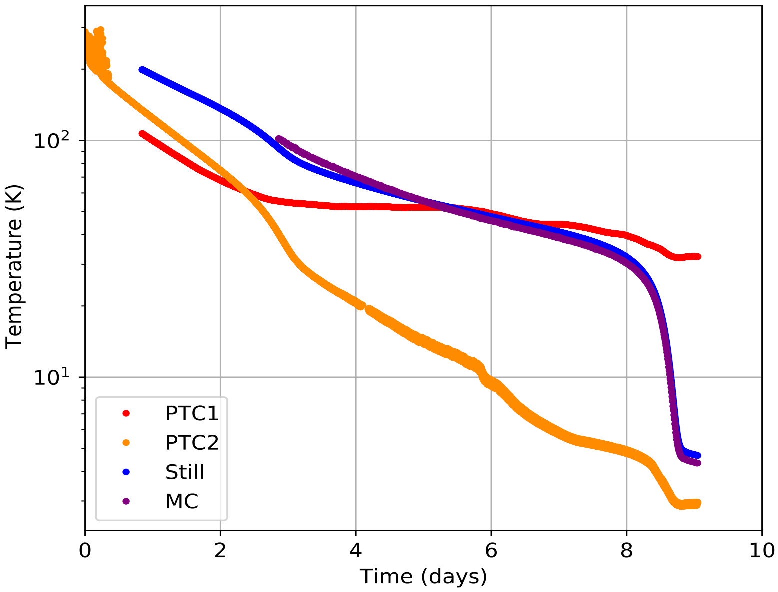

Figure 5.1. Cooldown timeline for SAT-MF1 to reach the base temperature of the PTCs. The solid dots are the measured temperature of the cold heads on the four temperature stages for a cooldown. It takes about 9 days to get down to the PTC base temperature and 4 more hours to the MC base temperature once the DR circulation is turned on.

The SAT is cooled by two PT420S to reach below 4 K: one standalone unit and another unit coupled to the dilution refrigerator (DR). The DR then cools the SAT to sub-Kelvin, in the temperature range that the detectors operate. The next two subsections dive into the loading estimates at the four temperature stages (PTC1/40K, PTC2/4K, Still/1K, and MC/0.1K) using various load curves and thermal tests. To ensure that cooling power is delivered efficiently from the DR to their corresponding temperature stage components (e.g. the Optic Tube on the Still and focal plane on the MC stage), I have analyzed the thermal conductivity of the heatstraps in section 5.1.3. Finally, section 5.1.4 examines the filter loading on the frontend.

5.1.1 PTC Stage Validation and Loading Estimates

To assess the loading, I attempted to keep most elements of the system within our control consistent between cooldowns and employed several strategies to obtain values that can be used for the validation of the cryogenic system. The PT420 standalone unit was assessed in a dedicated testbed before installation into SAT-MF1 and then re-validated after more than two years at the vertical and 27.5° from vertical. The re-validation in most cases shows less than 5% change in both temperature stages. Additionally, I extensively tested the orientation effect using a similar PT420 unit. Chapter 3 details the results of these tests. With this information, I used three load curve sets as the primary method to extract the loading values: the 27.5° set, the original 0° projected to 27.5° based on the formulation obtained in Chapter 3, and finally the re-validated 0° projected to 27.5°. Then I used linear interpolation to extract a best loading estimate per load curve set. The final values and error bars are the means and standard deviations. Table 5.1 summarizes the PTC loading for all of the cooldowns. The final best estimates in this table consider the base temperatures within a cooldown, and the error bars are the standard deviations from the results using the aforementioned three PTC load curves as references.

Extracting loading on the PTC stages is challenging due to several factors. First, the UCSD highbay lab is effectively at the local ambient temperature, which can fluctuate by over 10 K across cooldowns and sometimes even within a cooldown. This leads to a 0.6-1 K change on the PTC1 stage, which corresponds to an additional 3 W. Note that this is observed on just the PTC1 cold head and not the DR PTC1 cold head, as DR PTC becomes more influenced by the Still and MC heating environment and the diurnal effect becomes subdominant. The second complication comes from the DR PTC thermally coupled to the receiver PTC stages while also providing the pre-cooling of the He mixture for the DR circuit. The loading from the mix circulation is unknown, adding an unquantified and variable loading source to both PTC stages. Henceforth, unless otherwise specified, PTC1 and PTC2 loadings indicate the loadings based on the effect on the remote PTC cold heads. They do not include the additive heat load pulled by the DR PTC. As a result, when calculating the sub-components thermal contributions and their corresponding uncertainties, we look at the difference in loading across cooldowns and the error propagations, which tell us the uncertainty in our measurements between cooldowns. Then we examined the diurnal effect and took the largest uncertainty from both methods for our error bars. For the PTC1 stage, both the error propagation and diurnal check yield similar values of about 3 W. For the PTC2 stage, the diurnal impact became subdominant to the propagation of uncertainty across cooldowns, so we decided to go with the largest error bars when reporting. Hereafter, the error bars are 3 and 0.08 W for the PTC stages, respectively, when reporting sub-components loadings such as in Table 5.2 and 5.4.

Table 5.1. Estimated Loading for the PTC stages using load curves.

Cooldown	PTC $P_{1,est}$ (W)	PTC $P_{2,est}$ (W)	DR $P_{1,est}$ (W)	DR $P_{2,est}$ (W)
P2R1: PTC	19.8 ± 1.8	0.07 ± 0.05	–	–
P3R1: DR	21.6 ± 3[2]	0.109 ± 0.08[3]	28.0 ± 1.5	0.46 ± 0.04
P3R2: New G10 truss	11 ± 2	0.10 ± 0.03	16.0 ± 1.9	0.47 ± 0.04
P5R1: URH	18.4 ± 1.8	0.23 ± 0.04	25.2 ± 1.7	0.75 ± 0.05
P8R1: FPA & CRA	19.8 ± 1.8	0.17 ± 0.05	23.9 ± 1.5	0.69 ± 0.05
P7R1: CHWP & SPB	18 ± 2	0.20 ± 0.04	28 ± 2	0.75 ± 0.06
P7R3: SPB fixed	22.9 ± 1.4	0.22 ± 0.04	30.3 ± 1.5	0.82 ± 0.06
P4R1: Window, IR filters	33.0 ± 1.5	0.41 ± 0.05	41.1 ± 1.5	0.82 ± 0.08
P6R1: OT	31 ± 2	0.38 ± 0.06	37.0 ± 1.5	0.80 ± 0.06
P9R1: UFM, empty HWP	34.4 ± 1.5	0.57 ± 0.06	40.8 ± 1.5	1.00 ± 0.09
P10R1: Fully Integrated	38.9 ± 1.4	0.94 ± 0.10	41.2 ± 1.6	1.1 ± 0.1
P10R2[4]: Fully Integrated	31 ± 2	0.84 ± 0.12	31 ± 3	1.59 ± 0.08

---

[2] 3W uncertainty here is estimated rather than measured. It is based on later measurements of diurnal effects.
[3] Cannot calculate the stddev. Assume the nominal error bar for this stage. See Section 5.1.1 for more information.
[4] Similar to P10R1 but replaced PTC1 IR filter

P2R1 validated the thermal state of the SAT when we first installed the PTC. Then in the P3 runs, we added the DR and replaced the G10 truss. With both the DR and PTC in the SAT, we had a complete cryogenic system inside the telescope. Thus, P3R2 became the baseline cooldown that I used to compare against later cooldowns to extract thermal contributions from different subsystems. The measured baselines for both PTC stages are $P_1 = 11 \pm 3$ and $P_2 = 0.1 \pm 0.08$ W, which aligns closely with the predicted loadings of $P_1 = 12$ and $P_2 = 0.2$ W, respectively. Note that PTC has the DR PTC sharing the thermal radiation that the stages are seeing, while the predictions do not account for the impact from the DR PTC as this is not a straightforward linear effect. Thus in a sense, the predictions underestimate the expected thermal yield, which one can see in later comparisons between the expected and predicted for different subsystems (e.g. the universal readout harness and filters) and the almost fully integrated telescope.

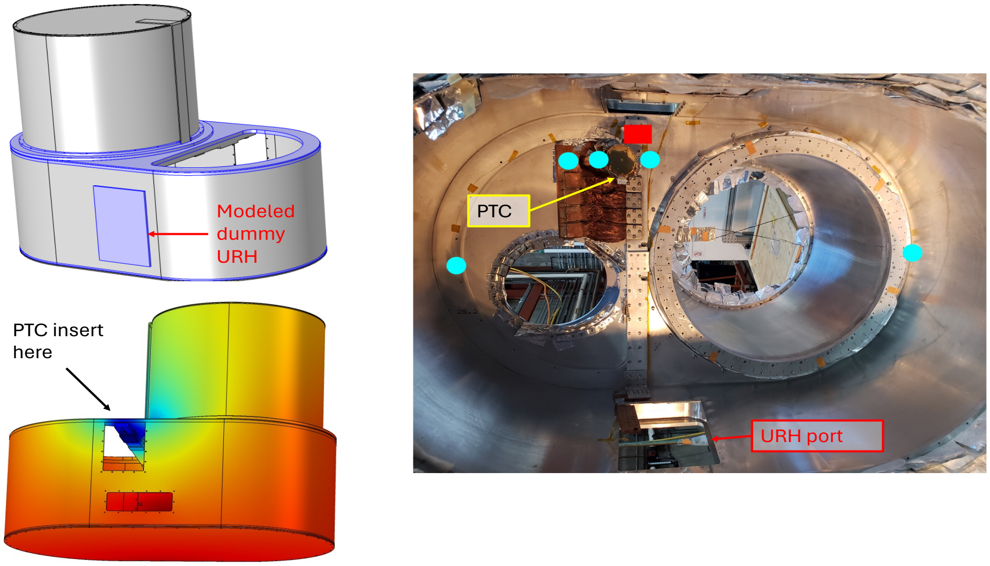

Figure 5.2. URH COMSOL thermal loading analysis. Top left: a 3D CAD model of PTC1 (40K) shell with a dummy URH. The simulation accounted for the material and thermal properties of all major components. Bottom left: a thermal study in COMSOL, a multiphysics package, showing the temperature gradient. The coldest point connects to the PTC. Right: backend view of the actual PTC1 shell. The cyan circles are the thermometers. The red box is the heater used for thermal tests.

The universal readout harness (URH) installation occurs in P5R1. The URH holds the radio-frequency (RF) and DC components that make up the readout chains from room temperature down to 4 K or PTC2 stage. See Section 5.3 and Figure 5.17 for more details on URH components. To calculate the URH loading, I used three approaches: PTC load curves (see Table 5.1 for the results), COMSOL multiphysics thermal simulation, and load tests. Figure 5.2 portrays the setup for the thermal simulation analysis. In this scenario, I imported the geometry of the SAT PTC 1 shell from Solidworks and simulated the SAT thermal environment and the temperature gradients across the shell. Then I simulated the temperature environment from P3R2 (the run before the URH install) as a base state to check how well the sim worked. Using the thermometer close to the PTC cold head as a fixed temperature point, I increased the load on the dummy URH until the simulated URH temperature reached the same level as the observed temperature and compared it to the base state to get an estimated loading for the URH. The right side of Figure 5.2 shows the distribution of thermometers. The third method involved applying a series of loads on the bus bar heater (red box in the right picture of Figure 5.2), then using the temperature increase of the cold head in P5R2 to extract the URH loading. These last two methods serve as consistency and sanity checks, and we report the differences between P5R1 and P3R2 PTC loads as the measured URH thermal loads in Table 5.2: $P_{1,est} = 7 \pm 3$ W and $P_{2,est} = 0.13 \pm 0.08$ W. The predicted loadings from the URH are 2 and 0.1 W, respectively. Excess in the PTC 1 stage is expected as the predictions do not account for added penetrations in MLI. We have tried to be rigorous in our MLI setup; however, the MLI will always be somewhat comprised of penetrations.

Table 5.2. URH measured loading vs predictions for the two PTC stages. The PTC1 stage measured loadings come from the PTC load curves (the difference between P5R1 and P3R2 values in Table 5.1). The error bar for PTC1 stage comes from our studies of diurnal effect and error propagation across cooldowns. The error bar for PTC2 is directly from the propagation of uncertainty across cooldowns.

Stage	Predicted Loading (W)	Measured Loading (W)
PTC1/40 K	2	7 ± 3
PTC2/4 K	0.13	0.13 ± 0.08

With SAT-MF1 almost optically fully integrated but not open to 300 K, the total measured loading comes out to be $P_{PTC1} = 31 \pm 2$ W and $P_{PTC2} = 0.38 \pm 0.06$ W. These values come from P6R1, where we have most of our optical components in place sans the CHWP with sapphire stacks. The HWP was a blackened blank-off instead. We did not have the full 7 detector wafers; however, we have dummy blankoffs to replicate the thermal environment to that of a fully integrated configuration. We experienced various cryogenic issues from a much hotter DR PTC 4K cold head to various circulation issues in P10s to longstanding problems such as subpar IR filters. These problems make it difficult to identify the exact cause of the increase in temperature in later cooldowns. Hence, I only quoted the values from P6R1 here and in Table 5.3. Compared to the predictions, the loads are higher than expected, especially in the PTC1 stage. It is about 11 W higher. Again, this may be partially due to penetration from MLI as previously mentioned since we started with about an 8 W difference when comparing the base states. Nevertheless, there is enough cooling capacity such that the SAT reaches the desired base temperature at all stages.

Table 5.3. Predicted and measured loadings for each temperature stage of SAT-MF1. The PTC cooling capacity at 45 K and 4.2 K is supplied by the PT420 (not the DR PTC). Hence, the predicted loadings on the PTC stages do not include the PTC integrated into the dilution refrigerator (DR) as it is difficult to model this contribution from the DR mix circuit. The cooling capacities for the Still and MC stage are advertised by the manufacturer for an SD-400 DR system. The predicted loadings account for contributions from radiation, mechanical support such as the trusses, cables, RF components, the optical system, and miscellaneous sources such as the mylar RF shield. The total numbers are taken from [24]. The measured loading values come from P6R1, which was the run where we have most of our optical components except for the sapphire HWP.

Stage (K)	Predicted Load (W)	Measured Load (W)	Cooling Capacity (W)
PTC1 (45)	19.61	31 ± 2	50
PTC2 (4.2)	0.579	0.38 ± 0.06	1.80
Still (1.0)	$4.7x10^{-3}$	(5.0 ± 0.4) x 10^{-3}	25 x 10^{-3}
MC (0.1)	$25.15x10^{-6}$	(22 ± 5) x 10^{-6}	400x10^{-6}

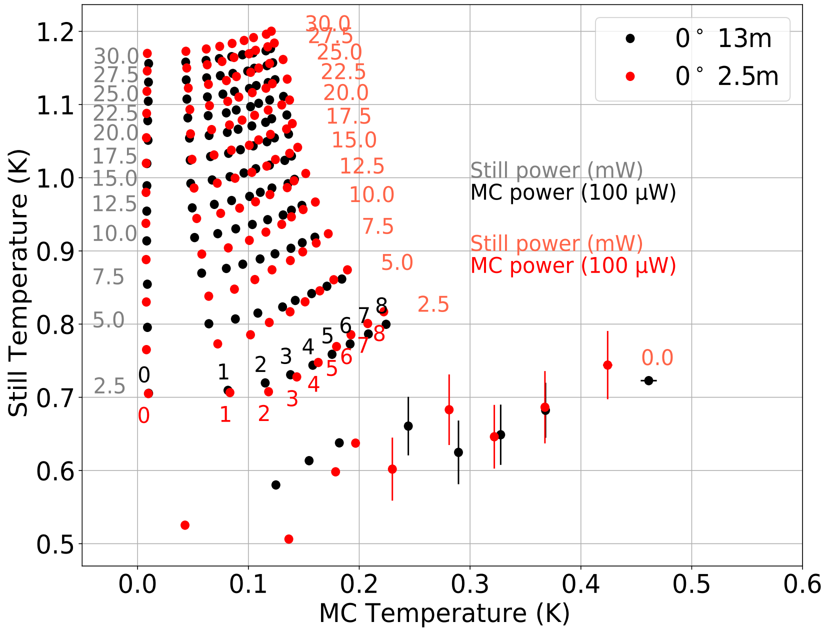

Figure 5.3. DR Validation. Load curves of the DR inside its own Bluefors cryostat. Power was applied from 0-800 μW on the MC stage and 0-30 mW on the Still stage. We repeated the tests, each time with a different set of helium hose lengths: 2.5 and 13 m. The Still cooling power decreases, while the MC cooling power increases slightly from going to a longer hose length.

5.1.2 Quantifying Thermal Performance on the DR Stages

In 2019, Bluefors delivered the DR in its cryostat. To understand the DR performance, we performed a few load curves on the DR inside its cryostat at 0°. Powers were applied from 0-800 μW on the MC cold head and 0-30 mW on the Still cold head. Two sets of load curves were carried out for 2.5 and 13 m helium hose lengths. These are the condensing and returning hoses that run from the DR to the gas handling system (GHS). During operation at the site, the GHS is located on the azimuth platform with these helium lines routed through the boresight and cable wraps such that the length needs to be 20 m long. Hence, the two tests here validate the DR performance and also examine the effect of longer hoses. Figure 5.3 displays the load curves during this initial validation, showing the temperature for the two hose lengths. According to the plot, the Still temperature changes slightly ($\leq 5\%$) by going to a longer hose length. We also observe that increasing the Still temperature slightly can lead to a lower and more stable MC temperature. Thus, we often utilize this to improve and stabilize our temperature on the MC stage during operation. Besides the load curve tests, we carried out another consistency check. 30 mW was applied to the Still in both configurations. Then we stepped in MC power until the temperature reached 100 mK. The 2.5 m configuration yielded a baseline cooling performance of 548 μW, while the 13 m one resulted in 516 μW. This test indicated a 6% decrease in cooling capacity, which is consistent with the result from the load curves.

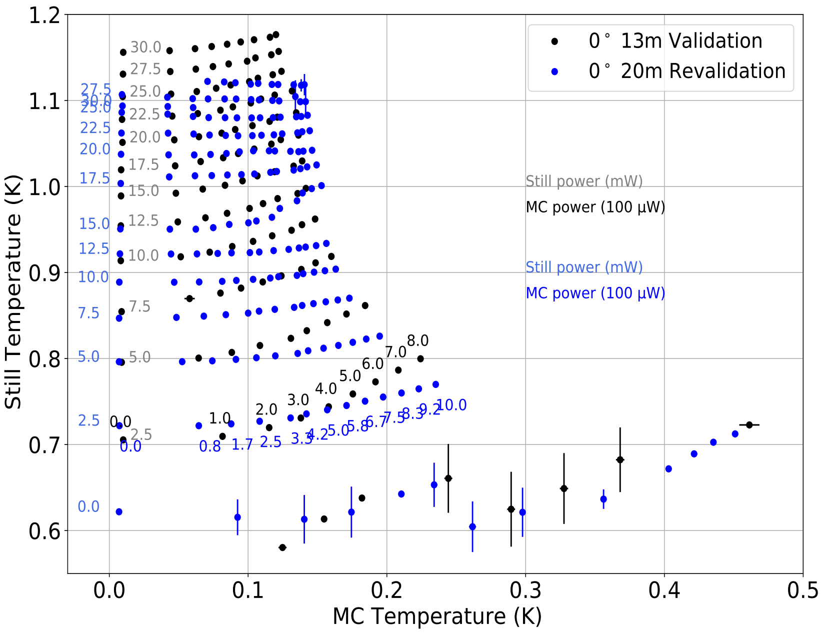

Figure 5.4. DR revalidation vs the original validation. Black is the original validation back in 2019 using the 13 m long helium hoses and blue is the re-validation 4 years later using the 20 m long helium hoses.

The DR was once again tested in its Bluefors cryostat (outside SAT-MF1) in 2023, almost 4 years after its initial validation and after 10 thermal cycles inside SAT-MF1 (from P3R1 to P9R1). Figure 5.4 compares the two load curves, where the revalidation has the 20 m lines installed. As the chosen power set points have changed slightly, I did not try to do a direct % difference comparison this time. Looking at the plot, the revalidation suggests a slight degradation in performance on both stages. This effect on the MC stage mellows out at higher Still power. Though the performance has changed slightly, the DR cooling capacity remains well within the advertised capacity of 400 μW.

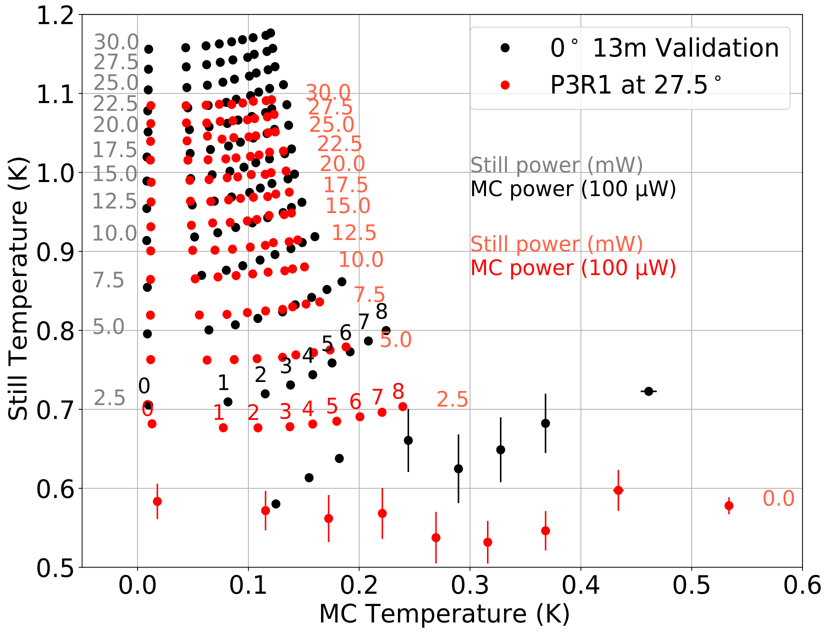

Figure 5.5. DR load curve inside SAT-MF1. The DR was installed inside the telescope during P3R1, where the same detail load curves was applied. This load curve serves as a baseline to extract loading estimates for later cooldowns.

After validating the DR for the first time, we installed it inside SAT-MF1 and performed another detailed load curve (LC) over the same loading ranges. Inside the telescope, all four cold heads tilted at 27.5° with respect to gravity. Figure 5.5 compares the load curves against the original 13 m validation set. I then use this P3R1 set as a baseline to extract estimates of the loading on the Still and MC stages for subsequent cooldowns and every installation of new components. For this analysis, I ran sparser sets of load curves at each cooldown and then extracted the power estimates using P3R1 LC. This forms a small population of loading from the SAT and its components extracted at different temperatures. We used the load information from this technique as a guide while we successively integrated the SAT in 10 cooldowns, leading to the final loading numbers shown in Table 5.1.

To make sure that our scan strategy works at all tilt angles without significant compromise on the MC stage's cooling capacity, the DR was cooled twice in SAT-MF1 and tilted at different angles. During these two cooldowns, SAT-MF1 rotated in different configurations: along its short and long axes. Figure 5.6 illustrates the rotation configurations and the test results corresponding to them. The 4 cold heads inside the DR were tilted relative to the vertical from 27.5° to 51.2° around the long axis of the telescope and 0.3° to 45.6° around the short axis of the telescope. Note that the tilt degree indicated in the figure is the angle of the cold head and not that of the SAT. The right side of the figure shows the SAT rotation axes and the components inside the DR. According to the tilt result, the PTC stages do not experience a sharp increase in temperature until past 40°, which is in line with the tilt test results of the remote PTC in Chapter 3. The Still behavior is a bit hard to decouple as there is no clear pattern as a function of tilt angle. As for the MC temperature, the spike happens around 50°, following the trend of the DR PTC stage but at a slower pace. Since the DR PTC serves to pre-cool the mix going into the Still and MC,

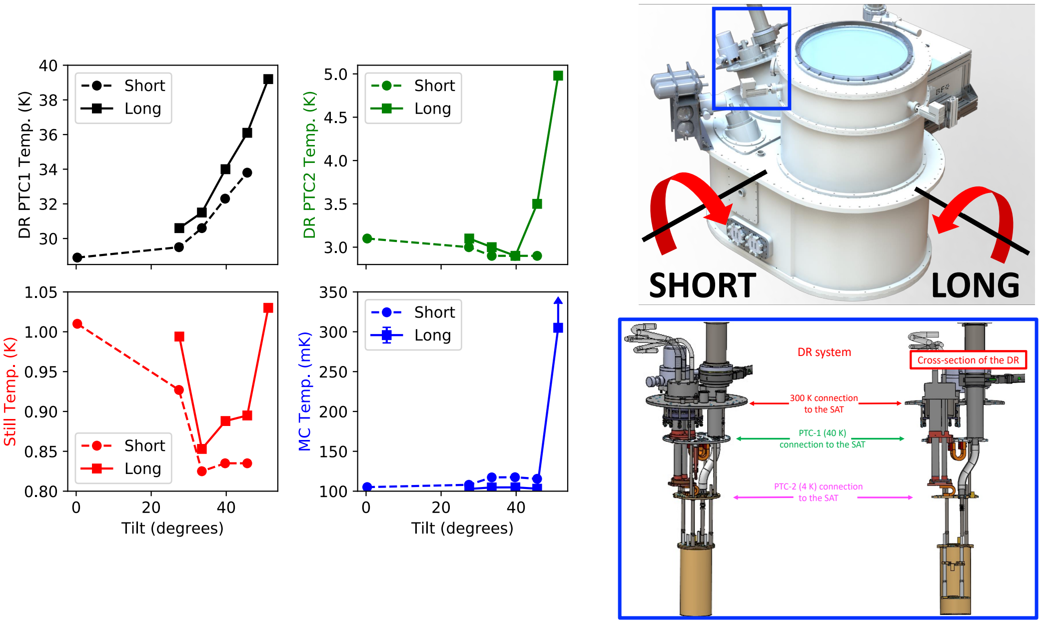

Figure 5.6. DR tilt test and the DR temperature response as a function of the cold heads' tilt angle. Left: the temperature changes for the DR PTC1/2 (40/4K), the Still, and MC cold head. Top right: a CAD figure of the SAT with the two rotation orientations demonstrated. The DR is circled in blue. Bottom right: a CAD model of the DR. The data was taken from two separate cooldowns. Note that the dashed and solid lines are for short and long rotations, respectively; however, the angles are the tilt of the cold head. So 0° is when the cold heads are verticle, opposite the direction of gravity.

the results make sense. However, to what extent is the influence of the PTC's convection effect due to gravity on DR circuit or whether this gravitational effect is intrinsic inside the DR circuit itself is hard to decouple.

5.1.3 Still and MC stage Heat Strap Conductivity Investigation

The DR Still and MC deliver cooling power to the Optics Tube (OT) and the focal plane array (FPA) through a series of gold-plated copper heatstraps, which are braided and solid rod copper. These straps are manufactured by Technology Applications, Inc. (TAI). Figure 5.7 and 5.8 describe the heatstrap, thermometer, and heater placement on the Still and MC stages, respectively. The left side of Figure 5.7 shows the actual heatstraps installed inside SAT-MF1; while the right side zooms into the CAD model of the heatstraps. Three separate heatstraps (HS) on the Still stage aid in delivering cooling power from the DR Still cold head to the OT: the double rod HS which connects directly to the DR Still cold head, the braided HS, and finally a copper rod that bolts to the OT near lens 2. Thermometers, placed at each end of the HS, read out the temperature gradients for each strap as the OT heater outputs different loads.

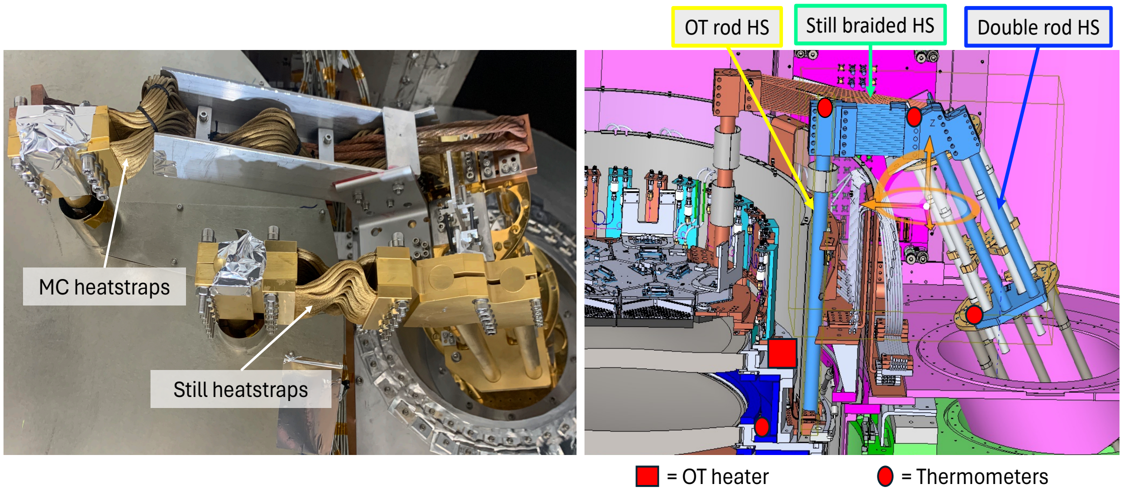

Figure 5.7. Heatstraps placement on the Still stage. The left side shows the actual straps inside the SAT's backend. The right side is a 3D CAD in Solidworks. Three heatstraps connect the DR Still to the OT, delivering cooling power to the rest of the OT. The heater and thermometers are used to apply various loads on the OT to investigate the straps' thermal conductivities.

For the MC stage, two gold-plated copper braided HS connect to the DR MC cold head on one end, while they bolt to a copper HS rod on the other end. This HS rod is bolted directly to the focal plane array (FPA) as seen in Figure 5.8. Three thermometers are placed at the DR MC cold head, the top of the HS rod, and the FPA to examine the temperature gradient of the straps. The non-gold-plated copper heatstrap was installed later at the site to increase cooling power as later investigation suggests possible degradation in the HS performance after several thermal cycles. Moreover, the FPA was too hot and we had trouble controlling the temperature of the FPA for biasing the detectors. See the analysis results below for more details.

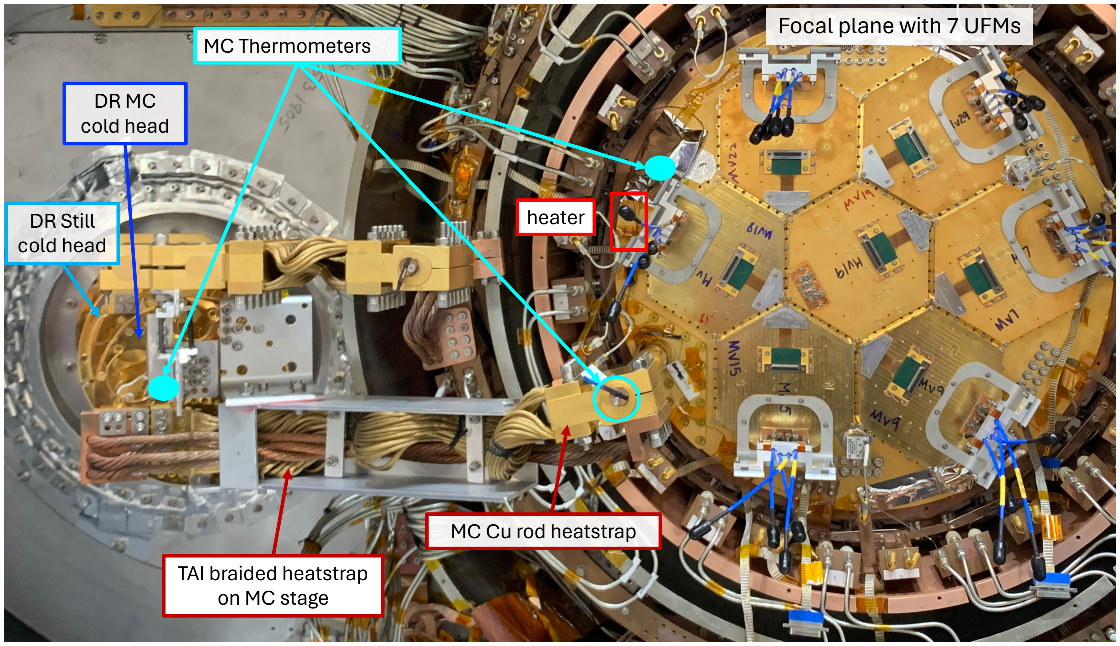

Figure 5.8. Heatstraps placement on the MC stage. Two heatstraps (braided and rod) connect the DR MC to the focal plane and deliver cooling power to the detectors. The heater and thermometers are used for thermal conductivity tests.

I first investigated the HS thermal conductivity in P6R1, during the OT installation run. Then I checked for performance consistency at a later cooldown, P10R1. During P10R1, the installation of the 1K superconducting magnetic shield interfered with the OT heater placement; hence, I did not install the heater. Thus, only the MC straps were checked for performance consistency. To examine the thermal conductivity of the Still straps, and thus their efficiency in delivering cooling power, I applied 0-15 mW on the OT heater, at 2-3 mW steps. For the MC HS tests, I applied 0-400 μW on the FPA, at 20 μW increments in P6R1. For P10R1 with SAT-MF1 fully integrated, I applied 10-60 μW on the FPA, at 10 μW increments.

The heat transfer formula through conduction is

$$\frac{dQ}{dt} = P = \frac{A}{l} \int_{T_1}^{T_2} k(T) dT, \tag{5.1}$$

where A is the cross-sectional area of the material that heat flows through. l is the thickness of the material or the length of the heat's travel path. T_1 and T_2 are the temperatures at the two ends of the material such that $T_2 > T_1$. k(T) is the thermal conductivity of the material. I tried to quantify and extract k(T) by assuming $k(T) = k_0 T^n$. Using the measured temperature and the input power, I analyzed k_0 as a function of n and tried to optimize n such that k_0 remains a constant. This happens when n is as small as possible, so n < 2. Over a small ΔT and small l, one can assume k(T) as a constant average even though k is changing with temperature. However, this method became insufficient as ΔT in P10R1 was 2-3 larger than those of P6R1. Thus, I focused on the instantaneous values of k: $dP/d(\Delta T)$. Equation 5.1 then becomes

$$k(T_2) = \frac{l}{A} \frac{dP}{d(\Delta T)}, \tag{5.2}$$

where $\Delta T = T_2 - T_1$, effectively treating k as a slope on a P vs ΔT plot. Figure 5.9 illustrates the results of the Still heatstraps. The solid and dashed lines are values taken from Adam Woodcraft's poster[5] for hard copper and electrolytic touch pitch (ETP) or commercial copper, respectively. Woodcraft's analysis of copper conductivity relies on a set of equations to predict the behavior, which is then supported by measurements. The fully hard copper line comes from equations and 1 single measurement. The ETP copper lines (there are two lines to set as boundary which one can see in Figure 5.10) come from the equation and 10 measurements. The results for Still HS

---

[5] https://reference.lowtemp.org/

are calculated using Equation 5.2, indicating that all three straps perform within the literature's values and expectations.

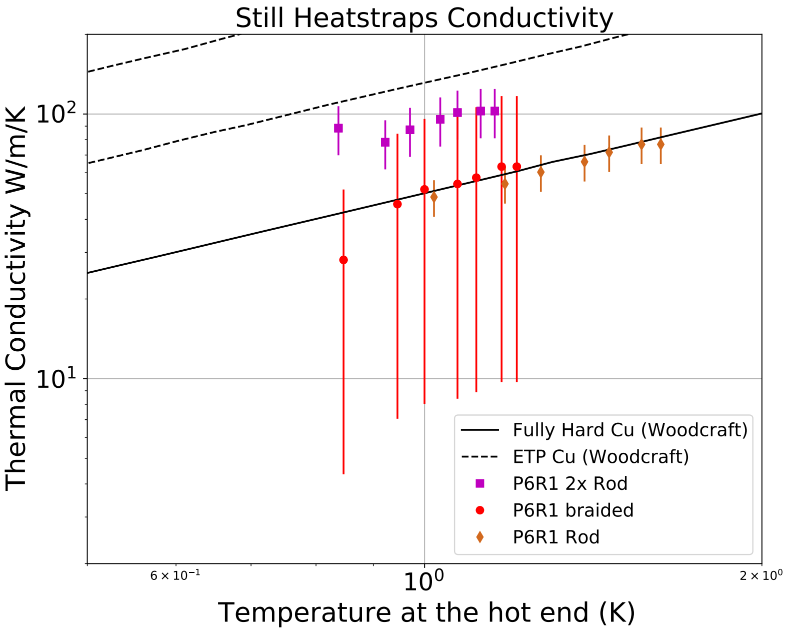

Figure 5.9. Heatstrap conductivity for the Still HS during P6R1. The thermal conductivity is calculated using the formulation in Equation 5.2. k here is plotted as a function of the temperature at the hotter end of the heatstrap. There are three straps on the Still stage: the 2x rod connects directly to the DR Still cold head, and the braided strap connects the 2x rod to the single is attached to the Optics Tube, close to lens 2. See Figure 5.7 for more details.

For the MC heatstraps, the initial measurements in P6R1 suggest that all the straps performed well, following very closely to the ETP Cu line as seen in Figure 5.10. However, a re-measurement when SAT-MF1 was fully integrated for the first time in P10R1 implies that the HS rod's performance (green squares) may have degraded or a mechanical connection may have loosened. As previously mentioned, the ΔT for P10R1 was more than twice what I saw for P6R1, suggesting that perhaps the problem may be a combination of both joint connection and degradation in performance after 3 thermal cycles. To improve performance, we installed additional braided copper heatstraps on the MC cold head as seen in Figure 5.8. This is the non-gold-plated one. SCR2 values in Figure 5.10 represent the measurement done at the site with SAT-MF1 installed on its platform. During this run, we reinforced the bolt joint connections

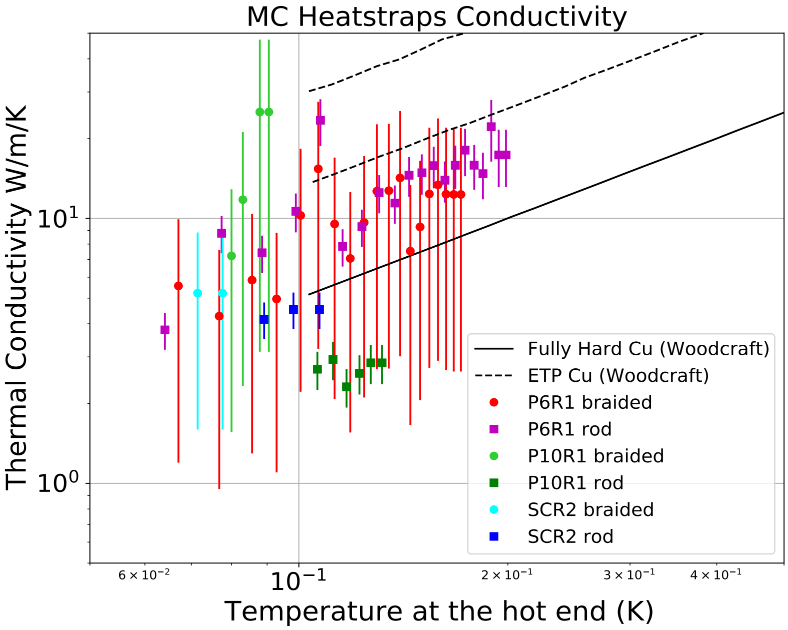

Figure 5.10. Heatstrap conductivity for the MC HS for laboratory tests (P6 and P10) and site run (SCR2). Similarly, the thermal conductivity is plotted as a function of the temperature at the hot end of the strap.

for all the heatstraps. As seen from the site data, we recovered our performance of the MC heatstraps to the state in P6R1.

5.1.4 Frontend Filters Loading

Table 5.4. Loading estimates for the frontend filters. The predicted optical loadings came from a ray tracing solver that took into account the system dimensions, the transmission, reflection, and conductivity of the optical elements as described in [24]. The measured loadings came from the load curve data before and after the frontend filters were fully integrated.

Stage	Predicted Loading (W)	Measured Loading (W)
PTC1/40 K	5	8 ± 3
PTC2/4 K	0.1	0.17 ± 0.08

SAT-MF1's frontend (set of optical elements closest to the sky) is composed of a window and a series of filter stacks from 300 - 4 K as mentioned in section 2.2.3. Understanding the loading from the frontend's optics is critical in assessing the thermal budget and possible contributions to temperature increase in the different stages. Given that SAT-MF1 has one of the largest apertures of mm cryogenic receivers to date, there is a large degree of uncertainty in the predictions. The predicted loading values were based on nominal transmission and absorption spectra as inputs into a ray tracing solver, which then estimated the radiative transfer between the elements. See [24] for more information. To estimate the measured loading, I utilized the power estimates from PTC load curves and cross-checked the results with COMSOL simulations, where I reenacted the thermal environment inside SAT-MF1. As Comsol assumes perfect conductivity of the materials, it serves as an upper limit sanity check to compare to our measurements. The methods followed a similar procedure used for the URH estimated loading described in section 5.1.1. The final values in Table 5.4, which came from the difference between P6R1 and P7R3 values in Table 5.1, provide the measured filters loading for the two stages. Note that P6R1 was the cooldown with a nearly complete set of frontend optics (without the sapphire stack HWP) and P7R3 was the closest run with minimal frontend optics. Hence, the difference in loading between these two cooldowns gives the optical loads measured on the frontend, which come out to be 8 ± 3 W and 0.17 ± 0.08 W for the PTC1 and PTC2 stages. The error bars come from the studies detailed in Section 5.1.1. Though the measurements are on the higher end, they are within one standard deviation of the predictions. The additional loading on the PTC1 stage is likely due to excess IR transmission through the reflective thermal filters, a higher effective emissivity from the cavity walls inside the receiver than simulated, and/or possible penetration in the MLI seam formed around the edge of the filter mount. The MLI is taped to the edge of the filter mount, leaving an area of exposed aluminum around the ring and possible penetration in the MLI that the simulation did not try to account for. To counter the possible higher effective emissivity of the walls, we installed an aluminum baffle that extends from the 300 K IR filter. See Figure 2.6 for the frontend configuration.

5.2 Mechanical Heating Characterization

Operating the SAT at sub-kelvin temperatures on a mobile platform presents a challenge due to potential vibrational coupling to resonant modes of the telescope's mechanical system. All mechanical structures at the Still and MC stages were designed to have their vibrational modes larger than 40 Hz to push all the resonance above the low-frequency vibrations of the telescope platform. To validate SAT-MF1's vibrational environment, Solidworks FEA vibrational mode simulations were used first to inform our designs and the possible resonance modes, then various shake tests were carried out to confirm the simulations. I focused on the components such as the cold readout assemblies (CRA1 from 4-1 K and CRA2 from 1-0.1 K), the FPA, and the solid copper heatstraps on the Still and MC stages. I did not try to model the braided strap as it is difficult to model the flexible strands and the overall straps' rigidity when bolted. Figure 5.11 illustrates the simulation for CRA2. The color gradient just displays Solidworks' arbitrary

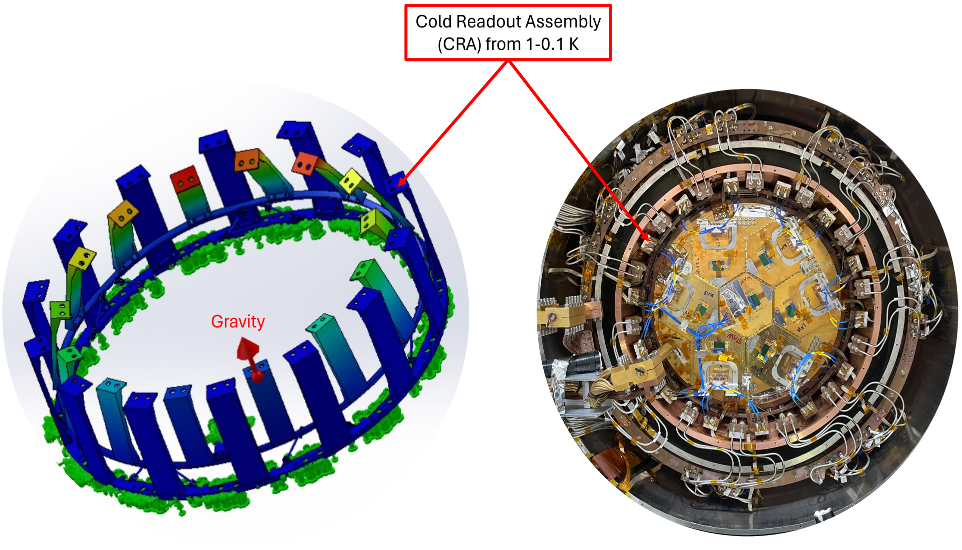

Figure 5.11. Frequency simulation of the 1-0.1 cold readout assembly (CRA) in Solidworks. Left: simulation setup and results. The red arrow indicates the direction of gravity. The simulation yields the first 20 resonant frequencies of the CRA. The first 4 modes range from 42-56 Hz, suggesting that the CRA may contribute to the temperature spike at 39 Hz and 58 Hz in Figure 5.13. Right: the CRA installed inside SAT-MF1. As previously mentioned, this CRA connects to the focal plane via a series of copper foil heatstraps.

color scale; however, one can extract the first 20 resonant modes from the results. From the simulation, CRA2's first 4 harmonics range from 42-56 Hz. This result was later confirmed when a prototype of CRA2 was tested warm on a shake table at Quanta Laboratories[6], which measured that the first two modes are very close to 40 Hz. Similar tests were done for the FPA with dummy detector wafers and CRA1 at Quanta to verify the resonances.

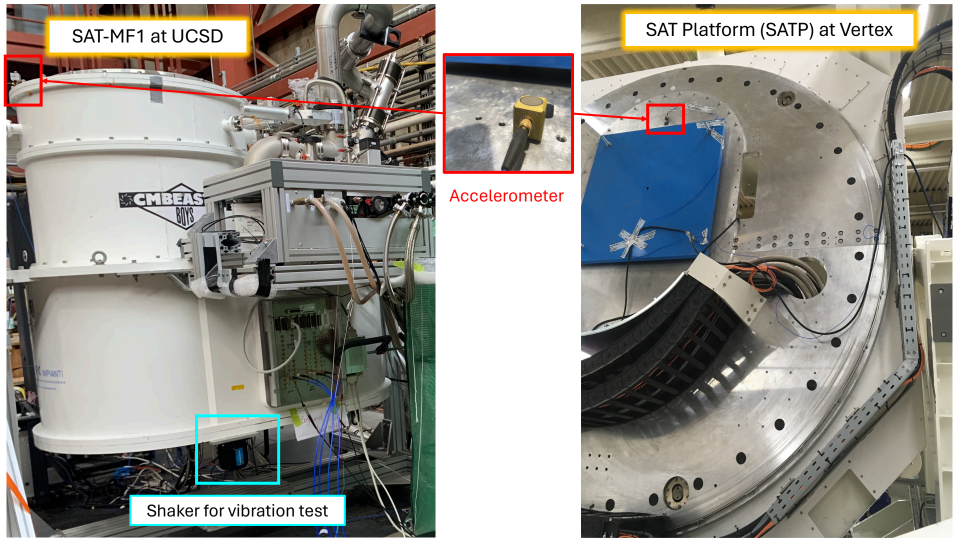

Figure 5.12. Setup for the vibration detector test for SAT-MF1 and SAT platform. Left: SAT-MF1 at UCSD. The accelerometer, the same one that SATP used, was mounted on top of SAT-MF1, near the window. The cyan highlight outlines the position of the shaker used for the vibration tests. Right: SATP and the same accelerometer at Vertex, Germany during the factory acceptance test. The figure was adapted from Michael Randall's pre-ship review slide, with the right figure of the SATP courtesy of Vertex.

The next step in the validation characterized the vibrational impact that the SAT platform (SATP) would experience. During the SATP factory acceptance test (FAT) at Vertex Antennentechnik in Germany, a model 356B18 triaxial accelerometer[7] was installed on a dummy SAT receiver model on top of the SATP. This receiver model weighed the same as a fully integrated SAT-MF1. During the SATP test scans, which tested different operational scanning patterns and turnarounds, accelerometer data were recorded. These data were then used in the subsequent analysis to help project the possible vibrational power that SAT-MF1 would experience during

---

[6] Quanta Laboratories, Santa Clara, CA 95

[7] PCB Piezotronics, 3425 Walden Avenue, Depew, NY 14

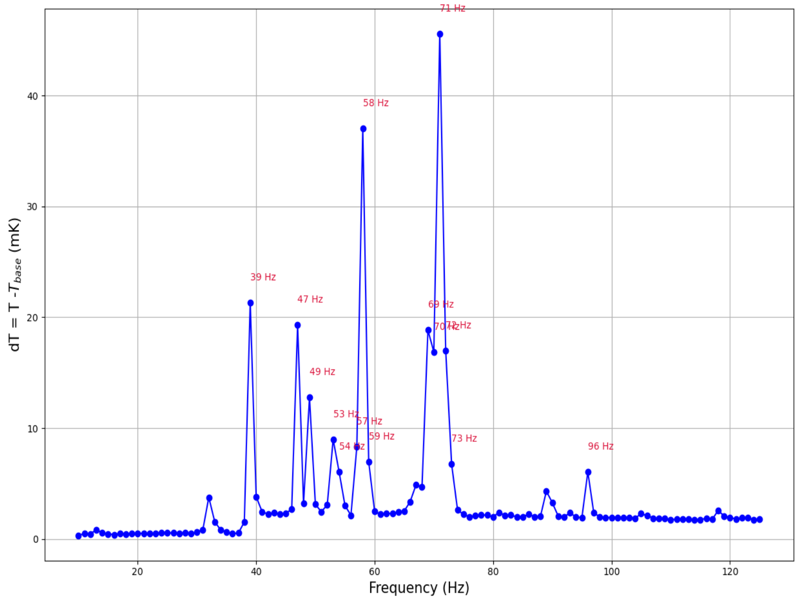

Figure 5.13. Temperature fluctuation as a function of frequency. As a baseline vibration test, I conducted a wide frequency sweep from 10-125 GHz at 1 Hz step and with an amplitude much higher than we expected to exist on the SATP and identified their corresponding temperature fluctuations. dT here is the measured temperature fluctuation after subtracting the base temperature. The base temperature consists of an hour average after the FPA got back to base state after the test. $T_{base} \sim$ 93-95 mK.

an observation scan. Finally, various shake tests were carried out on SAT-MF1. Figure 5.12 describes the setup for the shake test at UCSD and at Vertex. We bolted a Buttkicker LFE haptic transducer to the bottom flange of SAT-MF1 and used a function generator coupled to two analog amplifiers to provide an input impulse to shake the telescope. At the top of the SAT, near the window, we installed the same accelerometer that was used in the SATP FAT.

To excite the different vibrational coupling modes inside SAT-MF1, I conducted a wide frequency sweep from 10-125 Hz at 1 Hz steps. As the device did not provide consistent vibrations below a certain drive amplitude, I had to operate it at a higher amplitude, much higher than we expected to exist on the SATP. Figure 5.13 shows the temperature fluctuation as a function of frequency for this wide sweep. This was the temperature fluctuation that the focal plane experienced in comparison to its normal base state. A similar study of the Still-stage temperature was also carried out; however, the largest peaks at 58 and 69 Hz only caused 3-5

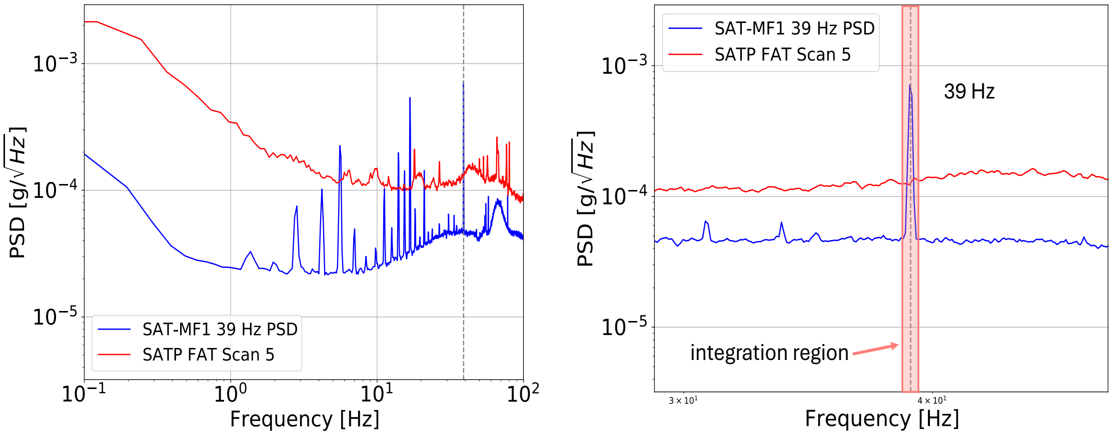

Figure 5.14. Power spectral density (PSD) for SAT-MF1 and SATP. Left: power spectral density plots for SAT-MF1 39 Hz at 5 V drive amplitude (blue) and SATP FAT (red). Scan 5 involved scanning around in azimuth from 0-360° at an elevation of 50° with a scan speed of 1°/s and turnaround acceleration of $2°/s^2$. Right: Zoom in view around the 39 Hz line. The light red shaded region is the integration region to get the total accelerometer power in units of g.

mK of change on the Optics Tube stop temperature. Hence the following analysis and result will focus on the MC stage, specifically at the 3 tallest peaks that caused dT $>$ 20 mK. From the Solidworks simulations and warm shake table tests, the most likely culprit for the 39 and 58 Hz was CRA2. As for the 71 Hz line, the simulation suggested that it was the FPA heatstrap rod. Focusing on these three resonances, I carried out a deep sweep at these frequencies at different drive amplitudes from 5-9 V, at 0.5 V steps, with the accelerometer recording full-bandwidth measurements for each drive amplitude and drive frequency.

The next step in the analysis involved integrating over the interest spectral lines to get the integrated accelerometer power in g. Figure 5.14 compares a PSD from SAT-MF1 at 39 Hz against the SATP FAT scan data on the left, while the right figure illustrates the integration region of about 0.6 Hz for the x-direction. Both the SAT-MF1's and SATP PSDs were integrated, and this process tried to project the narrow spectra onto a broadband spectrum in integrated power space. For each of the target frequencies, the SATP vibration PSD was integrated over the same frequency bandwidth as SAT-MF1's PSDs. There are three axes on the accelerometer, so I took the square root of the total sum square of the power at the three axes to get a net integrated power

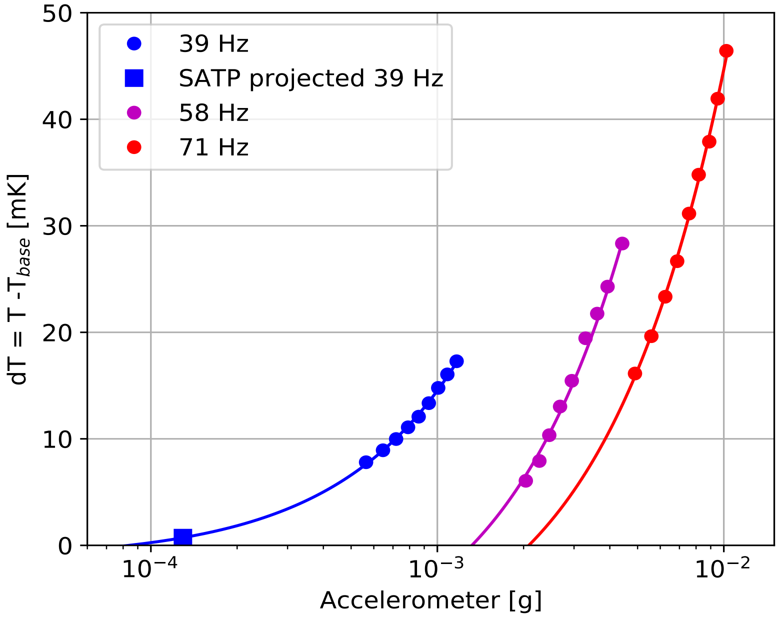

Figure 5.15. Total power of the vibration measured at the accelerometer vs the temperature fluctuation on the FPA. The circle data points are the vibrational integrated power at different drive amplitudes of the shaker. The solid lines are the linear fit on a log x-scale. The squares are the projected heating (dT) at SATP vibrational power. The integrated power for SATP was taken from FAT scan 5 as mentioned in Figure 5.14. The 71 and 58 Hz projections are below the predicted vibration floor (dT $<$ 0), so they do not appear here. The projected heating for 39 Hz yields $\sim$ 0.9 mK.

in g. Then I examined the rise in temperature of the FPA from a base temperature of 95 mK for the first two frequencies (39 and 58 Hz) and 93 mK for the last frequency. Note that these two base temperatures were observed during the deep sweep at the three specific frequencies, and they yielded the same base temperature as that of the wide frequency sweep in Figure 5.13. Figure 5.15 plots the total integrated power of the vibration measured at the accelerometer against the FPA's temperature fluctuations. A linear fit to each frequency's dT versus the vibrational integrated power was used to extrapolate the predicted heating at the SATP power level, or the dT corresponding to SATP's accelerometer integrated power. I expect the dissipated power to be directly proportional to the injected power down to a floor vibrational amplitude below which the injected power is too low to excite a significant vibrational heating response. As shown in Figure 5.15, the measured SATP vibration is below the predicted vibrational floor at the 71 and

58 Hz (dT $<$ 0), so I do not expect those modes to contribute to heating during operation. The 39 Hz mode is predicted to excite less than a mK of heating during scanning. This level of thermal fluctuation can be regulated using our active temperature control system through a PID loop.

5.3 RF and DC Validation

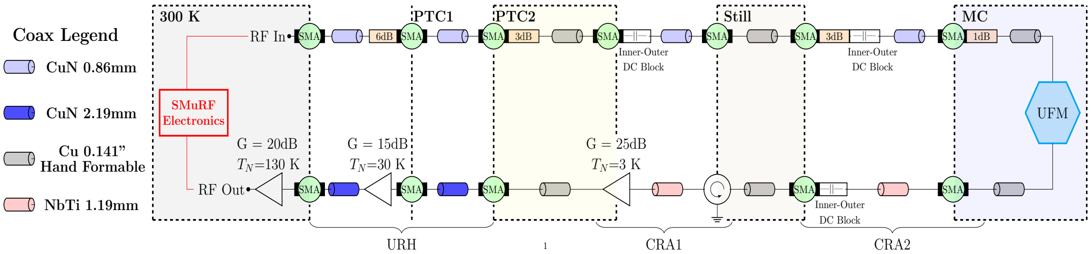

Figure 5.16. Schematic of the RF chain inside SAT-MF1. The figure is taken from [24]. The chain runs from room temperature to MC stage, then connects to the detector wafer and back. The universal readout harness (URH) houses the readout components from 300-4 K. Then CRA1 and CRA2 hold the readout components from 4-0.1 K. Connecting these three principal structures are isothermal hand formable copper coaxes. In this schematic, two RF chains (input and output) connect to a single UFM. The legend describes the different coax types. See [51] for more details on the cryogenic RF components and coaxial chain design.

The Simons Observatory uses microwave multiplexing system (μMUX) with SLAC microresonator radio frequency (SMuRF) electronics to read out the detector signals as mentioned in Chapter 2. SMuRF and μMUX can read out over 1000 detectors using a single coax pair, resulting in only two coax chains per UFM. There are 7 UFMs inside each SAT, totaling up to 14 chains. Each chain consists of direct current (DC) and radio frequency (RF) components such as DC block, SMA connectors, attenuators, low noise amplifiers (LNAs), and coaxes. Figure 5.16 outlines the components inside SAT-MF1 RF chains. The Universal Readout Harness (URH), CRA1, and CRA2 house all the readout components inside the SAT from room temperature down to the MC stage. Figure 5.17 and 5.18 describe the URH and the two CRAs, respectively, with some of the readout components called out. The URH holds the readout component from the 300-4 K stage. Then 14 isothermal copper hand-formable coaxes connect the URH to CRA1

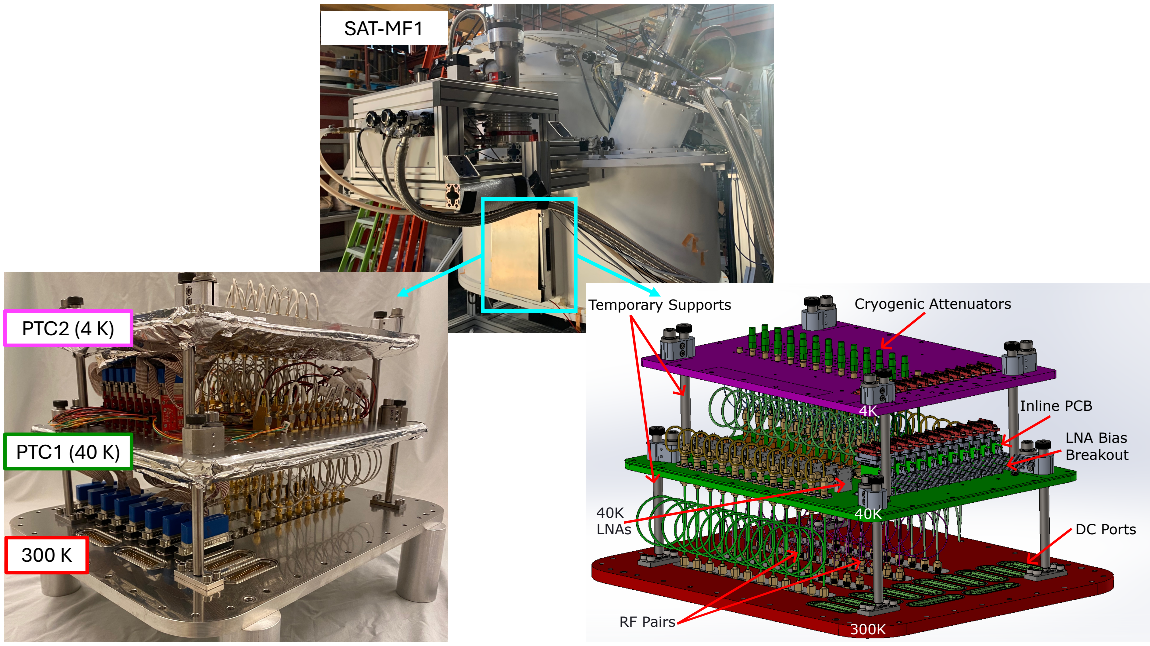

Figure 5.17. The Universal Readout Harness (URH) used for SAT-MF1. Top: the location of the URH inside SAT-MF1. Bottom left: picture of the actual URH on the benchtop with the three temperature stages called out. Bottom right: a CAD model of the URH with its components called out. The two bottom pictures are courtesy of Jenna Moore.

on the PTC2 (4K) stage. These coaxes range from 2 m for the farthest chains to $\sim$0.5 m long for the shortest chains. The cables are sourced from Mini-Circuits. Next, CRA1 is composed of two rings that house readout components from 4 K (bottom ring in Figure 5.18) to 1 K (top thinner ring). The same isothermal coaxes connect the CRA1 to CRA2 at the Still (1K) stage, but at shorter lengths ($\sim$ 0.2 m). The CRA2 then contains the rest of the components, which then route directly to the UFM wafers at the MC (0.1K) stage using isothermal copper cables from Centric RF.

5.3.1 Transmission Model Development

Understanding the readout cabling's transfer function was critical in optimizing the system to achieve photon-noise-limited performance. Hence I developed an RF transmission model to predict the SAT readout chains' performance and established criteria for the RF system's health check. Before integrating each of the three structures (URH, CRA1, and CRA2) inside

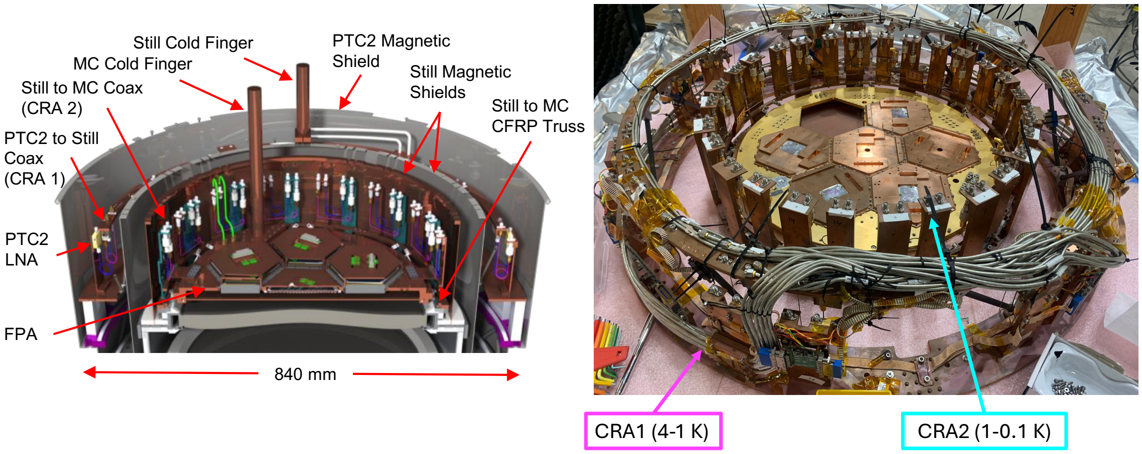

Figure 5.18. The two cold readout assemblies (CRAs). Left: Solidworks image of the two CRAs installed inside SAT-MF1. Right: CRA1 and CRA2 on the benchtop, together with the focal plane and the dummy wafers.

SAT-MF1 and after integration, a series of electrical "health" checks need to be carried out. These checks include grounding and DC probing (so continuity and shorts to ground check), biasing the amplifiers, and finally checking the RF transmission. See SO-RD-READ-014 for the full DC and RF validation procedure. This section focuses on the RF transmission health check, going over the model's formulation and the criteria for the health check.

To create a model that predicts the transmission of the full RF chain, I modeled the gain and loss of all the components inside a typical chain and created databases of principal components such as the low noise amplifiers (LNAs). The components inside an RF chain can be broken down into three categories: invariant in temperature space (e.g. SMA bulkhead or connector savers), database building (e.g. LNAs and isolators), and coaxes. The first type, invariant in temperature space, either has insertion loss as a constant in both frequency and temperature space (e.g. attenuator with fixed loss) or the typical loss is so small over the operational frequency range (4-8 GHz) such that any possible variation in temperature space would be negligible in the overall transmission calculation in units of dB. Components that fall into this category just use their loss from the datasheets. As for SMAs, the loss is modeled as transmission [dB] = $-0.03\sqrt{\nu}$, where ν is in units of GHz and the negative indicates loss.

The second category constructs a transmission model based on pre-existing databases. The components that fall into this category vary in both temperature and frequency space and there are sufficient measured data of these individual components at room temperature and at a cryogenic temperature such that I can just assume a naive model based on the measurements. Isolators and LNAs fall into this type. There are loss data from the manufacturer at two temperature ends in the frequency space: S(ν, T_1) and S(ν, T_2) in the GHz range. I then assumed that the transmission in dB varies linearly in the temperature space such that the slope is

$$m = \frac{S(\nu,T_2) - S(\nu,T_1)}{T_2 - T_1}, \tag{5.3}$$

and the intercept is

$$b = S(\nu,T_1) - mT_1. \tag{5.4}$$

So the complete equation to model this category is

$$Transmission[dB] = -(mT + b) = -\left(\frac{S(\nu,T_2) - S(\nu,T_1)}{T_2 - T_1} T + S(\nu,T_1) - mT_1\right). \tag{5.5}$$

All the SATs use LNAs from Low Noise Factory (LNF) for amplifiers at the PTC2 stage. These amplifiers have measurements at both room temperature and 4 K, such that one can create a database of them as more are being purchased and used inside the telescopes. The 40 K amplifiers are manufactured by our collaborators at Arizona State University (ASU). These LNAs were measured by ASU for their gains in a dedicated cryostat; thus they have measurements at 300 K and 60 K.

Finally, the third category is the modeling of transmission loss from coaxes. Two sources contribute to the insertion loss of a coax: loss due to the dielectric's loss tangent and loss due to the metals in the inner and outer conductors. The following formulation follows closely the one here[8]. The loss per length due to the dielectric's loss tangent can be modeled as

$$\alpha_D[dB/m] = 92.0216\sqrt{\varepsilon_R} tan(\delta)\nu, \tag{5.6}$$

where ε_R is the dielectric constant, tan(δ) is the loss tangent, and ν is the frequency in units of GHz. Note that α_D is negative as it is transmission loss. SAT-MF1 uses coaxes from CoaxCo, thus the dielectric is PTFE (Teflon). According to [52] and [53], ε_R is assumed to be 2.1 and constant in both temperature and frequency space. As for the loss tangent of Teflon, [52] measured it to be between 2-6 x 10^{-6} from 30-90 K at 18.92 GHz, and [53] gets a mean value of 3.66 x 10^{-6} scaled to 6.5 GHz at 4.2 K. So to model the loss tangent, I utilized the measurements from DuPont™[9] at room temperature to get the information from 2-10 GHz since the operational frequency range is from 4-8 GHz. Then once the dielectric is past a critical temperature (e.g. 90 K), assume tan(δ) = 3.66 x 10^{-6}. So for the temperature between 300-90 K, I assume that the loss tangent varies linearly as a function of temperature.

The second source contributing to the coax transmission loss comes from the metals in the two concentric conductors. The loss due to metal can be modeled as

$$loss[dB/m] = \frac{8.686}{2Z_0}\sqrt{\frac{\mu_{metal}}{\pi}}\left(\frac{1}{D}+\frac{1}{d}\right)\sqrt{\nu\rho}, \tag{5.7}$$

where Z_0, D, d, and μ_{metal} are the characteristic impedance in Ohms, the diameter of the outer and inner conductor in meters, and the permeability of the metal in H/m. These parameters can be taken from the coax's data sheet and the typical properties of the metal alloys. ν is the frequency in Hz and ρ is the resistivity in Ohms-meter. The Wiedemann-Franz law states that

$$\frac{k}{\sigma} = k\rho = LT, \tag{5.8}$$

---

[8] https://www.microwaves101.com/encyclopedias/coax-loss-calculations

[9] https://wiki.epfl.ch/thz/documents/Materials%20and%20Measurements%20-%20DuPont%20-%20Feb2015.pdf

where k is the thermal conductivity, σ is the electrical conductivity or the inverse of the resistivity, and L is the Lorenz constant. T is the temperature. Thus in Equation 5.7, only ρ varies with temperature. I took a two-prong approach to model $\rho(T,\nu)$, both of which rely on loss data from the manufacturer as a comparison and sanity check for the validity of the model. Three different alloys of coaxes are used inside SAT-MF1: copper-nickel (CuNi), copper, and niobium-titanium (NbTi), which all come from CoaxCo. Due to the limited loss data and/or thermal conductivity data of Cu and NbTi, the following formulation focuses on CuNi. Treatment for these two will be covered at the end of this section. The first approach uses the resistivity of the coax's metal found in the literature and calculates the loss directly. Unfortunately, the calculated loss did not yield comparable results to the data from the manufacturer at room temperature and 4 K. The second approach utilizes the thermal conductivity and loss data at cryogenic temperature for CuNi from CoaxCo to get the resistivity through the Wiedemann-Franz law. Through this method, I found that ρ does not vary a lot from 4-8 GHz at 4 K. Assuming this same behavior across different temperature stages, $\rho(T,\nu)$ becomes $\rho(T)$. Thus, with the loss data from CoaxCo for CuNi at 300 K and 4-1 K, the full profile of $\rho(T)$ can be extracted, completing the transmission model for loss due to metal.

5.3.2 RF Check Criteria

Using the model and the measured data, I established specific passing criteria for the URH, CRA standalone assemblies, and the full system (URH+CRA). These passing thresholds are determined to be within 1σ of the model-predicted values, with σ derived from analyzing the discrepancy between the model and the measured transmission data inside SAT-MF1 and the LAT receiver. Additionally, I considered the repeatability between cooldowns, where differences typically range around 1 dB or less for the full system. Figure 5.19 and 5.20 show the comparison of the model against the URH's transmission measurement on the benchtop and during a cooldown, respectively. The residuals, or the differences between the predictions and the measurements, are plotted for a single chain and for all chains. Most residuals center around

0.5 dB in both warm and cold cases, illustrating the model's accuracy against the data. Moreover, I have tested this model against the CRA and the residuals remain within a similar range as the URH. This information serves as the foundation for determining pass/fail criteria for future cooldowns inside other SATs and the LAT receiver (LATR). As one of the earliest receivers to install fully/partially populated readout chains, SAT-MF1 spearheaded the testing and validation phase, establishing a standard for comparison. In this case, the model facilitates formulating passing criteria for RF health checks in other testbeds across the collaboration.

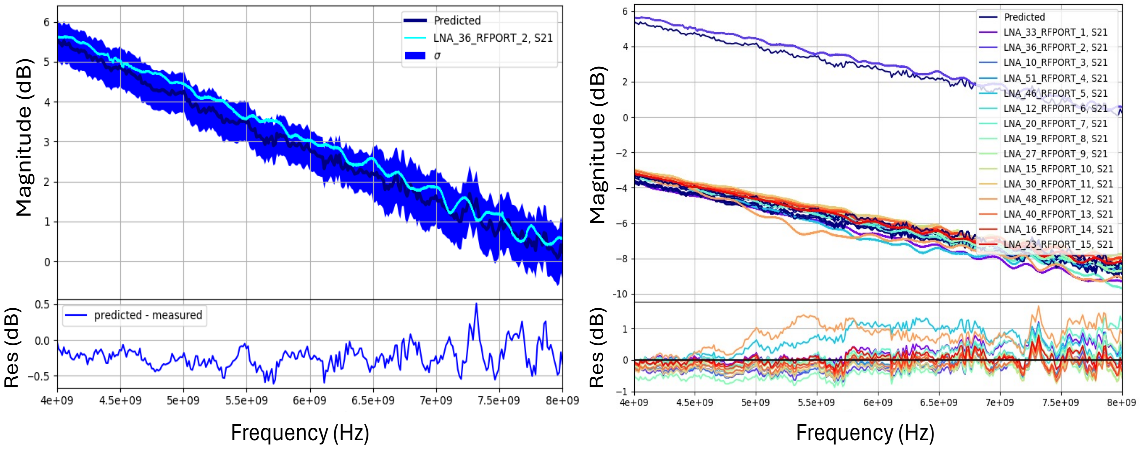

Figure 5.19. URH warm transmission measurement against the model. Left: transmission measurement in dB for chain 2 of the URH. Cyan and dark blue solid lines are measured and modeled, respectively. The blue σ spread indicates the passing criteria, which are 0.5 dB for $4 \leq \nu \leq 6.5$ GHz and 0.7 dB for $6.5 \leq \nu \leq 8$ GHz. The difference between the model and the measurement lingers between -0.5 and 0.5 dB. Right: All 15 chain measurements and their residues when compared against the model. Most residues are < 1 dB.

The pass criteria for standalone assemblies such as the URH and CRA is

$$\sigma = \begin{cases} 0.5\text{dB} & 4 \leq \nu < 6.5\text{GHz} \\ 0.7\text{dB} & 6.5 \leq \nu \leq 8\text{GHz} \end{cases} \tag{5.9}$$

For the full system, the passing criteria were also determined in a similar style to the one for the URH and CRA. I have also sourced measurements from the LATR to provide more

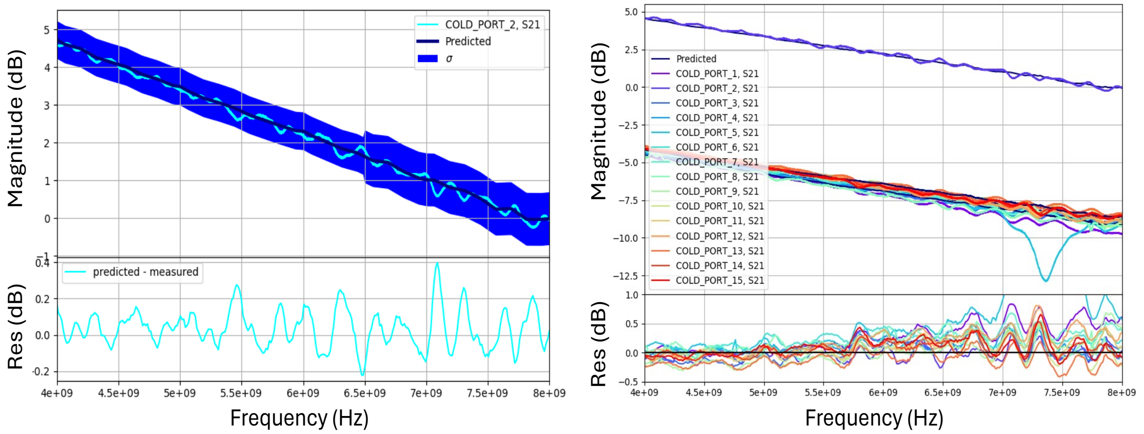

Figure 5.20. URH cold transmission measurement against the model. The large dip in chain 5 was due to a loose connector, which was then found and fixed based on this test result. Most of the residuals are between -0.5 dB and 1 dB.

comprehensive pass/fail criteria. The criteria for the full system is

$$\sigma = \begin{cases} 1.0\text{dB} & 4 \leq \nu < 6.5\text{GHz} \\ 1.5\text{dB} & 6.5 \leq \nu \leq 8\text{GHz} \end{cases} \tag{5.10}$$

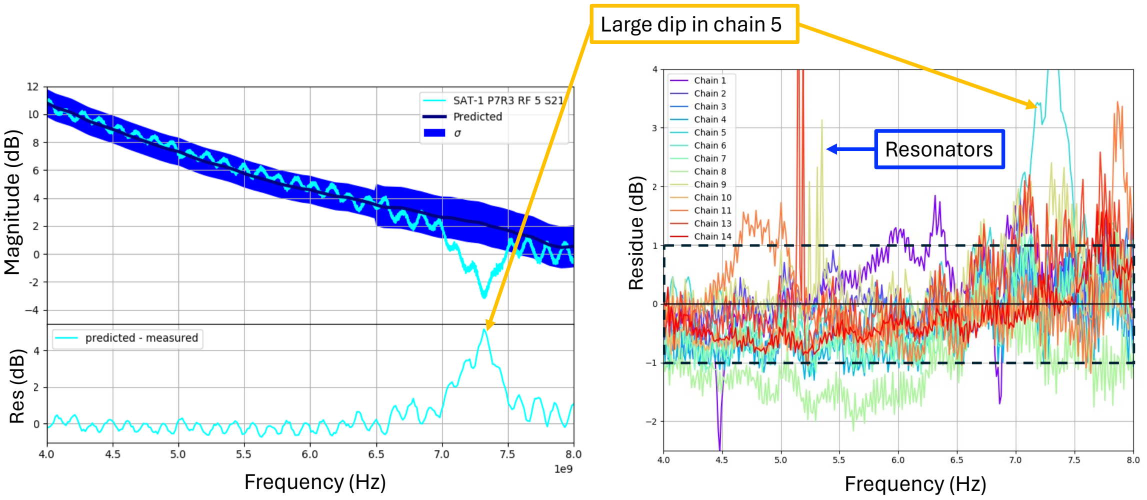

Figure 5.21. Full readout system (URH+CRAs) cold transmission measurements against the model. Left: measurement for a chain 5 against the model. This figure illustrates an example of a bad working chain. We later fixed the large dip in this chain. Right: residue plot of all the chains. Most of the chains' residues center around -1 to 1 dB, validating the model and also serving as a foundation to determine the passing criteria for future cooldowns and other SATs. The narrow dips in the residues were from resonators.

Note that this is the passing criteria for a full system cold. For the warm side, more studies are needed to refine the model. Figure 5.21 portrays an example of a bad chain where there was a dip outside the criteria. This dip came from a loose connection on an SMA connector, which was later fixed. The right plot of this figure shows the residuals for all 14 chains inside SAT-MF1, showing that most residuals are within -1 to 1 dB difference. The narrow lines that spike beyond this range come from detectors with resonators on a couple of chains. The standing waves seen in the measured data are most likely due to small and acceptable impedance mismatches in the system, which the model does not account for.

The criteria define the baseline performance of an RF chain within a readout system; however, failure to meet the criteria, fully or partially, does not automatically guarantee that the chain is non-functional. Dips in the transition would not affect detector biasing; however, they do affect readout noise. The noise is a function of the power integrated over each resonator. Thus, depending on the size of the dips, we may not be able to optimize the noise for the readout channels that fall within the dip. For example, the dip in Figure 5.21 is a serious case, where investigation was required and the system was fixed.

Chapter 5, in part, has been submitted for publication of the material to The Astrophysical Journal Supplement Series, 2024. Nicholas Galitzki, Tran Tsan, Jake Spisak, Michael Randall, Max Silva-Feaver, Joseph Seibert, Jacob Lashner, Shunsuke Adachi, Sean M. Adkins, Thomas Alford, Kam Arnold, Peter C. Ashton, Jason E. Austermann, Carlo Baccigalupi, Andrew Bazarko, James A. Beall, Sanah Bhimani, Bryce Bixler, Gabriele Coppi, Lance Corbett, Kevin D. Crowley, Kevin T. Crowley, Samuel Day-Weiss, Simon Dicker, Peter N. Dow, Cody J. Duell, Shannon M. Duff, Remington G. Gerras, John C. Groh, Jon E. Gudmundsson, Kathleen Harrington, Masaya Hasegawa, Erin Healy, Shawn W. Henderson, Johannes Hubmayr, Jeffrey Iuliano, Bradley R. Johnson, Brian Keating, Ben Keller, Kenji Kiuchi, Anna M. Kofman, Brian J. Koopman, Akito Kusaka, Adrian T. Lee, Richard A. Lew, Lawrence T. Lin, Michael J Link, Tammy J. Lucas, Marius Lungu, Aashrita Mangu, Jeffrey J McMahon, Amber D. Miller, Jenna E. Moore, Magdy Morshed, Hironobu Nakata, Federico Nati, Laura B. Newburgh, David V. Nguyen, Michael D.

Niemack, Lyman A. Page, Kana Sakaguri, Yuki Sakurai, Mayuri Sathyanarayana Rao, Lauren J. Saunders, Jordan E. Shroyer, Junna Sugiyama, Osamu Tajima, Atsuto Takeuchi, Refilwe Tanah Bua, Grant Teply, Tomoki Terasaki, Joel N. Ullom, Jeffrey L. Van Lanen, Eve M. Vavagiakis, Michael R Vissers, Liam Walters, Yuhan Wang, Zhilei Xu, Kyohei Yamada, and Kaiwen Zheng. The Simons Observatory: Design, integration, and testing of the small aperture telescopes, 2024.

Chapter 6

SO SAT-MF1 Site Commisioning

The first SO SAT, SAT-MF1, successfully finished in-lab testing at UCSD. All the subsystems of the SAT were integrated and passed testing requirements. SAT-MF1 started integration and testing in June 2019 when the SAT vacuum vessel first arrived and finished in March 2023. Then it passed the pre-ship review before shipping to Chile. SAT-MF1 arrived in Chile in July 2023 and started its first phase of site integration and commissioning. This chapter describes the integration at the site for SAT-MF1 and the thermal tests I did. Finally, the chapter ends with a future outlook and future commissioning plans for SO SAT.

6.1 SAT-MF1 Deployment

Upon arrival at the site, the SAT DR was tested with the 20 m lines in its dedicated test cryostat to ensure that the DR refrigeration unit was working. With 30 mW on the Still stage, the DR provided 510 μW at 100 mK on the MC stage, suggesting a 7% decrease in cooling capacity in comparison to the initial validation at UCSD with the 2.5 m lines. The result is consistent with the revalidation at UCSD. Then it was integrated into the SAT and the entire SAT-MF1 underwent a cooldown inside the site highbay to do a brief overall system check after shipping. These tests include full system operation with the CHWP spinning, detectors and readout performance, and cryogenic or thermal checks. Once we confirmed the SAT was operating as expected based on our laboratory tests, we started installing it onto the platform.

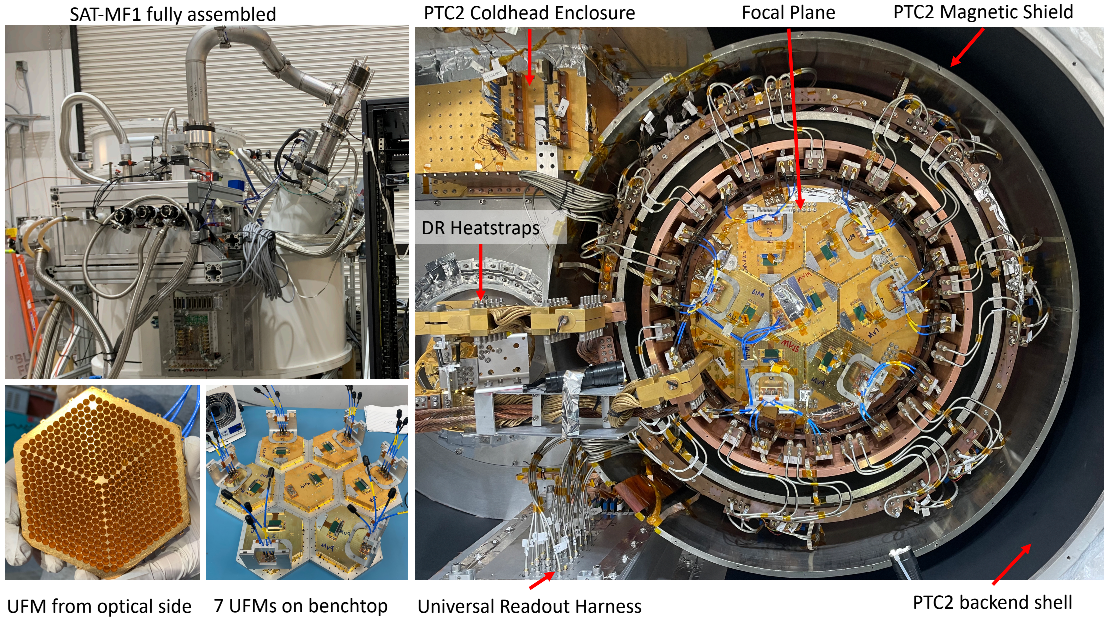

Figure 6.1. SAT-MF1 fully assembled inside the site highbay. Top left: outside view of the whole telescope with all the vacuum hoses and electronics. Bottom left: Pictures of the UFMs on the benchtop. Right: view of the backend with the fully 7 detector wafers installed onto the FPA.

The two cooldown names associated with these cooldowns are site cooldown run 1 (SCR1) (lab highbay) and SCR2 (on the platform). Figure 6.1 shows images from the SAT integration inside the site highbay. The top left picture shows the outside view of the telescope fully assembled with all its hoses and electronics. The right side shows the backend view with the 7 UFMs installed inside the focal plane. Then Figure 6.2 shows SAT-MF1 mounted on its platform with the forebaffle and comoving shield installed. During the first cooldown (SCR1), all the subsystems operated successfully, with the CHWP spinning and most of our enclosures for our electronics installed in a preliminary configuration that emulated their setup on the platform. The run validated some of the new cryogenic components inside the CHWP assembly. In terms of detectors and readout performance, we were able to bias 5112 detectors and demonstrated that they have nominal noise properties. With each SAT composed of about 10,000 detectors, this was about 50% yield, an overall low yield that was expected for this first-light instrument but will be increased with a detector retrofit later in 2024. The next section 6.1.1 outlines the thermal results for the two first runs at site: SCR1 and SCR2. For the run outside on the platform, we successfully installed all the electronics and vacuum enclosures. Operation on the platform to scan at different elevations, azimuth, and boresight angles went smoothly. The left side of Figure 6.2 shows SAT-MF1 doing a test scan in elevation and azimuth in preparation for a planet scan. A later run (SCR3) demonstrated the CHWP spinning at different elevations and azimuth.

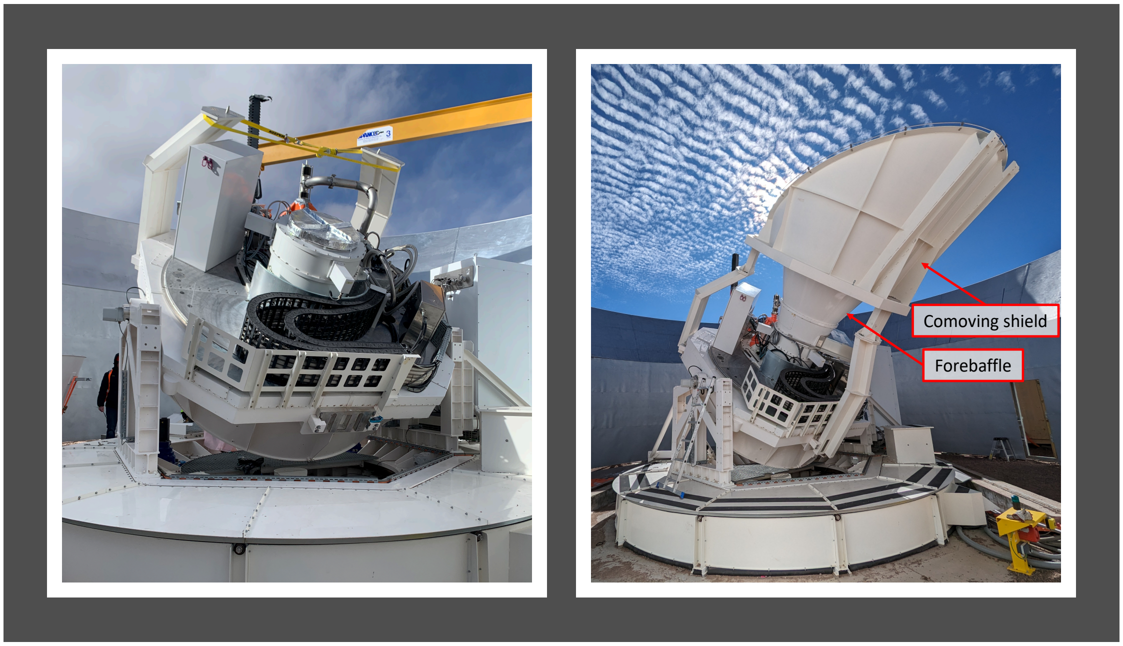

Figure 6.2. SAT-MF1 mounted on its platform. Left: The SAT with all the cables and electronics installed onto its platform. Here SAT-MF1 was doing a test run in rotating in azimuth, elevation, and boresight in preparation for a planet scan. Right: The SAT with the forebaffle and comoving shield installed. The right image is a courtesy of Nicholas Galitzki.

6.1.1 Thermal Test

Table 6.1. Loading estimates for the 40 and 4 K at the observation site. SCR1 is the first cooldown inside the site highbay, with SAT-MF1 fully integrated.

Cooldown	PTC $P_{1,est}$ (W)	PTC $P_{2,est}$ (W)	DR $P_{1,est}$ (W)	DR $P_{2,est}$ (W)
SCR1	44.6 ± 0.9	0.41 ± 0.04	49.2 ± 0.9	0.47 ± 0.02
SCR2	20.8 ± 0.8	0.387 ± 0.012	32.6 ± 1.1	0.85 ± 0.05

Temperatures for SCR1 and SCR2 were measured and used to extract the loading value on the PTC stages. The same method as the one used in Chapter 5.1 applies here. Table 6.2

outlines the loading extracted for the PTC and DR PTC. The load estimates for SCR2 were lower by almost 20 W and 0.1-0.3 W on the first and second stages, respectively. The corresponding temperature changes were 5 K and $\sim$ 0.4 K, respectively. The setup inside SAT-MF1 remained the same between the two cooldowns, so the difference in loads may be part of a diurnal effect. Unfortunately, we did not have a thermometer setup inside the lab highbay. However, our weather station contains two thermometers: one inside a container and part of the weather station module, while the other one is bolted to a pole on top of the same container. Looking at the history of the temperature readout, the inside ambient temperature fluctuated between 2-20 C (so room temperature). The outside ambient temperature during SCR2 fluctuated from 2-5 C. Previous in-lab testing suggested that a change in 10.6 C led to a change of 0.6 K, and thus a 3 W increase in PTC1 power. The weather station's values imply that there was about a 20 C difference, which should only lead to 1 K and 9 W increase in power. This estimation seems consistent with P10R2 PTC1 values in Table 5.1, but not SCR1. Hence, there may be other contributions to SAT-MF1 seeing a higher load on SCR1; which seems to go away in SCR2. Moreover, the loads extracted for SCR2 align much closer with the predictions in Table 6.3 for both PTC stages than previously measured.

Table 6.2. Loading estimates for the Still and MC at the observation site. The power difference between the two may partially be due to the diurnal effect. So the telescope was inside a heated highbay, so around 20 C. SCR2 was the cooldown on SATP on a snowy night at 0.3-4 Celcius. Thus DR PTC was at a lower base temperature in comparison to SCR1, such that it precooled the mix slightly more efficiently. The base temperature of the Still and MC with no applied loading on any of the stages were (0.72, 0.05) K for SCR1, respectively. (T_{Still}, T_{MC}) = (0.65, 0.047) for SCR2, which was taken after the DR load curves finished and the temperature had stabilized. In terms of temperature, they did not differ too much on the MC stage. Moreover, the estimated power on both stages are almost within one error bar of each other.

Cooldown	Still P_{est} (mW)	MCP_{est} (μW)
SCR1	1.2 ± 0.6	54 ± 5
SCR2	1.0 ± 0.4	39 ± 9

Sparse sets of DR load curves were also carried out during these two cooldowns to first re-validate the cryogenic performance of the DR and second examine the change in cooling power with SAT-MF1 on its platform. The SCR2 DR load curve was taken over a snowy night, with the outside ambient temperature ranging from 0 to 4 Celcius. The night test would better describe telescope's thermal environment when observing at night. Table 6.2 outlines the DR estimated loads for the two cooldowns. Both stages' loads are almost within 1 error bar of each other, with SCR2 experiencing lower loads. This may be due to the DR PTC seeing lower loads than it previously had, improving the precooling process of the mix circuit slightly and leading to a lower load estimate.

Table 6.3. Predicted and measured loadings for each temperature stage of SAT-MF1 Site Edition. The predictions and cooling capacity are the same as in Table 5.3; however, the measured loads come from the run that SAT-MF1 is installed onto the SATP. The colder outside ambient temperature decreased the PTC temperatures, which contributed to the lower PTC measurements. They align with the predictions. Load on the MC stage remains higher than expected but is still within acceptable range.

Stage (K)	Predicted Load (W)	Measured Load (W)	Cooling Capacity (W)
PTC1 (45)	19.61	20.8 ± 0.8	50
PTC2 (4.2)	0.579	0.387 ± 0.012	1.80
Still (1.0)	4.7×10^{-3}	$(1.0 \pm 0.3) \times 10^{-3}$	25×10^{-3}
MC (0.1)	25.15×10^{-6}	$(39.9 \pm 10.6) \times 10^{-6}$	400×10^{-6}

In summary, the thermal estimates for SAT-MF1's four stages are described in Table 6.3. The PTC and Still stage are within or very close to expectations. MC load is still higher than predicted; however, we have enough cooling capacity that this higher load is not a concern.

6.1.2 Thermal vibration pickup during scans

The in-lab testing done at UCSD as detailed in the previous chapter suggests possible resonant modes and the corresponding thermal fluctuation that SAT-MF1 may experience during observation scans. As shown in Figure 5.15, the most dominant mode would cause about 0.9 mK of thermal fluctuation on the focal plane. Note that the focal plane temperature was not regulated during these tests and the base temperature of the FPA was $\sim$ 55 mK. The analysis predicted that vibrational heating from operating the SAT on the platform would be minimal such that it can be regulated with a temperature-controlling program using PID. This has proven

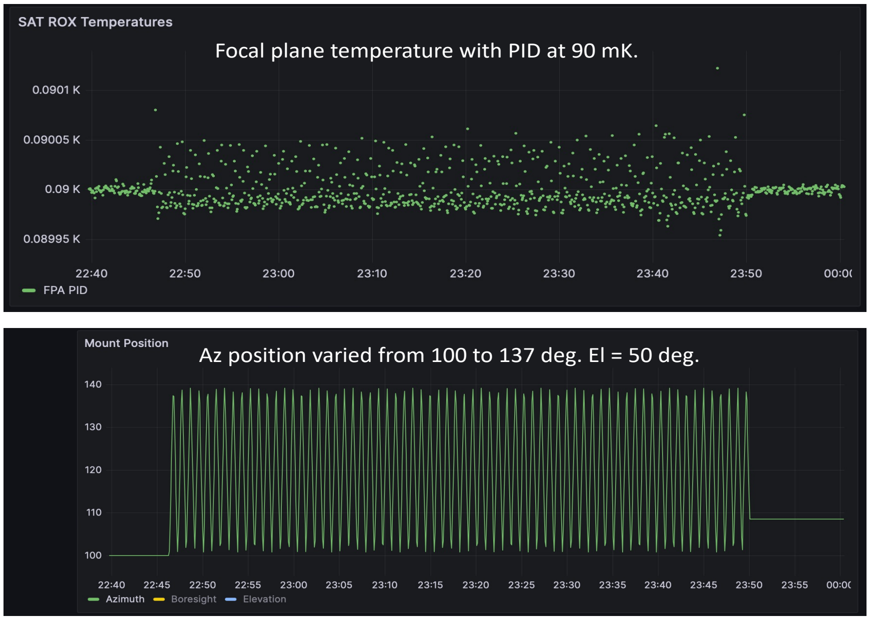

Figure 6.3. Temperature of the focal plane during a CMB scan. Top: the focal plane temperature was regulated at 90 mK using PID. Bottom: The position of the telescope as it varied in azimuth from 100° to 137° at a fixed elevation of 50°.

adequate as the SAT started observation scans on the SATP. Figure 6.3 displays the temperature of the focal plane during a CMB scan. The top picture is a snapshot of the FPA temperature in the live monitor. We had the FPA regulated to be at 90 mK using a PID loop. The bottom picture shows the position of the telescope as it changed from 100° to 137° in azimuth position at a fixed elevation of 50°. From this figure, the scan started around 22:46 UTC on 11/13/2023. The largest temperature spike during a turnaround (e.g. when the telescope switched direction or changed in acceleration) occurred at 90.1 mK, suggesting that dT $\sim$ 0.1 mK. The scan speed for this CMB scan was 1.5°/s. The SATP scan during the factory acceptance test that I used for the analysis had a scan speed of 1°/s at an elevation of 50° for a full azimuth scan from 0-360°. This suggests that thermal heating due to vibration during an observation scan is well-regulated with the current setup inside the telescope.

6.2 Discussion and Future Outlook

We have validated the SAT in lab and demonstrated that it meets the operational requirements at the site. SAT-MF1 has successfully reached base temperature on all stages and remains within the thermal budgets. After almost 4 years of in-lab testing, SAT-MF1 achieved its first light in October 2023, a major milestone that required enormous effort from everyone in the instrumentation and analysis group and the site team. All the subsystems such as the forebaffle and co-moving shield completed their installations (see Figure 6.2). The SAT has undergone commissioning observations since then and has a commissioning review in June of 2024. After completion of that review, it will start initial science operations and undergo a detector retrofit later in 2024 to improve the detector yield. As part of commissioning, SAT-MF1 made many planet and CMB observations, which were used for instrument characterization and calibration. One such calibration involves decomposing the SAT's beam using planet scans to establish a gain factor, which can then be used to convert raw data in unit proportional to the detectors' current to physical units such as Kelvin. This is the same calibration method that I studied and used for the Simons Array in Chapter 7. Together with SAT-MF1, the other two SATs have deployed and are currently integrating at site and transitioning to the commissioning phase. The three SATs will begin full CMB observations in this calendar year.

Chapter 7

The Simons Array (SA)

This chapter describes my beam reconstruction and gain calibration work for another ground-based CMB experiment, the Simons Array. The project centers around forming a gain model using planet data to calibrate the raw data. The chapter starts with an overview of SA and the Paul Simons Telescope that holds the POLARBEAR-2b (PB-2b) as its receiver in section 7.1. Then, section 7.2 details the formulation behind the gain model, followed by the beam reconstruction and gain model development using PB-2b data in section 7.3. Finally, section 7.4 provides a summary and future outlook for PB-2b.

7.1 Overview of SA

The Simons Array (SA) is a current ground-based CMB experiment located at the Atacama Desert in Chile, the same observation site as the Simons Observatory. SA aims to search for degree angular scale CMB B-mode polarization from inflationary gravitational waves and characterize arcmin angular scale B-modes from weak gravitational lensing. SA contains three identical telescopes, two currently coupled to their cryogenic receivers with heritage in the POLARBEAR experiment. The receivers are POLARBEAR-2a (PB-2a) and PB-2b; they observe in the 95 and 150 GHz bands. Figure 7.1 illustrates a picture of the site (top right) and 3D CAD models of the telescope (left) and PB-2b receiver (bottom right). The three telescopes are identical and line up from north (Nicholas Simons) to south (Paul Simons) in almost a straight line. The telescopes follow an off-axis Gregorian Mizuguchi-Dragone design with a 2.5-meter parabolic primary mirror and a 1.3-meter elliptical secondary reflector. A ring shield, composed of 8 separate panels on the primary reflector, deflects any spillover or ground reflection to the sky [54]. With this ring shield, the total diameter of the primary comes up to 3.5 m. This diameter (2.5 m) leads to an angular resolution of 5.2 and 3.5 arcmin for the 95 and 150 GHz band, respectively [55]. The field of view (FOV) of the telescope is 4.8° [55].

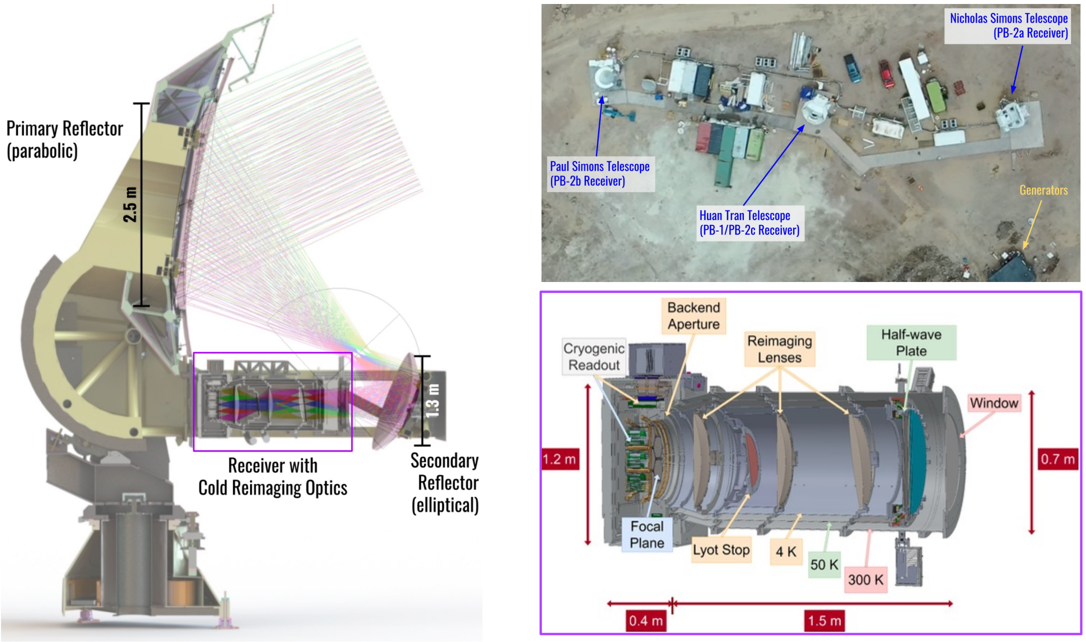

Figure 7.1. SA observation site and 3D CAD models of the telescope and receiver. Top right: a top-down view of the SA observation site in Chile, with the three telescopes highlighted. The left picture shows a CAD model of the telescope with the ray tracing from Fred Matsuda, and the bottom right is a cross-section of PB-2b with its principal components called out. Figure adapted from [54, 56].

7.1.1 PB-2b Optical and Cryogenic Design

The POLARBEAR-2b or PB-2b, the second receiver to be installed, achieved first light in early 2023. The receiver contains two main sections: the optics tube that makes up the frontend and the backend that contains the focal plane. The bottom right of Figure 7.1 portrays a cross-section view of the receiver model in Solidworks. Similarly to the SAT, PB-2b is also nested with aluminum shells at different temperature stages to lower the heat transfer between the stages and the heat loads that the coldest stage would see. The optics tube consists of the window at room temperature, a cryogenic half-wave plate, an alumina IR filter at 50 K, and three AR-coated alumina lenses at 4 K [56]. The lyot stop, which helps reduce stray lights, is placed at 4 K to reduce its optical load on the detectors. The backend of the receiver contains the focal plane and 7588 dichroic Al-Mn TES bolometers that are sensitive to two polarization directions in the 95 and 150 GHz bands [55].

PB-2b uses two pulse tubes (PT415 from BlueFors) to cool down to 4 K. One PTC provides cooling power to the optics tube, and the other one cools the backend. To limit the thermal noise that the detectors see below the photon noise from the atmosphere, the focal plane temperature has to be less than 0.3 K, slightly higher but similar to SAT-MF1's bath temperature (0.1 K). Different from SAT-MF1, PB-2b uses helium adsorption refrigerators from Chase Research Cryogenics[1] to get to the sub-kelvin temperature [56]. The fridges use evaporative cooling of ^3He and ^4He to achieve a bath temperature of 0.25 K.

7.1.2 Lenslet Sinuous Antenna Detectors

Each PB2 receiver contains a focal plane with seven hexagonal silicon wafers, totaling 7588 TES bolometers or equivalently 271 pixels. The bolometers used for SA are similar to the ones described for SO in section 2.3, through the negative electrothermal feedback during the detector's in transition phase. SA, however, utilizes lenslet arrays to optically couple to the detectors instead of the OMT-coupled detectors that SAT-MF1 uses.

Beneath the lenslets lie the sinuous antenna (the black signal in the middle of Figure 7.2), which is a "broadband antenna with a log-periodic design" [54] sensitive to two polarization directions. As incoming light hits the antenna, it separates the signal into two orthogonal polarizations. The signals then pass through the micro-strip filters and separate into either a 95 or 150 GHz band. Finally, the TES bolometers at the edge detect the separated signals. There

---

[1] Chase Research Cryogenics Ltd. 2 Albion Works, Savile Street, Sheffield S4 7UD, United Kingdom.

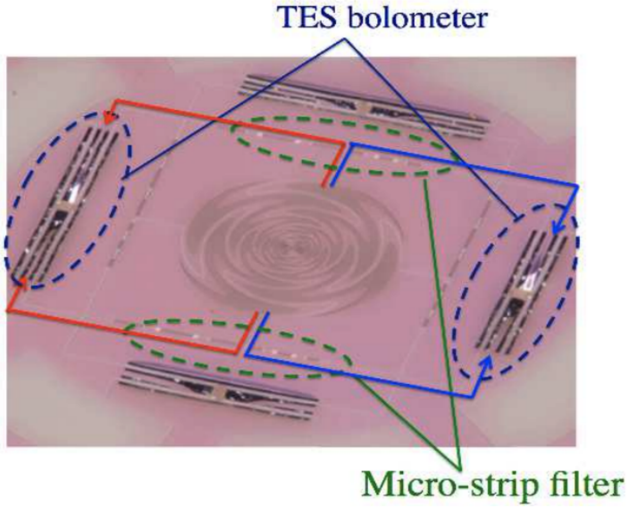

Figure 7.2. Sinuous antenna detectors for SA. The sinuous antenna (middle) separates the signal into two orthogonal polarization directions. The micro-strip filters then further separate the signal into two frequency bands: 95 and 150 GHz. Finally, the TES bolometers at the end detect the separated signals. This figure is taken from [55].

are four optical TES bolometers, forming a rectangular shape around the antenna in the figure.

7.1.3 DfMux Readout

SA employs frequency division multiplexing to read out thousands of detectors on a single pair of wires for the same reason as SO: better cable management and less conductive loads with fewer numbers of required cables. There are two types of frequency division multiplexing used in current CMB experiments: μmux (Section 2.3.2) and digital frequency-domain multiplexing (DfMux). SA uses DfMux for its readout system, similar to what the South Pole Telescope (SPT-3G) used. Figure 7.3 illustrates a circuit diagram for DfMux for a multiplexing factor of N=40, reading out 40 detectors on a single chain. This figure is taken from [54].

In this readout scheme, each TES (represented by $R_{TES,i}$) is in series with an LC resonator that has a unique resonant frequency within the 1.6-4.5 MHz range [54]. Then, N detectors are set up in parallel. All the resonators have the same inductance, L = 60 μH, but they vary in capacitance to form a distinct resonant frequency: $\nu_0 = \frac{1}{2\pi\sqrt{LC}}$. The detectors and resonators are at 250 mK, the temperature that puts the detectors in transition under a constant voltage bias.

Each "comb" or set of RLC circuits has one SQUID to amplify and read out the detectors. Since N = 40, each SQUID reads up to 40 channels per comb. As shown in the figure, the SQUID is at 4 K as indicated by the inductor L_{in}, while the electronics to probe and acquire data are at room temperature.

During operation, room-temperature electronics send out a signal, $I_{carrier}$, that contains multiple bias tones to probe individual resonators. As the TESs absorb optical power from an incoming light, they module the tones' amplitude due to the change in TES resistance. The tones or current coming from the detectors are then summed and nullified by I_{nuller} from DAC in a process called digital active nulling (DAN). DAN applies inverting feedback with the content of each resonant frequency, $f_{0,i}$ where i indicates the i-th detector, and f_{sky}. In the absence of a sky signal, I_{nuller} is the inverse of $I_{carrier}$. However, with the sky signal, the SQUID would then amplify this difference between the original nulling signal and the bolometer's signal and deliver

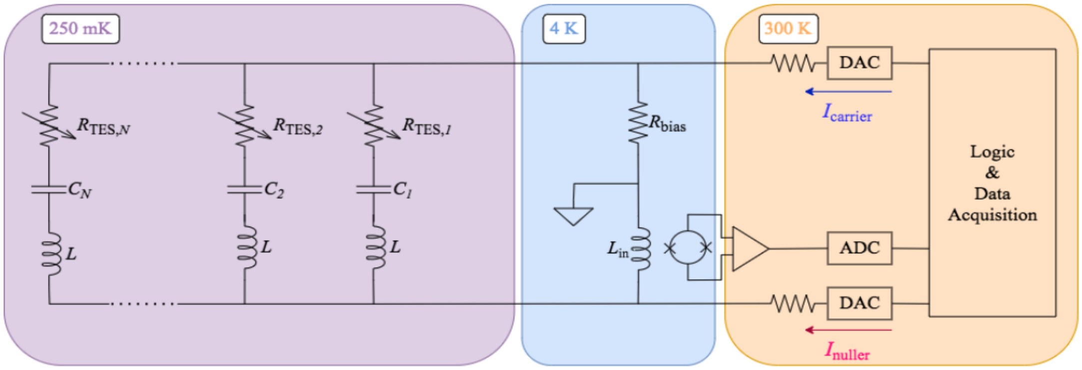

Figure 7.3. Digital frequency-domain multiplexing (DfMux) circuit diagram. Each TES is in series with an LC resonator with a unique resonant frequency, thus dividing N detectors across the frequency space from 1.6 to 4.5 MHz. The set of detectors and resonators represent one comb and they are at the mK stage. The SQUID, indicated by L_{in} in the circuit, amplified the output signal and it is located in the 4 K stage. A probe tone, signified by $I_{carrier}$, is sent from the room temperature electronics and carries multiple bias tones that correspond to each resonator. As TESs absorb optical power from the sky, they module the tones' amplitude. The tones are then summed up and nullified by an I_{nuller} from the DAC. The difference between the nuller signal and the bolometer signal is amplified by the SQUID before delivered to the room-temperature electronics. The signal is then modulated and used to adjust the nulling signal to cancel out the bolometer's signal completely. Measurement of the nulling signal during this process would then determine the magnitude of the sky signal. This figure is adapted from [54].

it to the electronics at room temperature. Inside the electronics, there is a comb of demodulators that would adjust and generate "a slow modulation envelope corresponding to f_{sky}" and cancel out the bolometer's signal [57, 56]. The measurement of this adjustment or demodulation to the nulling current then determines the magnitude of the optical signal.

7.2 Gain Calibration Overview

Data taken from the sky needs to go through several calibration steps before it can be reconstructed into CMB maps and power spectra for scientific analysis. Due to the telescope's diffraction-limited optics that constrain the spatial resolving power of the instrument, the measured data is a convolution of the sky signal and the instrument's beam. Thus, we need to understand the beam profile well to calibrate the raw data. One crucial calibration involves using the beam information to create an initial gain model and convert the raw data into temperature units.

When a bolometer observes a sky signal, it manifests as a current change in the TES circuit, which can be detected as a flux variation in the SQUID. The SQUID then acts as an ammeter to amplify and read out the signal using an operational amplifier (OpAmp) circuit and an analog-to-digital converter (ADC). Hence, the time-ordered data (TOD) from a TES bolometer is often recorded in uncalibrated units called ADC counts. To get to CMB maps, we need to convert the raw data in ADC to a physical unit such as Kelvin, and the multiplicative ratio between ADC counts and Kelvin temperature is called "gain" [58]. Hence, we call this process the gain calibration. The gain can be defined as

$$g_{\frac{ADC}{K}} \equiv -\frac{\partial I}{\partial T}, \tag{7.1}$$

where I is the current from the bolometer in ADC counts and T is the temperature in Kelvin. The negative sign accounts for the negative electrothermal feedback mechanism when the bolometer is in transition, which causes an inverse relationship between the current and optical power. This way, the gain is positive. Using this gain, we can then convert the TOD from ADC to Kelvin:

$$\text{TOD [Kelvin]} = \frac{\text{TOD [ADC]}}{g_{\frac{ADC}{K}}} = \text{TOD [ADC]} * g_{\frac{K}{ADC}} \tag{7.2}$$

Calibrations can be broken down into relative and absolute calibrators. For absolute calibration, one can co-add all the power spectra and then compare them against other experiments' data such as Planck's spectra. We can fit the difference between our measurements and Planck's to investigate how much the gain should change to minimize the difference. This measurement is often done using the C_l^{TT} spectra. As for relative gain calibration, we must account for both time-relative and focal-plane relative gain. Time-relative calibration tracks how the gain changes as a function of time, which is good for co-adding maps across different observations. Focal plane relative calibration relates the gains from different detectors across the focal plane to co-add them into a single map.

A stationary thermal source is a good option for a time-relative calibrator as it can be observed for a short time scale (e.g. $\mathcal{O}$(minutes)) and at any point in time. PB-2b uses a stimulator, which is a chopped thermal source located behind the secondary mirror. However, the intensity of the stimulator varies across the focal plane, so we cannot use it as a focal plane relative calibrator.

For focal-plane relative gain calibrators, planets or elevation nods serve as excellent choices. Given the angular resolution of the telescope, planets become high-intensity point sources. As for elevation nods, the telescope would be slewing up and down a few degrees in elevation while staring at the atmosphere. In both cases, the bolometers are staring at the same source, thus we can calibrate any difference between them to co-add them into one single map. Unfortunately, planets set and rise and are often time-consuming to observe. Moreover, they are not always available. So they cannot be used as a time-relative calibrator. Similarly, gain varies with the atmospheric opacity and across elevation and time, so elevation nods also present difficulties in being used as a time-relative calibrator [58]. In this sense, we can combine both planet and stimulator to develop a relative gain model, then use elevation nods as a consistency check. In operation, SA's strategy is to do a stimulator scan before and after every constant-elevation scan (CES) of either a planet or CMB. The next section, Section 7.2.1, explores how to go from optical power to temperature and extracts the conversion factor between temperature in Rayleigh-Jean (RJ) limit to the thermodynamic temperature variation of the CMB, which we often refer to this as CMB temperature. Planets operate in RJ limit, but ultimately, we want to convert the data into CMB temperature. So the final gain factor is in K_{CMB}. Then Section 7.2.2 outlines the process of how to get gain from planet data, followed by the description of getting the noise-equivalent temperature (NET) from gain in Section 7.2.3. Finally before diving into the analysis process and results, Section 7.2.4 describes how to extract gain from stimulator observations.

7.2.1 From Optical Power to Temperature

We want to know the amount of optical power or dP reaching the bolometer and how to equate this to temperature fluctuations. Let us derive this relationship between optical power and temperature fluctuation and how gain interplays into this process. Note that the following derivations in this section and the following ones reference [58, 59].

The power spectral density can be written as

$$p(T,\nu) = \eta(\nu)\varepsilon(\nu)S(T,\nu), \tag{7.3}$$

where $\eta(\nu)$ and $\varepsilon(\nu)$ are the transmission efficiency and emissivity, respectively. We know that CMB have a blackbody spectrum, thus $\varepsilon = 1$. For a polarimeter, an instrument that measures the polarization of light, the power spectral density function or $S(T,\nu)$ becomes

$$S(T,\nu) = \frac{h\nu}{e^{\frac{h\nu}{k_B T}} - 1}[59]. \tag{7.4}$$

Integrate Equation 7.3 and substitute Equation 7.4 into the integral, we get that the power received from the CMB for a single bolometer is

$$P_{opt}(T) = \int_0^\infty \eta(\nu)S(T,\nu)d\nu = \int_0^\infty \eta(\nu)\frac{h\nu}{e^\beta - 1}d\nu, \tag{7.5}$$

where $\beta \equiv \frac{h\nu}{k_BT}$. Taking the partial derivative of the above equation with respect to temperature, we get

$$\frac{\partial P}{\partial T_{CMB}} = \int_0^\infty \eta(\nu)h\nu d\nu(e^\beta - 1)^{-2}\left(\frac{h\nu}{k_BT^2}e^\beta\right) \tag{7.6}$$

$$\frac{\partial P}{\partial T_{CMB}} = \frac{h^2}{k_B}\int_0^\infty \eta(\nu)\left(\frac{\nu}{T_{CMB}}\right)^2 e^\beta n_{occ}^2 d\nu, \tag{7.7}$$

where $n_{occ} \equiv (e^\beta - 1)^{-1}$ is the average volume density of photons per spatial mode as a function of frequency. Measurements from the sky are taken over an integrated passband of the instrument as they pass through the band-defining filters on the detector wafer (see Figure 7.2). If we assume the spectral band is narrow with a center frequency, ν_c, then the equation becomes

$$\frac{\partial P}{\partial T_{CMB}} = k_B\beta_c^2\eta_c e^{\beta_c} n_{occ,c}^2 \Delta\nu. \tag{7.8}$$

For 150 GHz and at CMB Temperature, $\frac{\partial P}{\partial T_{CMB}} = 0.576 k_B\eta_c\Delta\nu$.

Since we use planets as a major source to extract the gain, let's move into the Rayleigh-Jeans (RJ) limit as our planets operate in this regime. Eventually, we want to switch back to units of CMB temperature to calibrate the CMB signal so getting a conversion factor between the two regimes is critical. In RJ limit, n_{occ} becomes

$$\lim_{\nu\to 0}\frac{1}{e^{\frac{h\nu}{k_BT}} - 1} \approx \frac{k_BT}{h\nu} \tag{7.9}$$

So Equation 7.5 becomes

$$P_{opt,RJ} = \int \eta(\nu) k_B T d\nu, \tag{7.10}$$

which for a narrow bandwidth, we have

$$\frac{\partial P}{\partial T_{RJ}} = \eta_c k_B \Delta\nu. \tag{7.11}$$

According to Equation 7.8 and 7.11, we have the following relation:

$$\frac{\partial P}{\partial T_{CMB}} = n_{occ,c}^2 \beta_c^2 e^{\beta_c} \frac{\partial P}{\partial T_{RJ}}. \tag{7.12}$$

Note that the above $n_{occ,c}$ and β_c are in the CMB temperature limit. Subsequently, unless specified, these two variables will always be in the CMB temperature limit. Thus, we now have a conversion factor between RJ limit and the temperature of the CMB, K_{CMB}. Again, for 150 GHz, that would be $\frac{\partial P}{\partial T_{CMB}} = 0.576 \frac{\partial P}{\partial T_{RJ}}$.

As the change in optical power is proportional to the measured current fluctuation through the bolometers, we have

$$\frac{\partial I}{\partial T_{CMB}} = n_{occ,c}^2 \beta_c^2 e^{\beta_c} \frac{\partial I}{\partial T_{RJ}}, \tag{7.13}$$

where $n_{occ,c}^2 \beta_c^2 e^{\beta_c}$ is the conversion to go from the gain in RJ to CMB and vice versa.

7.2.2 Using Planets to Extract Gain

We can first look at planet scans and use the beam information to establish a gain model that tracks how detectors' gain changes across the focal plane. Then using this model, one can co-add detectors to form a single co-added map. When scanning over a planet with an individual bolometer, we create a map from the TOD that is a convolution of the beam function with the source. So the power map is

$$m(\theta,\phi) = k_B\Delta\nu \int d\theta' d\phi' T(\theta',\phi') B(\theta-\theta',\phi-\phi'), \tag{7.14}$$

where $T(\theta',\phi')$ is the spatial distribution of the source temperature. With the arcmin resolution of the telescope, planets are point sources. So

$$T(\theta,\phi) = \delta(\theta)\delta(\phi) T_P \Omega_P. \tag{7.15}$$

T_P is the temperature of the planet, which has been measured from previous CMB experiments. Ω_P is the solid angle of the planet and can be extracted from planet catalogs online. Plugging the above equation into the power map, we get

$$m(\theta,\phi) = k_B \Delta\nu T_P \Omega_P B(\theta,\phi). \tag{7.16}$$

For a beam with a spatial profile, B(θ,ϕ), the efficiency is $\eta \equiv \int B(\theta,\phi) d\Omega$. So integrating the power map to get

$$\frac{\int m(\theta,\phi) d\Omega}{T_P \Omega_P} = k_B \Delta\nu \eta = g_{\frac{ADC}{K_{RJ}}}, \tag{7.17}$$

which is just the gain in RJ limit according to Equation 7.11. From planet maps, we can get the efficiency by integrating the beam profile and the integrated bandwidth through the integral of the power map.

Modeling the planet map as an elliptical Gaussian such that in the Cartesian coordinate, we get

$$m(x,y) = A_P e^{-1/2\left(\frac{(x-x_0)^2}{\sigma_x^2} + \frac{(y-y_0)^2}{\sigma_y^2}\right)}. \tag{7.18}$$

Integrating this planet map, we get

$$\int m(x,y)dxdy = 2A_P\pi\sigma_x\sigma_y, \tag{7.19}$$

where A_P is the planet amplitude in ADC. Thus the gain can be written as

$$\frac{1}{g_{\frac{ADC}{K_{RJ}}}} = g_{\frac{K_{RJ}}{ADC}} = \frac{T_P\Omega_P}{2A_P\pi\sigma_x\sigma_y}. \tag{7.20}$$

This result suggests that one can just fit an elliptical Gaussian to the planet signal in the TOD and extract the planet amplitude and beam size ($\sigma_x\sigma_y$) from the fit parameters and get the gain. T_P and Ω_P are the planet's thermodynamic temperature in RJ and the solid angle, respectively. These two parameters can be taken from astronomical catalogs.

7.2.3 From Gain to NET

An important detector characterization that uses the gain is the noise-equivalent temperature (NET). Generally, NET measures the sensitivity of the detectors of thermal radiation in the IR, THz, and microwave. It is the amount of incident signal temperature that would be needed to match the internal noise of the detector such that the SNR = 1. So NET$_{CMB}$ is the temperature anisotropy in 2.725 K CMB that if observed by detectors for 1 second would get an observed signal with an SNR = 1. A useful way to get NET is through the noise equivalent power or NEP, which measures the sensitivity of the detector system. NEP quantifies the amount of signal power one would see given an SNR = 1 in a 1 Hz output bandwidth. So

$$SNR = \frac{P}{NEP}, \tag{7.21}$$

where the unit for NEP is Watt/$\sqrt{Hz}$. According to the equation above, a smaller NEP yields a larger SNR. NEP can also be related to the current noise measured by the readout electronics, I_n, through the detector responsivity, S_I:

$$NEP = \frac{I_n}{S_I}. \tag{7.22}$$

Here, I_n is the detector's current noise for the n-th detector.

The relationship between NET and NEP can be described as

$$NET_{CMB} = \frac{NEP}{\sqrt{2}(dP/dT_{CMB})}. \tag{7.23}$$

The $\sqrt{2}$ comes from the Nyquist sampling rate. So when converting output bandwidth in $1/\sqrt{Hz}$ to integration time in $\sqrt{s}$.

Assume that we can fill the detector beam with temperature well in the RJ limit for our frequency band, then we can extract from Equation 7.11 that

$$\Delta P \approx \eta_c k_B \Delta\nu \Delta T, \tag{7.24}$$

where ΔT is the effective beam-filling temperature. We know that the responsivity is

$$S_I = \frac{\Delta I}{\Delta P_{opt}} = \frac{\Delta I}{k_B \eta_c \Delta\nu \Delta T}, \tag{7.25}$$

which plugging into Equation 7.22 and 7.23, we get

$$NET_{CMB} = \frac{I_n g_{\frac{T_{RJ}}{ADC}}}{\sqrt{2}\beta_c^2 e^{\beta,c} n_{occ}^2}, \tag{7.26}$$

where $g_{\frac{T_{RJ}}{ADC}}$ is the gain in RJ limit from planet scans and I_n can be found by estimating the white noise level of a power spectral density of the TOD.

7.2.4 Stimulator Gain

To co-add detectors from different observations taken at various times, we need a time-relative calibrator such as a stationary thermal source. PB-2b uses a stimulator, a thermal source behind the secondary mirror. Figure 7.4 illustrates a 3D model of the stimulator box. This whole box sits behind the secondary mirror and the light pipe pokes through the small hole at the center of the secondary mirror to direct the radiation from the heater to the receiver, PB-2b. The heater source is located in the back of the box. The chopper, between the heater and light pipe, is then spun at different frequencies to produce a square wave signal. The chopper's reference signal gives the square wave amplitude in each detector, A_f. Extracting the gain using the stimulator has been demonstrated on POLARBEAR [58] and PB-2a [60]. This section provides a summary of the formulation and calibration method, as PB-2b will be using the same method to generate the final gain model.

Calibration with the stimulator provides both the time constant and gain measurements. The detector's time constant, τ, characterizes the TES response to changes in incident radiation, including electrothermal feedback. So a smaller time constant indicates a faster response time. The time constant is observed to follow the one-pole response function as the observed signal decreases in amplitude at higher modulation frequencies. Hence, fitting these amplitudes (A_f) gives the amplitude of the overall DC response per detector or A_{therm} and τ:

$$A_f = \frac{A_{therm}}{\sqrt{1+(2\pi f\tau)^2}}, \tag{7.27}$$

where A_{therm} and τ are the extracted fitting parameters in ADC counts and seconds, respectively, based on modeling the thermal response of the bolometer as a single-pole thermal filter, which is well-motivated by the true response. The amplitude, A_f, varies at different chopped frequencies, while A_{therm} and τ remain the same.

We combine planet and stimulator methods to create a complete gain model that would

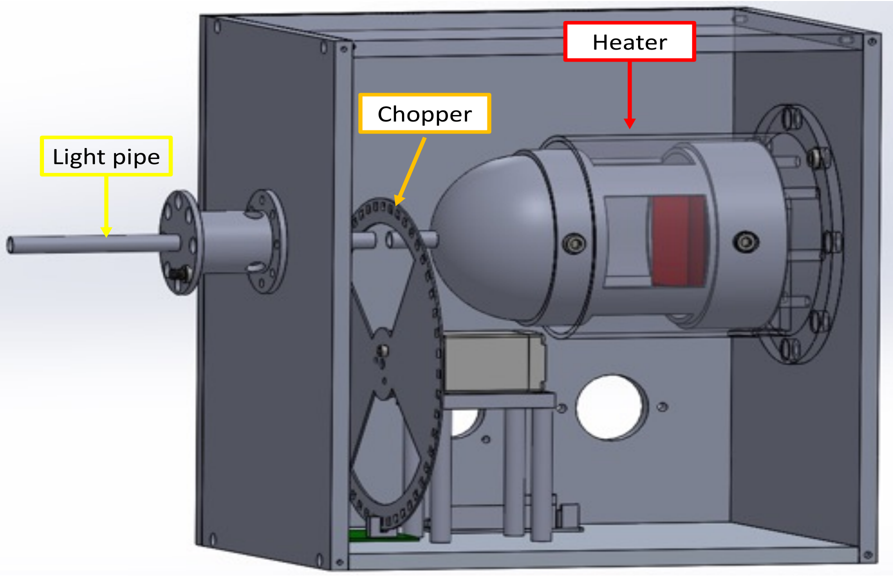

Figure 7.4. A 3D CAD of the stimulator for PB-2b. This whole assembly sits behind the secondary mirror. The light pipe goes through a hole in the center of the mirror to direct the radiation source to the receiver, PB-2b. The chopper is spun at different frequencies to chop the signal from the heater. Image courtesy of Lindsay Lowry. Designed and built by Praween Siritanasak.

allow us to co-add data from different detectors across the focal planes and observation scans. In operation, SA takes a stimulator measurement before and after each planet scan. The planet scans give $g_{\frac{ADC}{T_{RJ}}}$ as shown in Section 7.2.2. Stimulator measurements give $A_{therm,before}$ and $A_{therm,after}$ for before and after a planet scan. Combine the two would give the average of the overall DC response amplitude over the whole scan:

$$A_{therm} = \frac{A_{therm,before} + A_{therm,after}}{2}, \tag{7.28}$$

which if combined with the gain from the planet can generate an effective thermal source temperature for each detector:

$$T^i = \frac{A^i_{therm,planet}}{g^i_{\frac{ADC}{T_{RJ}}}}. \tag{7.29}$$

The *i* index represents the values for the i-th detector in the focal plane. The temperature template is further refined through multiple planet measurements taken at different times. Finally, we can use this T^i template to generate the gain for any measurements taken with the stimulator before and after the scan. So for a CMB observation, stimulator data would be taken before and after the CMB scan. Then the combined gain can be generated as

$$g^i_{\frac{T_{RJ}}{ADC},comb} = \frac{T^i}{A^i_{therm,CMB}}, \tag{7.30}$$

where $A^i_{therm,CMB}$ indicates the low-frequency limit of the response curve from stimulator measurements before and after a CMB scan. Apply this gain to the TOD and the conversion factor would then convert the data in ADC to the temperature variation of the CMB in Kelvin.

7.3 Beam Reconstruction and Planet Gain

This section describes the analysis process and results in reconstructing the instrument's beam and extracting beam information using planet observations such as Jupiter. SA adopts a constant elevation scan (CES) strategy where the telescope scans in azimuth at a constant elevation. Then it moves up an elevation and repeats the scan in the opposite azimuth direction. We define a subscan as a scan at a constant elevation such that a full run consists of multiple subscans at different elevations. We call at the end of each subscan where the telescope gets ready to turn around and scan in the opposite direction a "turnaround."

The calibration process starts with masking the spurious signals at the turnarounds due to the vibration from the mechanism. Then, I apply a series of polyfilters (e.g. 7-th then 3rd order) to each of the subscans to get rid of the low-frequency or 1/f noise in the TOD, flattening it. Following the process described in Section 7.2.2, I fit a 2D elliptical Gaussian with a rotation to the signal to account for any possible rotation of the planet due to the chosen coordinate system. The fit equation is similar to Equation 7.18 but with an additional rotation matrix, which when integrated would not make a difference in the result. The equation can be parameterized as

$$f(x,y) = Aexp\left(-\frac{1}{2}(\mathbf{u} - \mathbf{u}_0)^T K' (\mathbf{u} - \mathbf{u}_0)\right), \tag{7.31}$$

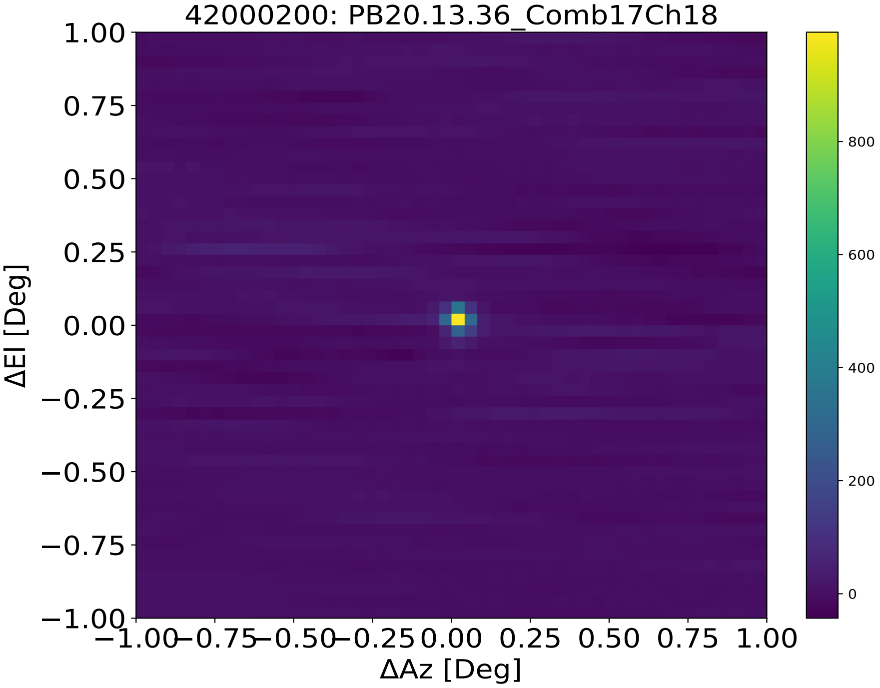

Figure 7.5. A source center map of Jupiter for a single detector with a pixel size of 0.04° or 2.4 arcmin.

where $K' = RK^{-1}R^T$ and R is the rotation matrix and K is the covariance matrix/sigma matrix.

$$K = \begin{pmatrix} \sigma_x^2 & \sigma_{xy} = 0 \\ \sigma_{xy} = 0 & \sigma_y^2 \end{pmatrix} \tag{7.32}$$

and the inverse of K is

$$K^{-1} = \begin{pmatrix} 1/\sigma_x^2 & 0 \\ 0 & 1/\sigma_y^2 \end{pmatrix} \tag{7.33}$$

and the rotation matrix is

$$R = \begin{pmatrix} cos\theta & -sin\theta \\ sin\theta & cos\theta \end{pmatrix} \tag{7.34}$$

Simplify everything and we get

$$RK^{-1}R^{T} = \begin{pmatrix} \frac{cos^2\theta}{\sigma_x^2} + \frac{sin^2\theta}{\sigma_y^2} & sin\theta cos\theta(\frac{1}{\sigma_x^2} - \frac{1}{\sigma_y^2}) \\ sin\theta cos\theta(\frac{1}{\sigma_x^2} - \frac{1}{\sigma_y^2}) & \frac{sin^2\theta}{\sigma_x^2} + \frac{cos^2\theta}{\sigma_y^2} \end{pmatrix} \tag{7.35}$$

and the fit equation for the analysis is

$$\begin{aligned} f(x,y) = A * exp\Bigg(-\frac{1}{2}\Bigg[(x-x_0)^2\left(\frac{cos^2\theta}{\sigma_x^2} + \frac{sin^2\theta}{\sigma_y^2}\right) + \\ 2(x-x_0)(y-y_0)sin\theta cos\theta\left(\frac{1}{\sigma_x^2} - \frac{1}{\sigma_y^2}\right) + (y-y_0)^2\left(\frac{sin^2\theta}{\sigma_x^2} + \frac{cos^2\theta}{\sigma_y^2}\right)\Bigg]\Bigg). \end{aligned} \tag{7.36}$$

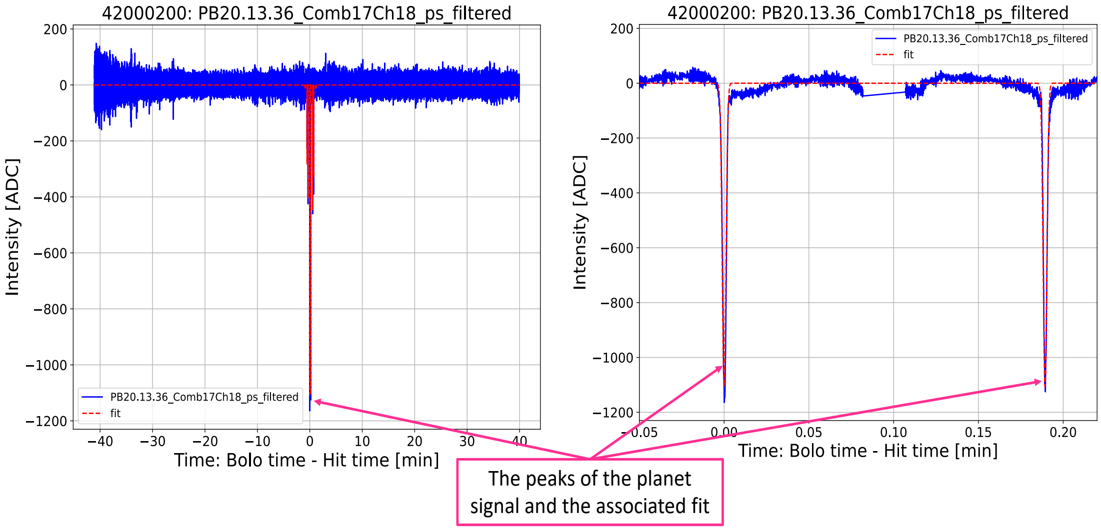

Figure 7.6. Fits to Jupiter Signal for a Detector. Left: the time-ordered data (TOD) for a detector that saw Jupiter (the large dips in the middle) as a function of time in minutes. The x-axis is the bolometer time minus the hit time, showing that the peak of Jupiter's signal is at 0. The planet signals are negative due to the negative electrothermal feedback mechanism when the bolometer is in transition. Right is a zoom-in view of the two largest peaks with the fit in red.

Figure 7.5 shows a map of Jupiter for a bolometer in the middle wafer on the focal plane as a function of change in elevation and azimuth. The signal here has been centered to be at (0, 0) degrees. This is the intensity plotted in ADC counts. Figure 7.6 demonstrates an example of the planet-fitting process. The TOD on the left is the polyfiltered TOD with all turnarounds masked. We can also see the masked turnarounds by looking at the jump in the blue data point in the right plot at about 0.10 min. The x-axis is the bolometer's time minus the hit time, where the fit thinks the planet is. This way the planet is centered at 0 min. The blue data point here is the same intensity data as that of Figure 7.5, except that I flip the sign in the map to make intensity positive. In fact, the measured signal from the planet is negative when the detector sees it due to the negative electrothermal feedback loop. In this process, the increase in optical signal from the planet would cause a negative change in electrical power and this manifests as a negative reading in ADC. The red line is the fit from Equation 7.36. The right plot zooms into the two highest peaks for a clearer view of the fit.

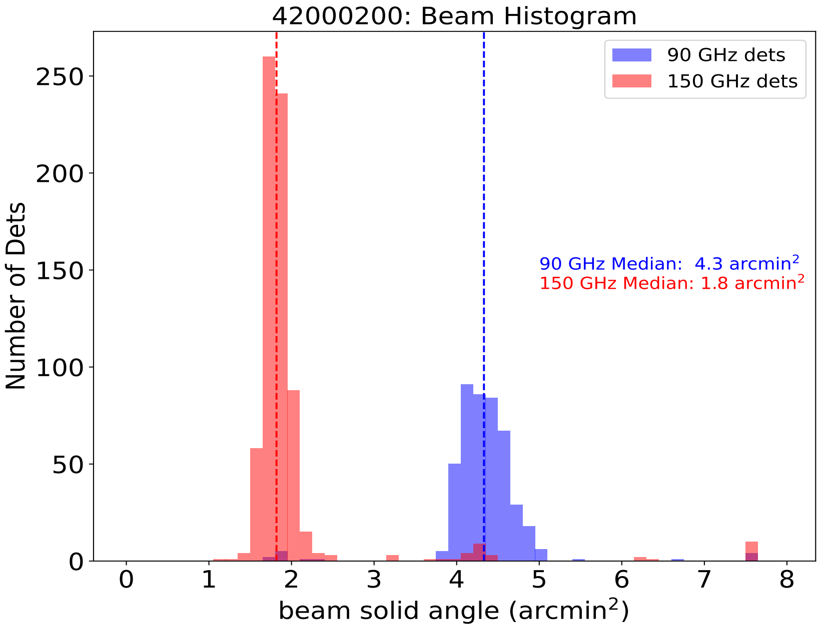

Figure 7.7. Historgram of the Beam Size for a Jupiter Observation. The two populations of detectors and their corresponding beam sizes are shown here. The beam size or beam solid angle is $\sigma_{beam}^2 = \sigma_x \sigma_y$ from the fit parameters. The 90 GHz detectors, sensitive to signal in this band, have a median beam size of 4.3 ± 0.5 arcmin^2. 150 GHz detects' beam size is 1.8 ± 0.8 arcmin^2.

Using the fit parameters, I then extract information on the beam solid angle ($\sigma_x \sigma_y$) and the planet's amplitude [ADC]. Figure 7.7 plots a histogram of the beam solid angle or beam size for the bolometers in the two frequency bands, 90 and 150 GHz. As previously mentioned, the angular resolution for a 2.5 primary mirror is 5.2 and 3.5 arcmin for 90 and 150 GHz, respectively. Approximating the angular resolution to be the full-width-half-max (FWHM) of the beam and using the relationship between FWHM and σ for a Gaussian distribution, we then have

$$\sigma = \frac{\text{FWHM}}{2\sqrt{2ln2}}. \tag{7.37}$$

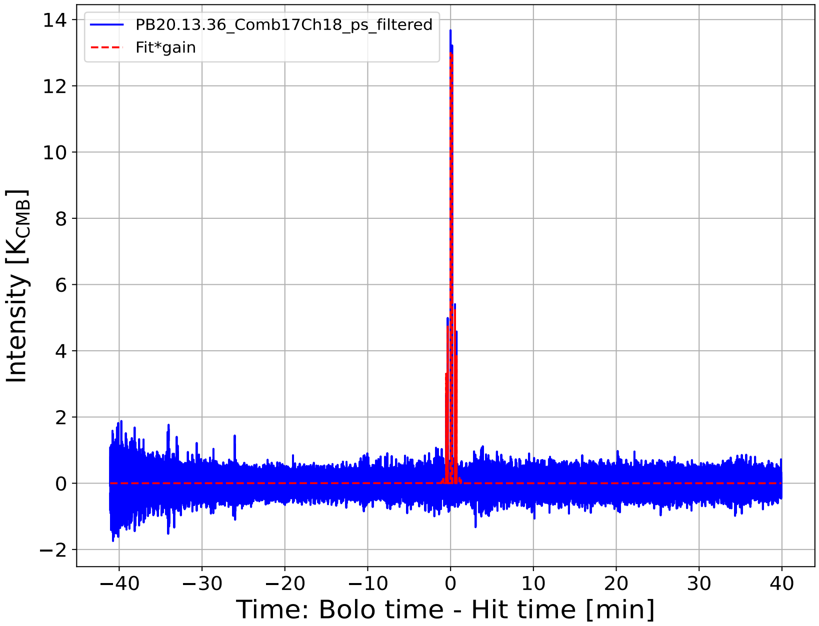

Figure 7.8. Time-ordered data in K_{CMB}. The same TOD as in Figure 7.6 but this time converted to Kelvin-CMB. Notice that the signal direction flips, which makes sense that the planet signal should be a positive number. Again, the data is in blue and the fit is in red.

According to the reported θ values, the beam design solid angles are 4.88 and 2.22 arcmin^2 for the two bands. From this Jupiter observation, the median beam sizes for the 90 and 150 GHz bands are (4.3 ± 0.5) and (1.8 ± 0.8) arcmin^2, respectively. The measurements are consistent with the designed beam sizes. From the yielded beam information, one can then get an initial gain factor following the process in Section 7.2.2 and using Equation 7.20. Then applying this initial gain factor to the raw TOD converts the data from ADC to Kelvin as shown in Figure 7.8. Notice that the planet's signal is now positive Kelvin. After calibrating all detectors into units of CMB temperature, we can add up detectors across the focal plane for a planet map of intensity. This is only the first part of the gain calibration. The next step is to use the stimulator measurements to get a combined gain factor to co-add data across observations at different times. This analysis is reserved for future work. See Section 7.4 for more details.

7.4 Future Outlook

PB-2b achieved its first light in early 2023 and has since conducted numerous planetary observations, leading to the development of an initial gain model for data calibration. After a temporary pause due to stimulator hardware issues, further measurements will be resumed and used for the gain calibration process as detailed in Section 7.2.4. The site team has been working to install the rest of the warm readout electronics and resolve various hardware problems. As the first SA receiver to deploy a cryogenic half-wave plate (CHWP) to module the polarization signal, it is crucial to understand the receiver's performance and the systematic effects from the CHWP, as these will impact the gain model. In summary, the PB-2b team is working on characterizing the CHWP performance, improving the NET, and initiating scientific operations.

Bibliography

[1] Wayne Hu and Martin White. A cmb polarization primer. *New Astronomy*, 2(4):323–344, 1997.

[2] Y. Akrami, M. Ashdown, J. Aumont, C. Baccigalupi, M. Ballardini, A. J. Banday, and et al. Planck2018 results: Iv. diffuse component separation. *Astronomy amp; Astrophysics*, 641:A4, September 2020.

[3] Peter Ade, James Aguirre, Zeeshan Ahmed, Simone Aiola, Aamir Ali, and et al. The simons observatory: science goals and forecasts. *Journal of Cosmology and Astroparticle Physics*, 2019(02):056–056, February 2019.

[4] Steven Weinberg. *Cosmology*. 2008.

[5] Scott Dodelson. *Modern Cosmology*. Academic Press, Elsevier Science, 2003.

[6] Brian Albert Robson. Introductory chapter: Standard model of cosmology. In Brian Albert Robson, editor, *Redefining Standard Model Cosmology*, chapter 1. IntechOpen, Rijeka, 2019.

[7] CHARLES H. LINEWEAVER. Inflation and the cosmic microwave background. In *The New Cosmology*. WORLD SCIENTIFIC, June 2005.

[8] P. de Bernardis, P. A. R. Ade, J. J. Bock, J. R. Bond, J. Borrill, A. Boscaleri, K. Coble, C. R. Contaldi, B. P. Crill, G. De Troia, P. Farese, K. Ganga, M. Giacometti, E. Hivon, V. V. Hristov, A. Iacoangeli, A. H. Jaffe, W. C. Jones, A. E. Lange, L. Martinis, S. Masi, P. Mason, P. D. Mauskopf, A. Melchiorri, T. Montroy, C. B. Netterfield, E. Pascale, F. Piacentini, D. Pogosyan, G. Polenta, F. Pongetti, S. Prunet, G. Romeo, J. E. Ruhl, and F. Scaramuzzi. Multiple Peaks in the Angular Power Spectrum of the Cosmic Microwave Background: Significance and Consequences for Cosmology. , 564(2):559–566, January 2002.

[9] Dorothea Samtleben, Suzanne Staggs, and Bruce Winstein. The cosmic microwave background for pedestrians: A review for particle and nuclear physicists. *Annual Review of Nuclear and Particle Science*, 57(1):245–283, November 2007.

[10] A. A. Penzias and R. W. Wilson. A Measurement of Excess Antenna Temperature at 4080 Mc/s. , 142:419–421, July 1965.

[11] R. H. Dicke, P. J. E. Peebles, P. G. Roll, and D. T. Wilkinson. Cosmic Black-Body Radiation. , 142:414–419, July 1965.

[12] J. C. Mather, E. S. Cheng, D. A. Cottingham, Jr. Eplee, R. E., D. J. Fixsen, T. Hewagama, R. B. Isaacman, K. A. Jensen, S. S. Meyer, P. D. Noerdlinger, S. M. Read, L. P. Rosen, R. A. Shafer, E. L. Wright, C. L. Bennett, N. W. Boggess, M. G. Hauser, T. Kelsall, Jr. Moseley, S. H., R. F. Silverberg, G. F. Smoot, R. Weiss, and D. T. Wilkinson. Measurement of the Cosmic Microwave Background Spectrum by the COBE FIRAS Instrument. , 420:439, January 1994.

[13] D. J. Fixsen. The temperature of the cosmic microwave background. *The Astrophysical Journal*, 707(2):916, nov 2009.

[14] J. M. Kovac, E. M. Leitch, C. Pryke, J. E. Carlstrom, N. W. Halverson, and W. L. Holzapfel. Detection of polarization in the cosmic microwave background using dasi. *Nature*, 420(6917):772–787, December 2002.

[15] Y. Akrami, T. Ghosh, J. J. Bock, B. P. Crill, O. Doré, G. M. Rocha, K. M. Górski, C. R. Lawrence, S. Mitra, G. Roudier, and et al. Planck 2018 results. x. constraints on inflation. *Astronomy and Astrophysics*, 641:Art. No. A10, Sep 2020. Funding by European Space Agency (ESA).

[16] Marc Kamionkowski and Ely D. Kovetz. The quest for b modes from inflationary gravitational waves. *Annual Review of Astronomy and Astrophysics*, 54(1):227–269, 2016.

[17] Wayne Hu and Takemi Okamoto. Mass reconstruction with cosmic microwave background polarization. *The Astrophysical Journal*, 574(2):566–574, August 2002.

[18] P. A. R. Ade et al. Improved constraints on primordial gravitational waves using planck, wmap, and bicep/keck observations through the 2018 observing season. *Phys. Rev. Lett.*, 127:151301, Oct 2021.

[19] Giuseppe Puglisi, Gueorgui Mihaylov, Georgia V Panopoulou, Davide Poletti, Josquin Errard, Paola A Puglisi, and Giacomo Vianello. Improved galactic foreground removal for b-mode detection with clustering methods. *Monthly Notices of the Royal Astronomical Society*, 511(2):2052–2074, January 2022.

[20] Maximiliano Silva-Feaver. *Microwave SQUID Multiplexing for the Simons Observatory Cosmic Microwave Background Telescopes*. PhD thesis, UC San Diego, 2023.

[21] Z. Xu and Simons Observatory Collaboration. The Simons Observatory: the Large Aperture Telescope (LAT). In *American Astronomical Society Meeting Abstracts*, volume 53 of *American Astronomical Society Meeting Abstracts*, page 214.03, January 2021.

[22] Ningfeng Zhu, Tanay Bhandarkar, Gabriele Coppi, Anna M. Kofman, John L. Orlowski-Scherer, Zhilei Xu, Shunsuke Adachi, Peter Ade, Simone Aiola, Jason Austermann, Andrew O. Bazarko, James A. Beall, Sanah Bhimani, J. Richard Bond, Grace E. Chesmore,

Steve K. Choi, Jake Connors, Nicholas F. Cothard, Mark Devlin, Simon Dicker, Bradley Dober, Cody J. Duell, Shannon M. Duff, Rolando Dünner, Giulio Fabbian, Nicholas Galitzki, Patricio A. Gallardo, Joseph E. Golec, Saianeesh K. Haridas, Kathleen Harrington, Erin Healy, Shuay-Pwu Patty Ho, Zachary B. Huber, Johannes Hubmayr, Jeffrey Iuliano, Bradley R. Johnson, Brian Keating, Kenji Kiuchi, Brian J. Koopman, Jack Lashner, Adrian T. Lee, Yaqiong Li, Michele Limon, Michael Link, Tammy J Lucas, Heather McCarrick, Jenna Moore, Federico Nati, Laura B. Newburgh, Michael D. Niemack, Elena Pierpaoli, Michael J. Randall, Karen Perez Sarmiento, Lauren J. Saunders, Joseph Seibert, Carlos Sierra, Rita Sonka, Jacob Spisak, Shreya Sutariya, Osamu Tajima, Grant P. Teply, Robert J. Thornton, Tran Tsan, Carole Tucker, Joel Ullom, Eve M. Vavagiakis, Michael R. Vissers, Samantha Walker, Benjamin Westbrook, Edward J. Wollack, and Mario Zannoni. The simons observatory large aperture telescope receiver. *The Astrophysical Journal Supplement Series*, 256(1):23, September 2021.

[23] A. Schillaci, P. A. R. Ade, Z. Ahmed, M. Amiri, D. Barkats, R. Basu Thakur, C. A. Bischoff, et al. Design and Performance of the First BICEP Array Receiver. *Journal of Low Temperature Physics*, 199(3-4):976–984, February 2020.

[24] Nicholas Galitzki, Tran Tsan, Jake Spisak, Michael Randall, Max Silva-Feaver, Joseph Seibert, Jacob Lashner, Shunsuke Adachi, Sean M. Adkins, Thomas Alford, Kam Arnold, Peter C. Ashton, Jason E. Austermann, Carlo Baccigalupi, Andrew Bazarko, James A. Beall, Sanah Bhimani, Bryce Bixler, Gabriele Coppi, Lance Corbett, Kevin D. Crowley, Kevin T. Crowley, Samuel Day-Weiss, Simon Dicker, Peter N. Dow, Cody J. Duell, Shannon M. Duff, Remington G. Gerras, John C. Groh, Jon E. Gudmundsson, Kathleen Harrington, Masaya Hasegawa, Erin Healy, Shawn W. Henderson, Johannes Hubmayr, Jeffrey Iuliano, Bradley R. Johnson, Brian Keating, Ben Keller, Kenji Kiuchi, Anna M. Kofman, Brian J. Koopman, Akito Kusaka, Adrian T. Lee, Richard A. Lew, Lawrence T. Lin, Michael J Link, Tammy J. Lucas, Marius Lungu, Aashrita Mangu, Jeffrey J McMahon, Amber D. Miller, Jenna E. Moore, Magdy Morshed, Hironobu Nakata, Federico Nati, Laura B. Newburgh, David V. Nguyen, Michael D. Niemack, Lyman A. Page, Kana Sakaguri, Yuki Sakurai, Mayuri Sathyanarayana Rao, Lauren J. Saunders, Jordan E. Shroyer, Junna Sugiyama, Osamu Tajima, Atsuto Takeuchi, Refilwe Tanah Bua, Grant Teply, Tomoki Terasaki, Joel N. Ullom, Jeffrey L. Van Lanen, Eve M. Vavagiakis, Michael R Vissers, Liam Walters, Yuhan Wang, Zhilei Xu, Kyohei Yamada, and Kaiwen Zheng. The simons observatory: Design, integration, and testing of the small aperture telescopes, 2024.

[25] C. A. Hill, A. Kusaka, P. Ashton, P. Barton, T. Adkins, K. Arnold, B. Bixler, S. Ganjam, A. T. Lee, F. Matsuda, T. Matsumura, Y. Sakurai, R. Tat, and Y. Zhou. A cryogenic continuously rotating half-wave plate mechanism for the POLARBEAR-2b cosmic microwave background receiver. *Review of Scientific Instruments*, 91(12):124503, 12 2020.

[26] Charles Alexander Hill. *Sensitivity Simulations and Half-wave Plate Polarization Modulators for Cosmic Microwave Background Observatories*. PhD thesis, UC Berkeley, 2020.

[27] K. Yamada, B. Bixler, Y. Sakurai, P. C. Ashton, J. Sugiyama, K. Arnold, J. Begin, L. Corbett, S. Day-Weiss, N. Galitzki, C. A. Hill, B. R. Johnson, B. Jost, A. Kusaka, B. J. Koopman, J. Lashner, A. T. Lee, A. Mangu, H. Nishino, L. A. Page, M. J. Randall, D. Sasaki, X. Song, J. Spisak, T. Tsan, Y. Wang, and P. A. Williams. The simons observatory: Cryogenic half wave plate rotation mechanism for the small aperture telescopes. *Review of Scientific Instruments*, 95(2), February 2024.

[28] Erin Healy, Daniel Dutcher, Zachary Atkins, Jason Austermann, Steve K. Choi, Cody J. Duell, Shannon Duff, Nicholas Galitzki, Zachary B. Huber, Johannes Hubmayr, Bradley R. Johnson, Heather McCarrick, Michael D. Niemack, Rita Sonka, Suzanne T. Staggs, Eve Vavagiakis, Yuhan Wang, Zhilei Xu, and Kaiwen Zheng. The simons observatory 220 and 280 ghz focal-plane module: Design and initial characterization. *Journal of Low Temperature Physics*, 209(5–6):815–823, July 2022.

[29] Erin Healy. *The Universal Focal-plane Module for Simons Observatory*. PhD thesis, Princeton University, 2023.

[30] Heather McCarrick, Erin Healy, Zeeshan Ahmed, Kam Arnold, Zachary Atkins, Jason E. Austermann, Tanay Bhandarkar, James A. Beall, Sarah Marie Bruno, Steve K. Choi, Jake Connors, Nicholas F. Cothard, Kevin D. Crowley, Simon Dicker, Bradley Dober, Cody J. Duell, Shannon M. Duff, Daniel Dutcher, Josef C. Frisch, Nicholas Galitzki, Megan B. Gralla, Jon E. Gudmundsson, Shawn W. Henderson, Gene C. Hilton, Shuay-Pwu Patty Ho, Zachary B. Huber, Johannes Hubmayr, Jeffrey Iuliano, Bradley R. Johnson, Anna M. Kofman, Akito Kusaka, Jack Lashner, Adrian T. Lee, Yaqiong Li, Michael J. Link, Tammy J. Lucas, Marius Lungu, J. A. B. Mates, Jeffrey J. McMahon, Michael D. Niemack, John Orlowski-Scherer, Joseph Seibert, Maximiliano Silva-Feaver, Sara M. Simon, Suzanne Staggs, Aritoki Suzuki, Tomoki Terasaki, Robert Thornton, Joel N. Ullom, Eve M. Vavagiakis, Leila R. Vale, Jeff Van Lanen, Michael R. Vissers, Yuhan Wang, Edward J. Wollack, Zhilei Xu, Edward Young, Cyndia Yu, Kaiwen Zheng, and Ningfeng Zhu. The simons observatory microwave squid multiplexing detector module design. *The Astrophysical Journal*, 922(1):38, November 2021.

[31] Heather McCarrick, Kam Arnold, Zachary Atkins, Jason Austermann, Tanay Bhandarkar, Steve K. Choi, Cody J. Duell, Shannon M. Duff, Daniel Dutcher, Nicholas Galitzk, Erin Healy, Zachary B. Huber, Johannes Hubmayr, Bradley R. Johnson, Michael D. Niemack, Joseph Seibert, Maximiliano Silva-Feaver, Rita F. Sonka, Suzanne T. Staggs, Eve M. Vavagiakis, Yuhan Wang, Zhilei Xu, Kaiwen Zheng, and Ningfeng Zhu. The 90 and 150 ghz universal focal-plane modules for the simons observatory, 2021.

[32] Jason R. Stevens, Nicholas F. Cothard, Eve M. Vavagiakis, Aamir Ali, Kam Arnold, Jason E. Austermann, Steve K. Choi, Bradley J. Dober, Cody Duell, Shannon M. Duff, Gene C. Hilton, Shuay-Pwu Patty Ho, Thuong D. Hoang, Johannes Hubmayr, Adrian T. Lee, Aashrita Mangu, Federico Nati, Michael D. Niemack, Christopher Raum, Mario Renzullo, Maria Salatino, Trevor Sasse, Sara M. Simon, Suzanne Staggs, Aritoki Suzuki, Patrick Truitt, Joel Ullom, John Vivalda, Michael R. Vissers, Samantha Walker, Benjamin

Westbrook, Edward J. Wollack, Zhilei Xu, and Daniel Yohannes. Characterization of transition edge sensors for the simons observatory. *Journal of Low Temperature Physics*, 199(3–4):672–680, February 2020.

[33] S. M. Duff et al. Advanced ACTPol Multichroic Polarimeter Array Fabrication Process for 150 mm Wafers. *J. Low Temp. Phys.*, 184(3-4):634–641, 2016.

[34] Aritoki Suzuki et al. Multi-chroic Dual-Polarization Bolometric Focal Plane for Studies of the Cosmic Microwave Background. *J. Low Temp. Phys.*, 167(5-6):852–858, 2012.

[35] A. Suzuki, P. Ade, Y. Akiba, C. Aleman, K. Arnold, C. Baccigalupi, B. Barch, D. Barron, A. Bender, D. Boettger, J. Borrill, S. Chapman, Y. Chinone, A. Cukierman, M. Dobbs, A. Ducout, R. Dunner, T. Elleflot, J. Errard, G. Fabbian, S. Feeney, C. Feng, T. Fujino, G. Fuller, A. Gilbert, N. Goeckner-Wald, J. Groh, T. De Haan, G. Hall, N. Halverson, T. Hamada, M. Hasegawa, K. Hattori, M. Hazumi, C. Hill, W. Holzapfel, Y. Hori, L. Howe, Y. Inoue, F. Irie, G. Jaehnig, A. Jaffe, O. Jeong, N. Katayama, J. Kaufman, K. Kazemzadeh, B. Keating, Z. Kermish, R. Keskitalo, T. Kisner, A. Kusaka, M. Le Jeune, A. Lee, D. Leon, E. Linder, L. Lowry, F. Matsuda, T. Matsumura, N. Miller, K. Mizukami, J. Montgomery, M. Navaroli, H. Nishino, J. Peloton, D. Poletti, G. Puglisi, G. Rebeiz, C. Raum, C. Reichardt, P. Richards, C. Ross, K. Rotermund, Y. Segawa, B. Sherwin, I. Shirley, P. Siritanasak, N. Stebor, R. Stompor, J. Suzuki, O. Tajima, S. Takada, S. Takakura, S. Takatori, A. Tikhomirov, T. Tomaru, B. Westbrook, N. Whitehorn, T. Yamashita, A. Zahn, and O. Zahn. The Polarbear-2 and the Simons Array Experiments. *Journal of Low Temperature Physics*, 184(3-4):805–810, August 2016.

[36] Erin E. Healy, Aamir M. Ali, Kam Arnold, Jason E. Austermann, James A. Beall, Sarah Marie Bruno, Steve K. Choi, Jake Connors, Nicholas F. Cothard, Bradley Dober, Shannon M. Duff, Nicholas Galitzki, Gene Hilton, Shuay-Pwu Patty Ho, Johannes Hubmayr, Bradley R. Johnson, Yaqiong Li, Michael J. Link, Tammy J. Lucas, Heather McCarrick, Michael D. Niemack, Maximiliano Silva-Feaver, Rita F. Sonka, Suzanne Staggs, Eve M. Vavagiakis, Michael R. Vissers, Yuhan Wang, Edward J. Wollack, Zhilei Xu, Benjamin Westbrook, and Kaiwen Zheng. Assembly development for the simons observatory focal plane readout module. In Jonas Zmuidzinas and Jian-Rong Gao, editors, *Millimeter, Submillimeter, and Far-Infrared Detectors and Instrumentation for Astronomy X*. SPIE, December 2020.

[37] Tran Tsan, Nicholas Galitzki, Aamir M. Ali, Kam Arnold, Gabriele Coppi, Tamar Ervin, Logan Foote, Brian Keating, Jack Lashner, John Orlowski-Scherer, Michael J. Randall, Joseph Seibert, Jacob Spisak, Grant P. Teply, Zhilei Xu, and Ningfeng Zhu. The effects of inclination on a two stage pulse tube cryocooler for use with a ground based observatory. *Cryogenics*, 117:103323, July 2021.

[38] W. E. Gifford and R. C. Longsworth. Pulse-Tube Refrigeration. *Journal of Engineering for Industry*, 86(3):264–268, 08 1964.

[39] R. Radebaugh. Development of the pulse tube refrigerator as an efficient and reliable cryocooler. In *London: IIR*, volume 96 of *Proceedings of the Institute of Refrigeration*, pages 11–31, 1999-2000.

[40] P. Goutham Raj, Animesh Biswas, and Subrata Kr. Ghosh. Phasor analysis of two-stage gm-type pulse tube refrigerator. In *Special Issue 3: ICERTSD 2013*, volume 3, pages 376–381, February 2013.

[41] J. Robert B. Laughlin. Pulse tube cryocoolers: A cryogen-free path to 2k.

[42] T. Fang, I. Mulcahey, P.S. Spoor, M.D. Perrella, T. J. Conrad, and S. M. Ghiaasiaan. Investigation of gravitational effects in pulse tube cryocooers using 3-d cfd simulations. In *Cryocoolers 19*, International Cryocooler Conference, Inc., Boulder, CO, pages 183–192, 2016.

[43] G. Thummes, M. Schreiber, R. Landgraf, and C. Heiden. Convective heat losses in pulse tube coolers: Effect of pulse tube inclination. In *Cryocoolers 9*, Proc. 9th International Cryocooler Conference, Waterville Valley, NH, USA, pages 393–492. Plenum Press, New York, 1997.

[44] C. Wang and P. E. Gifford. Development of 4 K pulse tube cryorefrigerators at cryomech. In Susan Breon, Michael Dipirro, David Glaister, John Hull, Peter Kittel, Radebaugh Ray Pecharsky, Vitalij, Jay Theilacker, Steven van Sciver, II Weisend, John, and Albert Zeller, editors, *Advances in Cryogenic Engineering CEC*, volume 47 of *American Institute of Physics Conference Series*, pages 641–648, May 2002.

[45] C. Wang and P. E. Gifford. A single-stage pulse tube cryocooler for horizontally cooling hts mri probe. *AIP Conference Proceedings*, 710(1):1805–1811, 2004.

[46] R. Ross and D. Johnson. Effect of gravity orientation on the thermal performance of stirling-type pulse tube cryocoolers. *Cryogenics*, 44:403–408, 2004.

[47] D. S. Swetz, P. A. R. Ade, C. Allen, M. Amiri, J. W. Appel, E. S. Battistelli, et al. *Instrument design and characterization of the Millimeter Bolometer Array Camera on the Atacama Cosmology Telescope*, volume 7020 of *Society of Photo-Optical Instrumentation Engineers (SPIE) Conference Series*, page 702008. 2008.

[48] Brian J. Koopman, Jack Lashner, Lauren J. Saunders, Matthew Hasselfield, Tanay Bhandarkar, Sanah Bhimani, et al. The Simons Observatory: Overview of data acquisition, control, monitoring, and computer infrastructure. *arXiv e-prints*, page arXiv:2012.10345, December 2020.

[49] Christophe Risacher, Rolf Guesten, Juergen Stutzki, Heinz-Wilhelm Hübers, Denis Buechel, Urs Graf, et al. First supra-THz heterodyne array receivers for astronomy with the sofia observatory. *IEEE Trans. Terahertz Sci. Technol.*, 6:199–2016, December 2016.

[50] Kevin D. Crowley, Peter Dow, Jordan E. Shroyer, John C. Groh, Bradley Dober, Jacob Spisak, Nicholas Galitzki, Tanay Bhandarkar, Mark J. Devlin, Simon Dicker, Patricio A. Gallardo, Kathleen Harrington, Jeffrey Iuliano, Bradley R. Johnson, Delwin Johnson, Anna M. Kofman, Akito Kusaka, Adrian Lee, Michele Limon, Federico Nati, John Orlowski-Scherer, Lyman Page, Michael Randall, Grant Teply, Tran Tsan, Edward J. Wollack, Zhilei Xu, and Ningfeng Zhu. The Simons Observatory: A large-diameter truss for a refracting telescope cooled to 1 K. *Review of Scientific Instruments*, 93(5):055106, May 2022.

[51] Mayuri Sathyanarayana Rao, Maximiliano Silva-Feaver, Aamir Ali, Kam Arnold, Peter Ashton, Bradley J. Dober, Cody J. Duell, Shannon M. Duff, Nicholas Galitzki, Erin Healy, Shawn Henderson, Shuay-Pwu Patty Ho, Jonathan Hoh, Anna M. Kofman, Akito Kusaka, Adrian T. Lee, Aashrita Mangu, Justin Mathewson, Philip Mauskopf, Heather McCarrick, Jenna Moore, Michael D. Niemack, Christopher Raum, Maria Salatino, Trevor Sasse, Joseph Seibert, Sara M. Simon, Suzanne Staggs, Jason R. Stevens, Grant Teply, Robert Thornton, Joel Ullom, Eve M. Vavagiakis, Benjamin Westbrook, Zhilei Xu, and Ningfeng Zhu. Simons Observatory Microwave SQUID Multiplexing Readout – Cryogenic RF Amplifier and Coaxial Chain Design. *arXiv e-prints*, page arXiv:2003.08949, March 2020.

[52] M.V. Jacob, J. Mazierska, K. Leong, and J. Krupka. Microwave properties of low-loss polymers at cryogenic temperatures. *IEEE Transactions on Microwave Theory and Techniques*, 50(2):474–480, 2002.

[53] Yufang Zhang and Zhenqing Wang. Measurement of dielectric loss tangent at cryogenic temperature using superconducting film resonator. *Journal of Theoretical and Applied Physics*, 10, 11 2015.

[54] Lindsay Ng Lowry. *Preparation and Deployment of the Telescopes and POLARBEAR-2b Receiver for the Simons Array Cosmic Microwave Background Polarization Experiment*. PhD thesis, UC San Diego, 2021.

[55] Y. Inoue, P. Ade, Y. Akiba, C. Aleman, K. Arnold, C. Baccigalupi, B. Barch, D. Barron, A. Bender, D. Boettger, J. Borrill, S. Chapman, Y. Chinone, A. Cukierman, T. de Haan, M. A. Dobbs, A. Ducout, R. Dünner, T. Elleflot, J. Errard, G. Fabbian, S. Feeney, C. Feng, G. Fuller, A. J. Gilbert, N. Goeckner-Wald, J. Groh, G. Hall, N. Halverson, T. Hamada, M. Hasegawa, K. Hattori, M. Hazumi, C. Hill, W. L. Holzapfel, Y. Hori, L. Howe, F. Irie, G. Jaehnig, A. Jaffe, O. Jeong, N. Katayama, J. P. Kaufman, K. Kazemzadeh, B. G. Keating, Z. Kermish, R. Keskitalo, T. S. Kisner, A. Kusaka, M. Le Jeune, A. T. Lee, D. Leon, E. V. Linder, L. Lowry, F. Matsuda, T. Matsumura, N. Miller, K. Mizukami, J. Montgomery, M. Navaroli, H. Nishino, H. Paar, J. Peloton, D. Poletti, G. Puglisi, C. R. Raum, G. M. Rebeiz, C. L. Reichardt, P. L. Richards, C. Ross, K. M. Rotermund, Y. Segawa, B. D. Sherwin, I. Shirley, P. Siritanasak, N. Stebor, R. Stompor, J. Suzuki, A. Suzuki, O. Tajima, S. Takada, S. Takatori, G. P. Teply, A. Tikhomirov, T. Tomaru, N. Whitehorn, A. Zahn, and O. Zahn. POLARBEAR-2: an instrument for CMB polarization measurements. In Wayne S. Holland and Jonas Zmuidzinas, editors, *Millimeter, Submillimeter, and Far-Infrared Detectors and Instrumentation for Astronomy VIII*, volume 9914 of *Society of*

Photo-Optical Instrumentation Engineers (SPIE) Conference Series, page 99141I, July 2016.

[56] Jennifer Chiemi Ito. *Characterization and Deployment of the POLARBEAR-2b Receiver to Measure the Cosmic Microwave Background Polarization*. PhD thesis, UC San Diego, 2022.

[57] Logan Howe. *The POLARBEAR-2 Cryogenic Receiver for Cosmic Microwave Background Polarization Science*. PhD thesis, UC San Diego, 2019.

[58] David Boettger. *CMB Polarization Measurements with the Polarbear Experiment*. PhD thesis, UC San Diego, 2014.

[59] Charles A. Hill, Sarah Marie Bruno, Sara M. Simon, Aamir Ali, Kam S. Arnold, Peter C. Ashton, Darcy Barron, Sean Bryan, Yuji Chinone, Gabriele Coppi, Kevin T. Crowley, Ari Cukierman, Simon Dicker, Jo Dunkley, Giulio Fabbian, Nicholas Galitzki, Patricio A. Gallardo, Jon E. Gudmundsson, Johannes Hubmayr, Brian Keating, Akito Kusaka, Adrian T. Lee, Frederick Matsuda, Philip D. Mauskopf, Jeff McMahon, Michael D. Niemack, Giuseppe Puglisi, Mayuri S. Rao, Maria Salatino, Carlos Sierra, Suzanne Staggs, Aritoki Suzuki, Grant Teply, Joel N. Ullom, Benjamin Westbrook, Zhilei Xu, and Ningfeng Zhu. Bolocalc: a sensitivity calculator for the design of simons observatory. In Jonas Zmuidzinas and Jian-Rong Gao, editors, *Millimeter, Submillimeter, and Far-Infrared Detectors and Instrumentation for Astronomy IX*. SPIE, July 2018.

[60] Daisuke Kaneko, Sayuri Takatori, Masaya Hasegawa, Masashi Hazumi, Yuki Inoue, Oliver Jeong, Nobuhiko Katayama, Adrian T. Lee, Frederick Matsuda, Haruki Nishino, Praween Siritanasak, Aritoki Suzuki, Satoru Takakura, and Takayuki Tomaru. Design and performance of a gain calibration system for the POLARBEAR-2a receiver system at the Simons Array cosmic microwave background experiment. *Journal of Astronomical Telescopes, Instruments, and Systems*, 10(1):018003, 2024.